




Universitat Autònoma de Barcelona

ADVERTIMENT. L'accés als continguts d'aquesta tesi queda condicionat a l'acceptació de les condicions d'ús establertes per la següent llicència Creative Commons:  http://cat.creativecommons.org/?page_id=184

ADVERTENCIA. El acceso a los contenidos de esta tesis queda condicionado a la aceptación de las condiciones de uso establecidas por la siguiente licencia Creative Commons:  <http://es.creativecommons.org/blog/licencias/>

WARNING. The access to the contents of this doctoral thesis it is limited to the acceptance of the use conditions set by the following Creative Commons license:  <https://creativecommons.org/licenses/?lang=en>

On the Displacement Current in THz Quantum Nanodevices: Application to the Simulation of Graphene Transistors

by

Zhen Zhan

B.S. in Materials Physics, 2010

M.S. in Condensed Matter Physics, 2013

Submitted to the
Departament d'Enginyeria Electrònica
in partial fulfillment of the requirements for the degree
of
PhD in Electronic Engineering and Telecommunication
at the
Universitat Autònoma de Barcelona
May 2017

Certified by.....

Xavier Oriols Pladevall

Titular d'Universitat, Departament d'Enginyeria Electrònica

Thesis Supervisor

The undersigned, Dr. **Xavier Oriols Pladevall**, professor of the Department of Electronic Engineering (Engineering School) of the *Universitat Autònoma de Barcelona*,

CERTIFY:

That the thesis entitled “**On the displacement current in THz quantum nanodeivces: application to the simulation of graphene transistors**” has been written by the Ph. D. candidate **Zhen Zhan** under his supervision, in fulfillment of the requirements for the PhD degree of Electrical Engineering and Telecommunication.

And hereby to acknowledge the above, sign the present.

Xavier Oriols Pladevall

Zhen Zhan

Bellaterra (Cerdanyola del vallès), May 22 2017

On the Displacement Current in THz Quantum Nanodevices: Application to the Simulation of Graphene Transistors

by

Zhen Zhan

Submitted to the Departament d'Enginyeria Electrònica
on May 25, 2017, in partial fulfillment of the
requirements for the degree of
PhD in Electronic Engineering and Telecommunication

Abstract

Nowadays, the scientific community envisions nanoscale electronic devices working at TeraHertz (THz) frequencies. For such frequencies, the displacement current—the temporal variation of the electric flux—has a role as relevant as the particle current. In addition, for such dimensions, typical semi-classical simulation tools have to be substituted by quantum ones. However, the correct modelling of the electrical displacement current in quantum scenarios implies important fundamental and practical challenges. The first issue is the quantum measurement problem, which requires a multi-time measurement process to extract information of the open system at THz frequencies. The second challenge is related with the many-body problem, which implies that the Coulomb interaction among all particles needs to be taken into account to properly get the time-dependent electric flux. In this dissertation, it has been presented a practical solution on both problems based on Bohmian mechanics—an explanation of quantum phenomena based on particles moving choreographed by the wave function. In particular, the conditional wave function, the Bohmian definition of a wave function of an open system, has been used to provide a practical solution to both problems. The mentioned Bohmian solution for the computation of the displacement current in quantum devices has been included into the BITLLES simulator. The correct modelling of the quantum dissipation inside the open system and its spatial boundary conditions with the conditional wave function have been discussed. The same problems have many difficulties when trying to be tackled with orthodox theories.

As practical applications, the high frequency behaviors of graphene-based nanodevices are investigated with special attention to the proper computation of particle and displacement currents. From such computations, it is argued that the definition of the intrinsic cut off frequency (f_T) of nanodevices based on the current gain equals to one (0 dB) needs to be carefully revisited. In particular, a condition for the validity of the quasi-static estimation of f_T is established in terms of the temporal variations of the electric charge and electric flux. For electron devices working at THz frequencies, the quasi-static estimation becomes inaccurate and prediction models beyond the quasi-static approximation are required. A proposal based on the time-dependent simulation of the intrinsic delay time (including particle and displacement currents) following the Bohmian-type ideas mentioned above has been presented.

Sobre la corriente de desplazamiento en nanodispositivos cuánticos de THz: aplicación a la simulación de transistores de grafeno

Resumen: En la actualidad, la comunidad científica está trabajando en dispositivos electrónicos en la nanoscala para frecuencias de TeraHertzios (THz). Para tales frecuencias, la corriente de desplazamiento -la variación temporal del flujo eléctrico- tiene un papel tan relevante como la corriente de la partícula. Además, para tales dimensiones, las típicas herramientas de simulación semi-clásicas tienen que ser sustituidas por otras cuánticas. Sin embargo, el modelado correcto de la corriente de desplazamiento eléctrico en los escenarios cuánticos implica importantes desafíos fundamentales y prácticos. El primer problema es el problema de la medición cuántica que requiere un proceso de medición multi-tiempo para extraer información del sistema abierto en las frecuencias THz. La segunda cuestión está relacionada con el problema de muchos cuerpos, lo que implica que la interacción de Coulomb entre todas las partículas debe tenerse en cuenta para obtener correctamente el flujo eléctrico dependiente del tiempo. En esta tesis, se presenta una solución práctica para ambos problemas basados en la mecánica Bohmiana, una explicación de los fenómenos cuánticos en términos de partículas moviéndose coreografiadas por una función de onda. En particular, se aprovecha la función de onda condicional, la definición Bohmiana de una función de onda de un sistema abierto, para proporcionar una solución práctica a ambos problemas. La solución Bohmiana mencionada para el cálculo de la corriente de desplazamiento en dispositivos cuánticos se ha incluido en el simulador BITLLES. También se discute sobre el correcto modelado de la disipación cuántica dentro del sistema abierto y sus condiciones de contorno espaciales con la función de onda condicional. Los mismos problemas tienen muchas dificultades al intentar abordarse con teorías ortodoxas.

Como aplicaciones prácticas, se investigan los comportamientos de alta frecuencia de los nanodispositivos a base de grafeno con especial atención al cálculo de las corrientes de partículas y desplazamiento. A partir de estos cálculos, se argumenta que la definición de la frecuencia de corte intrínseca (f_T) de los nanodispositivos basada en la ganancia de corriente igual a uno (0 dB) necesita ser revisada cuidadosamente. En particular, se establece una condición para la validez de la estimación cuasi estática de f_T en términos de las variaciones temporales de la carga eléctrica y del flujo eléctrico. Para los dispositivos electrónicos que trabajan en las frecuencias THz, la estimación cuasi-estática se vuelve inexacta y se requieren modelos de predicción más allá de esta aproximación. Se ha presentado una propuesta basada en la simulación en función del tiempo del retardo intrínseco que sufren las señales (incluyendo corrientes de partículas y desplazamiento) basada en las ideas mencionadas anteriormente.

This dissertation is dedicated to my beloved little B.

*“It is only with the heart that one can see rightly;
what is essential is invisible to the eye.”
—Le Petit Prince, Antoine de Saint-Exupéry.*

Acknowledgments

Undertaking this PhD has been a life-changing experience for me and it could not have been completed without the support and guidance that I received from dozens of people.

First of all, I am greatly indebted to my supervisor Dr. Xavier Oriols Pladevall for accepting me as his PhD student and introducing me to the uncertain Quantum World. His zeal for research, passion for “problems”, unflinching courage has always inspired me to do more. I remember there was one time he told me that the PhD study was like climbing a mountain. Up to now, I wish I would have arrived at the top of the mountain of my PhD. Once again, my special thanks to him for constant help and support during these four years.

I gratefully acknowledge the financial support for my PhD study from the China Scholarship Council (CSC). I would like to express my sincere thanks to my previous supervisors Prof. Qin Ye and Prof. Pengyi Liu at Jinan University for contributing significantly towards the CSC grant application and for valuable suggestions for my future career.

Some faculty members of the department of electronic engineering at UAB have also been very kind to extend their help for this these, whenever I approached them. The members of the NANOCOMP group have contributed immensely to my professional time at UAB. I would like to acknowledge Dr. David Jiménez, Dr. Xavier Cartoixó, Dr. Guillermo Albareda and Dr. Fabio Traversa for their valuable advices and stimulating discussions, which led to the successful completion of my research work. I thank Dr. Marc Porti and Dr. Enrique Miranda for their intriguing questions in the annual evaluation. My thanks to Dr. Ferran Martín, Dr. Rosana Rodríguez and Dr. Arantxa Uranga for their generous help.

I would like to thank my colleagues in the department of electronic engineering at UAB. I thank Ferney Chaves and Francisco Pasadas for helping me find the comfortable flat. My thanks to Enrique Colomé and Damiano Marian for the excellent dinner. Thank to Qian Wu, Ferran Jovell, Laura Urquiza and Martí Raya for sharing the office with me. Special thanks to Pedro Carlos Feijoo, Marcos Maestro, Devashish Pandey, Pau Aguilà, Lijuan Su.

I wish to thank my friends Liu He, Tong Liu, Min Cao, Liang Li, Yanyan Meng and Depeng Chen. They have offered me unlimited encouragement and help for my life in Barcelona.

This thesis could not have been accomplished without Hu Huang, my partner who is always with me no matter how bold my decisions were (like the decision to study abroad). He always gives me encouragement and love in every situation. Thanks to the rest of

my family, my parents Fuying Lu and Xinmin Zhan, my beloved niece Yajie Zhan, my brother Hao Zhan for their encouragement and support.

Contents

Acknowledgments	v
1 Fundamental Issues in THz Quantum Transport	1
1.1 Historical Development of Electronics	1
1.1.1 Graphene and other 2DMs based FETs	3
1.1.2 Physical theories for electron devices	4
1.2 Displacement Current and Electronics	5
1.2.1 Particle Current Versus Displacement Current	5
1.2.2 Equivalence between Computed and Measured Currents	7
1.3 The Many-Body Problem in Electronics	8
1.4 Electron Device as Open and Stochastic Systems	10
1.4.1 Internal Openness of the System	11
1.4.2 External Openness of the System	11
1.5 Equilibrium and Non-Equilibrium in Electron Devices	13
1.6 Irreversible Phenomena in Electron Devices: a Fundamental Law of Nature	14
2 Measurement of Quantum Transport	17
2.1 The Measurement Problem	17
2.1.1 The Orthodox Approach	19
2.1.2 The Bohmian Approach	20
2.1.3 The Many-Worlds Approach	21
2.2 The Quantum Measurement Problem in Electron Devices	22
2.2.1 A Preliminary Discussion	22
2.2.2 The Multi-Time Measurement with Orthodox Approach	24
2.2.3 The Multi-Time Measurement with Bohmian Approach	26
2.3 Prediction of DC and Total Currents with Orthodox Approach	29
2.3.1 The DC Current	30
2.3.2 The Total Current	32
2.4 Prediction of DC and Total Currents with the Bohmian Approach	35

3	Stochastic Injection of Electrons	41
3.1	Introduction	41
3.1.1	Irreversible Boundary Conditions for Open System	42
3.1.2	Frenseley Boundary Conditions for Open System	43
3.1.3	Limitations of the Frenseley Boundary Conditions	45
3.1.4	SISOW as irreversible Boundary Conditions in Time-Dependent Picture	48
3.2	Electron Injection Model for 2D Materials	49
3.2.1	2D Materials with a Parabolic Dispersion Relation	49
3.2.2	2D Materials with a Linear Dispersion Relation	52
3.3	Implementation of the Injection Model into the BITLLES Simulator . . .	55
4	Dissipative Transport Through Collisions	63
4.1	Preliminary Discussions	63
4.1.1	The Density Matrix Formalism	64
4.1.2	The Wigner Distribution Function Formalism	65
4.1.3	Unphysical Negative Charge Density Found in the Literature for Quantum Transport Models	66
4.2	To Know or not to Know the Quantum States	67
4.2.1	Collisions Without Knowing the Quantum States	70
4.2.2	Collisions Knowing the Quantum States	76
4.3	Collisions with Conditional Wave Functions	80
4.3.1	Conditioned Hamiltonian for the Electron-Phonon Interaction . .	83
4.3.2	Equation of motion of the conditional wave functions	88
4.3.3	Example of Collisions in a Resonant Tunneling Device	89
5	High-Frequency Behaviour of FETs: Practical Computations of Graphene Devices	93
5.1	The Theoretical Discussion	93
5.1.1	The Ramo-Shockley-Pellegrini Theorem	93
5.1.2	The Role of Different Dielectric Constants on the Total Current Behaviour	95
5.1.3	The Role of Device Geometry on the Total Current Behaviour . .	96
5.2	Practical Computations for Graphene FETs	99
5.2.1	PSD without Klein Tunneling and only Positive Energy Injection	103
5.2.2	PSD with Klein Tunneling and only Positive Energy Injection . .	104
5.2.3	PSD with Klein Tunneling and Positive-Negative Energy Injection	106

6	Limitations of f_T to Correctly Quantify the Speed of Nanoscale Transistors: Practical Computations of 2D Devices	109
6.1	The Theoretical Discussion	109
6.1.1	Fourier Analysis of f_T	111
6.1.2	Conditions for the Validity of the Quasi-Static Estimation of f_T .	115
6.2	Practical Computations for 2D FETs	116
6.2.1	Example 1 (Device A): Conditions for the Validity of the Quasi-Static Approximation	117
6.2.2	Example 2 (Device B and Device C): Limitations of the Quasi-Static Approximation	120
6.2.3	Example 3 (Device D): the Infinite Value of f_T	125
7	Conclusions	129
	Bibliography	133
A	A Primer on Bohmian Mechanics	147
A.1	The Bohmian Mechanics for Many-Particle Systems	148
A.1.1	Rediscovering of the Bohmian Mechanics	150
A.2	Conditional Wave Function	151
A.2.1	Bohmian Velocity Computed from the Conditional Wave Function	152
A.2.2	Equation of Motion of the Conditional Wave Function	152
A.3	Bohmian Mechanics in Phase Space	154
A.3.1	The Bohmian Phase Space Distribution	155
A.3.2	The Wigner and Husimi Distributions	157
A.3.3	Comparing the Bohmian, Wigner and Husimi Distributions	158
B	Using the Image Method to Solve the Problem of a Point Charge in Presence of Three Dielectric Media with Planar Interfaces	165
C	Publications and Conferences	167

CHAPTER 1

Fundamental Issues in THz Quantum Transport

1.1 Historical Development of Electronics

The electronics and their usages have changed our life style dramatically since the beginning of the 20th century when the electronics took birth. Over one century passed, a huge number of electronic devices are used to simplify our life and the electronics become so important that it is impossible for people to spend even a few hours without them. In this Chapter 1, firstly, I will give some important milestones of the evolution of electronics. In order to achieve higher performance, the dimensions of electronic devices are becoming smaller and smaller. As a consequence, the understanding of electron transport in such devices is changing from classical (or semiclassical) theories into quantum ones. Therefore, after the introductory history, I will discuss some fundamental issues in the computation of quantum electron transport, which also plays an important role in the continuous and rapid development of electronics.

The electronics took birth in 1904 when John Ambrose invented a two-element vacuum tube—the diode, where electric current can flow in one direction through the diode between two electrodes. Electronics became a more versatile discipline in 1906 when Lee Deforest invented the three-element tube called a vacuum triode for use as an electronic amplifier in radio communications. In the triode, an additional electrode between the cathode and anode makes the device able to amplify signals for all frequencies. The tubes dominated the field of electronics at that time. However, the tubes have major limitations: its macroscopic size, its reliability and they consumed electrical power even when not be used. In 1947, William Shockley, John Bardeen and Walter Brattain fabricated the first solid-state transistor, which made them awarded the Nobel Prize in Physics in 1956. The Silicon transistors were developed in 1954. In 1958, Jack Kilby conceived the concept of building an entire electronic circuit on a single silicon substrate. Kilby was awarded

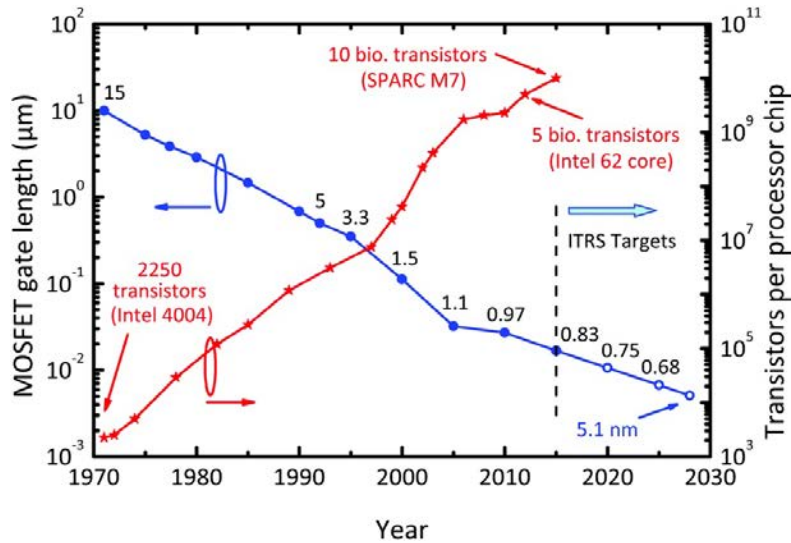


Figure 1.1.1: Evolution of the metal-oxide-semiconductor field-effect transistor (MOSFET) gate length and the number of transistors integrated on a single microprocessor chip. The numbers above the gate length curve indicate the processor supply voltage V_{DD} . Note the continuous decrease of V_{DD} in the past and the required continuation of this trend in the future. The ITRS targets refer to MOSFETs for high-performance logic as specified in the 2013 ITRS edition [1].

the Nobel Prize in Physics in 2000 for the invention of the integrated circuit. The field-effect transistors (FETs) become the backbone of today's electronics. Since then, the size of the transistors was reduced drastically, and the number of the integrated components on a chip was doubled every year. Based on such an empirical evidence, Gordon Moore stated that the number of components per integrated circuit would double in performance every two years [2]. At this point, it is important to mention the roadmap published for the semiconductor industry, which is named the International Technology Roadmap for Semiconductors (ITRS). This roadmap is probably the most important blueprint in the electronic industry, and it presents an industry-wide consensus on the best estimate of the research and developments needed in a 15-year horizon. The core progress in the first versions of the ITRS was the geometrical scaling and equivalent scaling (i.e., strained silicon, multigate transistors, high-K/metal gate, use of non-silicon semiconductors in general) of semiconductor logic and memory devices, which successfully supported the regularly double growth of the density of integrated circuits according to the Moore's Law. According to the ITRS roadmap, transistors with gate lengths below 5 nm will be required in 2028 [1]. At this stage of scaling, it becomes more difficult to achieve the needed device performance due to the problems of short-channel effects, parasitics effects, etc.[3]. In order to keep on with Moore's Law, new device geometries and new materials are required [1, 3–5]. Two-dimensional (2D) materials, i.e., graphene and other

2D materials like transition metal dichalcogenides (TMDs), Bi_2Se_3 and Bi_2Te_3 , provide ultimate thin ‘channel’ transistors and the opportunity for new device concepts [5, 6]. Hereafter, I will mainly concentrate on the devices based on 2D materials.

1.1.1 Graphene and other 2DMs based FETs

Although many new materials have been proposed as candidates to substitute the old-fashioned Silicon FETs, a recent article concluded that : “*many such saviours have come and gone, yet the reliable silicon CMOS continues to be scaled and to reach even higher performance levels* ” [7]. Among these new materials, graphene was viewed by the scientific community as a new material with a great potential impact in our society, in general, and in electronics, in particular [4, 8]. Graphene is a single 2D layer of carbon atoms with a hexagonal lattice [8]. It has a linear energy-momentum dispersion (which provides massless Dirac fermions), an extraordinary elasticity (allowing flexible electronics) and extremely large electrical conductivity (with electron velocities of 10^6 m/s) [9]. However, graphene has a zero bandgap implying a small on-off ratio for graphene digital FETs. It is important to notice that reliable techniques to create a sizeable gap degrade a lot the properties mentioned above. Therefore, it seems that successful graphene logic applications are not currently feasible. On the contrary, the large conductivity of graphene is very welcome for (small-signal) radio frequency applications (such as amplifiers or mixers) [4, 10, 11] which are not required to switch off.

Although the best performance of nowadays radio-frequency graphene transistors is still quite below the one obtained from Silicon and III-V HEMTs [4], significant progress has been made since the experimental demonstration of the first GigaHertz graphene transistors in 2008 [12]. Most notably, a research group reported graphene FETs breaking the 100-GHz cut-off frequency (f_T) mark in 2010 [13]. Furthermore, only a few months later, researchers demonstrated [14] a graphene FET that has a f_T of 300 GHz. In 2012, graphene FETs with cut-off frequency exceeding 400 GHz has been reported [15]. Undoubtedly, graphene FETs consist a very young class of devices compared to the traditional FETs. After the enthusiastic days of research, the electronic community realizes that the graphene would not be able to fulfill these high expectations owing to its zero bandgap since a reasonable bandgap is mandatory needed for proper device operation [3].

In 2011, a paper on the fabrication of single-layer MoS_2 gave new momentum to the research on 2D materials [16]. The ITRS has mentioned other 2DMs as candidates for future electronics since 2011 [17]. In fact, already in 2005, the Novoselov-Geim group reported the preparation of single-layer materials (for instance, MoS_2 , $MoSe_2$, $MoTe_2$ and WS_2) other than graphene [18]. The experimental MoS_2 FETs show reasonable mobilities and excellent switch-off [16, 19]. On the theoretical work, simulation results

qualitatively confirm the experimental results and predict very high ON-OFF ratios with monolayer dichalcogenide channels [20, 21].

1.1.2 Physical theories for electron devices

Generally, the success of the rapid evolution of electronics has been supported by sophisticated physical theories to make prediction on the characteristics of new electron devices. The modeling of electron transport in electronic devices has become a mandatory tool to characterize these devices before the fabrication. During the last decades, due to the increase of the complexity and cost of the technological processes necessary to fabricate device prototypes, predictions of their functionality allow to rule out certain designs, which lead to the research and development cost reduction amount to 35% and to increase up to 40% in the near future [22]. Inspiring by these compelling demands from the electronic community, an uncountable number of electron device approaches, with more or less physical complexities, from simple circuit-based simulations till many-body quantum approaches, have been developed by the scientific researchers in last years. Most of them (specially those involving quantum features like tunneling or energy quantization) are mainly focus on DC simulations.

The ITRS reports that electron devices are entering into the nanoscale era with working frequencies of few TeraHertz (THz). As indicated above, the predictions of the high-frequency features of nanoelectronic devices are based on quasi-static approximations, where the time derivative of the electric fields is neglected. Undoubtedly, there are many successful examples in the literature on how quasi-static approaches are still capable of getting reliable THz information of quantum devices. Among many others, we mentioned those based on time-independent solutions of the Non-Equilibrium Green's function framework, for example the Klimeck's group with the NEMO simulator [23] or Fiori and Iannaccone's group with the NANOTCAD ViDES simulator [6]. In this regard, the *ab initio* (time-independent ground-state) density functional theory (DFT) has also been successfully used in the literatures for such graphene THz predictions [24, 25]. The strategy of all these time-independent (steady-state) quantum simulators for predicting, for example, the cut-off frequency is, first, simulating the dependence of DC currents and charges on (gate voltages), then, calculating transconductances and capacitances from such simulations. Finally, they plug these values of transconductances and capacitances into analytical expressions of the cut-off frequency (usually obtained from a small-signal circuit model). In any case, Such procedure has been demonstrated to be very successful, providing very-valuable physical insight of the high frequency quantum problems while greatly reducing the computational burden associated to explicit time-dependent simulations [5, 5, 26].

An important part of this dissertation will concentrate on discussing the origin of

the potential limitations of these quasi-static quantum electron transport models. Due to its enormous physical complexity, approximations are required in the computation of electron transport. Some fundamental problems that requires approximations are, for example, the many-body problem and quantum measurement problem. After this brief introduction of the electronics, in the following, I will explicitly discussed the fundamental problems appear in the computation of quantum transport at THz frequencies.

1.2 Displacement Current and Electronics

The displacement current is somehow ignored in the quantum modeling of electron transport with the DC approximation. In this section, I will discuss the relevance of the displacement current in quantum transport simulation.

1.2.1 Particle Current Versus Displacement Current

Historically, the first scientists who realized on the relevance of the displacement current in electronics were S. Ramo and W. Shockley. In 1938, Ramo wrote in his paper that [27]: *“in designing devices in which the electron transit time is relatively long, it is necessary to discard the low-frequency concept that the instantaneous current computed on a particular surface is proportional to the number of electrons crossed this surface per second (i.e., the particle current, which is also named as the conduction current), and a proper concept of current must also consider the instantaneous change of electrostatic flux lines which end on the surface (i.e., the displacement current)”*. At the same time, Shockley also mentioned this issues [28]: *“in the scenario that the electron transit time is of comparable duration with the periods of alternating circuits, it is consequently of interest to know the instantaneous value of the current induced by the moving charge over its entire time of transit”*. Their work relating microscopic electron dynamics with macroscopic displacement currents is known now as the Ramo-Shockley theorem. This theorem was originally proposed for vacuum tubes, which was the state-of-the-art device at that time. Since then, its extension to semiconductors and any conducting medium has been performed [29–31]. Indeed, it is of great importance in the semiclassical simulation of electron devices beyond DC behaviour, i.e., for investigating AC, transient and noise characteristics.

At this point, let us give a simple theoretical estimation on why we pay attention to the displacement current. A direct expression of the typical drift (particle) current $I_p(t)$ on surface S is:

$$I_p(t) = \int_S \vec{J}_c(\vec{r}, t) \cdot d\vec{s} \approx nq\vec{v}A_S \quad (1.1)$$

where $\vec{J}_c(\vec{r}, t)$ is the particle current density, n is the number of electrons crossed the

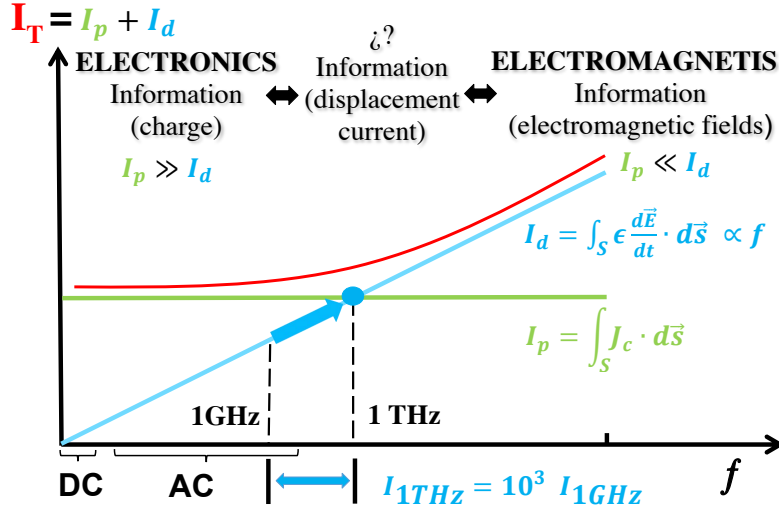


Figure 1.2.1: Frequency dependence of the particle and displacement currents.

surface S per unit volume, q is the electron charge with sign, \vec{v} is the drift velocity, A_S is the cross-sectional area of surface S . The particle current (i.e. the flux of electrons on a particular surface) is basically related to the injection rate of electrons from the contact and its order of magnitude is not modified when the input signal frequency f of the device is increased. Assuming that $n \approx 10^{20} \text{ m}^{-3}$, $q \approx 1.6 \times 10^{-19} \text{ C}$, $\vec{v} = 10^5 \text{ m/s}$ and $A_S = 10^{-12} \text{ m}^2$, we get a typical estimation of the particle current on the order of micro Amperes (A), $I_p(t) \approx 10^{-6} \text{ A}$, independent of the frequency. On the other hand, the direct expression of the displacement current $I_d(t)$ on surface S is:

$$I_d(t) = \int_S \epsilon(\vec{r}) \frac{d\vec{E}(\vec{r}, t)}{dt} \cdot d\vec{s} \quad (1.2)$$

where $\epsilon(\vec{r})$ is the electric permittivity, $\vec{E}(\vec{r}, t)$ is the electric field. Imaging that the electric permittivity is $\epsilon(\vec{r}) \approx 10^{-12} \text{ F/m}$, the electric field is $\vec{E}(\vec{r}, t) \approx E_0 \cos(\omega t)$ being $E_0 \approx 10^6 \text{ V/m}$ a constant and $\omega = 2\pi f$ the angular frequency, then the displacement current expression is rewritten as:

$$I_d(t) \approx A_S \cdot \epsilon(\vec{r}) \frac{d\vec{E}(\vec{r}, t)}{dt} \approx 2\pi A_S \epsilon(\vec{r}) E_0 f \approx 10^{-18} f \quad (1.3)$$

which is linearly dependent on the input signal frequency f . The simple estimation of the frequency-dependent particle and displacement currents are plotted in figure 1.2.1. At very low frequencies, only the particle current is relevant, while the displacement current becomes negligible in front of the particle current. This is the typical working region of electronics. On the contrary, at frequencies high enough, the displacement current (proportional to the frequency growth) becomes the only relevant current. It can be

orders of magnitude larger than the particle current. This is the typical working scenario for applications based on electromagnetics. The two lines cross at a frequency around $f = 1$ THz, at which the particle current equals the displacement one. Certainly, in the frontier between typical electronics and electromagnetism there is a spectrum where both displacement and particle currents become relevant. We argue that nanoelectronics is reaching this new area where one also envisions new concepts of devices, between electronics and electromagnetism.

1.2.2 Equivalence between Computed and Measured Currents

Next, let us discuss a general relationship between the current measured in a laboratory and the current predicted. It is common to compute the electrical current on the (simulated) surface S_D ($S_D=S_1$ at the device contact) of the active region in figure 1.2.2, while a real measurement is performed on the (non-simulated) surface S_A in the ammeter. Then, the question appears: *Does the current simulated on S_D equals to the current on S_A measured by the ammeter?* In fact, these currents will only be identical if we consider the total current $I_T(t) = I_p(t) + I_d(t)$. The justification comes from Maxwell equations. Let us start from the current conservation law:

$$\vec{\nabla} \cdot \vec{j}_c(\vec{r}, t) + \frac{\partial \rho(\vec{r}, t)}{\partial t} = 0 \quad (1.4)$$

where ρ is the free electric charge density in the wire volume Λ enclosed by a larger surface $S = \{S_D, S_A, S_L\}$. As we have discussed previously, the first term on the left hand side of equation (1.4) is the particle current density, the ρ in the second term can be related to the electric field by using the Gauss's law, which is:

$$\vec{\nabla} \cdot (\epsilon(\vec{r}) \vec{E}(\vec{r}, t)) = \rho(\vec{r}, t) \quad (1.5)$$

Rewriting the ρ in equation (1.4) with the expression (1.5), we obtain:

$$\begin{aligned} \vec{\nabla} \cdot \vec{j}_c(\vec{r}, t) + \frac{\partial}{\partial t} \vec{\nabla} \cdot (\epsilon(\vec{r}) \vec{E}(\vec{r}, t)) &= \vec{\nabla} \cdot \vec{j}_c(\vec{r}, t) + \vec{\nabla} \cdot \epsilon(\vec{r}) \frac{\partial \vec{E}(\vec{r}, t)}{\partial t} \\ &= \vec{\nabla} \cdot \left(\vec{j}_c(\vec{r}, t) + \epsilon(\vec{r}) \frac{\partial \vec{E}(\vec{r}, t)}{\partial t} \right) = 0 \end{aligned} \quad (1.6)$$

From the equation (1.6), we can define the total current density $\vec{J}_T(\vec{r}, t)$, which is a combination of the particle current density $\vec{J}_c(\vec{r}, t)$ and the displacement current density $\vec{J}_d(\vec{r}, t)$, as:

$$\vec{J}_T(\vec{r}, t) = \vec{J}_c(\vec{r}, t) + \vec{J}_d(\vec{r}, t) = \vec{j}_c(\vec{r}, t) + \epsilon(\vec{r}) \frac{\partial \vec{E}(\vec{r}, t)}{\partial t} \quad (1.7)$$

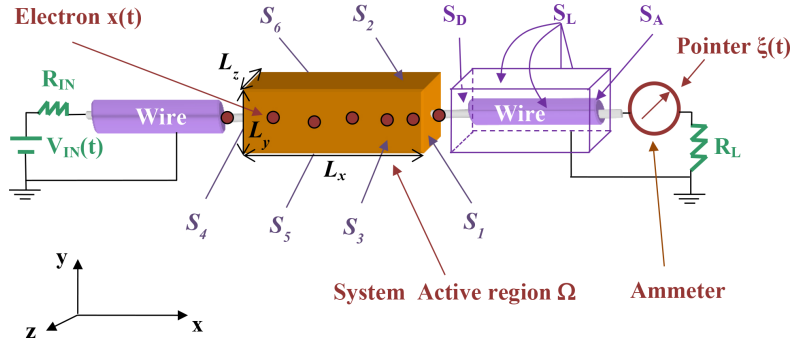


Figure 1.2.2: Schematic representation of a typical electrical circuit used for studying the difference between the computed and the measured currents in electrical devices.

Using the divergence theorem in the current conservation law in equation (1.6), we can rewrite the expression as:

$$\int_{\Lambda} \vec{\nabla} \cdot \vec{J}_T(\vec{r}, t) dv = \int_{S_D + S_L + S_A} \vec{J}_T(\vec{r}, t) \cdot d\vec{s} = 0 \quad (1.8)$$

Owing to the current conservation law, an integral of the total current density $\vec{J}_T(\vec{r}, t)$ on a closed surface in the wire $S = \{S_D, S_A, S_L\}$ in figure 1.2.2 is zero. We have defined S_L as the surface parallel to the transport direction in the cable. In particular, for a cable we can assume $\int_{S_L} \vec{J}_T(\vec{r}, t) d\vec{s} = 0$, so finally we get $\int_{S_D} \vec{J}_T(\vec{r}, t) d\vec{s} = -\int_{S_A} \vec{J}_T(\vec{r}, t) d\vec{s}$. The irrelevant sign for the total current on surfaces S_A or S_D is related with the direction of the vector $d\vec{s}$. Therefore, the important point is that we have to simulate the total current (not only the particle current) on S_D if we want to ensure that the simulated result is equal to the measured one on S_A . Since the time-average of the displacement current $I_d(t)$ equals zero, in a DC transport, one can only concentrate on the computation of the particle current $I_p(t)$. For a quantum device working beyond the DC picture, we have to properly compute the displacement current many times where two fundamental issues—the many-body problem and the measurement problem—appear. In the following, I will focus on these two fundamental problems.

1.3 The Many-Body Problem in Electronics

The displacement current is a magnitude related to the Coulomb interaction among electrons. The computation of the Coulomb interaction among electrons in a quantum systems is part of the so-called many-body problem.

In quantum mechanics, in principle, an accurate description of the *closed* system could be obtained by solving the many-particle Schrödinger equation governing the system dynamics when the initial state of the system is perfectly well known [32, 33]. That is

to say, the many-particle wave function in huge configuration spaces gives a complete description of the closed system. In electronics, for instance, a closed system can be a circuit including the battery, the contacts, the active region and all the set-up that is needed to measure the electron flow. The dynamic of the circuit is governed by the Schrödinger equation, which can be written in the first quantization as:

$$i\hbar \frac{\partial \Psi}{\partial t} = H_{circuit} \Psi \quad (1.9)$$

where Ψ is the many-particle wave function and $H_{circuit}$ is the Hamiltonian of the circuit. Assuming the whole circuit contains M_T electrons and $M_S - M_T$ atomic cores, then, the $H_{circuit}$ in the position representation is written as:

$$\begin{aligned} H_{circuit} = & \sum_{i=1}^{M_T} \left\{ K(\vec{p}_i) + \frac{1}{2} \sum_{\substack{j=1 \\ j \neq i}}^{M_T} q U_0(\vec{r}_i, \vec{r}_j) \right\} + \sum_{i=1}^{M_T} \sum_{j=M_T+1}^{M_S} q Z_j U_0(\vec{r}_i, \vec{r}_j) \\ & + \sum_{i=M_T+1}^{M_S} \left\{ K(\vec{p}_i) + \frac{1}{2} \sum_{\substack{j=M_T+1 \\ j \neq i}}^{M_S} q Z_i Z_j U_0(\vec{r}_i, \vec{r}_j) \right\} \end{aligned} \quad (1.10)$$

where the i -th particle has momentum \vec{p}_i and position \vec{r}_i , q is the elementary charge (without sign), Z_i is the atomic number of the i -th atom, $K(\vec{p}_i)$ is the kinetic energy of the i -particle and $U_0(\vec{r}_i, \vec{r}_j)$ is the Coulomb interaction between the i and j particles. It's important to emphasize that along the whole dissertation, only *non-relativistic* quantum system will be discussed¹. Then, the *local* Coulomb interaction is approximately defined as $U_0(\vec{r}_i, \vec{r}_j) = \frac{1}{4\pi\epsilon_0} \frac{q}{|\vec{r}_i - \vec{r}_j|}$.

From a computational point of view, except for trivially simple cases (i.e., a toy-model of two-particle system), the direct solution of equation (1.9) is inaccessible. The main reasons are in the following: First of all, the correlation terms in (1.10) prevent a separation of the many-body wave function degrees of freedom into M_S single-body problems. Secondly, the entire system has huge degrees of freedom, for instance, one mole of a solid contains $M_T \sim 10^{23}$ electrons resulting the wave function contains at least $3M_T$ degrees of freedom. From a numerical point of view, these two points make the equation (1.9) unsolvable. Let us give a simple example to describe the complexity of this intractable problem of solving the many-body Schrödinger equation (1.9). Assuming that the computation of a single-particle wave function needs $100 \times 100 \times 100$ cells, which means

¹In principle, in the time-dependent theory, a retarded potential is generally considered for the interaction between the i and j particles $U(\vec{r}_i, \vec{r}_j, t) = \frac{\rho(\vec{r}_j, t')}{4\pi\epsilon_0} \frac{\delta(t-t'-|\vec{r}_i - \vec{r}_j|/c)}{|\vec{r}_i - \vec{r}_j|}$ being ϵ_0 the vacuum permittivity, c the speed of light and $\rho(\vec{r}, t)$ the charge density at position \vec{r} at time t . Imaging two electrons i and j has a distance $|\vec{r}_i - \vec{r}_j| \approx 10^{-9}$ m, then, the additional term in the Coulomb interaction $|\vec{r}_i - \vec{r}_j|/c$ gives an advanced time of around 10^{-17} s, which can be reasonably neglected.

the single-particle wave function defined in a matrix contains 10^6 elements. Imaging the whole system has 10 electrons, then, the number of elements consisting the matrix for the 10-particle wave function becomes 10^{60} . If the information of each element is saved as numbers which take 10 bits, the information of the 10-particle wave function needs 10^{61} bits. The current largest hard drive has storage capacities of 10 Terabyte $\approx 10^{14}$ bits. In order to exactly manipulate the 10-particle wave function, I need at least 10^{47} computers! Such tough technical issue, known as the *many-body problem*, is the core of almost all the unsolved problems in nature. As Dirac wrote in his paper in 1929:

The underlying physical laws necessary for the mathematical theory of a large part of physics and the whole of chemistry are thus completely known, and the difficulty is only that exact application of these laws leads to equations much too complicated to be soluble. It therefore becomes desirable that approximate practical methods of applying quantum mechanics should be developed, which can lead to an explanation of the main features of complex atomic systems without too much computation — P. A. M. Dirac[34]

Thus, from a practical perspective, approximations are required to make the Schrödinger equation (1.9) solvable, whilst retaining as much of the key physics as possible. Hereafter, starting from the many-body theory in equation (1.9), we will mention the standard approximations used in the literature to solve the many-particle Schrödinger equation by *opening* our quantum electron system.

1.4 Electron Device as Open and Stochastic Systems

A closed system is *deterministically* governed by the Schrödinger equation (1.9) when its initial state is perfectly well known and when it does not interact with anything else (for example, the measuring apparatus). Nevertheless, a system not interacting with a necessary apparatus will be a quite useless experiment. The Schrödinger equation is linear, unitary and time-reversible. The truth is that no system is really closed, except for the universe itself. Since it is impossible to deal with the universe, a common strategy is to reduce the system degrees of freedom as much as possible. In particular, let us try to anticipate in next two subsections which degrees of freedom can be reduced in the Hamiltonian expression (1.10) of a closed circuit. In equation (1.10), the first two terms on the right hand side gives the electronic kinetic energy and electron-electron interaction, the third term represents the interaction of the electrons with bare nuclei, the nuclear kinetic energy and the nuclei-nuclei interaction are described by the last two terms.

1.4.1 Internal Openness of the System

The Born-Oppenheimer approximation [35] is assumed to decouple the nuclear and electronic degrees of dynamics. As the nuclei mass is ($10^3 - 10^5$ times) higher than that of electrons, the nuclei may be considered stationary on the timescale of the motion of the electrons, i.e. the nuclei position are fixed to their central value. As a result of this, it is possible to eliminate the nuclear kinetic energy from the *total* energy of the system. The internuclear repulsions are neglected in the *total* energy of the system as well. Moreover, since the atoms remain in their equilibrium positions, somehow frozen, the interactions between electrons and atoms can be treated through the effective mass approximation [36]. For instance, for a material with the parabolic band structure, the treatment of the electron–nuclear attractions is realized by replacing the electron mass in the Hamiltonian with the effective one. However, in reality, the atoms are not really frozen. They have perturbations around their equilibrium positions. In order to have a proper and realistic understanding of the system behaviour, the information of the influence of the atom movements for the electron-nuclear interactions can be reintroduced by including phonon scatterings in the equation of motion of the open system. The phonon scatterings are *stochastic processes* for the electrons which are the only degrees of freedom simulated. The information of this process is assumed to be statistically known. For example, for electrons in a particular material like GaAs, one can know the average values of the scattering rate changing with energies and temperatures. More details about the collisions will be discussed in Chapter 4. Furthermore, the degrees of freedom of core electrons $3M_C$ are also eliminated from the Hamiltonian expression (1.10). Since the core electrons are relatively tightly bound to the nuclei, which remain intact during the timescale of the motion of the $M_T - M_C$ conduction electrons, simply refer to as “(free) electrons”. All these standard approximations discussed above can be considered as the internal decoupling of the whole system degrees of the freedom, i.e. the *internal openness* of the system.

1.4.2 External Openness of the System

Up to now, although the degrees of freedom in equation (1.9) have been reduced to $3(M_T - M_C)$, the complexity of the problem still remains unaffordable, and some additional measures must be taken to continuously reduced the degrees of freedom of the whole circuit. From a computational point of view, instead of taking into account of the whole system, one can approximately partition the universe into a system² of interest (named *open* system) and “everything else”, i.e., the environment, and only focus on this

²Except when specified to the contrary, I will use the word “system” in the whole dissertation represents open system.

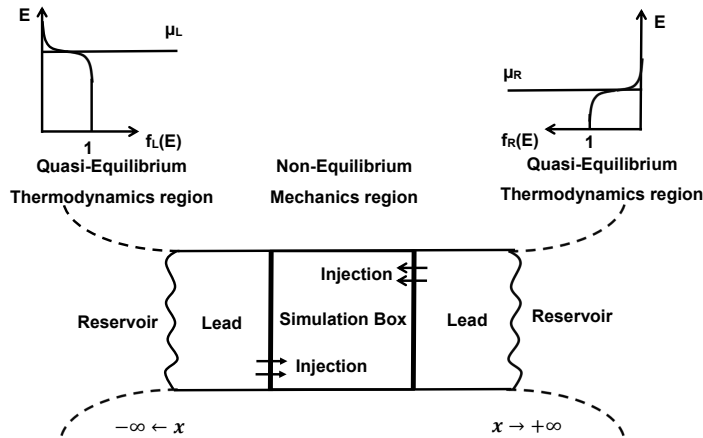


Figure 1.4.1: Schematic of a closed system, which is approximately constructed by the device active region (simulation box) of interest coupled with spatial boundary conditions. Basing on the educated guess, the boundary conditions in the borders of the simulation box have properties analogous to the reservoirs at different electrochemical potentials. The boundary conditions prepare electrons in the distant past and far away from the simulation box into wave packets.

open system. For example, in electronics, as the complexity of integrated circuit grows exponentially, instead of describing a whole closed circuit, the engineers are interested in a portion of the whole system with respect to electron flow, i.e. the device active region. The device active region is the most relevant region in determining the flow of electrons. In this regard, the $M_T - M_C$ electrons is reduced to N electrons inside the device active region. Within these standard approximations, the Hamiltonian for N electrons in the open system is given by:

$$H_{open} = \sum_{i=1}^N \left\{ K(\vec{p}_i) + \frac{1}{2} \sum_{\substack{j=1 \\ j \neq i}}^N qU_0(\vec{r}_i, \vec{r}_j) \right\} = \sum_{i=1}^N K(\vec{p}_i) + U(\vec{r}_1, \dots, \vec{r}_N, t) \quad (1.11)$$

The truth is, even by replacing the Hamiltonian in (1.10) with a reduced one in (1.11), the many-particle Schrödinger equation is still intractable. Various attempts to provide reasonable approximations for the many-body problem in an open system are proposed, and some of the approaches are very successful and well-accepted. For example, the Density functional theory [37, 38] and the Hartree-Fock approximation [39–41] are some of the most accepted theories. Along the whole dissertation, I will use the Bohmian trajectories to describe the quantum transport, and the many-body problem in the Bohmian mechanics will be approximated by a *natural* and *original* approach based on the so-called conditional wave function [42].

Since I am interested in the simulation of quantum transports at THz region, along

the whole dissertation, the definition of the *external* open system implies dealing with spatial boundary conditions. The open system exchanges energy or particles with the environment through the boundary conditions, namely, the injection of electrons, as illustrated in figure 1.4.1. The injection of electrons into the simulation box is also a source of *stochasticity* [43]. More details about the stochastic injection will be discussed in the Chapter 3. On the other hand, there are Coulomb interactions among electrons inside and outside of the open system. As a consequence, the boundary conditions of the electric fields and potentials at the borders of the simulation box have to be defined in the solution of the Poisson equation in the active device region. For instance, the possibilities of the boundary conditions can be the Dirichlet or Neumann boundary conditions (or the combinations of the Dirichlet and Neumann boundary conditions).

1.5 Equilibrium and Non-Equilibrium in Electron Devices

As seen in figure 1.4.1, an open system in electronics is a spatially well-defined structure in between two electrodes which include the role of the battery into the system. It is relevant to realize that there is no electrical current (in a time average sense) flowing in one direction if the system is under thermodynamical equilibrium. Then, needless to say, in the study of quantum transport, one basic issue we have to deal with is the natural fact that an open system coupled to a battery implies that *quantum electrical transport problem is a non-equilibrium problem*. The current flowing in the device active region can be considered as a fundamental non-equilibrium process (where our thermodynamical knowledge developed for equilibrium systems is not directly applicable).

As we have mentioned, in principle, the battery is too complicated to be exactly described. Then the electron source is approximately considered as a reservoir³ of electrons in figure 1.4.1. The reservoir is considered as a system in a thermodynamical equilibrium or quasi-equilibrium (many-body) state. In this ideal reservoir, an additional particle will not modify the internal state of the reservoirs. Similarly, if we remove a particle from it, we will not change the reservoir state. That is to say, the reservoirs are in the local equilibrium.

As we have said, the device active region with an applied bias V is indeed an open quantum system far from thermodynamics equilibrium, as in the figure 1.4.1. The device active region is sandwiched between two reservoirs. On one hand, since the reservoirs represent a battery, the electrochemical potential associated with the left reservoir, μ_L ,

³The definition of reservoir is that an ideal system supplies and receives particles and energy without changing its internal system state. The theoretical concept of reservoir fits the definition of infinite electrodes, which have infinite Poincaré recurrence time.

differs from the electrochemical potential of the right reservoir, μ_R , with the relationship $V = \mu_R - \mu_L$. Let us assume that the electrons injected from the reservoirs have a local equilibrium distribution appropriate to the corresponding electrochemical potential, namely, following the Fermi-Dirac statistical distribution. On the other hand, we know that the device active region (which is also named as the simulation box) has to be modeled under non-equilibrium conditions. In summary, as plotted in figure 1.4.1, the basis of the transport theories is ***the combination of the (thermodynamical) statistical mechanics with the (mechanical) quantum mechanics***. In the reservoir (or in the stochastic injection model), the system is in a quasi-equilibrium condition, where the information for the electrons is statistically known. In the simulation box, however, the system is in a non-equilibrium state and is ruled by the mechanical Schrödinger equation (or similar quantum mechanical equations of motion).

1.6 Irreversible Phenomena in Electron Devices: a Fundamental Law of Nature

In principle, an ideal closed system is governed by time-reversible laws (like the Schrödinger equation) so the entropy of such ideal system does not change. In open system, however, there is no guaranty that the equations of motion become time-reversible so that entropy, in general, increases in open systems. This property of the entropy, as Plank said, is the second law of thermodynamics in open (sub) systems:

Every process occurring in nature proceeds in the sense in which the sum of the entropies of all bodies taking part in the process is increased. In the limit, i.e. for reversible processes, the sum of the entropies remains unchanged.[44]

At the microscopic level, electron in a real device interact with phonons, impurities or other electrons. This interactions makes the electron lose its energy, and finally, this energy is dissipated as heat. While the Schrödinger equation (1.9) describes a reversible system, once collisions are properly included into the equation of motion of a electronic systems, time-irreversibility appears in the open system evolution. For instance, we generally know that the scattering rate of emission phonon is larger than that of absorption phonon. Furthermore, due to the many-body problem, ignoring the degrees of freedom outside of those explicitly simulated in an open system also introduces irreversibility. When the Hamiltonian of a system is given by the expression (1.11), it implies an irreversible degradation of the whole system's available information, i.e. the influence of the degrees of freedom of the environment into the simulation box cannot be know exactly. In the computation of quantum transport, the boundary condition is necessary in solving the dynamic equation, and it reintroduce these *outside* openness by fixing the different

electrostatic potential in the borders of the simulation box. It has been proved that some boundary conditions of a system also introduce irreversibility to the open system. [45, 46].

In conclusion, although time-irreversible appears because we are dealing with an open (sub) systems, it is natural to adopt the view that ***irreversibility is a fundamental law of nature***. The consideration of irreversibility in the modeling of quantum transport is of paramount importance to provide realistic predictions. A typical strategy to deal with dissipative processes in open systems is using the density operator $\hat{\rho}(t)$. The equation of motion of $\hat{\rho}(t)$ is $\partial\hat{\rho}/\partial t = [\hat{H}_{open}, \hat{\rho}] + \hat{C}[\hat{\rho}]$, which is a linearly combination of the so-called Liouville-von Neumann equation and a collision term $\hat{C}[\hat{\rho}]$. As we know, the Liouville-von Neumann equation describes a closed system. Here, the collision term $\hat{C}[\hat{\rho}]$ introduces the openness of the environment. More details about dissipation in the quantum transport will be explicitly described in Chapter 4.

CHAPTER 2

Measurement of Quantum Transport

2.1 The Measurement Problem

As indicted in the previous chapter, the measurement of the electrical current in a nano-electronic device is not trivial, if such nanoelectronic devices behave quantum mechanically. Since the beginning of the twentieth century, different quantum theories have been developed to explain non-classical phenomena. However, the interpretations of these quantum theories are still a topic of lively controversy because these quantum theories imply different interpretations of the reality of our world. Generally, physical theories are human attempts to connect the reality with the experiments. While different quantum theories predict identical results for experiments¹, they have different visions of what is the reality. In particular, in the quantum transport, most of the discussions are focused on how the different theories explain the reality behinds the measurement of quantum systems. In this section, I will concentrate on the measurement problem by explaining the paradox of Schrödinger's cat. As Erwin Schrödinger wrote in his paper in 1935:

One can even set up quite ridiculous cases. A cat is penned up in a steel chamber, along with the following device (which must be secured against direct interference by the cat): in a Geiger counter, there is a tiny bit of radioactive substance, so small, that perhaps in the course of the hour one of the atoms decays, but also, with equal probability, perhaps none; if it happens, the counter tube discharges and through a relay releases a hammer that shatters a small flask of hydrocyanic acid. If one has left this entire system to itself for an hour, one would say that the cat still lives if meanwhile no atom has decayed. The first atomic decay would have poisoned it. The Ψ -function of

¹For simplicity, in the thesis, I will refer to the different explanations of the quantum phenomena, with identical experimental predictions, as different quantum theories, interpretations or approaches. For instance, the orthodox theory and the Bohmian theory. On the contrary, some people consider that different explanations have to give different empirical results to be considered as different physical theories.

the entire system would express this by having in it the living and dead cat (pardon the expression) mixed or smeared out in equal parts.

It is typical of these cases that an indeterminacy originally restricted to the atomic domain becomes transformed into macroscopic indeterminacy, which can then be resolved by direct observation. That prevents us from so naively accepting as valid a "blurred model" for representing reality. In itself, it would not embody anything unclear or contradictory. There is a difference between a shaky or out-of-focus photograph and a snapshot of clouds and fog banks.—

Erwin Schrödinger [47].

In Schrödinger's experiment, one possible state for the macroscopic system is the cat dead Ψ_D , and the other possible state is the cat alive Ψ_L . If the equation of motion of the system is linear (for instance, the Schrödinger equation), then the superposition of the dead cat and alive cat states, like $\Psi = 1/\sqrt{2}\Psi_D + 1/\sqrt{2}\Psi_L$, is also a valid state for the system. If the wave function of the macroscopic system contains full information (nothing else is needed to define a quantum state), as it happens in the Copenhagen or orthodox theory, the cat is described by $\Psi = 1/\sqrt{2}\Psi_D + 1/\sqrt{2}\Psi_L$, i.e. the cat is simultaneously dead and alive. This explanation of Copenhagen reality is beyond the intuition of most of the people who believe that in a reality the cat is either dead or alive, but not both! Then, the Copenhagen interpretation argues that the state of a quantum system gets a definite value (the cat is either dead or alive) only when the system is measured. Albert Einstein criticized this idea—a definite value of reality depends on the measurement—with a simple example: *Do you really think the moon isn't there if you aren't looking at it?* Max Born, one of fathers of Copenhagen school, in response, would say, *however hard you try, you will not be able to detect the moon without some types of measurement.* Yet, when the door of the chamber is opened, the quantum system is measured by an observer who sees the cat either dead or alive, but not both! According to the Copenhagen school, the wave function $\Psi = 1/\sqrt{2}\Psi_D + 1/\sqrt{2}\Psi_L$ is collapsed into $\Psi = \Psi_D$ or $\Psi = \Psi_L$ because someone has observed the cat. However, the Copenhagen explanation of the measurement opens many intriguing questions: Who is the observer? A well educated Ph.D student? A dog looking at the cat will collapse the system? At what time exactly will the superposition ends? How? In any case, even if you like or not the theory, the orthodox quantum mechanics provides predictions in excellent agreement with all quantum experiments.

As we have said previously, different quantum theories give different explanations of the processes of measuring a quantum system. All these quantum theories have both advantages and disadvantages. It has been shown that in any explanations of the measurement problem, one cannot construct a quantum theory which satisfies completely the following three claims [48–51]:

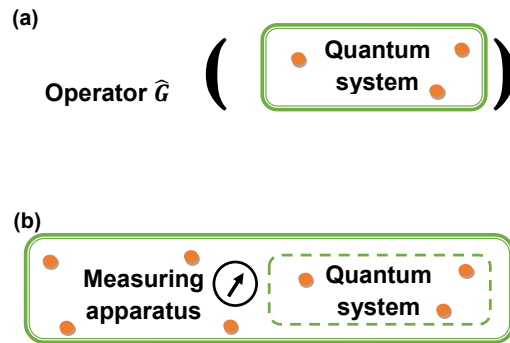


Figure 2.1.1: (a) The orthodox approach assumes that only the quantum system is explicitly simulated, and the measuring operator is replaced by a proper but imprecise operator \hat{G} acting on the wave function of the subsystem. (b) The Bohmian approach assumes that both the quantum system and the measuring apparatus are explicitly simulated.

- (A) The wave function is only governed by a *linear* dynamical equation (for instance, the Schrödinger equation).
- (B) The wave function of a system is *complete*, i.e. the wave function specifies (directly or indirectly) all of the information of a system.
- (C) Measurements provide a *determinate* outcomes, i.e. at the end of the measurement process of the cat, the measuring system is either in a state which indicates cat alive (and not dead) or cat dead (and not alive).

The measurement problem derives from the incompatibility of these three claims. Proposed solutions to it can be classified by which claims they abandon [48]. There are several quantum theories available in the literature to explain the quantum measurement problem. In the following, I will briefly concentrate on how the orthodox, Bohmian and many-worlds approaches explain the quantum measurement.

2.1.1 The Orthodox Approach

Theories which abandon (A) and retain (B) and (C) are generally called *non-linear* theories. In the non-linear theory, one must specify exactly when and what way the non-linear evolution takes place. The *orthodox* quantum theory (also referred as the Copenhagen interpretation of quantum mechanics) is a non-linear theory due to the collapse law. Its pioneers explicitly rejected the argument that the orthodox theory is incomplete, and they also asserted that the macroscopic measuring device is described by the language of classical physics. Obviously, they denied (A). According to the orthodox theory, the time evolution of the wave function of a system is governed by two different laws — the

Schrödinger equation (linear) plus the *collapse* law (non-linear), to successfully reproduce the experimental results in a laboratory. As illustrated in figure 2.1.1(a), the orthodox outcomes are described through the use of an operator \hat{G} whose *eigenvalues* g give the possible values of the measurement, i.e., $\hat{G}|\Psi_g\rangle = g|\Psi_g\rangle$ with $|\Psi_g\rangle$ one of eigenvectors of the operator \hat{G} . This is the so-called von Neumann measurement [52]. Many physicists and philosophers believe that the orthodox approach gives an ambiguous answer to the measurement process. The orthodox theory only points out that such operator exists. However, it does not specify which operator \hat{G} is needed. As stressed by Bell: *The traditional theory papered over this defect by describing the collapses in terms of imprecise notions such as ‘observation’ or ‘measurement’* [53]. That is to say, the orthodox theory did not explain with total accuracy under what circumstances, and in what way the non-linear evolution (collapse) takes place. It does not define clearly where is the separation between the classical measuring apparatus and the quantum system. It does not explain who is the observer. Therefore, the orthodox approach solves the measurement problem and provide correct statistical results (collapses randomly to one of the eigenstates of the particular operator \hat{G}), but it still contains many ambiguities in the definition of a particular operator \hat{G} associated to each experiment.

2.1.2 The Bohmian Approach

Theories which abandon (B) and retain (A) and (C) are generally called *hidden variable* theories. In the hidden variable theory, one must specify exactly what the hidden variables are and what laws govern them. The Bohmian explanation of the quantum phenomena is the most famous one among these hidden variable theories. In Bohmian theory, the quantum system is completely described by both the wave function Ψ and the Bohmian trajectory. Therefore, it denies the claim (B). The extra variables are particle positions and the dynamics of these variables is governed by the so-called *guidance equation*. In this sense, the entire quantum system is described by the wave function plus the trajectory following two evolution laws:

- (1) The dynamics of the wave function (independently of whether a measurement process takes place or not) in the entire configuration spaces is governed by the Schrödinger equation (with a proper Hamiltonian of the quantum system plus the measuring apparatus).
- (2) The time evolution of a trajectory (independently of whether a measurement

²As described in most textbooks, the collapse law mentioned here is called *strong* measurement. The effect of the operator \hat{G} interacting with the quantum system is that the initial wave function Ψ collapses into Ψ_g . There also exists another type of measurement known as *weak* measurement, which is useful to describe situations where the effects of the operator on the measured system is just a small perturbation.

process takes place or not) is determined by the time integration of the Bohmian velocity.

The Bohmian measurement processes are treated similarly as any other quantum process of interacting particles, and there is no need to introduce operators in the Bohmian approach [54–56]. As depicted in figure 2.1.1(b), imagining that some kind of pointer indicates the measured quantity, for instance, a pointer in an ammeter moves to a position that indicates the current measured of the whole circuit in the laboratory. The particle pointers (degrees of the freedom of the system) associated with Bohmian trajectories must be present in the Hamiltonian of the quantum system. In fact, in spite of being referred as hidden variables, the particles of the pointer is the only elements that we really “see”. Bell expressed this point in one of his didactic sentences:

In physics the only observations we must consider are position observations, if only the positions of instrument pointers. It is a great merit of the de Broglie-Bohm picture to force us to consider this fact. —J. S. Bell [57]

Therefore, a proper modeling of the Bohmian measurement process only needs the explicit consideration of the degrees of the freedom of the pointers (particle positions) in the many-body wave function and in the many-body Bohmian trajectories that define the entire system. The trajectories specify which state in a spatial superposition of states is the relevant one. The position of the particle is only in the support of one of the states (for instance, the cat alive state), and the rest of states are empty waves. The quantum randomness is implicit by the probability distributions of the initial conditions of trajectories. The effects of the collapse of the wave function are easily taken into account by the trajectories. For instance, in the case of an electron interacting with a barrier, after the interaction is completed, the electron that is transmitted at time t_1 will remain as a transmitted electron with full certainty at future time t_2 . In fact, while the Bohmian approach and the orthodox approach provide the same probabilistic outcomes in the prediction, the mathematical implementation of the equations of motion in these approaches are quite different. Let us emphasize again that, as shown in figure 2.1.1, the orthodox approach needs a proper operator \hat{G} with all its conceptual difficulties, while this operator is not needed in the Bohmian descriptions of the quantum measurement. It is substituted by a proper description of the Hamiltonian that provides the interaction between the system and measuring apparatus.

2.1.3 The Many-Worlds Approach

Theories which retain (A) and (B) while abandoning (C) are less common. The Many-worlds theory [58] is one of the interpretation of the quantum phenomena that denies the

wave function collapse and that still asserts that the wave function is complete. It implies that, at the end of the measurement, all possible outcomes given by the superpositions of states are real and each represents an actual “world” (or “Universe”). In the many-worlds interpretation of the Schrödinger’s cat, the cat is both dead and alive even before the measurement. But the dead and alive cats are in different branches of worlds – a world with the cat dead and a world with the cat alive. Both of the worlds are equally real and not interact with each other. In fact, denying (C) entails other difficulties. In this thesis, we will not discuss about this type of solutions to the measurement problem.

Up to now, different interpretations of the quantum measurement problem have been explicitly discussed with the Schrödinger’s cat example. Since, the quantum transport in the THz range is the core issue being focused on along the whole dissertation, in the following, the orthodox and Bohmian approaches will be used to explain the measurement problems that appear in the quantum transport computation, in particular, in the prediction of quantum noise, DC current and total current in nano electronic devices.

2.2 The Quantum Measurement Problem in Electron Devices

In the literature, the study of quantum transport in electron devices is mainly devoted to DC properties [59]. However, a better understanding of well-designed electronic devices needs to compute some properties related to their noise, transient and AC behaviours, which is intrinsically linked to the understanding of multi-time measurement processes in a quantum system [60]. Indeed, the multi-time measurement issue is a relevant problem in electron devices. Therefore, in this section, firstly, I will discuss about the definitions of quantum noise emphasizing the need of the multi-time measurement. Then, the interpretation of the multi-time measurement from both the orthodox and Bohmian perspectives will be explained with an example of electrons impinging upon a partially transparent barrier.

2.2.1 A Preliminary Discussion

Let us assume that a signal that we are interested in an electrical device is the DC value of the current $\langle I \rangle$. Once we have the signal $\langle I \rangle$, in principle, the noise can be quantified by time averaging the difference between the measured value of the current $I(t)$ and the signal $\langle I \rangle$ in a unique device:

$$\Delta I^2 = \lim_{T \rightarrow \infty} \frac{1}{T} \int_0^T \left(I(t) - \langle I \rangle \right)^2 dt \quad (2.1)$$

At this point, it is very important to point out that $I(t)$ presents very rapid fluctuations that cannot be captured by the standard laboratory apparatuses. Any experimental setup that measures the current fluctuations behaves as a low-pass filter (i.e., the current fluctuations at frequencies higher than the apparatus cut-off frequency are not measured). Then, the experimentally accessible information about the fluctuation is not given by equation (2.1), but by the power spectral density of noise $S^N(\omega)$ where ω is the angular frequency and the superindex “ N ” represents noise. In explaining the procedure to compute $S^N(\omega)$, firstly, the time average definition of the autocorrelation function, $\Delta R(\tau)$, is defined as:

$$\Delta R(\tau) = \lim_{T \rightarrow \infty} \frac{1}{T} \int_0^T \Delta I(t_1) \Delta I(t_1 + \tau) dt_1 = \lim_{T \rightarrow \infty} \frac{1}{T} \int_0^T I(t_1) I(t_1 + \tau) dt_1 - \langle I \rangle^2 \quad (2.2)$$

where we use the definition $\Delta I(t) = I(t) - \langle I \rangle$. From the Wiener-Khinchine relation, the $S^N(\omega)$ can be defined as the Fourier transform of $\Delta R(\tau)$:

$$S^N(\omega) = \int_{-\infty}^{\infty} \Delta R(\tau) e^{-j\omega\tau} d\tau \quad (2.3)$$

It is quite natural to realize that the definition of $S^N(\omega)$ in equation (2.3) is consistent with the previous expression given by (2.1):

$$\Delta I^2 = \int_{-\infty}^{\infty} S^N(\omega) d\omega \quad (2.4)$$

From equations (2.2) and (2.3), we realize that the measurement of $S^N(\omega)$ requires the knowledge of the measured current $I(t)$ in almost all time t . Thus, we have to make predictions about the evolution of the electrical device while being measured many times. In a quantum system, the measurement process has very relevant implications because the evolution of a system with or without measurement (with or without collapse law in the orthodox theory) can be dramatically different.

Let us see in what sense ergodicity [61] can simplify the quantum noise predictions. From expression (2.1), the quantum noise is computed from a unique measurement in ergodic systems:

$$\Delta I^2 = \sum_i (I_i(t_1) - \langle I \rangle)^2 P(I_i(t_1)) \quad (2.5)$$

where $P(I_i(t_1))$ is the probability of getting $I_i(t)$ at time t_1 . Once again, the noise measured in a laboratory is not given by ΔI^2 , but by $S^N(\omega)$ in (2.3). The amount of noise generated by an instantaneous current evolving, for example, from $I(t_1) = 5$ mA to $I(t_2) = 10$ mA during a time interval of $t_2 - t_1 = \tau = 1$ fs, is not captured from state-of-the-art laboratory apparatuses (which already have difficulties to capture

noise at frequencies higher than a few of Terahertz). The average over an ensemble of experiments of the autocorrelation defined in equation (2.2) is:

$$\Delta R(t_1, t_2) = \sum_i \sum_j I_j(t_2) I_i(t_1) P(I_j(t_2), I_i(t_1)) - \langle I \rangle^2 \quad (2.6)$$

In general, it is reasonable to assume that the instantaneous current in an electronic device behaves as a wide-sense stationary random process. Then, the signal $\langle I \rangle$ is constant and time-independent. Identically, the autocorrelation function in (2.6) depends only on the time difference $\Delta R(t_1, t_1 + \tau) = \Delta R(\tau)$ with $t_2 = t_1 + \tau$. Finally, using expression (2.3) with $\Delta R(\tau)$ computed from (2.6), the noise power spectral density $S^N(w)$ in an ergodic system is obtained.

Note that the probability $P(I_j(t_2), I_i(t_1))$ implies a two-measurement process for each electronic device. That is, the system evolves freely (without interaction with the measuring apparatus) from an initial time t_0 till t_1 when the current is measured, which gives the value I_i . Then, the system evolves freely again till time t_2 when the system current is measured again, which gives value I_j . Even the ergodicity is invoked, the computation of the quantum noise through the autocorrelation function $\Delta R(\tau)$ in equation (2.6) still requires, at least, two measurements at different times in a single experiment (and then the average over all experiments). Thus, the quantum noise is specially sensible to the fundamental quantum mechanics issues—the quantum measurement problem. This explains why the concept of quantum noise have such a halo of mystery around, while its mathematical definition seems so trivial. As a consequence, the multi-time measurement issue is quite relevant in quantum transport. Next, I will focus on how the probabilities $P(I_j(t_2), I_i(t_1))$ in a multi-time measurement process are computed according to the orthodox and Bohmian theories. In particular, we discuss an experiment with a flux of electrons impinging upon a tunneling barrier.

2.2.2 The Multi-Time Measurement with Orthodox Approach

When a flux of electrons impinge upon a partially transparent barrier, electrons are either transmitted or reflected, but not both! This is true in the orthodox and Bohmian theories. For simplicity, to focus on the importance of the measurement process, I consider spinless electrons without Coulomb and exchange interaction. Then, a flux of electrons is assumed to be constantly injected (at zero temperature), one by one. Each electron, after measuring at time t_1 , will appear randomly at the left or at the right of the tunneling barrier. The time averaged number of transmitted electrons will be proportional to the transmission probability, but the number of transmitted electrons fluctuates instantaneously because of the randomness of the transmission. These fluctuations are named

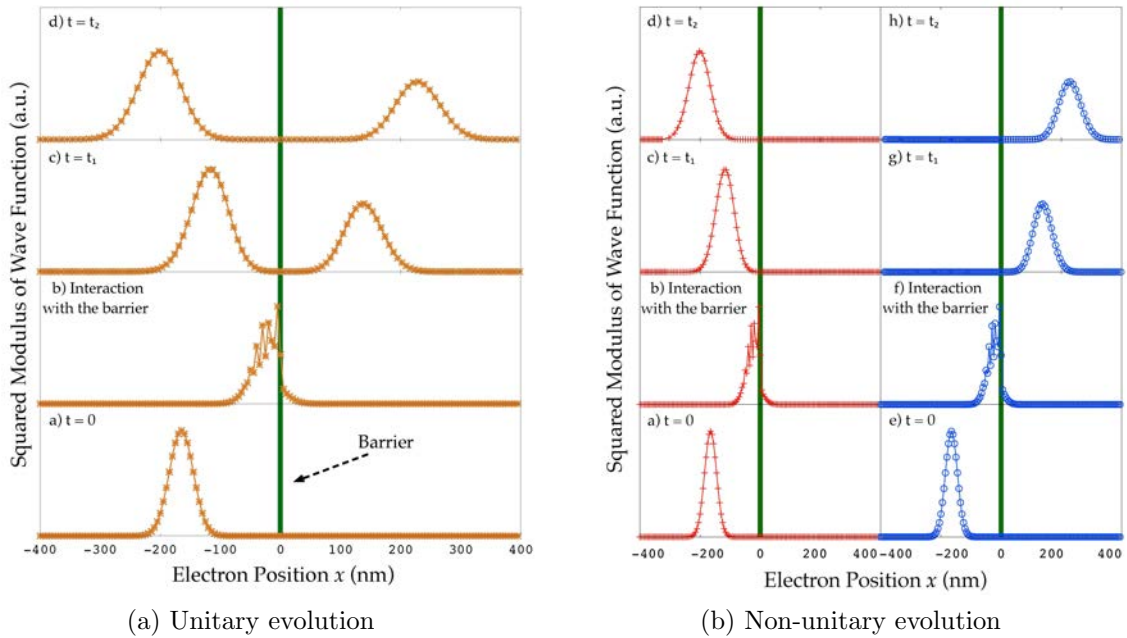


Figure 2.2.1: (a) Unitary evolution of the squared modulus of the wave function $\Psi(x_1, t)$ of an electron impinging on a tunneling barrier located at $x = 0$ (green solid line). Four different times corresponding to a) initial time, b) the moment when the wave function interacts with the barrier, c) the time t_1 when the first measurement occurs and d) time t_2 corresponding to the second measurement. At time t_1 and t_2 , because of the unitary evolution, the electron can be detected at both sides of the barrier. (b) The same experiment for a non-unitary evolution guided by the Schrödinger equation and collapse law. **a, b, c** and **d** for a reflected electron detected at time t_1 at the *left* side. **e, f, g** and **h** for a transmitted electron detected at time t_1 at the *right* side.

partition noise³. Of course, there are many other sources of noise in electrical device. For instance, the $1/f$ noise is very relevant at low frequency. But only the multi-time measurement of the partition noise due to a tunneling barrier will be discussed in this part.

Now I will give a detailed discussion of the role played by the measuring apparatus (for example, an ammeter here). For a single-particle wave function $\Psi(x_1, t)$, according to the Copenhagen interpretation, the wave function is firstly ruled by the unitary and deterministic Schrödinger equation (1.9) in Chapter 1. The unitary evolution of such wave function is depicted in figure 2.2.1(a). Obviously, it does not explain correctly the experiment without collapse. From this unitary evolution, there exist a non-zero probability that an electron found at time t_1 at the right side of the barrier (as a transmitted

³In the literatures [62–66], the fluctuations due to both the partition noise of the barrier and the thermal noise of the injection of electrons at finite temperature are known as quantum *shot* noise. For the sake of simplicity, the injection is assumed to be happened at zero temperature, so the *thermal* noise will not be considered here, which will be explicitly discussed in Chapter 3.

one) can be found in a later time t_2 at the left side as a reflected electron. That is nonsense! As from an experimental point of view, one electron is detected at one side in time t_1 will always find in the same side in a later time t_2 .

As has been discussed in the Subsection 2.1.1, in order to reproduce the experimental outcomes, a second law, collapse of the wave function, is taken into account in the orthodox approach. A new non-unitary (and *ad-hoc*) operator \hat{G} provides the effects of the interaction of a measuring apparatus with the quantum system. As illustrated in figure 2.2.1(b), once an electron is randomly measured as a reflected (or transmitted) electron at time t_1 , the transmitted (or reflected) part of the wave function is eliminated. In order to explain correctly this temporal correlations, a unitary and non-unitary time-evolution of the system from a initial time until the final one is required.

The new operator \hat{G} is the only tool provided by the theory to determine the possible results of a measurement. In principle, we only know that the operator is a (hermitian $\hat{G} = \hat{G}^*$) function acting on Hilbert spaces whose (real) eigenvalues g of its spectral decomposition are the possible results of the measurement. Over the years, physicists have identified the operators, by developing instincts on which are the effects of measurements on the wave function. There are scenarios (as the one depicted in figure 2.2.1(b)) where it is quite obvious which operator is the *right* one. On the contrary, for example, when measuring the total (particle plus displacement) current, it is not at all obvious which are the relevant operators. There are many other problems, for instance, is this measurement process *continuous* or *instantaneous*? Does it provide a *strong* or a *weak* perturbation of the wave function? The answers to these questions are certainly not simple. The postulates of the Copenhagen theory themselves does not answer these *technical* questions on how to find the *right* operator \hat{G} in a practical problem.

2.2.3 The Multi-Time Measurement with Bohmian Approach

As we have seen, there are alternative theories to explain the multi-time measurement issue in quantum transport. The one I will discuss in this subsection is the Bohmian theory. In this approach, there is no need to introduce operator in the measurement process. Here, I will concentrate on its interpretation of the multi-time measurement. All details of the formalism can be found in Appendix A and in literatures [67, 68]. Considering the apparatus (here is a *transmitted charge detector*) as another (big and complex) quantum system interacting with our measured system. The entire system is an electron labeled as X_1 impinging on an external tunneling barrier plus a measuring device which is located behind the barrier, indicated as a single degree of freedom X_2 (thought as the *pointer* of the apparatus). The many-particle wave function $\Psi(x_1, x_2, t)$ described in a configuration space, is ruled by the following many-particle Schrödinger

equation:

$$i\hbar \frac{\partial \Psi(x_1, x_2, t)}{\partial t} = \left(-\frac{\hbar^2}{2m} \frac{\partial^2}{\partial x_1^2} - \frac{\hbar^2}{2M} \frac{\partial^2}{\partial x_2^2} + U(x_1) - i\hbar\lambda Q(x_1) \frac{\partial}{\partial x_2} \right) \Psi(x_1, x_2, t) \quad (2.7)$$

where M is the mass of the apparatus pointer which is assumed to be $M = 75000 m$, $U(x_1)$ is the external potential energy barrier and $-i\hbar\lambda Q(x_1) \frac{\partial}{\partial x_2}$ is interpreted as the interaction between the electron and the pointer with λ the interaction constant and $Q(x_1)$ a function that equals to zero when the electron is outside the detector ($x_1 < 75$ nm in figure 2.2.2(a)), and equals to one when the particle is inside the detector ($x_1 > 75$ nm). The measurement interaction introduces a channelling of the wave function in the configuration space such that the desired property of the “measured system” (whether the electron is reflected or transmitted) can be read off from the final position of the pointer X_2 of a particle.

In the figure 2.2.2(a), four trajectories $\{X_1^\alpha[t], X_2^\alpha[t]\}$ (being $\alpha = 1, \dots, 4$) with different initial positions are considered. The property of the measured system is described by the conditional wave function $\psi(x_1, t) = \Psi(x_1, X_2[t], t)$, which is defined from the many-particle wave function $\Psi(x_1, x_2, t)$ in configuration space with all the actual particle positions being fixed excluding the measured system. More details about the conditional wave function can be found in Appendix A. The main feature of a transmitted charge detector is that the center of mass of the wave function in the x_2 direction has to move if the electron is transmitted and it has to be at rest if the electron is reflected. All details about the simulation can be found in [68]. At the initial time $t = 0$, the wave function is defined as $\Psi(x_1, x_2, 0) = \psi(x_1, 0)\phi(x_2, 0)$. At time t_0 , the wave function has split up into reflected and transmitted parts due to the barrier, see figure 2.2.2(a) **b** and (b) **b**, **f**. For time $t > t_0$, the measured system starts to interact with the detector, which produces two channels in the configuration space, one corresponding to the electron being transmitted (the pointer X_2 moves) and the other corresponding to the electron being reflected (the pointer does not move). Therefore, by looking at the pointer position, one can perfectly certify if the particle has been reflected ($X_1[t] < -50$ nm and $X_2[t] = 0$ nm) or transmitted ($X_1[t] > -50$ nm and $X_2[t] \neq 0$ nm). Of the four possible evolutions shown in figure 2.2.2(a), three show the electron being transmitted ($\alpha = 2, 3, 4$) and one being reflected ($\alpha = 1$).

The same measurement can also be described in a physical space by using the conditional wave function $\Psi(x_1, X_2[t], t)$ for the measured system (see Appendix A). The figure 2.2.2(b) is the time evolution of the conditional wave functions for the electron, for trajectories $\alpha = 1$ (reflected electron) and $\alpha = 3$ (transmitted electron). The key point illustrated here is that the collapse of the wave function for an electron arises naturally

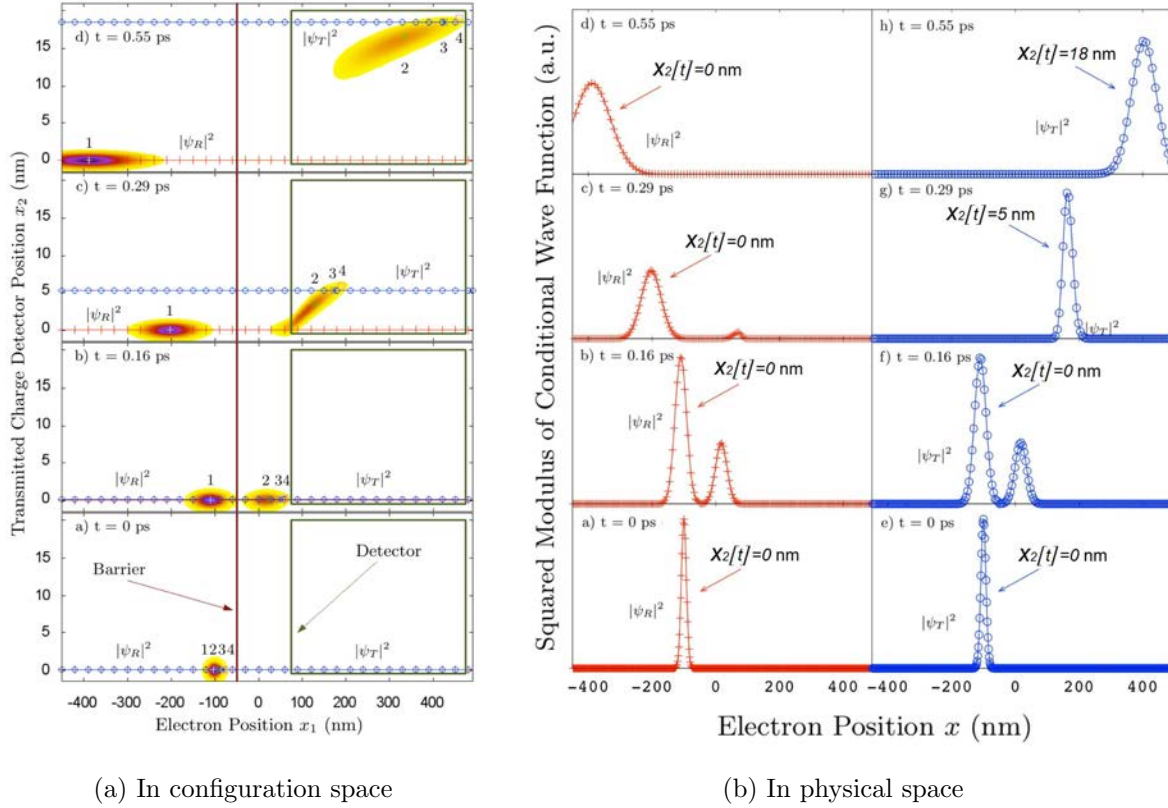


Figure 2.2: (a) Time evolution of the squared modulus of $\Psi(x_1, x_2, t)$ at four different times. In configuration space region, the *transmitted charge detector* is present by a green rectangle, and the barrier by a red solid line located at $x_1 = -50$ nm. Four trajectories $\{X_1^\alpha[t], X_2^\alpha[t]\}$ with different initial positions are presented with \square , $*$, \times and $+$. (b) The $+$ line in **a**, **b**, **c** and **d** is the time evolution of the squared modulus of the conditional wave function $\psi_R = |\Psi(x_1, X_2^{\alpha=1}[t], t)|$ in physical space. The \odot line in **e**, **f**, **g** and **h** is the squared modulus of the conditional wave function $\psi_T = |\Psi(x_1, X_2^{\alpha=3}[t], t)|$.

and automatically in Bohmian approach. For the trajectory $\alpha = 1$, the position of the pointer does not change with time, and after the interaction with the detector has been performed, the electron's conditional wave function includes only a reflected part. For the trajectory $\alpha = 3$, after the electron transmitted, it is the reflected part of the conditional wave function collapses away. The conditional wave function $\Psi(x_1, X_2[t], t)$ is not unitary, even though the evolution of the many-particle wave function $\Psi(x_1, x_2, t)$ is. Let us emphasize again that the collapse within the Bohmian theory in a very natural way. Such a natural derivation of the collapse behaviour demystifies the measurement process and the quantum noise. The non-unitary evolution of the conditional wave function of the measured system $\psi(x_1, t)$ is simply achieved by slicing the enlarged wave function $\Psi(x_1, x_2, t)$ (which includes the apparatus) in the configuration space.

Up to here, it is enlightening to give an answer to one question: *What is the ultimate*

origin of quantum noise according to the orthodox and Bohmian interpretations? In the orthodox approach, because of the collapse of the wave function due to measurements, the transmission or reflection of a single electron impinging upon a tunneling barrier becomes unpredictable. The partition noise in the tunneling barrier is owing to the action of the operator. The collapse implements randomness by selecting the final wave function stochastically among the set of its available eigenstates. In the Bohmian approach, the randomness in the values of the measured current $I(t)$ is provided by the α distributions (i.e., the initial positions of Bohmian trajectories). Although the Bohmian mechanics is deterministic, an *appearance* of randomness emerges in the subsystems. The ultimate origin of the unpredictability is the fact that the uncertainty principle does not allow us to know the (ontologically well-defined in the Bohmian theory) initial position of the particles in each experiment (see the *Quantum equilibrium hypothesis* in Appendix A). It is important to notice that the measurement of the system does not introduce any source of randomness.

Let us return to the questions posed at the end of the Subsection 2.2.2 about the technical problems that appear in a multi-time measurement process with the orthodox approach, when selecting the proper operator. Is such operator compatible with a *continuous* measurement process or with an *instantaneous* one? Does it provide a *strong* or a *weak* perturbation of the wave function? The Bohmian theory, as far as we include the measuring apparatus, clearly indicates the path to answer these questions without operator.

2.3 Prediction of DC and Total Currents with Orthodox Approach

In this part, I will concentrate on how the orthodox theory predicts the measurable properties of quantum electron devices. Firstly, I will theoretically discuss how to measure the DC current⁴ and prove that the measurement problem can be completely relaxed in this case for an ergodic system. Secondly, attempts to compute the total (particle plus displacement) current in the high-frequency scenario ($\omega \rightarrow \infty$) will be discussed.

⁴Generally, one can extract the DC information from a time-dependent total (particle plus displacement) current by using the expression (2.8), which is commonly adopted by the Bohmian approach (I will explicitly explain it in the following Section 2.4). Alternatively, since the time-average of the displacement component in equation (2.8) goes to zero, in the prediction of DC current, one can only consider the particle component. This method is usually adopted by the orthodox approach. For example, when use the expression (2.9) to compute the DC current, we can only know the particle current operator \hat{G}_{J_e} , which appears in any fundamental quantum books.

2.3.1 The DC Current

As we have explained, an important set of properties that a well-designed electronic device has to satisfy, comes from the study of DC current for fixed DC bias conditions, the so called current-voltage characteristic. From an experimental point of view, what measured in a laboratory for the DC signal is the time average value of the instantaneous current $I(t)$ in a unique device during a large period of time T :

$$\langle I \rangle = \lim_{T \rightarrow \infty} \frac{1}{T} \int_0^T I(t) dt \quad (2.8)$$

It is relevant to point out that the prediction of DC current from expression (2.8) requires the knowledge of the measured current $I(t)$ in all time t , where the multi-time measurement problem appears.

If the electronic device satisfies the ergodic theorem [61], a continuous measurement of the system can be avoided. Let us see in what sense ergodicity can simplify our DC current measurements. Assuming an ensemble of *identical* electrical devices⁵ is considered with each one labeled by a sample space variable γ . The (instantaneous) current is labeled by a random process $I^\gamma(t)$. For a fixed time, t_1 , the quantity $I^\gamma(t_1)$ is a random variable while $I^\gamma(t_1)$ is just a real number. Generally, the sample space variable γ is omitted in the notation and a distribution of $I_i(t_1)$ values with $i = 1, \dots, W$ is obtained with a probability $P(I_i(t_1))$ of getting I_i at time t_1 . The DC value of the current in equation (2.8) can be alternatively defined for an ergodic system as:

$$\langle I \rangle = \sum_{i=1}^W I_i(t_1) P(I_i(t_1)) \quad (2.9)$$

The probability $P(I_i(t_1))$ is defined as the ratio of the number of devices (experiments) providing I_i divided by the total number of devices (experiments). It is important to realize that the experimental evaluation of (2.9) requires only one measurement of the current at t_1 in a large number of *identical* γ -devices. Therefore, the theoretical predictions of DC value in (2.9) do only need to determine the free (without measuring apparatus) evolution of the electronic device from the initial time t_0 till t_1 . Expression (2.9) explains why the measurement problem can be completely relaxed in the prediction of DC current.

Once we know the definition of the DC current, let us see how to compute it from a

⁵At this point, the reader will wonder that, in typical laboratory experiments, only one electronic device is available (not an ensemble of them). Then, as a practical definition of ensemble, I can define the instantaneous currents for an ensemble of devices by measuring one electronic device in different time-intervals: $I^{\gamma_1}(t)$ for the instantaneous current measured during the first time interval, $I^{\gamma_2}(t)$ for the second interval, and so on.

practical point of view. Imaging that the DC current is measured on an arbitrary surface S_i . In the orthodox theory, the measured quantum system is described by a (normalized) many-body wave function $\Psi(\vec{r}_1, \dots, \vec{r}_N, t)$ in the configuration space $\{\vec{r}_1, \dots, \vec{r}_N\}$, which is ruled by the unitary Schrödinger equation (1.9) in Chapter 1 with the Hamiltonian described in expression (1.11) and by the non-unitary *collapse* law. For DC quantum transport measurements in the orthodox approach, equation (2.9) is greatly preferred in front of expression (2.8) because it deals directly with the probabilistic interpretation of the wave function. Let us discuss this point in more detail. Defining the eigenstates $|\Psi_i\rangle$ of the current operator \hat{G}_{I_i} , as these vectors that satisfy the equation $\hat{G}_{I_i}|\Psi_i\rangle = I_i|\Psi_i\rangle$. The eigenvalue I_i is one of the W possible measured values in (2.9)⁶. Since the entire set of eigenstates form a basis for the Hilbert space, the many-body wave function Ψ can be decomposed as $|\Psi(t)\rangle = \sum_{i=1}^W c_i(t)|\Psi_i\rangle$, with $c_i(t) = \langle\Psi_i|\Psi(t)\rangle$. Then, the ensemble average value of the current is:

$$\langle I \rangle = \langle \Psi(t) | \hat{G}_{I_i} | \Psi(t) \rangle = \sum_{j=1}^W c_j^*(t) \langle \Psi_j | \sum_{i=1}^W I_i c_i(t) | \Psi_i \rangle = \sum_{i=1}^W I_i P(I_i) \quad (2.10)$$

where we have used the orthonormal property of the eigenstates $\langle \Psi_j | \Psi_i \rangle = \delta_{ij}$, an observable is computed from the expression $\langle G \rangle_{\Psi} = \langle \Psi | \hat{G} | \Psi \rangle$ and the definition of the (Born) probability $P(I_i) = |c_i(t)|^2$.

In fact, in the prediction of DC current, the explicit knowledge of the eigenstates $|\Psi_i\rangle$ is not needed if the free evolution of the state $|\Psi(t)\rangle$ and the *measuring* operator \hat{G} are completely known. That is, the mathematical burden of the collapse of the wave function can be largely relaxed. Supposing the system is only measured at a final time $t = t_1$. As discussed previously, we only require the knowledge of the particle current operator, which is:

$$\hat{G}_{J_c}(\vec{r}_1, \dots, \vec{r}_N) = \sum_{k=1}^N \frac{1}{2m} \left(|\vec{r}_k\rangle \langle \vec{r}_k | \hat{P}_k + \hat{P}_k | \vec{r}_k\rangle \langle \vec{r}_k | \right) \quad (2.11)$$

where \hat{P}_k is the k -component momentum operator. Then, the ensemble value of the

⁶For simplicity, I assume that there is no degeneracy. Our qualitative discussion does not change if degeneracy is considered.

particle current density $\langle \vec{J}_c(\vec{r}, t_1) \rangle$ in the physical space is:

$$\begin{aligned} \langle \vec{J}_c(\vec{r}, t_1) \rangle &= \langle \Psi(t_1) | \hat{G}_{J_c}(\vec{r}_1, \dots, \vec{r}_N) | \Psi(t_1) \rangle \\ &= \frac{i\hbar}{2m} \sum_{k=1}^N \int_{\Omega_\infty} dv_1 \cdots \int_{\Omega_\infty} dv_{k-1} \int_{\Omega_\infty} dv_{k+1} \cdots \int_{\Omega_\infty} dv_N \cdot \\ &\quad \left(\Psi(\vec{r}_1, \dots, \vec{r}_N, t_1) \frac{\partial \Psi^*(\vec{r}_1, \dots, \vec{r}_N, t_1)}{\partial \vec{r}_k} - \Psi^*(\vec{r}_1, \dots, \vec{r}_N, t_1) \frac{\partial \Psi(\vec{r}_1, \dots, \vec{r}_N, t_1)}{\partial \vec{r}_k} \right) \Bigg|_{\vec{r}_k = \vec{r}} \end{aligned} \quad (2.12)$$

where Ω_∞ represents an infinite three dimensional space for the volume-integration. Then, the DC current on the surface S_i can be written as:

$$\langle I_{S_i}(t_1) \rangle = \int_{S_i} \langle \vec{J}_c(\vec{r}, t_1) \rangle \cdot d\vec{s} \quad (2.13)$$

From the expressions (2.12) and (2.13), it is clear that once the many-particle wave function $\Psi(\vec{r}_1, \dots, \vec{r}_N, t_1)$ is known, the DC current $\langle I_{S_i}(t_1) \rangle$ of the electron devices is known as well.

In summary, the prediction of the DC current with the orthodox approach has been discussed in this subsection. For an ergodic quantum system, the measurement problem can be relax in the prediction of the DC current in the quantum transport. Since the time-average of the displacement current goes to zero, in a low frequency ($\omega \rightarrow 0$) application, the measurement of the total (particle plus displacement) current is equivalent to the prediction of DC behavior of the electronic devices. Therefore, in this section, the measurement of DC current $\langle I \rangle$ in an electron device also represents the prediction of total current in a low frequency ($\omega \rightarrow 0$) case. In the following section, I will discuss how to predict the total current in a high frequency ($\omega \gg 0$) case.

2.3.2 The Total Current

As we have discussed in Chapter 1, nowadays, the current ITRS roadmap envisions the state-of-the-art device working at THz range. Such devices are in the frontier between electronics (dealing mainly with particle current) and electromagnetism (dealing with displacement current). Therefore, the proper measurement of the displacement current in a time-dependent quantum simulation is urgently demanded in the prediction of future devices. Up to here, a natural question appears: *how to properly extract the time-dependent displacement current in an open quantum system?*

From a practical computation of point, in the high frequency applications ($\omega \gg 0$), the rapid change of total current $I(t)$ in a unique device cannot be captured by the standard laboratory apparatuses. Similar to the prediction of the quantum noise discussed in

Section 2.2, any experimental setup that measures the instantaneous current behaves as a low-pass filter (i.e. the current fluctuations at frequencies higher than the apparatus cut-off frequency are not measured.) Therefore, the experimentally accessible information about the instantaneous current is given by the power spectral density of the total current, $S(\omega)$, which is defined as:

$$S(\omega) = \int_{-\infty}^{\infty} R(\tau) e^{-j\omega\tau} d\tau \quad (2.14)$$

where the autocorrelation function $R(\tau)$ is:

$$R(\tau) = \lim_{T \rightarrow \infty} \frac{1}{T} \int_0^T I(t_1) I(t_1 + \tau) dt_1 \quad (2.15)$$

From equation (2.15), one has to note that the prediction of $R(\tau)$ requires the knowledge of the measured current $I(t)$ in almost all time t . The quantum system has to be sequentially measured during the time evolution, where the measurement problem occurs and even by invoking ergodicity do not simplify its mathematical treatments.

If the system is ergodic [61], the ensemble average version of the autocorrelation defined in equation (2.15) is rewritten as:

$$R(t_1, t_2) = \sum_i \sum_j I_j(t_2) I_i(t_1) P(I_j(t_2), I_i(t_1)) \quad (2.16)$$

In general, the autocorrelation function in (2.16) depends only on the time difference $R(t_1, t_1 + \tau) = R(\tau)$ with $t_2 = t_1 + \tau$. Finally, using expression (2.14) with $R(\tau)$ computed from equation (2.16), the current power spectral density $S(w)$ in an ergodic system is obtained. From equation (2.16), let us see what the computational difficulties are if we compute the total current with the current power spectral density in equation (2.14). The probability $P(I_j(t_1 + \tau), I_i(t_1))$ implies a multi-time measurement of the quantum system. That is, at time t_1 , a total current operator $\hat{T}_{I_i} = \hat{G}_{I_i} + \hat{D}_{I_i}$ being \hat{G}_{I_i} the particle current operator and \hat{D}_{I_i} the displacement current operator, acts on the quantum system, which gives an eigenvalue of $I_i(t_1)$ and the initial quantum state $|\Psi\rangle$ collapse into a state $|\Psi_{I_i}\rangle$. Then, the system evolves freely again until the time $t_1 + \tau$ when the system is measured again by using an operator \hat{T}_{I_j} , which gives the eigenvalue $I_j(t_1 + \tau)$ and eigenstate $|\Psi_{I_j}\rangle$. The probability $P(I_j(t_1 + \tau), I_i(t_1))$ is:

$$P(I_j(t_1 + \tau), I_i(t_1)) = \left| \langle \Psi_{I_j} | U(t_1 + \tau, t_1) | \Psi_{I_i} \rangle \langle \Psi_{I_i} | \Psi(t_1) \rangle \right|^2 = P(I_j(t_1 + \tau) | I_i(t_1)) \cdot P(I_i(t_1)) \quad (2.17)$$

where $U(t_1 + \tau, t_1)$ is a linear operator, the probabilities $P(I_i(t_1)) = |\langle \Psi_{I_i} | \Psi(t_1) \rangle|^2$ is the probability of obtaining the value I_i when the system is measured at time t_1 and $P(I_j(t_1 + \tau) | I_i(t_1)) = |\langle \Psi_{I_j} | U(t_1 + \tau, t_1) | \Psi_{I_i} \rangle|^2$ is the probability of extracting I_j when

the system is measured again at time $t_1 + \tau$. In the computation of $P(I_j(t_1 + \tau), I_i(t_1))$, two different laws—the Schrödinger equation and the collapse law—are required. The probability $P(I_j(t_1 + \tau)|I_i(t_1)) = |\langle \Psi_{I_j} | U(t_1 + \tau, t_1) | \Psi_{I_i} \rangle|^2$ in equation (2.17) represents multi-time measurement, where the measurement problems discussed in Subsection 2.1.1 dramatically appear.

In the previous development, we have used $|\Psi_{I_i}\rangle$ as the eigenstates of the particle current operator \hat{G}_{I_i} presented in (2.11) without discussing the practical problems that appears when trying to give a more detailed information about $|\Psi_{I_i}\rangle$. Such detailed information of $|\Psi_{I_i}\rangle$ is required to compute the probabilities in (2.17). If we are only interested in ensemble values of the particle current (not in the time correlations mentioned above) such technical problems can be ignored. From expressions (2.12) and (2.13), the ensemble value of the particle current $\langle I_{S_i}^p(t_1) \rangle_O$ at one particular time (without previous measurements) is given by:

$$\langle I_{S_i}^p(t_1) \rangle_O = \int_{S_i} \langle \vec{J}_c(\vec{r}, t_1) \rangle \cdot d\vec{s} \quad (2.18)$$

The technical problems mentioned above in the proper description of the eigenstates associated to the current operators are even more dramatically present when dealing with displacement currents. To elaborate such discussion let us first compute the ensemble value of the displacement current at one particular time (without previous measurements) as $\langle I_{S_i}^d(t_1) \rangle_O$, whose expression can be obtained from (1.2) in Chapter 1. The vector field $\vec{E}(\vec{r}, \vec{r}_1, \dots, \vec{r}_N, t)$ can be interpreted as the electric field ‘seen’ by an additional ‘probe’ electron located at position \vec{r} at time t due to a distribution of electrons given by $\vec{r}_1, \dots, \vec{r}_n$. The probability at each position is given by the (normalized) many-particle wave function $|\Psi(\vec{r}_1, \dots, \vec{r}_N, t)|^2$. Thus, the mean value of the electric field is:

$$\langle \vec{E}(\vec{r}, t) \rangle = \int_{\Omega_\infty} dv_1 \dots \int_{\Omega_\infty} dv_N |\Psi(\vec{r}_1, \dots, \vec{r}_N, t)|^2 \cdot \vec{E}(\vec{r}, \vec{r}_1, \dots, \vec{r}_N, t) \quad (2.19)$$

Then, the orthodox expression of the displacement current $\langle I_{S_i}^d(t) \rangle_O$ on surface S_i at time t_1 (without previous measurements) can be written as [69]:

$$\langle I_{S_i}^d(t_1) \rangle_O = \int_{S_i} \epsilon(\vec{r}) \left. \frac{d\langle \vec{E}(\vec{r}, t) \rangle}{dt} \right|_{t=t_1} \cdot d\vec{s} \quad (2.20)$$

From the expressions (2.20), it seems easy to find the operator \hat{D} that provides the displacement current. Equation (2.20) contains a time-derivation of the electric field

$d\langle\hat{E}\rangle/dt$, which can be rewritten as:

$$\frac{d\langle\Psi|\hat{E}|\Psi\rangle}{dt} = \left\langle\frac{d\Psi}{dt}|\hat{E}|\Psi\right\rangle + \langle\Psi|\frac{d\hat{E}}{dt}|\Psi\rangle + \langle\Psi|\hat{E}|\frac{d\Psi}{dt}\rangle = \langle\Psi|[\hat{E}, \hat{H}]|\Psi\rangle + \langle\Psi|\frac{d\hat{E}}{dt}|\Psi\rangle \quad (2.21)$$

where \hat{H} is the Hamiltonian that determines the evolution of Ψ . It seems obvious that the displacement current operator can be written as $\hat{D} = [\hat{E}, \hat{H}] + \frac{d\hat{E}}{dt}$. The computation of the eigenstates of this operator \hat{D} are, at least, equally intriguing as the eigenstates of the particle current. Without the eigenstates of the particle current and displacement current operators, the evaluation of time-correlations becomes almost impossible. We can compute ensemble values (measured only one time), but we cannot compute time correlations to get noise and power spectral densities. The alternative to overcome this problem seems clear. Let us look for a solution of the quantum measurement problem where such operators (and its associated eigenvalues) are not needed. As discussed in the previous subsections of this chapter, such solution is the Bohmian theory (see Appendix A).

2.4 Prediction of DC and Total Currents with the Bohmian Approach

In the Bohmian theory, the N -particle system is described by the many-particle wave function $\Psi(\vec{r}_1, \dots, \vec{r}_N, t)$ plus the Bohmian trajectories $\{\vec{r}_1^j[t], \dots, \vec{r}_N^j[t]\}$. As we have discussed in Appendix A, in principle, any measured quantity is simply calculated as a function of the actual particle positions over an infinite ensemble of trajectories. What really matters in the computation of an expectation value of the quantum system are only the trajectories of the Bohmian particles (not the wave function). Due to the second postulate (*quantum equilibrium hypothesis*) and the local continuity equation, at any time t , the probability density can be reproduced with an infinite ensemble of Bohmian trajectories $|\Psi(\vec{r}_1, \dots, \vec{r}_N, t)|^2 = \lim_{W \rightarrow \infty} \frac{1}{W} \sum_{j=1}^W \prod_{k=1}^N \delta(\vec{r} - \vec{r}_k^j[t])$ where the trajectories are obtained from the many-particle Schrödinger equation. A great simplification can be obtained when using the (single-particle) equation of motion of a conditional wave function, which avoids an explicit solution of the many-particle Schrödinger equation. A mathematical description of the equation of motion of the conditional wave function can be found in Appendix A. From a computational point of view, in the prediction of the Bohmian trajectories, an approximation for the interaction between the electron in the measured quantum system (for instance, the active region in electron devices) and the measuring apparatus (ammeter, cables, the environment, etc in a whole circuit) is needed. Such approximation, however, is only technical (without great implications) because there is no

collapse law in the Bohmian theory and the measurement process is treated as any other many-body interaction, where approximations are routinely accepted. In the following, I explain briefly the algorithm to obtain the Bohmian trajectories $\{\vec{r}_1^j[t], \dots, \vec{r}_N^j[t]\}$ by using the conditional wave function:

- Step 1: At the initial time t_0 , define the initial conditional wave function $\phi_a(\vec{r}_a, t_0) = \Psi(\vec{r}_a, \vec{r}_b[t_0], t_0)$ and the initial position $\vec{r}_a(t_0)$ for $a = 1, \dots, N$ particles. This is the stochastic injection model will be discuss in Chapter 3.
- Step 2: At each time step dt , solve the following N charge densities and associated N potential $U_a(\vec{r}_a, \vec{r}_b[t], t)$ equations:

$$\rho_a(\vec{r}_a, \vec{r}_b[t], t) = \sum_{\substack{k=1 \\ k \neq a}}^N q \cdot \delta(\vec{r}_a - \vec{r}_k[t]) \quad (2.22)$$

$$\nabla_{\vec{r}_a}^2 (\epsilon(\vec{r}_a) \cdot U_a(\vec{r}_a, \vec{r}_b[t], t)) = \rho_a(\vec{r}_a, \vec{r}_b[t], t) \quad (2.23)$$

Instituting the N potential profiles and N educated guesses of potentials $G_a(\vec{r}_a, \vec{r}_b[t], t)$ and $J_a(\vec{r}_a, \vec{r}_b[t], t)$, the N single-particle pseudo-Schrödinger equations are solved

$$i\hbar \frac{\partial \phi_a(\vec{r}_a, t)}{\partial t} = \left(-\frac{\hbar^2}{2m} \frac{\partial^2}{\partial \vec{r}_a^2} + U_a(\vec{r}_a, \vec{r}_b[t], t) + G_a(\vec{r}_a, \vec{r}_b[t], t) + iJ_a(\vec{r}_a, \vec{r}_b[t], t) \right) \phi_a(\vec{r}_a, t) \quad (2.24)$$

to obtain the N conditional wave functions.

- Step 3: compute the next position $\vec{r}_a[t + dt]$ using the equations:

$$v_a(\vec{r}_a, t) = \frac{J_a(\vec{r}_a, t)}{|\Psi(\vec{r}_a, \vec{r}_b[t], t)|^2} \quad (2.25)$$

$$\vec{r}_a[t] = \vec{r}_a[t_0] + \int_{t_0}^t v_a(\vec{r}_a[t'], t') dt' \quad (2.26)$$

where the particle current density $J_a(x_a, t)$ is defined as (also the standard quantum definition of the expectation value of the particle current density):

$$J_a(\vec{r}_a, t) = i \frac{\hbar}{2m} \left(\Psi(\vec{r}_a, \vec{r}_b[t], t) \nabla_{\vec{r}_a} \Psi^*(\vec{r}_a, \vec{r}_b[t], t) - \Psi^*(\vec{r}_a, \vec{r}_b[t], t) \nabla_{\vec{r}_a} \Psi(\vec{r}_a, \vec{r}_b[t], t) \right) \quad (2.27)$$

- Step 4: Repeat the same algorithm (Step 1 to Step 3) for an infinite ensemble of experiments $j = 1, \dots, W$ with $W \rightarrow \infty$. Each experiment includes N trajectories

$\vec{r}_k^j[t]$ for $k = 1, \dots, N$ with different initial positions, to ensure:

$$|\Psi(\vec{r}, t)|^2 = \lim_{W \rightarrow \infty} \frac{1}{W} \sum_{j=1}^W \prod_{k=1}^N \delta(\vec{r} - \vec{r}_k^j[t]) \quad (2.28)$$

at any time t (also including the initial time t_0) when ergodicity is taken into account in the quantum system.

Once the Bohmian trajectories $\{\vec{r}_1^j[t], \dots, \vec{r}_N^j[t]\}$ with $j = 1, \dots, W$ for the many-particle quantum system are known, the computation of the electrical current (DC, AC, noise, etc.) follows very simple receipts. The reader will realize that these receipts are exactly those used in classical modelling of electron devices. In a particular experiment j , the Gauss equation related the electrical field seen by an additional Bohmian ‘probe’ at position \vec{r} and time t can be written as:

$$\vec{\nabla} \cdot (\epsilon(\vec{r}) \vec{E}^j(\vec{r}, t)) = q \sum_{k=1}^N \delta(\vec{r} - \vec{r}_k^j[t]) \quad (2.29)$$

As an example, if the boundary conditions are an electric field equal to zero at infinite, the solution of the Gauss equation gives the electric field at position \vec{r} and time t , as:

$$\vec{E}^j(\vec{r}, t) = \frac{1}{4\pi\epsilon(\vec{r})} \sum_{k=1}^N q \frac{\vec{r} - \vec{r}_k^j[t]}{|\vec{r} - \vec{r}_k^j[t]|^3} \quad (2.30)$$

In typical electron device scenarios, a numerical solution of (2.29) is required. Once the electric field $\vec{E}^j(\vec{r}, t)$ is known, we can compute the displacement current associated to the experiment j on a particular surface S_i as [69, 70]:

$$I_{S_i, B}^{d, j}(t) = \int_{S_i} \epsilon(\vec{r}) \frac{d\vec{E}^j(\vec{r}, t)}{dt} \cdot d\vec{s} \quad (2.31)$$

Identically, the particle current associated to electrons crossing the surface S_i in the j experiment can be trivially written as [69, 70]:

$$I_{S_i, B}^{p, j}(t) = \int_{S_i} \sum_{k=1}^N q \vec{v}_k^j[t] \delta(\vec{r} - \vec{r}_k^j[t]) \cdot d\vec{s} \quad (2.32)$$

Finally, the total current is the sum of the displacement plus the particle currents:

$$I_{S_i, B}^j(t) = \int_{S_i} \epsilon(\vec{r}) \frac{d\vec{E}^j(\vec{r}, t)}{dt} \cdot d\vec{s} + \int_{S_i} \sum_{k=1}^N q \vec{v}_k^j[t] \delta(\vec{r} - \vec{r}_k^j[t]) \cdot d\vec{s} \quad (2.33)$$

Once we know the time-dependent total current $I_{S_i,B}^j(t)$, associated to one j experiment, the DC, AC and noise current can be just computed averaging over all j -experiments. Technically, in numerical simulations, instead of repeating numerically the experiment in the electron device many times, a unique numerical simulation is conducted in the electron device during a time long enough (electrons entering and leaving) so that many different scenarios are considered in such unique experiment. For example, by using the expression (2.8), the DC current on the surface S_i is extracted by the time averaging $I_{S_i,B}^j(t)$ in one experiment j :

$$\langle I_{S_i}(t) \rangle = \lim_{T \rightarrow \infty} \frac{1}{T} \int_{-T/2}^{T/2} I_{S_i,B}^j(t) dt = \lim_{T \rightarrow \infty} \frac{1}{T} \int_{-T/2}^{T/2} \int_{S_i} \sum_{k=1}^N q \cdot \vec{v}_k(\vec{r}_k^j[t]) \delta(\vec{r} - \vec{r}_k^j[t]) \cdot d\vec{s} \quad (2.34)$$

where we have used that the time-average of displacement current is zero.

Next, let us see what is the mean value of the displacement and particle currents in equations (2.31) and (2.32), and how it related to the mean values computed from expressions (2.20) and (2.18) with the orthodox approach. The ensemble values of the displacement $\langle I_{S_i}^d(t) \rangle_B$ and particle $\langle I_{S_i}^p(t) \rangle_B$ currents at any time t in the Bohmian approach are:

$$\langle I_{S_i}^d(t) \rangle_B = \frac{1}{W} \sum_{j=1}^W I_{S_i,B}^{d,j}(t) = \frac{1}{W} \sum_{j=1}^W \int_{S_i} \epsilon(\vec{r}) \frac{d\vec{E}^j(\vec{r}, t)}{dt} \cdot d\vec{s} \quad (2.35)$$

$$\langle I_{S_i}^p(t) \rangle_B = \frac{1}{W} \sum_{j=1}^W I_{S_i,B}^{p,j}(t) = \frac{1}{W} \sum_{j=1}^W \int_{S_i} \sum_{k=1}^N q \vec{v}_k^j[t] \delta(\vec{r} - \vec{r}_k^j[t]) \cdot d\vec{s} \quad (2.36)$$

If the quantum system is only measured once at time t_1 , the ensemble values of the displacement and particle currents computed from (2.35) and (2.36) in the Bohmian approach are equivalent to that measured from (2.20) and (2.18) in the orthodox approach. However, if the system has to be measured, at least, two times (for example, in the high frequency scenario), then the advantages of the Bohmian approach become evident.

The reader can wonder now why the autocorrelation of the current at two different times, t and $t + \tau$, cannot be computed from the unproblematic orthodox values $\langle I_{S_i}^p(t) \rangle_O$ and $\langle I_{S_i}^p(t + \tau) \rangle_O$. We explain why such option is wrong below. If we use the expressions (2.20) and (2.18) to compute the currents at time $t + \tau$, then, the probability $P(I_j(t_1 + \tau), I_i(t_1))'$ in the autocorrelation (2.16) becomes:

$$P(I_j(t_1 + \tau), I_i(t_1))' = \left| \langle \Psi_{I_j} | U(t_1 + \tau, t_1) | \Psi(t_1) \rangle \langle \Psi_{I_i} | \Psi(t_1) \rangle \right|^2 = P(I_j(t_1 + \tau)) \cdot P(I_i(t_1)) \quad (2.37)$$

which is dramatically different from the probability $P(I_j(t_1 + \tau), I_i(t_1))$ computed from the expression (2.17). In fact, in the expression (2.37), only the Schrödinger equation is required, which clearly shows why it is wrong: no measurement collapse in the quantum system in the middle time appears. On the contrary, the Bohmian solution can safely compute the autocorrelation of the current without the need to know the correct displacement current operator \hat{D} or its eigenstates.

In summary, a comparison between the orthodox and Bohmian approaches is made in the prediction of total current for an electronic device. We have emphasized the advantages that the Bohmian computation has over the orthodox ones when tackling the many-body problem and the quantum measurement problem. The fact that Bohmian mechanics do not require the knowledge of the displacement current operator and its eigenvalue is a great numerical advantage for the reliable computations of high frequency performances of nanoscale electron devices.

CHAPTER 3

Stochastic Injection of Electrons

3.1 Introduction

A closed quantum system can be fully described by a many-body wave function $\Psi(\vec{r}, t) = \langle \vec{r} | \Psi(t) \rangle$, which is ruled by the unitary, time-reversible and linear Schrödinger equation (1.9) if the initial state is well known. As we have explained in Chapter 1, due to the many-body problem, one has to reduce the degrees of freedom of the system. By internally and externally opening the closed system, we end with an open system. We partition the closed system into a system of interest (named *open* system, for example, the device active region) and everything else (the *environment*).

A closed quantum system can be fully described by a many-body wave function $\Psi(\vec{r}, t) = \langle \vec{r} | \Psi(t) \rangle$, which is ruled by the unitary, time-reversible and linear Schrödinger equation (1.9) if the initial state is well known. As we have explained in Chapter 1, due to the many-body problem, one has to reduce the degrees of freedom of the system. By internally and externally opening the closed system, we are interested in dealing with an open system, that is, partitioning the closed system into a system of interest (named *open* system, for example, the device active region) and everything else (the *environment*).

In order to have a fully understanding of the effect of the boundary conditions¹ (also called electron injection model here) on the open system, let us start by discussing a closed system by decomposing the many-body wave function as $|\Psi(t)\rangle = \sum_j p_j(t) |\psi_j\rangle$ and describing the closed system with the density matrix operator $\hat{\rho}(t)$, which is:

$$\hat{\rho}(t) = |\Psi(t)\rangle \langle \Psi(t)| = \sum_i \sum_j p_i(t) p_j^*(t) |\psi_i(t)\rangle \langle \psi_j(t)|, \quad (3.1)$$

where $p_j(t) = \langle \psi_j | \Psi(t) \rangle$ specifies the probability that the system described by the pure state $|\psi_j\rangle$. The time evolution of the density operator $\hat{\rho}(t)$ is given by the so-called

¹In fact, the boundary condition enter the simulation of electronic devices at two levels: in the solution of Poisson's equation and in the carrier injection. In this part, unless otherwise specified, we talk about the boundary conditions in the carrier injection.

Liouville-von Neumann equation:

$$\frac{\partial \hat{\rho}(t)}{\partial t} = \frac{1}{i\hbar} [\hat{H}, \hat{\rho}(t)] \equiv \mathcal{L}[\hat{\rho}(t)], \quad (\text{Closed quantum system}), \quad (3.2)$$

where \hat{H} is the Hamiltonian of the closed system, and \mathcal{L} is the Liouville superoperator. Under the typical effective mass approximation, the equation (3.2) in the position representation becomes:

$$i\hbar \frac{\partial \rho(\vec{r}, \vec{r}', t)}{\partial t} = -\frac{\hbar^2}{2m^*} \left[\frac{\partial^2}{\partial \vec{r}^2} - \frac{\partial^2}{\partial \vec{r}'^2} \right] \rho(\vec{r}, \vec{r}', t) + [U(\vec{r}) - U(\vec{r}')] \rho(\vec{r}, \vec{r}', t), \quad (3.3)$$

where $U(\vec{r})$ is the Coulomb interactions and m^* is the effective electron mass. The spatial boundary conditions for an closed system are assumed to be unproblematic. For example, one can assume that $\rho(\vec{r}, \vec{r}', t) \rightarrow 0$ when $\vec{r} \rightarrow \pm\infty$ and $\vec{r}' \rightarrow \pm\infty$.

3.1.1 Irreversible Boundary Conditions for Open System

An approach to model the behaviour of the open system is to apply the Liouville-von Neumann equation (3.2) to a finite spatial domain representing the open system (for example, the active device region) and included the boundary conditions that model the openness of the environment [45, 71]. A large list of various approaches have been proposed to deal with the boundary conditions [45, 46, 66, 72–76].

We assume that the open system is sandwiched between two electric contacts, which are located at positions $\vec{r}_{b,l} = -\vec{r}_b$ and $\vec{r}_{b,r} = \vec{r}_b$. The subscripts “ b, l ” and “ b, r ” represent the left and right spatial boundaries. As we have discussed in Chapter 1, the closed system is internally and externally opened. We have shown that the fact that we open internally the system (by neglecting the degrees of freedom of the atoms/ions for example) and we later reintroduce the effect of the electron-ion interaction into the equation of motion of the open system, implies that a time irreversible evolution of the open system [45, 71]. That is, an additional collision term is included in the Liouville-von Neumann equation (3.2) to take into account the electron-phonon or electron-impurity interactions. Note that analysis of the dissipative interactions within the open system will appear in Chapter 4. If the external openness of the environment is to be modeled by spatial boundary conditions, these boundary conditions should preserve the *time irreversible* of the dynamics of the open system. A physical picture to obtain such **time-irreversibility** in the open system model is the following:

- The distribution of particles flowing into the open system depends upon the properties of the reservoirs to which the system is connected.

- The distribution of particles moving out of the open system depends on the stochastic (time-irreversible) equation of motion of the system.

Moreover, the behaviour of the reservoirs connected to the open system (a two terminal device is assumed along this chapter) is analogous to that of an optical blackbody [45]. However, for the sake of simplicity and to better understand the role played by the boundary conditions, in this chapter, we assume that there is no damping within the open system.

The practical implementation of the boundary conditions mentioned above can be easily done for (conditional) wave packets, since we can fix its initial momentum and know if they are entering or leaving the open system. However, the implementation of such boundary conditions with the density matrix $\rho(\vec{r}, \vec{r}', t)$ is quite complicated since we do not have the detailed information of the momentum of each electron. The Wigner function provides, somehow, such momentum information.

3.1.2 Frenley Boundary Conditions for Open System

Based on the Wigner function formalism, starting from the pioneering work by Frenley [45], the quantum transport simulations of open systems have been performed by coupling the Wigner transport expression (3.5) with the irreversible boundary conditions. In order to distinguish between particles flowing into and those flowing out of the system, it is relevant to change from the density matrix formalism $\rho(\vec{r}, \vec{r}', t)$ to a Wigner picture $F_W(\vec{r}, \vec{p})$ in phase space (\vec{r}, \vec{p}) being \vec{p} the particle momentum. The Wigner distribution is defined as the Weyl-Wigner transform of the density matrix [77]:

$$F_W(\vec{r}, \vec{p}) = \int d\vec{r}' \langle \vec{r} + \frac{\vec{r}'}{2} | \Psi \rangle \langle \Psi | \vec{r} - \frac{\vec{r}'}{2} \rangle e^{-i\vec{p}\vec{r}'/\hbar}, \quad (3.4)$$

Then, the Liouville-von Neumann equation becomes:

$$\frac{\partial F_W(\vec{r}, \vec{p})}{\partial t} = \mathcal{L}_W[F_W(\vec{r}, \vec{p})] \quad (\text{Closed system}), \quad (3.5)$$

Under the effective mass approximation, the term $\mathcal{L}_W[F_W(\vec{r}, \vec{p})]$ is given by:

$$\begin{aligned} \mathcal{L}_W[F_W(\vec{r}, \vec{p})] &= -\frac{\vec{p}}{m^*} \frac{\partial F_W(\vec{r}, \vec{p})}{\partial \vec{r}} \\ &- \frac{1}{\hbar} \int_{-\infty}^{\infty} d\vec{p}' \int_{-\infty}^{\infty} d\vec{r}' \frac{1}{2\pi\hbar} \sin((\vec{p} - \vec{p}')\vec{x}'/\hbar) [U(\vec{r} + \frac{\vec{r}'}{2}) - U(\vec{r} - \frac{\vec{r}'}{2})] F_W(\vec{r}, \vec{p}'). \end{aligned} \quad (3.6)$$

From the expressions (3.5) and (3.6), it is clear that the Liouville-von Neumann equation is of first order with respect to the position \vec{r} and does not contain derivative with respect

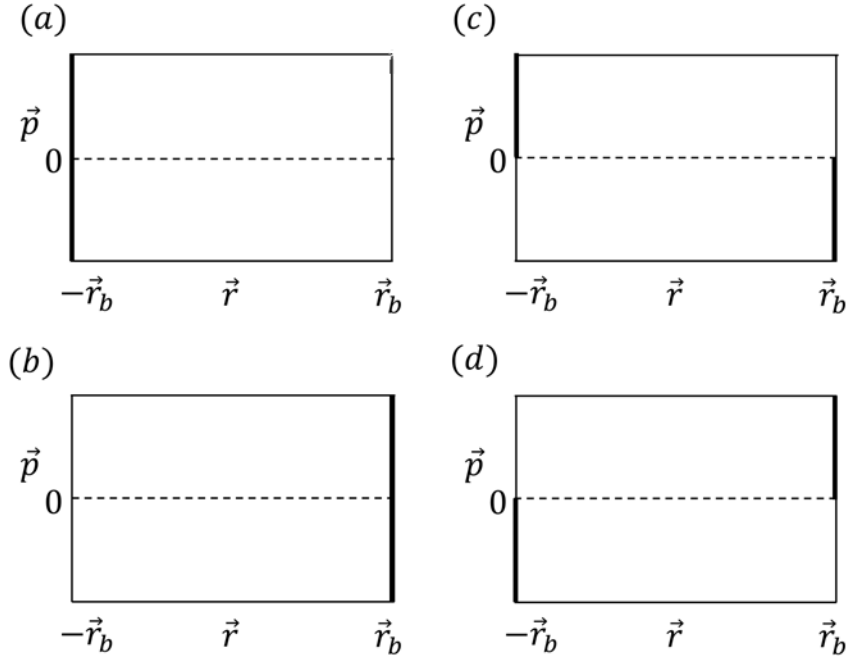


Figure 3.1.1: Possible boundary conditions for the Liouville-von Neumann equation (3.5) in phase space. We only need to specify one boundary value (indicated by heavy lines) for the position. It can be at position $\vec{r} = -\vec{r}_b$ in (a), or at position $\vec{r} = \vec{r}_b$ in (b), or divided between to spatial boundaries, related to the sign of the momentum in (c) and (d). In the vertical axis, positive momenta are on the top and negative ones in the bottom. According to the concept of the irreversible boundary conditions, (c) is the proper one need for the open system.

to momentum \vec{p} . From a mathematical point of view, in order to have a unique solution of equation (3.5), we need only one boundary value of the Wigner function at only one particular position \vec{r}_b . Assuming the open system region is bounded by $\vec{r}_{b,l} = -\vec{r}_b$ and $\vec{r}_{b,r} = \vec{r}_b$, all kinds of appropriate boundary conditions for equation (3.5) are plotted in figure 3.1.1. As we have discussed in the previous subsection, an irreversible boundary condition describes a picture that particles entering the device active region depend only on the reservoirs and that the particles leaving the device depend on the equation of motion of the device. Therefore, the figure 3.1.1(c) is the proper boundary condition for the system. We specify the value for the spatial boundaries:

$$F_W^b(\vec{p}) \equiv F_W^b(\vec{r}_b(\vec{p}), \vec{p}) = \begin{cases} F_W^b(-\vec{r}_b, \vec{p}), & \text{for } \vec{p} > 0 \\ F_W^b(\vec{r}_b, \vec{p}), & \text{for } \vec{p} < 0 \end{cases} \quad (3.7)$$

where $\vec{r}_b(\vec{p}) = -\text{sign}(\vec{p}) \cdot \vec{r}_b$. In an electronic device, $F_W^b(-\vec{r}_b, \vec{p})$ is the distribution associated to the left reservoir of the system, $F_W^b(\vec{r}_b, \vec{p})$ is the distribution of the right reservoir of the system. Within such boundary value $F_W^b(\vec{r}_b(\vec{p}), \vec{p})$, the mathematical solution of the

Liouville-von Neumann equation in steady state conditions (time-independent picture) can be written as:

$$F_W(\vec{r}, \vec{p}) = F_W^{nb}(\vec{r}, \vec{p}) + F_W^b(\vec{r}_b(\vec{p}), \vec{p}) \quad (3.8)$$

where the superindex “nb” denotes that $F_W^{nb}(\vec{r}, \vec{p})$ is the homogeneous solution of the Liouville-von Neumann equation without boundary conditions, and $F_W^b(\vec{r}_b(\vec{p}), \vec{p})$ is the particular solution given by the values in equation (3.7).

For an open system, where the Wigner function is limited to the bounded region Ω of the phase space in 3.1.1, we can deduce the equation of motion of the Wigner function of the open system from the Wigner function of the closed system in (3.5). We define $F_{W,0}(\vec{r}, \vec{p}) = F_W(\vec{r}, \vec{p})\Theta(\vec{r} + \vec{r}_b)\Theta(\vec{r}_b - \vec{r})\Theta(\vec{p} + \vec{p}_b)\Theta(\vec{p}_b - \vec{p})$ where $\pm\vec{p}_b$ are the boundaries in the momentum. We introduce this Wigner function bounded in the region Ω in to the transport equation in (3.5). Since there is no momentum derivatives and the spatial derivative of $\Theta(\vec{r} + \vec{r}_b)$ is just a delta function at the spatial boundary, including the appropriate boundary conditions in (3.7), we get:

$$\frac{\partial F_W(\vec{r}, \vec{p})}{\partial t} = \mathcal{L}_W[F_W(\vec{r}, \vec{p})] + \delta(\vec{r} - \vec{r}_b(\vec{p}))\vec{v}^{in}(\vec{p})F_W^b(\vec{r}_b(\vec{p}), \vec{p}) \quad (\text{Open system}) \quad (3.9)$$

where we assume $\vec{v}^{in}(\vec{p}) = d\vec{r}/dt$ denotes the incoming part of particle velocity in the transport direction. For particles exiting the device active region Ω , the group velocity $\vec{v}^{in}(\vec{p})$ is always equal to zero. On the contrary, for electrons entering the device active region, the velocity $\vec{v}^{in}(\vec{p})$ is always different from zero. The irreversible boundary conditions are illustrated in figure 3.1.1 (c).

We notice that this irreversible boundary conditions discussed here are mathematically different from those employed in the Landauer approach, where both the particles both entering and leaving the volume Ω) are specified [66]. The Landauer boundary conditions are perfectly valid for system without collisions, but not in systems where the collisions introduce time-irreversibility.

In the following, we will have an explicit description of the effect of the source term $\delta(\vec{r} - \vec{r}_b(\vec{p}))\vec{v}^{in}(\vec{p})F_W^b(\vec{r}_b(\vec{p}), \vec{p})$ of the spatial boundaries on the dynamical equation of the open system Ω , in particular, the problem of application the boundary conditions to an open system described with the density matrix formalism in steady state conditions ($\partial F_W(\vec{r}, \vec{p})/\partial t = 0$).

3.1.3 Limitations of the Frenselly Boundary Conditions

We discuss here some limitations of the Frenselly boundary conditions mentioned above. In particular, we discuss the limitations when applied to a time-independent system and the limitations that appears because of the continuous (non-discrete) injection of

electrons.

Limitations because of Using a Time-Independent Picture

In an open system, the irreversible boundary conditions give the value of the distribution function inside the device active region Ω at the initial time t_0 as well as the value of the incoming particle distribution on the boundaries \vec{r}_b at any later time t . First of all, to better clarify the interplay between the volume Ω and the boundary conditions, let us consider a simply case, i.e., there has no potential barrier in the volume Ω . We inject from the left side $-\vec{r}_b$ of volume Ω a source term $\delta(\vec{r} - \vec{r}_b(\vec{p}))\vec{v}^{in}(\vec{p})F_W^b(\vec{r}_b(\vec{p}), \vec{p})$ and investigate the steady state ($\partial F_W(\vec{r}, \vec{p})/\partial t = 0$). Then, the equation of motion (3.9) is reduced to:

$$\frac{\partial F_W(\vec{r}, \vec{p})}{\partial t} = -\frac{\vec{p}}{m^*} \frac{\partial F_W(\vec{r}, \vec{p})}{\partial \vec{r}} + \delta(\vec{r} - \vec{r}_b(\vec{p}))\vec{v}^{in}(\vec{p})F_W^b(\vec{r}_b(\vec{p}), \vec{p}) = 0 \quad (3.10)$$

Integrating both side from initial position $-\vec{r}_b^+$ (avoid the point $\vec{r} = -\vec{r}_b$) to \vec{r} and assuming the value of $F_W(\vec{r}, \vec{p})$ on the position $\vec{r} = -\vec{r}_b^+$ (adjacent to the position $-\vec{r}_b$) equals $F_W^b(-\vec{r}_b, \vec{p})$, finally, we obtain:

$$\begin{aligned} & \int_{-\vec{r}_b^+}^{\vec{r}} -\frac{\vec{p}}{m^*} \frac{\partial F_W(\vec{r}, \vec{p})}{\partial \vec{r}} d\vec{r} + \int_{-\vec{r}_b^+}^{\vec{r}} \delta(\vec{r} - \vec{r}_b(\vec{p}))\vec{v}^{in}(\vec{p})F_W^b(\vec{r}_b(\vec{p}), \vec{p})d\vec{r} \\ &= -\frac{\vec{p}}{m^*} (F_W(\vec{r}, \vec{p}) - F_W(-\vec{r}_b^+, \vec{p})) + \int_{-\vec{r}_b^+}^{\vec{r}} \delta(\vec{r} + \vec{r}_b)\vec{v}^{in}(\vec{p})F_W^b(-\vec{r}_b, \vec{p})d\vec{r} \\ &= -\frac{\vec{p}}{m^*} (F_W(\vec{r}, \vec{p}) - F_W^b(-\vec{r}_b, \vec{p})) + 0 = 0 \end{aligned} \quad (3.11)$$

Therefore, the solution of the Wigner transport equation (3.10) is:

$$F_W(\vec{r}, \vec{p}) = F_W^b(-\vec{r}_b, \vec{p}) \quad (3.12)$$

which means that the distribution $F_W^b(-\vec{r}_b, \vec{p})$ can be moved from the left side of the volume Ω to the right side if the open system has no potential barrier. However, the problem appears when a potential barrier is included. See figure 3.1.2. In a time-independent picture, one expect that the the density matrix is build from Hamiltonian eigenstates. Therefore, trying to inject a plane wave from the left (which is not an eigenstate of a system with barrier) implies that we are, in fact, injecting unexpected waves from the right.

The time-independent picture of the injection model in equation (??) shows that the injection of a particle with well-defined momentum \vec{p} is described by a coherent superposition of states α_1 and α_2 , which is different with the concept of ideal reservoir—injection from a thermal (diagonal) charge reservoir. For equilibrium, the generic scattering state

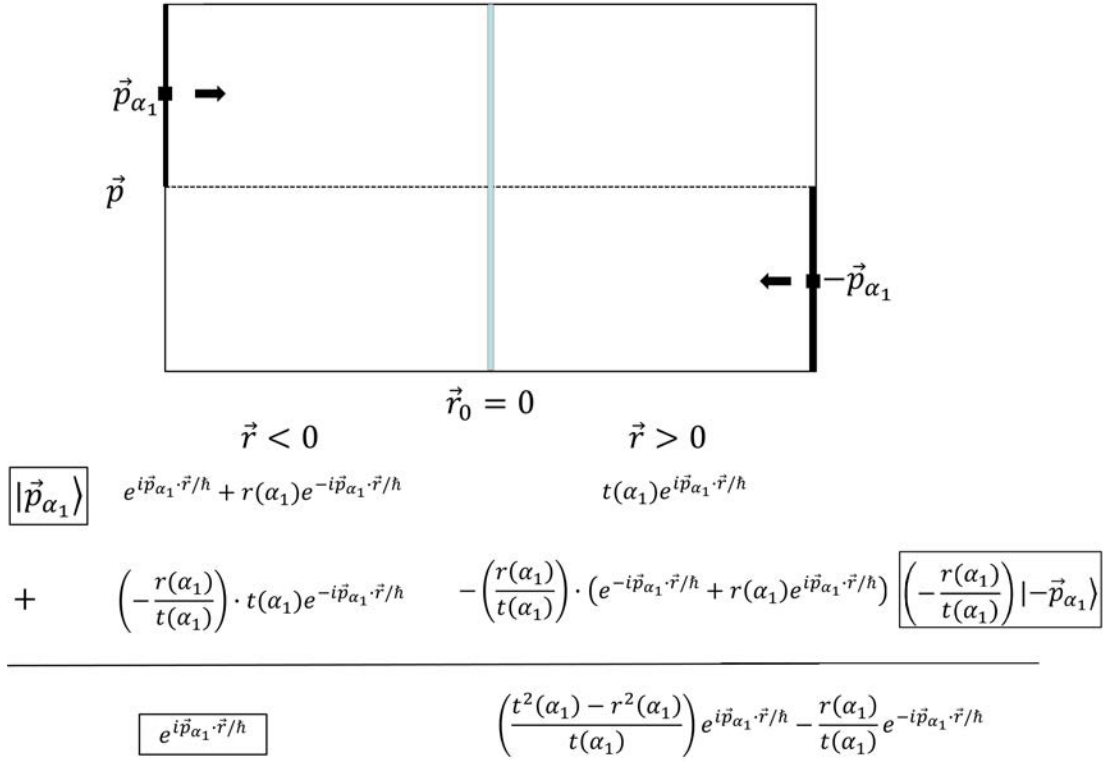


Figure 3.1.2: Schematic representation of injection a plane wave with momentum \vec{p}_{α_1} from the left reservoir, which is a superposition of the left and right scattering states in a particular one-dimensional case. Imaging a barrier is located at position $\vec{r}_0 = 0$, $t(\alpha_1)$ and $r(\alpha_1)$ are the transmission and reflection coefficients for wave vector \vec{p}_{α_1} , respectively.

α_1 on the left side of volume Ω comes out to be a superposition of positive momentum \vec{p}_{α_1} and negative momentum $-\vec{p}_{\alpha_1}$. Consequently, the picture of injecting a plane-wave with momentum $\vec{p}_{\alpha_1} > 0$ from the left contact is almost identical to that of the superposition of scattering states injected from both left and right contacts, which can be seen from figure 3.1.2. An electron injected from the left contact coupled to left as well as to right scattering states, which is unphysical in a quantum-mechanical system.

The solution to this problem of the Frensel boundary conditions, due to a time-independent model, is simple solved by using a time-dependent model. Then, a wave packet can be close to a plane wave in the left reservoir at the initial time (without unexpected injections from other sides) and such wave packet will become reflected and transmitted in a latter time.

Limitations because of continuous injection

In the following subsection, we will use SISOW (an acronym for the Stationary Incoherent Superposition of Wave packets) to describe the source term of the boundary conditions for the open system [78]. By injecting a constant flux of time-dependent wave packets, all the

problems (i.e., non-diagonal, electrons injected from left couples to left as well as to right scattering states) discussed in the previous part will disappear. Such wave packets can be understood as conditional wave functions (see Appendix A) associated to individual electrons. The dynamical information of states that constructed the density matrix of the open system are well known. Providing all the detailed dynamical information known, the irreversible collisions can be straightforwardly implemented in the open system. The dissipative scattering in a quantum transport will be investigated in Chapter 4.

In addition, the continuous injection implicit in the Frenley model is also a handicap for the correct modeling of quantum transport. We know that the charge of electrons is a constant and discrete magnitude, not a continuous one, of value q . Therefore, we expect that the injection process has to be done with quantized values of charge q at each time an electron is entering. We cannot inject $0.5q$ values of the charge. Our injection model with a detailed information of the injection wave packets allows us to inject one electron q or not inject it. The average value will be obviously $0.5q$, but our injection model will allow us to compute DC, AC and also noise due to the fluctuations of the injected electron (thermal noise).

3.1.4 SISOW as irreversible Boundary Conditions in Time-Dependent Picture

We define a time-dependent wave packet $\Psi_{\vec{k}_c, t_0}(\vec{r}, t) = \langle \vec{r} | \Psi_{\vec{k}_c, t_0}(t) \rangle$ which is a linear superposition of Hamiltonian eigenstates $|\psi_\alpha\rangle$ as:

$$|\Psi_{\vec{k}_c, t_0}(t)\rangle = \sum_{\alpha} C_{\alpha}^{\vec{k}_c} e^{-i\frac{E_{\alpha}(t-t_0)}{\hbar}} |\psi_{\alpha}\rangle \quad (3.13)$$

where the coefficient $C_{\alpha}^{\vec{k}_c} = \langle \psi_{\alpha} | \Psi_{\vec{k}_c, t_0}(t_0) \rangle$ with the superindex “ \vec{k}_c ” represents the center momentum of the wave packet, E_{α} is the kinetic energy of the state $|\psi_{\alpha}\rangle$ and t_0 is the time the wave packet entering the open system. The wave packet is described by the conditional wave functions (see Appendix A). Now, we describe the reservoir in the density matrix formalism:

$$\hat{\rho} = \sum_{\vec{k}_c} f(\vec{k}_c) |\Psi_{\vec{k}_c, t_0}(t)\rangle \langle \Psi_{\vec{k}_c, t_0}(t)| \quad (3.14)$$

where $f(\vec{k}_c)$ satisfy Fermi-Dirac statistics to take into account the quantum statistics in the quantum-mechanical system. Substituting the wave packet in equation (3.13) into

the density matrix, we obtain:

$$\begin{aligned}\hat{\rho} &= \sum_{\vec{k}_c} f(\vec{k}_c) \sum_{\alpha} C_{\alpha}^{\vec{k}_c} e^{-i\frac{E_{\alpha}(t-t_0)}{\hbar}} |\psi_{\alpha}\rangle \sum_{\beta} C_{\beta}^{\vec{k}_c*} e^{i\frac{E_{\beta}(t-t_0)}{\hbar}} \langle\beta| \\ &= \sum_{\vec{k}_c} f(\vec{k}_c) \sum_{\alpha} \sum_{\beta} C_{\alpha}^{\vec{k}_c} C_{\beta}^{\vec{k}_c*} e^{-i\frac{(E_{\alpha}-E_{\beta})t}{\hbar}} e^{i\frac{(E_{\alpha}-E_{\beta})t_0}{\hbar}} |\psi_{\alpha}\rangle \langle\psi_{\beta}| \end{aligned} \quad (3.15)$$

In the macroscopic scenario, the carrier injection picture can be considered as a constant flux of identical time-dependent wave packets with each one leaving the reservoir and entering the open system at different time t_0 . The probability of the electron entering the volume Ω or not depends on $f(\vec{k}_c)$, which satisfies the Fermi-Dirac distribution. The time-average of the density matrix $\hat{\rho}$ approaches to:

$$\begin{aligned}\langle\hat{\rho}\rangle &\approx \frac{1}{2T} \int_{-T}^T dt_0 \sum_{\vec{k}_c} f(\vec{k}_c) \sum_{\alpha} \sum_{\beta} C_{\alpha}^{\vec{k}_c} C_{\beta}^{\vec{k}_c*} e^{-i\frac{(E_{\alpha}-E_{\beta})t}{\hbar}} |\psi_{\alpha}\rangle \langle\psi_{\beta}| e^{i\frac{(E_{\alpha}-E_{\beta})t_0}{\hbar}} \\ &= \sum_{\vec{k}_c} f(\vec{k}_c) \sum_{\alpha} \sum_{\beta} C_{\alpha}^{\vec{k}_c} C_{\beta}^{\vec{k}_c*} e^{-i\frac{(E_{\alpha}-E_{\beta})t}{\hbar}} |\psi_{\alpha}\rangle \langle\psi_{\beta}| \frac{\sin((E_{\alpha}-E_{\beta})T/\hbar)}{(E_{\alpha}-E_{\beta})T/\hbar} \end{aligned} \quad (3.16)$$

The equation (3.16) is the definition of the SISOW, which is quasi-diagonal in the time-independent picture. The SISOW describes a equilibrium system.

In the microscopic scenario, the SISOW describes a non-equilibrium system. For example, at time t_0 , the wave packet will either succeed in entering the system with $f(\vec{k}_c)$ equals to one or fail to enter with $f(\vec{k}_c)$ equals to zero. As a consequence, in the time-dependent picture, the SISOW introduce the thermal noise of injecting electron into the open system. On the contrary, the boundary conditions in equation (3.7) does not provide such enrich information. For example, in Frensley's paper, he assumed the boundary value to be $F_W^b(-\vec{r}_b, \vec{p}) = (m^*/(\pi\hbar^2\beta)) \times \ln[1 + e^{-\beta(\vec{p}^2/(2m^*)-\mu)}]$ being μ the Fermi energy and $\beta = 1/(k_B\Theta)$ with k_B the Boltzmann's constant and Θ the absolute temperature [45]. In a time-independent picture, this boundary condition gives the same result as that of SISOW, which satisfies the Fermi-Dirac distribution. However, in the time-dependent picture, it does not provide the thermal noise.

3.2 Electron Injection Model for 2D Materials

3.2.1 2D Materials with a Parabolic Dispersion Relation

As we have discussed previously, the electron injection model (boundary conditions) is essentially important to affect the performance of the device. In this section, the electron injection model for the nanoscale devices with parabolic dispersion relations of carriers in

the channel material (for example the Silicon) is explicitly discussed. For the purpose of investigating how the energy dispersion relations affect the injection model in the electron transport simulation of nanoscale transistors, firstly, a 2D material with parabolic band structure is considered and the details (for instance, the number of particles needed to be injected at each time step, the velocity of each new state of the particles, and so on) of carrier injection will be discussed.

Phase-Space Density

The parabolic dispersion relations in the 2D material is given by:

$$E(\vec{k}) = E_0 + \frac{\hbar^2 |\vec{k}|^2}{2m^*} = E_0 + \frac{\hbar^2 |k_x^2 + k_z^2|}{2m^*} \quad (3.17)$$

where the m^* is the electron effective mass, E_0 is assumed to be zero, \vec{k} is the wave vector in 2D (x-z) plane with k_x and k_z are respectively wave vectors in the x and z directions and $|\vec{k}|^2 = k_x^2 + k_z^2$. As the consequence of the Pauli exclusion principle, the number of available states n_{2D}^p inside the spatial cell $x_0 < x < x_0 + \Delta x$ and $z_0 < z < z_0 + \Delta z$ and inside the reciprocal cell $k_{x0} < k_x < k_{x0} + \Delta k_x$ and $k_{z0} < k_z < k_{z0} + \Delta k_z$ is:

$$n_{2D}^p = g_s g_v \frac{\Delta x \Delta z \Delta k_x \Delta k_z}{(2\pi)^2} \quad (3.18)$$

where the g_s and g_v are the spin and valley degeneracies, respectively. The superindex “p” represents the parabolic band structure.

The ultimate reason the phase-space density of states is limited is because the Pauli exclusion principle. It can be understood, equivalently, from the exchange interaction among electrons. Due to the position and momentum uncertainty, each state needs “its own” volume of the phase-space (equal to 2π) for each pair of the conjugate variables, for example, one pair of variables Δx and Δk_x . Owing to the Pauli exclusion principle, the probability of finding another state close to the first state (inside “its own volume” of the phase-space) is zero.

Minimum Temporal Separation t_0^p

We have explicitly computed the maximum number of states n_{2D}^p in an arbitrary phase-space cell $\Delta x \Delta z \Delta k_x \Delta k_z$ closed to the contact surface. At any particular time t , all electrons with wave vector $k_x \in [k_{x0}, k_{x0} + \Delta k_x]$ inside the cell must attempt to be injected during the time-interval Δt^p , which is defined as the time needed for the electrons with velocity component in the transport direction v_x^p to move a distance Δx . Therefore, the

time-interval Δt^p can be written as:

$$\Delta t^p = \frac{\Delta x}{v_x^p} = \frac{\Delta x m^*}{\hbar k_x} \quad (3.19)$$

The minimum temporal separation, t_0^p , defined as the time step between the injection of two consecutive electrons into the system, can be computed as the time-interval divided by the number of available carriers in a arbitrary cell:

$$t_0^p = \frac{\Delta t^p}{n_{2D}^p} = \left(g_s g_v \frac{1}{(2\pi)^2} \frac{\hbar k_x}{m^*} \Delta z \Delta k_x \Delta k_z \right)^{-1} \quad (3.20)$$

From equation (3.20), it is clear that the minimum temporal separation t_0^p is only affect by the wave vector k_x , and an electron with higher k_x needs less time injection t_0^p to enter in the system. That is to say, the injection model will inject more electrons with higher k_x than that with lower wave vector. Then, the number N^p of attempts of injecting electrons with wave vector k_x during the time interval Δt is:

$$N^p = \frac{\Delta t}{t_0^p} = \Delta t g_s g_v \frac{1}{(2\pi)^2} \frac{\hbar k_x}{m^*} \Delta z \Delta k_x \Delta k_z \quad (3.21)$$

Probability of Injecting N Electrons During τ

In non-degenerate conditions, the injection process for a particular phase-space cell is a periodic sequence of electrons injected with period t_0^p , and the injection statistics of the corresponding k -state obey Poisson distribution in average time. The electrons that are being injected are only correlated because of the Pauli exclusion principle. Two electrons in the same states are forced to have a spatial separation, which finally lead to a temporal separation t_0^p after being successfully injected into the system.

In degenerate conditions, for temperature $\Theta > 0$, the possibility of finding or not an electron in a particular state is uncertain, which obeys the occupation probability. The injection processes is assumed to follow the Binomial statistics with probability $f_{sum}(E)$, which explicitly depends on temperature Θ . The probability $P^i(N, \tau)^p$ that N electrons are effectively injected into a particular cell i adjacent to the contact during a time-interval τ is defined as:

$$P^i(N, \tau)^p = \frac{M_\tau^p!}{N!(M_\tau^p - N)!} f_{sum}(E)^N (1 - f_{sum}(E))^{M_\tau^p - N} \quad (3.22)$$

where M_τ^p is the number of attempts of injecting carriers in a time-interval τ , defined as a number rounds the quotient τ/t_0^p to the nearest natural number towards zero. The number of injected electrons is $N = 1, 2, \dots, M_\tau^p$. Note that the electron injection model

includes the exchange (Fermi) interaction among electrons inside the injection contact, as well as the exchange interaction among electrons at different contacts.

3.2.2 2D Materials with a Linear Dispersion Relation

Now we change to a material with the linear band structure, for example, the graphene material, and check how the energy band structure will affect the carrier injection.

Phase-Space Density

The dispersion of mobile electrons in graphene in the first Brillouin zone (BZ) is given by:

$$E(\vec{k}) = s\hbar v_f |\vec{k}| \quad (3.23)$$

where the band index $s = +1$ is the conduction band (CB) and $s = -1$ is the valence band (VB), \hbar is the reduced Planck's constant, $v_f \sim 10^6$ m/s is the Fermi velocity of carriers in graphene, and $|\vec{k}| = \sqrt{k_x^2 + k_z^2}$ is the wave vector of carriers in the 2D (x-z) plane of the graphene sheet. The point $|\vec{k}| = 0$, referred to as the ‘‘Dirac point’’ is a convenient choice for the reference of energy, i.e. $E(|\vec{k}| = 0) = 0$ eV.

In the graphene sheet, the number of available states n_{2D} inside the spatial cell $x_0 < x < x_0 + \Delta x$ and $z_0 < z < z_0 + \Delta z$ and inside the reciprocal cell $k_{x0} < k_x < k_{x0} + \Delta k_x$ and $k_{z0} < k_z < k_{z0} + \Delta k_z$ is:

$$n_{2D} = g_s g_v \frac{\Delta x \Delta z \Delta k_x \Delta k_z}{(2\pi)^2} \quad (3.24)$$

Each \vec{k} point is twofold spin with the spin degeneracy factor $g_s = 2$, and there are two valleys in the first BZ (the K and K' valleys) with the valley degeneracy factor $g_v = 2$. Deviations from the conical bandstructure are neglected in this work. In the following, we will only focus on the injection of electron (with $s = 1$) from the conduction band, but an analogous expression with band index s replaced by -1 is valid for the hole.

Minimum Temporal Separation t_0

Up to now, we have known exactly the maximum number of states in an arbitrary phase-space cell $\Delta x \Delta z \Delta k_x \Delta k_z$ closed to the contact surface. At any particular time, all states with wave vector component in transport direction (x direction) $k_x \in [k_{x0}, k_{x0} + \Delta k_x]$ in a phase-space cell must attempt to be injected during the time-interval Δt . The Δt is defined as the time needed for a carrier with x component velocity v_x to travel a distance

Δx , i.e. $\Delta t = \frac{\Delta x}{v_x}$. For a specified linear dispersion $E(\vec{k})$, the carrier velocity is given by:

$$\vec{v}(\vec{k}) = \frac{1}{\hbar} \nabla_{\vec{k}} E(\vec{k}) \quad (3.25)$$

Then, the x component carrier velocity v_x is:

$$v_x = \frac{1}{\hbar} \times s\hbar v_f \frac{k_x}{|\vec{k}|} = s v_f \frac{k_x}{|\vec{k}|} \quad (3.26)$$

From the equation (3.26), it is important to emphasize that the x component electron velocity v_x is explicitly dependent on both wave vector component k_x and k_z , which is different from the expression in equation (3.19) for the case of materials with parabolic dispersion. In the parabolic dispersion relation, the electron velocity is $v_x = \frac{\hbar k_x}{m^*}$, which is only determined by the k_x . Then, the time-interval Δt can be written as:

$$\Delta t = \frac{\Delta x |\vec{k}|}{s v_f k_x} \quad (3.27)$$

The minimum temporal separation t_0 , between the injection of two electrons from a particular cell is defined as the time-interval divided by the number of the available states in the phase-space cell:

$$t_0 = \frac{\Delta t}{n_{2D}} = \left(g_s g_v \frac{s v_f k_x}{(2\pi)^2 |\vec{k}|} \Delta z \Delta k_x \Delta k_z \right)^{-1} \quad (3.28)$$

According to the equations (3.26) and (3.28), an electron injected with larger k_z will obtain a lower velocity in the transport direction. In fact, electrons with lower v_x need more injection time interval t_0 to enter into the system. As a consequence, almost all electrons in graphene are injected closed to the maximum velocity v_f . The number of attempts of injecting electrons, N , during the time interval Δt is:

$$N = \frac{\Delta t}{t_0} = \Delta t g_s g_v \frac{s v_f k_x}{(2\pi)^2 |\vec{k}|} \Delta z \Delta k_x \Delta k_z \quad (3.29)$$

The effect of the material energy spectrum on the number of attempts of injecting electrons into the system is plotted in figure 3.2.1. As we have discussed in Section 3.2, in figure 3.2.1(b), only electrons with larger k_x are tried to be injected into the system. However, in the case of material with linear dispersion relations, as shown in figure 3.2.1(a), the majority of injected electrons have smaller k_z . As a consequence, most injected electrons moving in the system at the saturation velocity v_f in the transport

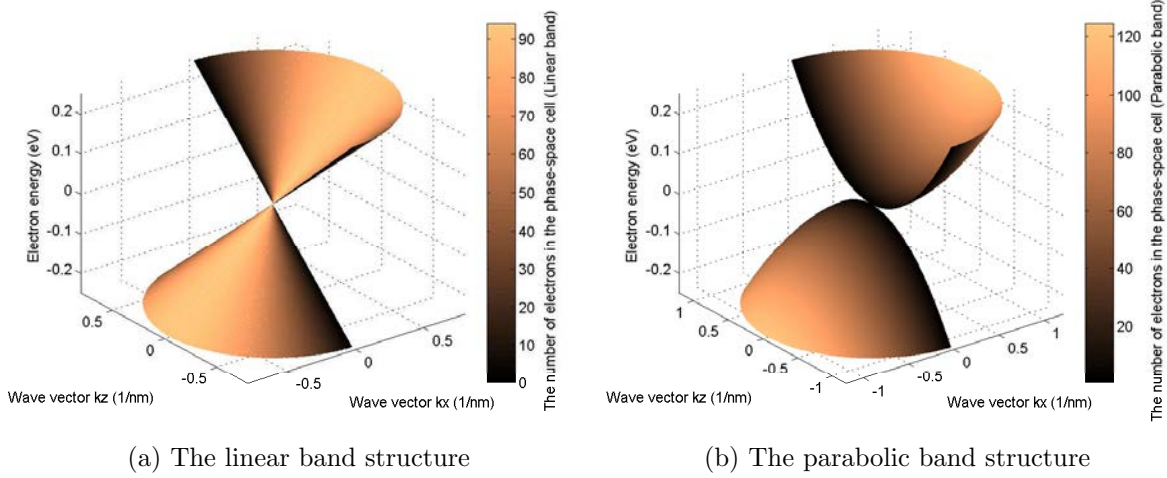


Figure 3.2.1: Number of attempts of injecting electrons computed from equation (3.28) plotted in (a) and from equation (3.20) in (b) for a particular phase space cell $\Delta x \Delta z \Delta k_x \Delta k_z$ during a simulation time $\Delta t = 10$ ns at 300 K. The parameter $m^* = 0.2m_0$ being m_0 the free electron mass, $g_s = 2$, $g_v = 2$, fermi velocity $v_f = 5 \times 10^5$ m/s, the dimensions of the phase-space cell are selected as $\Delta z = L_z = 20$ nm, $\Delta k_x = \Delta k_z = 3 \times 10^6$ m⁻¹.

direction.

Probability $P(N, \tau)$ of Injecting N Electrons During τ

The probability $P^i(N, \tau)$ that N electrons are effectively injected into a particular cell i adjacent to the contact during a time-interval τ is defined the same as that in Section 3.2, which is:

$$P^i(N, \tau) = \frac{M_\tau!}{N!(M_\tau - N)!} f_{sum}(E)^N (1 - f_{sum}(E))^{M_\tau - N} \quad (3.30)$$

where M_τ is the number of attempts of injecting carriers in a time-interval τ , defined as a number rounds the quotient τ/t_0 to the nearest natural number towards zero. The number of injected electrons is $N = 1, 2, \dots, M_\tau$.

As a simply estimation, we assume a ballistic transport in the electronic device and compute the (instantaneous) current I taken by each electron when it manage to enter the device active region. The current I is computed by using the expression $I = qv_x/L_x$ being q the electron charge without sign, v_x the electron velocity component and L_x the distance in the transport direction. As plotted in figure 3.2.2(a), almost all electrons injected from a contact with linear band structure have the same velocity and carry the same instantaneous current I . On the contrary, in figure 3.2.2(b), electrons injected from a parabolic band structure materials have large dispersion in both the velocity and

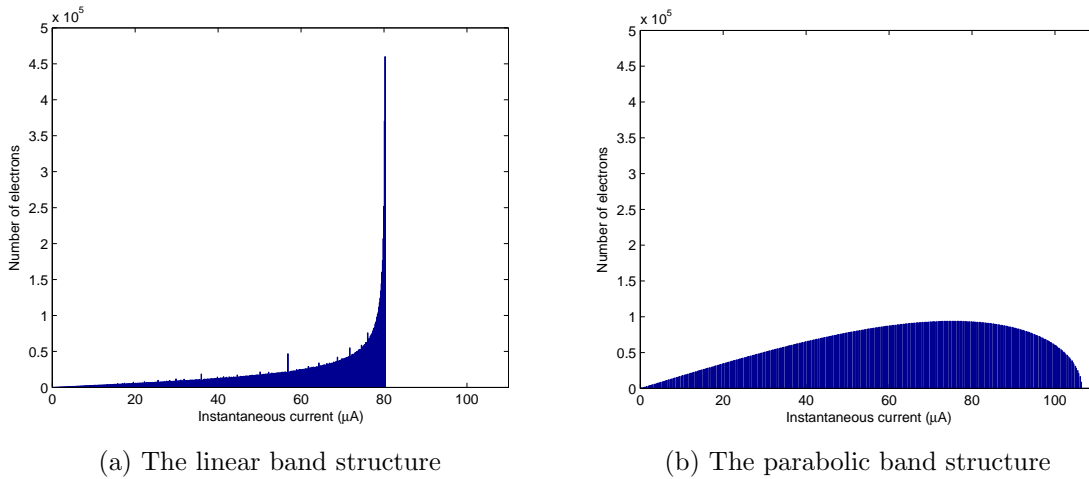


Figure 3.2.2: Number of electrons as a function of instantaneous current I during a simulation time $\tau = 10$ ns at temperature $\Theta = 300$ K, with Fermi level $E_f = 0.1$ eV for materials with (a) a linear band structure and (b) a parabolic band structure.

instantaneous current I . The current dispersion (noise) of both types of band structures are dramatically different, which can have relevant effect in the intrinsic behaviour of AC and noise performances.

3.3 Implementation of the Injection Model into the BITLLES Simulator

An algorithm for the general injection of electrons with parabolic $\epsilon(k_x, k_y, k_z)$ dispersion in nanoscale devices and with (or without) electron confinement for degenerate (or non-degenerate) conditions is extensively described in the literature[79]. Therefore, in this part, we will only provide specific attributes to the injection model suitable for the graphene transistor in BITLLES simulator. Firstly, we will explicitly compute the occupation probability that a new state of electron with energy E , which will eventually attempt to inject from the ideal contact into the 2D channel. Generally, the fluctuating occupancy of the incoming electron at the injection contact, and particularly, the energy occupation at the opposite of the injection contact associated with a Fermi-Dirac distribution, and the conservation of the momentum projection k_z will be investigated. We will focus on the carrier injection from the source contact. The injection from drain contact is identical. Then, an algorithm to implement the injection model to the simulator will be briefly described.

Using the FET transistor nomenclature, source contact for left injection and drain contact for right injection. Now we consider the Pauli exclusion principle at the injection

contact, i.e. the source contact. The Fermi-Dirac distribution gives the occupation probability that a state with energy E exists in thermal equilibrium, as

$$f_s(E) = \frac{1}{\exp[(E - E_{fs})/(k_B\Theta)] + 1} \quad (3.31)$$

where E_{fs} is the Fermi-level (chemical potential) at the source contact, k_B is the Boltzmann constant and Θ is the temperature. The electron energy E is related to its wave vector by the appropriate energy dispersion $E(\vec{k})$.

Due to the peculiar tunneling properties of two-dimensional massless Dirac electrons in graphene sheet, injections from the contact have to consider carriers from both the valence band (VB) and the conduction band (CB), which is different from the case in conventional semiconductors (for example, the Silicon semiconductor). In the literature, the electrons with positive energy called electrons and with negative energy called holes. In order to avoid confusing the electron moving in the valence band with the hole, in our injection model, we do not use the name hole but directly inject electrons in VB (electrons with negative energy) and in CB (electrons with positive energy) ².

In graphene sheet with the linear dispersion relations, it is convenient to choose the Dirac point which has energy $E(|\vec{k}| = 0) = 0$ as the reference of energy. At the drain contact, for the electrons with positive energy $E = E(\vec{k})$, only the electrons with $k_x < 0$ are considered, and the energy distribution is described by the Fermi-Dirac distribution. On the contrary, for the electron with negative energy moving in the VB, the energy distribution is also determined by the Fermi-Dirac distribution, but only the electrons with $k_x > 0$ are considered. The electrons injected from the drain contact have the energy distribution determined by:

$$f_d(E) = \frac{1}{\exp[(E - E_{fd})/(k_B\Theta)] + 1} \quad \begin{cases} \text{for } E = E(\vec{k}) > 0 & \text{with } k_x < 0 \\ \text{for } E = E(\vec{k}) < 0 & \text{with } k_x > 0 \end{cases}$$

In (or near) equilibrium, according to the Fermi-Dirac distribution, band with all energies many $k_B\Theta$ above the Fermi energy E_{fs} will be unoccupied. Furthermore, below the bands that all energies many $k_B\Theta$ less than E_{fs} are completely filled. Thus, we do not need to consider infinitely many carriers of different types, but only those in bands within a few $k_B\Theta$ of, or lower than Fermi level E_{fs} . This restriction can be utilized as one of the following selected rules for the maximum wave vector in the injection model.

²It must be emphasized that pictures of electron and hole can not be mixed within a given band, i.e., if one wishes to regard electrons as carrying the current, then the holes make no contribution; if one wishes to regard the hole as carrying the current, then the electrons make no contribution.

Correlation Between the Source and Drain Contact

It is reported[80, 81] that electrons in the graphene approach ballistic transport. The total energy E for an electron moving inside graphene channel satisfies the fundamental conservation law. Assuming that the applied fields do not cause interband transitions, it is reasonable to consider that each band has limitation to contain the maximum number electrons. This can be explained equivalently from a quantum mechanical point of view. As a consequence of the Pauli exclusion principle at the contact and inside the active region, in the 2D graphene case, each electron needs a volume for itself in a four-dimensional phase-space. Given any region of four-dimensional phase-space Ω , on the condition that no two electrons can occupy the same state, the Ω contains a maximum number of electrons allowed. The number of electrons in the Ω region can only be reduced if there are some incompletely filled states in the band for those electrons to move into. The probability that a state at energy E will be unoccupied at the drain contact in thermal equilibrium is:

$$f_{sd}(E) = \left(1 - \frac{1}{\exp[(E - E_{fd})/(k_B\Theta)] + 1} \right)^{C_t} \quad (3.32)$$

where the exponent $C_t = 1$ for the case of ballistic transport and Pauli exclusion principle included, the exponent $C_t = 0$ for non-ballistic transport. On the condition that the correlation between the source and drain contact is considered, before an electron is attempted to inject from the source contact into the system, one need to make sure that when the electron move to the drain contact, there has a vacancy for the electron to move into, because it is no sense to have more than one electron occupy one state. The probability distribution is determined by equation (3.32).

Conservation of Momentum Projection k_z

When considering a massless Dirac particle incident on a potential barrier that is translationally invariant in the z direction (perpendicular to the transport direction) $V(x, z) = V(x)$, in addition the conservation law of electron energy E as a result of time translational invariance, the conservation of the momentum projection k_z is also need to be considered as a result of translational invariance along z dimension.

Let us give an example how the conservation of momentum projection k_z affect our injection model. Considering one electron with energy E injected successfully from the source contact into the system. Assuming that the electron transmitted the potential barrier and finally manage to arrive at the drain contact. Due to the applied voltage drop V_{DS} cross the system, the electron has energy $E + qV_{DS}$ after it move into the drain contact. According to the linear dispersion relation in graphene sheet, the maximum

absolute value of momentum projection k_z that the electron can obtain is $|k_z|_{max} = |(E + qV_{DS})/(\hbar v_f)|$, being \hbar the reduced Planck's constant and v_f the Fermi velocity of particles in graphene sheet. If one electron is injected at the source contact with $|k_z| > |k_z|_{max}$, according to the general conservation law of total energy and momentum projection k_z , at the drain contact, no state is extant to allow the electron to move into. therefore, at the source contact, owing to the conservation law of momentum projection k_z , the energy distribution for an electron with energy E can be described as:

$$P_{k_z} = \left(1 - H(|k_z| - |k_z|_{max}) \right)^{C_k} \quad (3.33)$$

where $H(|k_z| - |k_z|_{max})$ is a Heaviside step function and the maximum absolute value of k_z is calculated from the formula $|k_z|_{max} = |(E + qV_{DS})/(\hbar v_f)|$. The exponent $C_k = 1$ for the case of the channel with linear dispersion relations and $C_k = 0$ for other cases.

Up to now, three fundamental laws, which we utilize to explicitly compute the occupation probability $f_{sum}(E)$ for an electron with energy E , have been briefly described. At the source contact, the $f_{sum}(E)$ is a product of the distributions given in this subsection as:

$$f_{sum}(E) = f_s(E) f_{sd}(E) P_{k_z} = \frac{1}{\exp[(E - E_{fs})/(k_B\Theta)] + 1} \times \left(1 - \frac{1}{\exp[(E - E_{fd})/(k_B\Theta)] + 1} \right)^{C_t} \left(1 - H(|k_z| - |k_z|_{max}) \right)^{C_k} \quad (3.34)$$

The occupation probability formula $f_{sum}(E)$ in equation (3.34) is more general than the expression in equation (3.31), which was used as the energy distribution for our previous injection model[79]. The Fermi-Dirac distribution in equation (3.31) is a more general law used in most nanoscale simulators. The other two additional laws in equations (3.32) and (3.33) are options in the improved injection model. In the case of an electron with energy described by the linear dispersion expression and ballistic transport, the two additional laws are valid (i.e. the exponents $C_t = 1$ and $C_k = 1$). Otherwise, the value for the terms $f_{sd}(E)$ and P_{k_z} are all the time equal to 1, and the probability expression in equation (3.34) equals to that in equation (3.31).

The figure 3.3.1 illustrated how the additional two laws affect the energy distribution in the new injection model in the case of injected electrons has ballistic transport in graphene transistors. In figure 3.3.1(a), all the electrons move in VB are attempt to inject into the system, only the Pauli exclusion principle is considered in the injection contact. However, in figure 3.3.1(b), when the relation between the source contact and drain contact and the k_z conservation laws are also included, the energy distribution in

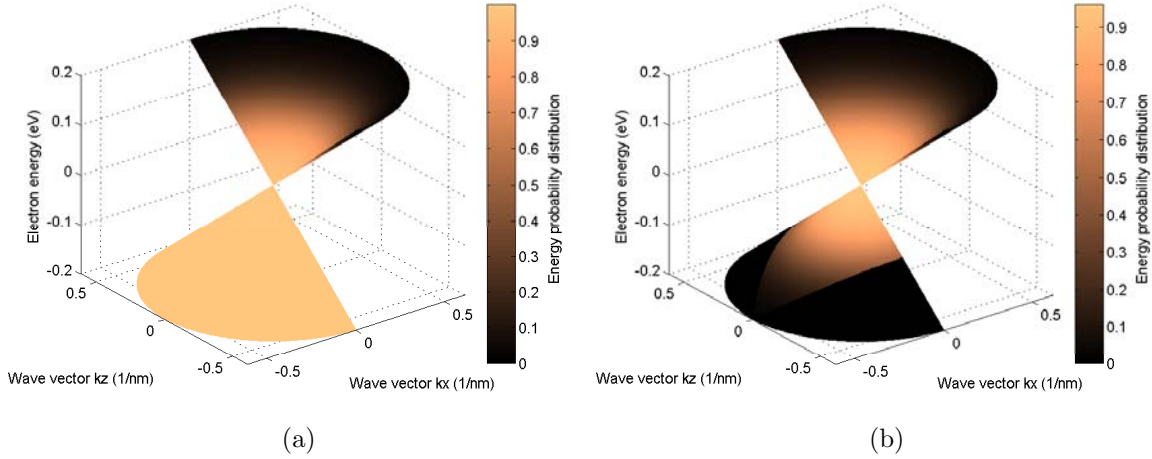


Figure 3.3.1: The energy distribution of the electrons with positive energies (in CB) (on the right side of (a) and (b) for $k_x > 0$) and with negative energies (in VB) (on the left side of (a) and (b) for $k_x < 0$) injected from the source contact plotted in (a) which computed from equation (3.31) and in (b) which computed from equation (3.34). The absolute temperature $\Theta = 300$ K, Fermi-level at the source contact $E_{f_s} = 0.1$ eV, an voltage drop $V_{DS} = 0.3$ V applied to the device and the Fermi velocity $v_f = 5 \times 10^5$ m/s.

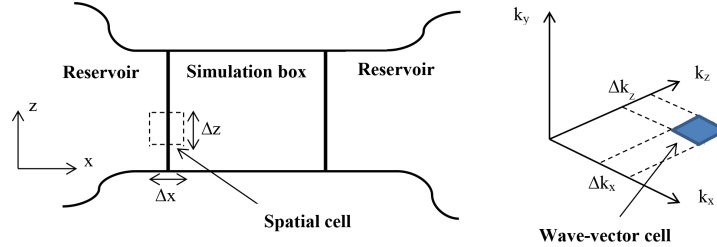


Figure 3.3.2: Schematic representation of a 4 dimensional phase-space cell where the injection probability is computed.

VB is different to that in figure 3.3.1(a). In figure 3.3.1(b), less electrons from VB are attempt to be injected into system. The occupation probability for the electrons in VB with $k_z > 0.5$ 1/(nm) equals to 0, which is a result of the k_z conservation. The probability for the electrons in VB with energy $E > 0.2$ eV (for $|\vec{k}| > 0.5$ 1/(nm)) approximate to 0, which is a result of the correlation between the source and drain contact.

The electron injection model in the time-dependent formalism needs to specified details of the carrier injection: (a) the way to determine the number of carriers needed to be injected in each time step; (b) the moment at which the injected particle enter into the system; (c)the coordinates for the injected particle; (d) the velocity for the new state of the particle. The particles and current processes in the model are all considered to be stationary and ergodic, i.e., the distribution for one ensemble element (for example

the number of injected carriers, the current and fluctuations in the current) over time is identical to the distribution over the whole ensemble at a chose point in time. The injection model in the time-dependent picture can be utilized to study the AC and transient current as well as noise performance in nanoscale devices.

The injection model is mainly described by equations (3.28) and (3.30) for materials with the linear band structure (or equations (3.20) and (3.22) for contact with a parabolic dispersion). The procedure of the injection model in implementing to the BITLLES simulator for the whole simulation time is as following:

- *Step 1. Define a mesh (see figure 3.3.2) for the whole phase-space associated to the injecting surface:* The limits of the spatial space are selected by the boundaries of the contact surfaces. It is proved [79] that the selection of dimensions of each spatial cell is arbitrary. In the 2D case, in order to speed the computational algorithm, the spatial cell can be chosen as large as the contact surface (i.e. $\Delta z = L_z$ being L_z the lateral width). In the $\{k_x, k_z\}$ space, The limits of the reciprocal space is selected indirectly by the occupation distribution. That is, the maximum value of the wave vector components, $k_{x,max}$ and $k_{z,max}$ must be selected large enough to be sure that $f_{sum}(E(k_{x,max})) = f_{sum}(E(k_{z,max})) \approx 0$. The minimum value of the wave vector components is assumed to be $k_{x,min} = -k_{x,max}$ and $k_{z,min} = -k_{z,max}$. The Dirac point as the reference energy. The wave-vector cell width is assumed to be $\{\Delta k_x, \Delta k_z\}$. Then, the wave vector components are specified as $k_{x,i} = i\Delta k_x$ and $k_{z,j} = j\Delta k_z$ with $i, j \in \mathbb{N}$. The step Δk_x has to be small enough to assure a rough constant transport velocity for electrons. From the expressions for the minimum temporal separation in equations (3.28) and (3.20), the selection of step Δk_z can be different for the material with parabolic or linear dispersion relations. For the material with parabolic band, the dimension of k_z is arbitrary[79]. We can select $\Delta k_z = 2 \cdot k_{z,max}$. However, for the material with linear band, due to the fact that v_x is explicitly dependent on both wave vector component k_x and k_z , the interval Δk_z should be also selected small enough to roughly maintain the constant v_x .
- *Step 2. Select the minimum temporal separation t_0 (or t_0^P) for each phase-space cell:* At each simulation time equals to multiples of t_0 , an attempt to inject an electron from this particular phase-space cell into the active device region happens.
- *Step 3. Compute the kinetic energy E of the electron:* At this point, a random number r uniformly distributed between zero and one is generated, and the electron is considered to successfully be injected only if $r < f(E)$. This procedure reproduces the Binomial probability described in equation (3.30).
- *Step 4. Select the properties of the effective injected electron:* Since a phase-space cell manages to inject an electron enter the system, the information about the

moment, the velocity and x position for the electron are specified. Next, we need to select its y and z positions. There is no confinement in z direction, the positions of the electron are selected with a uniform random distribution along the lateral width of the spatial cell Δz . As the y direction is confined, the y position of the electrons is selected according to the non-uniform distribution $|\Psi_z(z)|^2 = \frac{2}{T} \sin^2(\pi \cdot z/T)$ being T the length of the device in y direction. Up to here, the procedure for one attempt is completed, and the complete process is repeated for the whole simulation time.

- *Step. 5 Repeat the complete injection procedure:* The same procedure is repeated for all valleys, and all subbands participating in the electron transport. The injection model has to be implemented to all contacts of the device.

CHAPTER 4

Dissipative Transport Through Collisions

4.1 Preliminary Discussions

As I have discussed in previously, owing to the many-body problem, people are interested in partitioning a closed system into an *open system* and “everything else”. An electron device with an applied bias is indeed a quantum open system far from thermodynamic equilibrium. The electrons inside the active region of the device are part of the simulated degrees of freedom of the open system, while many other degrees of freedom (like the electrons in the battery, the phonons, etc.) are not included in the simulations. From a practical perspective, an open system is described by the density matrix in terms of mixed states (a statistical ensemble of several quantum states)[82–84]. In the usual perturbation theory, the dynamics of the simulated electrons of interest are modeled through a well defined *unperturbed* Hamiltonian H_0 . The interchange of energy between the simulated electrons and the environment¹, like electron-phonon or electron-impurity interactions, is added into the *unperturbed* equation of motion as an additional term, the so-called *collision* term [71]. The *unperturbed* Hamiltonian term can be easily treated, while the *collision* term requires typically important approximations [45, 71, 85].

The consideration of the collision term in the modeling of quantum transport is of paramount importance because it converts a unitary and reversible equation of motion for the density matrix into a non-unitary and irreversible one, accounting for the phenomena of dissipation and decoherence. The proper treatment of such phenomena is mandatory for a realistic simulation of electron devices [46, 86, 87]. There are many proposals for the collision operator in the literature [88–94]. Some simple versions of the collision term have a wide practical applicability, but in some scenarios they can lead to unphysical results, in

¹Although phonons and impurities are in the same physical space as the electrons, since their degrees of freedom are not simulated, we consider them “outside” of the system.

terms of negative values of the probability presence of electrons at some locations. In this Chapter, I will discuss the influence of knowing or not knowing the quantum states that build the density matrix when modeling dissipative transport in electronic devices. First of all, I introduce a simple and widely used algorithm in treating the scattering through the Boltzmann collision operator for a quantum transport. A numerical example, a toy-model of an electron in a double barriers interacting with a phonon, will be discussed to illustrate the advantage of knowing the quantum states. Secondly, I will discuss the equation of motion of the conditional wave function when dissipation is introduced. I will apply this model to compute dissipative quantum transport in a resonant tunneling device (RTD).

Before introduce the collision, let me explain briefly the equation of motion of the density matrix and Wigner distribution function formalisms, which are usual used to described the open system. For the sake of simplicity, we will assume a mean field approximation that allows us to discuss quantum transport in terms of a set of non-interacting individual electrons. As the same in Chapter 2, I will still consider a one-dimensional (1D) physical space x or a 1D phase space $x - k$.

4.1.1 The Density Matrix Formalism

As we have discussed previously, a *natural* approach to describe the *open* system state is the density matrix. The equation of motion of the density matrix for the open system is the so-called Liouville Von-Neumann equation (3.2) plus an additional collision term [71, 75]:

$$\frac{\partial \rho}{\partial t} = \frac{1}{i\hbar} [H_0, \rho] + C[\rho] \quad (4.1)$$

where H_0 is the *unperturbed* Hamiltonian and $C[\rho]$ is the collision term that describes the effect of the interaction with the environment.

An important quantity in the modeling of electrical devices can be obtained by the trace of the density matrix:

$$Q(x, t) = \text{tr}(\hat{\rho}(t)) = \sum_j p_j(t) |\psi_j(x, t)|^2. \quad (4.2)$$

where $p_j(t)$ specifies the probability that the open system is described by the pure state $\psi_j(x, t)$. It is important to notice that the states $\psi_j(x, t)$ in (4.2) are, from the orthodox point of view, an *improper* mixture of states, which means that none of the states alone provides a proper ontological description of the open system, only the mixture. In other words, there is no orthodox wave function of an open system. On the contrary, we will see later that $\psi_j(x, t)$ in (4.2) are, from the Bohmian point of view, the conditional wave

function of the system, with full ontological Bohmian meaning. The state $\psi_j(x, t)$ is the conditional wave function of the degree of freedom x of the quantum system in the j experiment.

The function $Q(x, t)$ is often referred in the literature as the charge (or probability presence) density of the system. By definition, either interpreted as a probability presence or as the system charge, negative values² cannot be accepted in equation (4.2).

4.1.2 The Wigner Distribution Function Formalism

Alternatively, an open system can also be described by the Wigner distribution function (3.4). The transport equation of the Wigner distribution function for the open system can be written as a sum of a term given by $L_W [F_W(x, k, t)]$ plus a generic collision term $C_W [F_W(x, k, t)]$ as:

$$\frac{\partial F_W(x, k, t)}{\partial t} = L_W [F_W(x, k, t)] + C_W [F_W(x, k, t)]. \quad (4.3)$$

The term $L_W [F_W(x, k, t)]$ is:

$$L_W [F_W(x, k, t)] = -\frac{\hbar k}{m} \frac{\partial F_W(x, k, t)}{\partial x} - \frac{2}{\pi \hbar} \int_{-\infty}^{\infty} dk' \int_0^{\infty} dx' e^{[-i(k-k')2x']} \times [V(x+x') - V(x-x')] F_W(x, k, t) \quad (4.4)$$

under the effective mass approximation. $V(x)$ is the potential energy. The collision term $C_W [F_W(x, k, t)]$ has many different practical implementations (based on different approximation).

The charge density in (4.2) can also be obtained by integrating the Wigner distribution over all momenta:

$$Q(x, t) = \hbar \int F_W(x, k, t) dk. \quad (4.5)$$

In the literatures [95–99], there is a large list of different approaches that are used to define the collision operator, either in the density matrix formalism $C[\rho]$ or in the Wigner formalism $C_W [F_W]$.

²Although not relevant for this work, strictly speaking, as seen for a pure state $Q(x, t) = |\psi(x, t)|^2$, equation (4.2) represents the probability presence density. To avoid any misunderstanding, if one wants to interpret (4.2) as charge, then I can also argue that it is unacceptable of a positive value of $-qQ(x, t)$ (with $-q = -1.6e^{-19}$ C the electron elementary charge) as the charge of electrons in an open quantum system.

Table 4.1: Some unphysical behaviors found in the literature when modeling dissipative quantum transport with the density matrix or Wigner distribution function formalisms using different implementations of the collision operator.

Collision term	Unphysical problem	Ref.
Non-Markovian treatment of collision	Without adding the Markovian approximation negative charge appears.	[100]
Barker-Ferry equation and Levinson equation	The simulation time has to be small enough to avoid negative probability in the momentum space.	[101]
Boltzmann collision operator, plus Fermi Golden rule	It can give negative charge in some scenarios due to the fact that the “rates derived based on the Fermi Golden rule rely on a well-defined kinetic energy pre- and post-scattering states”.	[102]
Relaxation time approximation	The final (thermodynamical) equilibrium state used in the approximation can be unknown or unphysical.	[87]
Any type of collision operator	A phenomenological injection model (without inclusion of a collision term) can provide negative charge.	[46]

4.1.3 Unphysical Negative Charge Density Found in the Literature for Quantum Transport Models

As I said previously, a proper treatment of the interaction of electrons with the environment by a collision term in equations (4.1) or (4.3) is mandatory for a realistic simulation of electron devices. Such a collision term cannot be treated exactly and some approximations are required. However, the approximations do not only imply deviations from the exact result but, in some circumstances, they imply that the simulated results are unphysical (for example, the negative values of the charge density discussed in this section). In Table 4.1, I list some recent works of the literature explaining the negative values of the charge density, obtained from quantum transport formalisms dealing with the density matrix or the Wigner distribution function, with different implementations of the collision terms. Indeed, there are many different reasons that explain why we can obtain negative charge densities. One can realize the important conceptual and practical difficulties of the proper modeling of the collision term with the recent work of Rossi and co-workers [100]. There, the authors show that a quite detailed treatment (including only a mean-

field approximation) of electron-phonon scattering in the density matrix formalism leads to negative values of the charge. Surprisingly, such unphysical results disappear when a simpler treatment (including mean-field and Markovian approximations) is considered [100]. Similarly, a detailed treatment of scattering within the Barker-Ferry equation (or the Levinson equation) with a generalized Wigner distribution function formalism shows the relevance of the simulation times in the description of the collision interaction. For such approaches, unphysical results appear if the simulation time is not short enough (such limitation being related to the first order perturbation done in the development of the electron-phonon coupling) [101]. The implementation of the spatial boundaries conditions on the equation of motion of the density matrix at the borders of the simulation box can also be the origin of some unphysical results [46]. In this sense, it is very enlightening the discussion about mathematical and physical solutions of equation (3.4) done by Rossi and co-workers in [76]. We assume that $f_\alpha(x, k)$ is a physical (and mathematical) solution of (3.4), and that $f_\beta(x, k)$ is another physical (and mathematical) solution. Then, because of the superposition principle, $f(x, k) = c_\alpha f_\alpha(x, k) + c_\beta f_\beta(x, k)$ is by sure a mathematical solution of (3.4). However, we can select the coefficients c_α and c_β in such a way (for example, a negative value of c_β) so that $f(x, k)$ may give rise to a negative charge distribution at some location, which means that $f(x, k)$ will be an unphysical solution of equation (3.4), although it is a perfect mathematical solution.

In the following subsection, I will analyze, indeed, a much simpler and widely used treatment of the collision term. We discuss why in some circumstances the use of the Boltzmann collision operator can produce unphysical results if we do not know the quantum states during the collisions. It is important to notice here that the Boltzmann collision operator is usually implemented through the use of the Fermi Golden rule that determines the scattering rates³ [33, 97, 103]. In this work, we do not discuss the range of validity of the approximation of the Fermi Golden rule, but only some inherent difficulties that can be found in the practical implementation of the Boltzmann collision operator in quantum simulators. Then, these potential problems could be solved once the quantum states are known.

4.2 To Know or not to Know the Quantum States

The Boltzmann collision operator was initially proposed for classical systems [104]. For such systems, it has a very easy and understandable interpretation. The Boltzmann collision operator is just a rule for counting the number of electrons in and out of a

³The Fermi Golden rule itself is developed under some approximations. First, the interaction time has to be small enough to make the first order perturbation development correct [32]. Second, the interaction time has to be large enough to ensure that the sinc function approaches a delta function in the development of the Fermi Golden rule [32].

volume of the phase space ΔV due to a collision. The total number of electrons at time $t + \Delta t$ in ΔV is equal to the previous number of electrons that were there at t , before the collision, *plus* the number of electrons that arrive at ΔV from outside due to collision, *minus* the number of electrons that leave ΔV during the collision.

Let us imagine a classical electron at x_0 with a velocity v_0 that interacts with another particle (for example, a phonon). Because of the interaction, the electron loses kinetic energy and its final velocity is v_f . For simplicity, we assume that the initial position remains unchanged. Such collision process can be easily modeled in terms of the previous Boltzmann collision operator. The initial classical distribution function in phase space before the collision (apart from constant factors), at time t_0 , is:

$$F_c(x, k, t_0) = \delta(x - x_0)\delta(k - k_0) \quad (4.6)$$

being k_0 the wave vector associated to v_0 . The Boltzmann collision operator generates the effect of the collision by subtracting an electron with momentum k_0 and adding a new electron with momentum k_f . The final classical distribution function in phase space after the collision, at time $t = t_0 + \Delta t$, is:

$$\begin{aligned} F_c(x, k, t + \Delta t) &= \delta(x - x_0)\delta(k - k_0) - \delta(x - x_0)\delta(k - k_0) + \delta(x - x_0)\delta(k - k_f) \\ &= \delta(x - x_0)\delta(k - k_f). \end{aligned} \quad (4.7)$$

Up to here, the discussion seems very trivial in the classical system. Let us emphasize that the negative part of the distribution function generated by the Boltzmann collision operator $-\delta(x - x_0)\delta(k - k_0)$ is completely compensated by the original positive one $\delta(x - x_0)\delta(k - k_0)$. In this sense, the use of the Boltzmann collision operator in classical systems will always give positive charge probability in equation (4.5).

Now, let us change to the quantum system where we have to add/subtract quantum states or wave functions, not point particles. As we will see next, the problems will appear when we do not know the states that built the density matrix of the open system.

We consider an electron device as an open system with M electrons which can be distributed in N different states. Say, there are M_1 electrons described by state $\psi_1(x, t)$ where we define $p_1 = M_1/M$. There are M_2 electrons with probability $p_2 = M_2/M$ described by the state $\psi_2(x, t)$ and so on. Although it is not relevant in the present discussion, we emphasized again that there is no orthodox wave function of an open system. Therefore, the states $\psi_1(x, t)$ and $\psi_2(x, t)$ are defined only to construct an *improper* mixed state. According to (3.1), we construct a mixed state through the density

matrix that describes our open system at initial time t_0 before the collision:

$$\rho_B(x, x', t_0) = \sum_{i=1}^N p_i(t_0) \psi_i(x, t_0) \psi_i^*(x', t_0) \quad (4.8)$$

with the conditions $\sum_{i=1}^N p_i(t_0) = 1$ and $\sum_{i=1}^N M_i = M$. Because of the interaction of one electron with a phonon, the Boltzmann collision operator will add a new final state of the electron $\psi_F(x, t)$ and will subtract another state associated to the electron $\psi_O(x, t)$. Then, the new density matrix after the scattering, at time $t_S = t + \Delta t$, will be:

$$\rho(x, x', t_S) = \rho_B(x, x', t) - \frac{1}{M} \psi_O(x, t) \psi_O^*(x', t) + \frac{1}{M} \psi_F(x, t) \psi_F^*(x', t) \quad (4.9)$$

The details of explanation that the collision effects through the Boltzmann collision operator could effectively be written in the (4.9), will be discussed later in Subsection 4.2.1 and can be found in paper [105]. The problem with the expression (4.9), due to Boltzmann collision operator, is that if we subtract a state $\psi_O(x, t) = \psi'_2(x, t)$ that is not present in the density matrix before the collision, $\rho_B(t_0)$, then we cannot simplify the density matrix to remove the negative sign that appears in the second term of the right hand side of (4.9). By a simple computation, the new expression of the charge density with (4.2) using the density matrix in (4.9) is:

$$Q(x, t_S) = \sum_{i=1}^N p_i |\psi_i(x, t)|^2 - \frac{1}{M} |\psi'_2(x, t)|^2 + \frac{1}{M} |\psi_F(x, t)|^2 \quad (4.10)$$

This charge density is a sum of positive and negative terms. The dramatic problem with expression (4.10) is that, when the time-evolution of the negative term $\psi'_2(x, t)$ is not perfectly balanced by the positive term $\psi_2(x, t)$ (or by other states that build ρ_B) and $\psi_F(x, t)$ at every time and position, the possibility of getting negative values $Q(x, t)$ (unphysical result) is opened.

The solution to this problem is, in principle, quite simple. If we subtract a state $\psi_O(x, t)$ which is present in the density matrix $\rho_B(t)$, for example, $\psi_O(x, t) = \psi_2(x, t)$, then, we can write the density matrix in (4.9) at any time t after the scattering as:

$$\rho(x, x', t_S) = \sum_{i=1; i \neq 2}^N p_i(t) \psi_i(x, t) \psi_i^*(x', t) + \frac{M_2 - 1}{M} \psi_2(x, t) \psi_2^*(x', t) + \frac{1}{M} \psi_F(x, t) \psi_F^*(x', t) \quad (4.11)$$

The relevant point now is that, by construction, the term $(M_2 - 1)/M$ will be positive at any time t . Obviously, in the selection of the scattering process we have to ensure that $M_2 \geq 1$, because if not, we will subtract a non existent state. If the condition $\psi_O(x, t) =$

$\psi_2(x, t)$ is satisfied during the collision, then, independent of the time-evolution of all the states, the charge density computed from (4.2) using the density matrix in (4.11) is just a sum of positive terms:

$$Q(x, t_S) = \sum_{i=1; i \neq 2}^N p_i |\psi_i(x, t)|^2 + \frac{M_2 - 1}{M} |\psi_2(x, t)|^2 + \frac{1}{M} |\psi_F(x, t)|^2 \quad (4.12)$$

It is important to emphasize that this procedure requires a knowledge of the pure states that build the density matrix (or the Wigner distribution function) at all times of our open system. This information is usually not available in most quantum transport simulations, because the states build an *improper* mixed state (with no ontological meaning for each individual state). However, such states and its ontological meaning is trivially accessible in the Bohmian formulation of quantum transport in terms of conditional wave function [42]. Hereafter, firstly, I will show with some simple numerical examples where the problems of not knowing the quantum states are present.

4.2.1 Collisions Without Knowing the Quantum States

I will firstly deduced the collision term when we do not know the quantum states (I called the Hamiltonian eigenstates scattering approach), which is a combination of the Wigner formalism with the Boltzmann collision operator where the scattering rates are obtained from the Fermi Golden rule. Then, an example of electrons suffering a collision with a phonon while traveling through a typical double barrier potential will be discussed by using the Hamiltonian eigenstates scattering approach to deal with the scattering.

The Boltzmann collision operator in the Wigner formalism is rewritten:

$$C_W [F_W(x, k, t)] = \frac{1}{2\pi} \int_{-\infty}^{\infty} \left\{ W_{k'k} F_W(x, k', t) - W_{kk'} F_W(x, k, t) \right\} dk' \quad (4.13)$$

where the transition probabilities $W_{k'k}$ are obtained from the Fermi Golden rule according to [106]:

$$W_{\vec{k}'\vec{k}} = \frac{2\pi}{\hbar} |M_{\vec{k}'\vec{k}}|^2 \delta(E_{\vec{k}} - E_{\vec{k}'} \mp \hbar\omega) \quad (4.14)$$

where $M_{\vec{k}'\vec{k}}$ are the matrix elements for the transitions from state \vec{k}' to \vec{k} , and ω is the frequency of the phonon for inelastic scattering. The bold symbols represent vectors in the 3D space. For technical reasons, since only one dimension is considered in subsection (4), the 3D scattering rates must be “projected ” onto the one-dimensional model to find $W_{k'k}$ defined in (4.13):

$$W_{k'k} = \frac{\lambda_T^2}{(2\pi)^3} \int_{-\infty}^{\infty} d^2 k'_\perp \int_{-\infty}^{\infty} d^2 k_\perp W_{\vec{k}'\vec{k}} \exp\left(-\frac{\lambda_T^2 k_\perp^2}{2}\right) \quad (4.15)$$

where k' and k are now the 1D initial and final states respectively.⁴ A very relevant point in the discussion is that the Fermi Golden rule (4.14) forces us to use Hamiltonian eigenstates (of the Hilbert space without the interacting potential) to compute the matrix elements $M_{\vec{k}'\vec{k}}$.

Let me note here that we are not focused on the simulation of realistic nanodevices, but only in showing with a very simple example an unexpected result when combining the Boltzmann collision operator and the Fermi Golden rule. The violation of the requirement $Q(x, t) \geq 0$ in only one simple system is enough to warn that such implementation of the collision operator can lead to unphysical results in more complex or realistic simulations. As seen in the inset of Fig. 4.2.1, we consider an electron that suffers a collision with a phonon while traveling through a typical double barrier potential. We consider a 1D Hilbert space with the following uniform grid $x_j = j\Delta x$, for $j = 1, 2, \dots, M$ with $\Delta x = 0.2$ nm the spatial step and $M = 3000$ the number of grid points. The simulation box is large enough (it extends from 0 till 600 nm) to avoid any spurious interaction of the wave packet with the spatial boundaries. In the simulation, the temporal step is $\Delta t = 3$ fs.

At the initial time t_0 we consider an arbitrary initial pure state $\langle x|\psi_B\rangle$ whose support fits perfectly inside the simulation box. Since we are interested in describing such system with the Wigner distribution function, the density matrix of this initial pure state is given by $\hat{\rho}_B = |\psi_B\rangle\langle\psi_B|$, and the Wigner distribution function just needs the Wigner-Weyl transform given by equation (3.4). The time-evolution of the Wigner distribution function can be computed directly by solving the Schrödinger equation (plus a Wigner-Weyl transform) or by solving the equation (4.3) without the collision operator. Then, at time t_S , a scattering process takes place according to the Boltzmann collision operator. Assuming that the scattering process is sufficiently instantaneous⁵ that the evolution of the Wigner distribution function from the $t_S - \Delta t$ till t_S is:

$$\begin{aligned} \left. \frac{\partial F_W(x, k, t)}{\partial t} \right|_{t=t_S-\Delta t} &\simeq \frac{F_W(x, k, t_S) - F_W(x, k, t_S - \Delta t)}{\Delta t} \\ &= \frac{1}{2\pi} \int \{W_{k'k} F_W(x, k', t_S - \Delta t) - W_{kk'} F_W(x, k, t_S - \Delta t)\} dk' \end{aligned} \quad (4.17)$$

⁴Here I assume that the distribution of electrons is Maxwellian with respect to the transverse wave vector k_\perp of the initial state, and λ_T is the spatial dimension factor given by:

$$\lambda_T = \frac{\hbar^2}{KTm^*} \quad (4.16)$$

where K is the Boltzmann constant and T is the absolute temperature.

⁵As indicated in [107], such assumption is not always valid. In any case, the consideration of a larger time will not significantly change the drawbacks of the Boltzmann collision operator mentioned here.

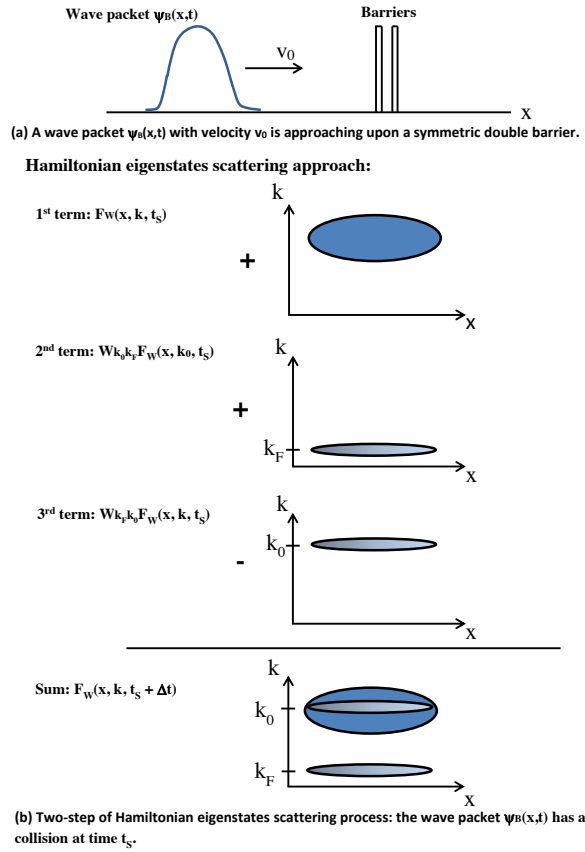


Figure 4.2.1: Schematic representation of the Hamiltonian eigenstates scattering process. (a) Simulation of a wave packet impinging on double barriers, the collision is performed at time t_S before the wave packet touches the barriers. (b) A simple physical picture of the two-step Hamiltonian eigenstates scattering process in the x - k space. During the collision, one term (3rd term) is eliminated and a new term (2nd term) is added. The eliminated state does not coincide with any of the old (before the collision) states of the system.

A further elaboration of equation (4.17) requires the specification of the scattering rates $W_{k'k}$ and $W_{kk'}$. As I just account for one collision process of one electron with one phonon, because of the collision, the initial wave vector of the electron k_0 changes to a final value k_F . By using the Fermi Golden rule in (4.15), such electron-phonon interaction (*ad hoc*) can be associated to the terms:

$$W_{k'k} = \alpha \delta(k' - k_0) \lim_{\sigma \rightarrow 0} e^{-\frac{(k-k_F)^2}{\sigma^2}} \quad (4.18a)$$

$$W_{kk'} = \alpha \delta(k' - k_F) \lim_{\sigma \rightarrow 0} e^{-\frac{(k-k_0)^2}{\sigma^2}} \quad (4.18b)$$

where the parameter α takes into account all (irrelevant for our simple example) details of the specific computation of the Fermi Golden rule. The parameter $\sigma \rightarrow 0$ means that rates $W_{k'k}$ and $W_{kk'}$ are localized closely to momentum $k = k_F$ and $k = k_0$, respectively.

For numerical reasons, I avoid writing explicitly delta functions in the right hand side of equations (4.18a) and (4.18b). In simple words, $W_{k'k}$ is the transition rate associated to an electron initially in $k' = k_0$ that appears finally at $k = k_F$, and $W_{kk'}$ is associated to an electron initially in $k = k_0$ that finally disappears from k_0 . The summary of this scattering process described in (4.17) is just that an electron with initial momentum $\hbar k_0$ gets a final momentum to $\hbar k_F$ because of the interaction with a phonon. Such scattering process is explained in figure (4.2.1). This is the quantum version of the classical collision explained in subsection (4.2).

Substituting the scattering rates written in (4.18a) and (4.18b) into equation (4.17) and rearranging it, to obtain:

$$F_W(x, k, t_S) = F_W(x, k, t_S - \Delta t) + \frac{\alpha \Delta t}{2\pi} F_W(x, k_0, t_S - \Delta t) e^{-\frac{(k-k_F)^2}{\sigma^2}} - \frac{\alpha \Delta t}{2\pi} F_W(x, k, t_S - \Delta t) e^{-\frac{(k-k_0)^2}{\sigma^2}} \quad (4.19)$$

Since there is a one-to-one correspondence between the Wigner distribution function and the density matrix [77, 108], one can obtain the density matrix by the inverse Wigner-Weyl transform of the Wigner distribution function as:

$$\rho(x, x', t) = \int_{-\infty}^{\infty} F_W\left(\frac{x+x'}{2}, k, t\right) e^{ik(x-x')} dk \quad (4.20)$$

As a consequence, the equation (4.19) can be rewritten as,

$$\begin{aligned} \rho(x, x', t_S) &= \rho_B(x, x', t_S) + \frac{\alpha \Delta t}{2\pi} F_W\left(\frac{x+x'}{2}, k_0, t_S - \Delta t\right) e^{ik_F(x-x')} \\ &\quad - \frac{\alpha \Delta t}{2\pi} F_W\left(\frac{x+x'}{2}, k_0, t_S - \Delta t\right) e^{ik_0(x-x')} \\ &= \psi_B(x, t_S) \psi_B^*(x', t_S) + \psi_F(x, t_S) \psi_F^*(x', t_S) - \psi_O(x, t_S) \psi_O^*(x', t_S) \end{aligned} \quad (4.21)$$

Up to here, I proved that the collision effects through the Boltzmann collision operator can be written in the form of equation (4.9). The first term on the right-hand side of equation (4.21), ρ_B , describes the density matrix before the collision, the second and third terms are the terms generated (by the Boltzmann collision operator) due to the collisions. It is important to underline that we are selecting α small enough to ensure that the charge probability of the density matrix $\rho(x, x', t_S)$ in (4.21) is strictly non-negative everywhere just after the scattering. As commented previously, it would be a nonsense to subtract more probability presence than what we have in one specific location at t_S . Even with this important requirement, the problem may appear later when the time evolution of $\rho_B(x, x', t_S)$ and $-\frac{\alpha \Delta t}{2\pi} F_W\left(\frac{x+x'}{2}, k_0, t_S\right) e^{ik_0(x-x')}$ in (4.21) becomes different.

I compute the charge probability distribution from equation (4.5) at four different

times corresponding to the initial time $t_0 = 0$ ps, just after the scattering time $t_S = 0.006$ ps, at $t_2 = 0.315$ ps when the wave packets ψ_B and ψ_O are interacting with the barriers, and at time $t_3 = 0.66$ ps when the interaction is nearly finished and the initial wave packets ψ_B and ψ_O are clearly split into transmitted and reflected components. The information corresponding to these four times is plotted in figure 4.2.2.

In order to enlarge the typical interference effects, at the initial time t_0 we consider the following initial state $\langle x|\psi_B\rangle = C\langle x|\psi_1 + \psi_2 + \psi_3\rangle$ with C a normalization constant. Each wave function $\psi_j(x, t_0)$ at the initial time t_0 is a Gaussian wave packet $\psi_j(x, t_0) = \left(\frac{2}{\pi a_0^2}\right)^{\frac{1}{4}} e^{ik_0(x-x_{0j})} \exp\left(-\frac{(x-x_{0j})^2}{a_0^2}\right)$ but with different initial central positions x_{0j} . In particular, the left wave packet ψ_1 has $x_{01} = 250$ nm, the middle wave packet ψ_2 has $x_{02} = 280$ nm and the right wave packet is ψ_3 has $x_{03} = 310$ nm. The initial spatial variance of the three wave packets is $a_0 = 15$ nm, its central wave vector $k_0 = 0.69$ nm⁻¹ and the effective mass $m^* = 0.2 m$ with m being the free electron mass. The center of the barriers is at $x = 350$ nm. Both barriers have a 0.8 nm width, the energy height is 0.2 eV, and they are separated by 4 nm.

After the scattering process at time t_S , The two additional wave packets ψ_O and ψ_F are Gaussian wave packets with the same very large dispersion $a_{0S} = 2a_0 \left(\sqrt{1 + \frac{4\hbar^2 t_S^2}{m_*^2 a_0^4}}\right)$ (to mimic a plane wave) and the same central position $x_{0S} = x_0 + \frac{\hbar k_0}{m_*} t_S$. The wave vectors for ψ_O and ψ_F are k_0 and $-k_0$ (here we assume $k_F = -k_0$), respectively. The results of the charge (or probability presence) densities in the right hand side of the figure (4.2.2) are just (4.5), that is the integral of the Wigner distribution function in the left-hand side of the figure over all momenta (for a fixed position). The negative values of the Wigner distribution function in the figures is not at all problematic as far as the marginal integral in (4.5) satisfies $Q(x, t) \geq 0$ [109]. Before and just after the collision, there is not unphysical evolution of the charge. Just after the collision, the new state $\psi_F(x, t)$ gives only positive charge density and the negative contribution of the new state $\psi_O(x, t)$ is, obviously, smaller than the positive one provides by $\psi_B(x, t)$ at each location. Figure (4.2.2) (e) and (f) show the same information at the new time $t_2 = 0.315$ ps when the wave packets $\psi_B(x, t)$ and $\psi_O(x, t)$ have evolved with time and interacting with the barriers. At position $x = 300$ nm, negative charge (presence probability) appears. This result is unphysical in the same sense that a wave function with a negative modulus will be unphysical, i.e. inconsistent with the probabilistic (Born law) interpretation of quantum mechanics. After the interaction is completed, at time $t_2 = 0.66$ ps, the spurious phenomenon becomes even worse. In this particular simple example, there are more positions (for example $x = 492$ nm) with negative value probabilities.

We have also performed simulations (not shown in the present paper) where the scattering process is strictly performed according to (4.21) using $-\frac{\alpha\Delta t}{2\pi} F_W\left(\frac{x+x'}{2}, k_0, t_S\right) e^{ik_0(x-x')}$

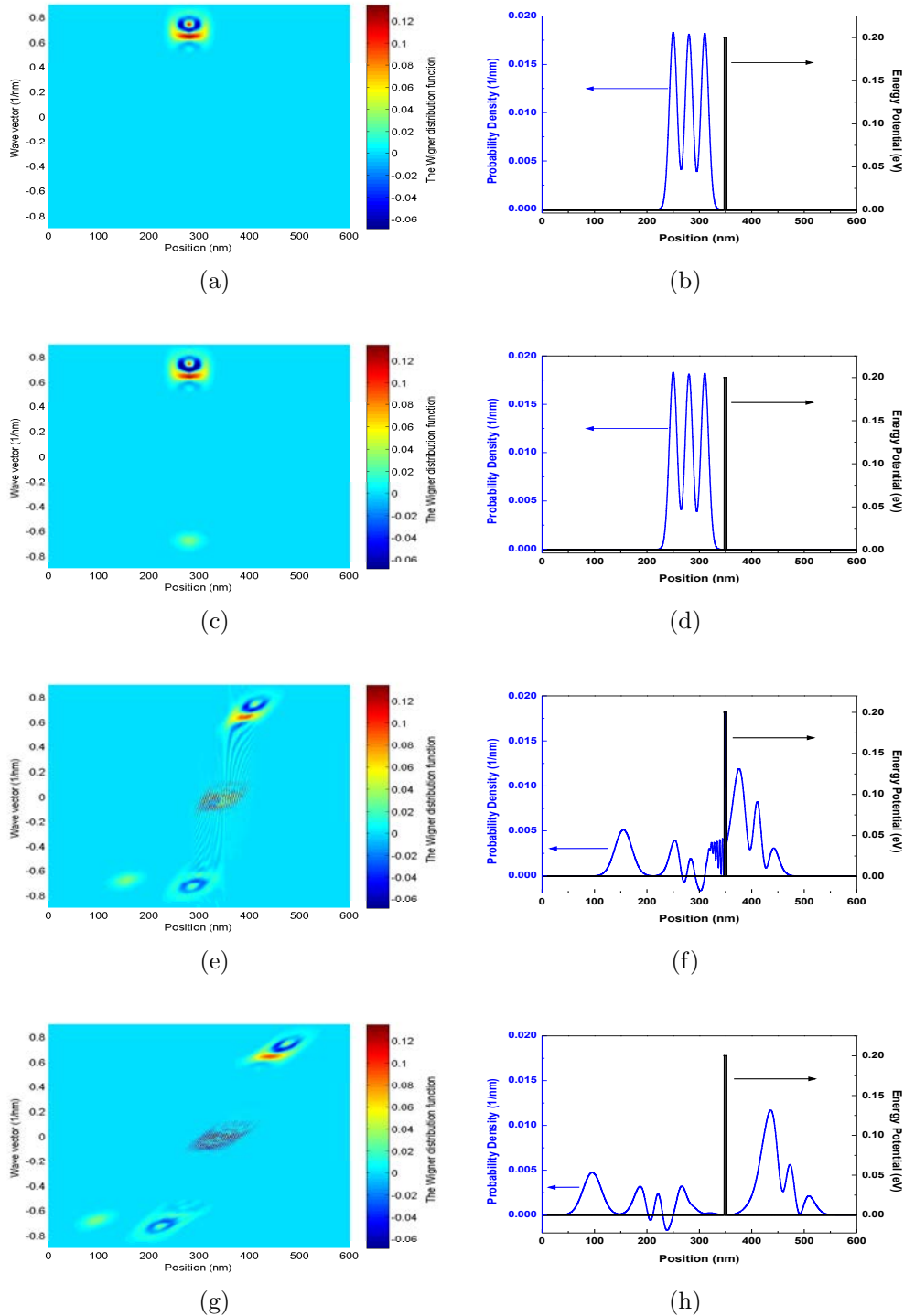


Figure 4.2.2: (Color online) Evolution of Gaussian wave packets coupled with the Hamiltonian eigenstates scattering approach moving towards barriers. (a), (c), (e), (g) are the Wigner distribution function and (b), (d), (f), (h) are the corresponding probability (charge) density at four different times: initial time $t_1 = 0$ ps, scattering time $t_S = 0.006$ ps before touching the barriers, time $t_2 = 0.315$ ps when wave packets are interacting with the barriers and time $t_3 = 0.66$ ps when the interaction is completely done. The collision is implemented with the Hamiltonian eigenstates scattering model. Because of such model, negative charge density appears.

instead of $\psi_O(x, t)\psi_O^*(x', t)$. The results are quite similar to the ones shown in figure (4.2.2), but because of the own positive/negative oscillation of the $F_W(\frac{x+x'}{2}, k_0, t)$, the charge probability results are even worse than the ones plotted here. The amplitude where the negative probability occurs is larger and such negative values appear in more positions, which is affected by the factor $\frac{\alpha\Delta t}{2\pi}F_W(x, k_0, t_S)$ describing the scattering strength. It is important to point out that the unphysical spurious behaviors become even worse with longer time evolutions (related to the device active region). In conclusion, the presence of negative charge is not because of the exact shape of the $\psi_O(x, t)\psi_O^*(x', t)$ and $\psi_F(x, t)\psi_F^*(x', t)$, either pure states or mixed states, but because the time-evolution of the states $\psi_O(x, t)$ is different from $\psi_B(x, t)$ because, at some times t , their positive and negative contributions cannot be compensated (even if they were compensated at t_0). In simpler words, the problem appears because we develop a collision term that subtracts a part of the Wigner function during the collision process, but we ignore if such procedure is correct or not because we cannot translate our collision term into the unproblematic language of collision between quantum states.

4.2.2 Collisions Knowing the Quantum States

As indicated previously, the solution to avoid these unphysical results of figure 4.2.2, while still using the Boltzmann collision operator, is having an exact knowledge of the states involved in the description of the density matrix. By construction, this way of working will not provide any negative charge density. In fact, the idea in the expression (4.11) can also be presented with the Wigner formalism. Let us see what is the Boltzmann collision operator once all the states $\psi_i(x, t)$ with $i = 1, \dots, N$ that build the density matrix of an open system are perfectly known. Firstly, define $F_W^i(x, k, t)$ as the Wigner-Weyl transform with respect to the element of the density matrices $p_i(t)\psi_i(x, t)\psi_i^*(x', t)$ in (4.8). Then, because of the linearity of the Wigner distribution function with respect to the density matrix, before the collision, we can write the whole Wigner distribution function as follows:

$$F_W(x, k, t_0) = \sum_{i=1}^N F_W^i(x, k, t_0) \quad (4.22)$$

Inspired in the classical application of the Boltzmann collision operator, we define a collision operator in (4.13) that provides transitions between different states as:

$$C_W [F_W(x, k, t)] = \frac{1}{2\pi} \sum_{i=1}^N \sum_{j=1}^N \{Z_{ji}F_W^j(x, k, t) - Z_{ij}F_W^i(x, k, t)\} \quad (4.23)$$

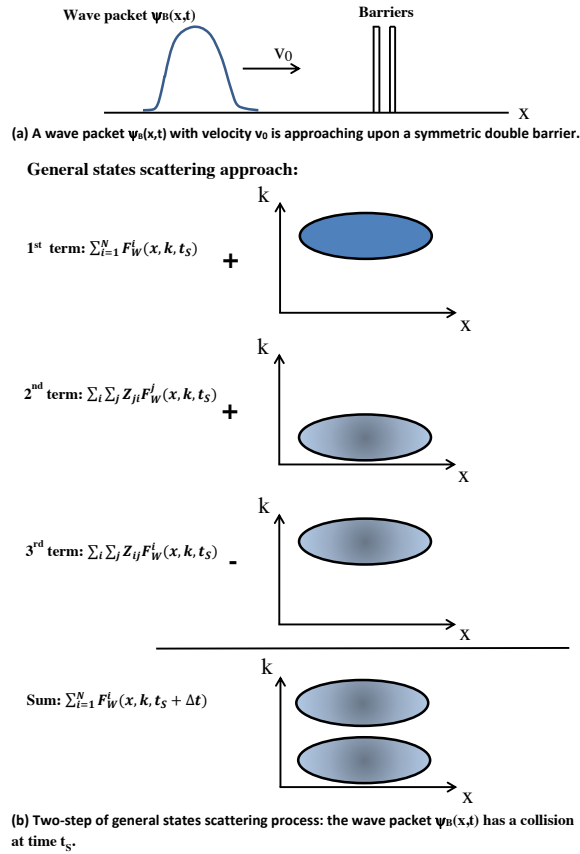


Figure 4.2.3: Schematic representation of the general states scattering process. (a) Simulation of a wave packet impinging on double barriers, the collision is performed at time t_S before the wave packet touches the barriers. (b) A simple physical picture of the two-step general states scattering process in the x - k space. During the collision, one term (3rd term) is eliminated and a new term (2nd term) is added. The eliminated state coincides with one of the old (before the collision) states of the system.

where the terms Z_{ji} provides the scattering rate (for the *general* states used in each case) from the j -state $\psi_j(x, t)$ to the i -state $\psi_i(x, t)$. After the collision at time t_S , the quantum system state in the Wigner formalism is:

$$\begin{aligned}
 F_W(x, k, t_S) &= \sum_{i=1}^N F_W^i(x, k, t) + \frac{1}{2\pi} \sum_{i=1}^N \sum_{j=1}^N \left\{ Z_{ji} F_W^j(x, k, t) - Z_{ij} F_W^i(x, k, t) \right\} \\
 &= \sum_{i=1}^N \left[1 - \frac{1}{2\pi} \sum_{j=1}^N Z_{ij} \right] F_W^i(x, k, t) + \frac{1}{2\pi} \sum_{i=1}^N \sum_{j=1}^N Z_{ji} F_W^j(x, k, t) \quad (4.24)
 \end{aligned}$$

The sums in (4.24) are carried out over the N possible existent terms (which are in principle infinite, but we can limit them to a reasonable number of possible states in a practical application). We do not use $W_{k'k}$ in (4.23) because, in principle, they are computed only for Hamiltonian eigenstates, while we define Z_{ji} using our general states

$\psi_j(x, t)^6$. This collision process is called *general states scattering approach*, which is illustrated in figure (4.2.3).

We discuss here the same numerical example presented in Section 4.2.1, but here with our new general collision operator in figure 4.2.3. We use the same initial density matrix $\hat{\rho}_B(t_0) = |\psi_B\rangle\langle\psi_B|$ in expression (4.8). We consider that there are two electrons with such state, $M_1 = M = 2$. Then, when the scattering take place, one of the two electrons with initial state $|\psi_B\rangle$ changes its state, while the other remains unaffected. The new density matrix in (4.9) is $\hat{\rho}(t_S) = \hat{\rho}_B - (1/2)|\psi_B\rangle\langle\psi_B| + (1/2)|\psi_F\rangle\langle\psi_F|$. The new density matrix after scattering can be greatly simplified to $\hat{\rho}(t_S) = (1/2)|\psi_B\rangle\langle\psi_B| + (1/2)|\psi_F\rangle\langle\psi_F|$ because $|\psi_N\rangle \equiv \frac{1}{\sqrt{2}}|\psi_B\rangle$. This collision process is explained in figure 4.2.3. Before the collision, both electrons are described by identical states that share the same x-k support because the two electrons have the same (mean) momentum. After the collision, one electron has higher (mean) momentum than that of the other. Thus, electrons are described by different states with different x-k supports.

In our numerical example, we use the same initial wave packet $|\psi_B\rangle$ discussed in figure 4.2.2. At the initial time $t_1 = 0$ ps, the information of the Wigner function and the charge probability distribution plotted in figure 4.2.4 are identical to that in figure 4.2.2. Then, at time $t_S = 0.006$ ps, the new collision operator in equation (4.23) acts on the Wigner distribution function. After the scattering, the system state is $\hat{\rho} = |\psi_B\rangle\langle\psi_B| + |\psi_P\rangle\langle\psi_P| - |\psi_N\rangle\langle\psi_N| = \frac{1}{2}|\psi_B\rangle\langle\psi_B| + \frac{1}{2}|\psi_F\rangle\langle\psi_F|$. As a consequence, the negative values disappear. Therefore, the unphysical results are removed. These conclusions are perfectly corroborated by figure 4.2.4.

In principle, a wave function with a negative modulus will be unphysical, i.e. inconsistent with the probabilistic (Born law) interpretation of quantum mechanics. It is relevant to note that the charge probability is always positive by using the general states scattering approach to treat the scattering in a dissipative quantum transport. However, in the Hamiltonian eigenstates scattering approach, negative unphysical values for the charge probability appear in some simulations. In table (4.2), a comparison of these two approaches in treating the scattering in the simulation of two electrons interacting with a phonon while traveling through a double barriers is plotted. I have discussed the ultimate reasons of such unphysical results in equation (4.9): the different time-evolutions of the states ρ_B that build the density matrix in the Wigner distribution function and the Hamiltonian eigenstates ρ_O generated by the Boltzmann collision operator after a collision. This problem will never occur if the transition between states during the collision process is done according to the set of states that built the density matrix in (4.11).

⁶As a reasonable approximation, if the general wave packet has (a more or less) well defined momentum (for example, the mean momentum of the wave packet) the terms $W_{k'k}$ can be numerically used instead of Z_{ji} in (4.23) by using some relations between j (and i) and k' (and k).

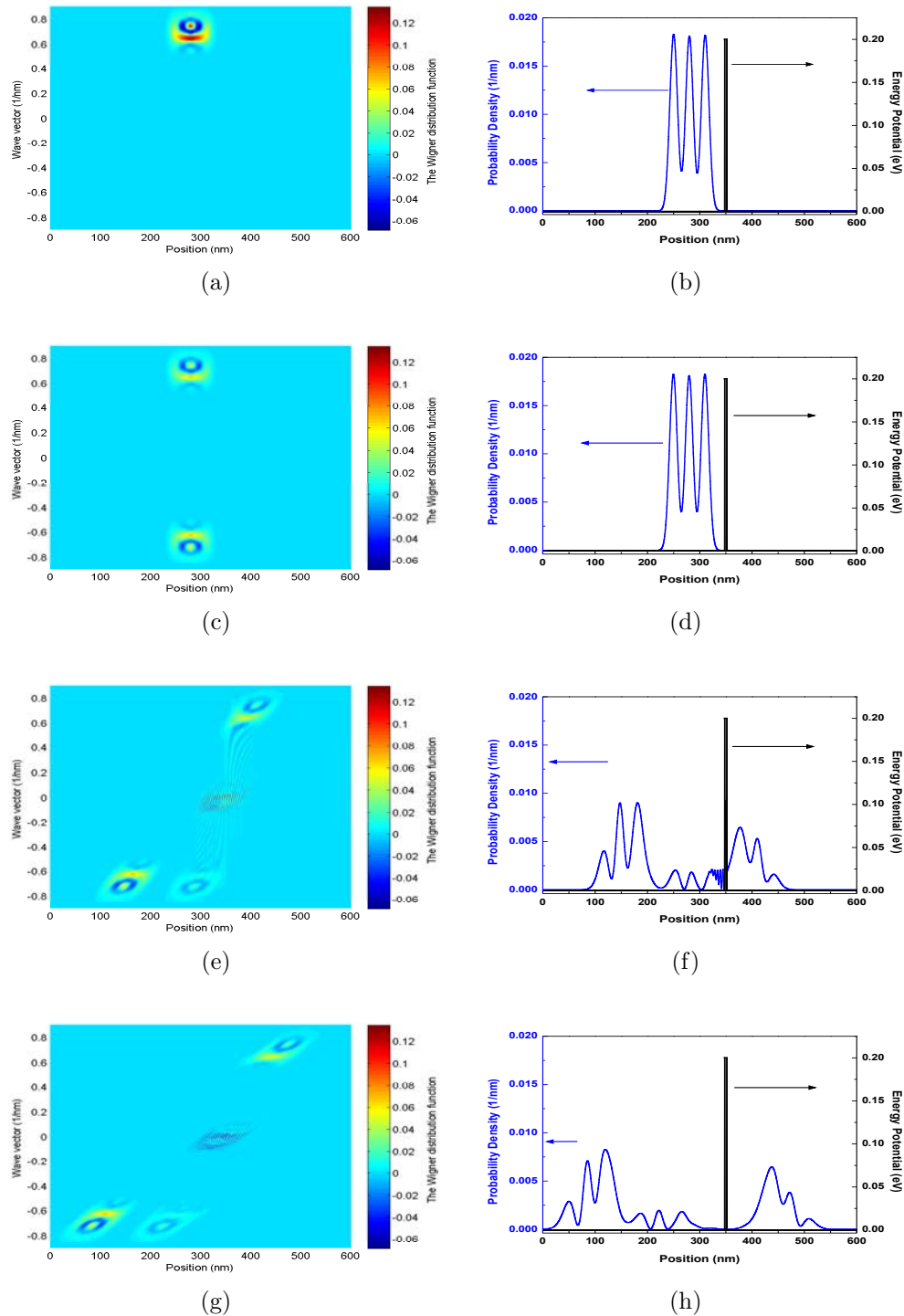


Figure 4.2.4: Evolution of Gaussian wave packets coupled with general states scattering approach moving towards barriers. (a), (c), (e), (g) are Wigner distribution and (b), (d), (f), (h) are corresponding probability density of state at for different times, which is identical to the time in : initial time $t_1 = 0$ ps, scattering time $t_S = 0.006$ ps before touching the barriers, time $t_2 = 0.315$ ps when wave packets are interacting with the barriers and time $t_3 = 0.66$ ps when the interaction is completely done. The collision is implemented with the general sates scattering approach. Because of such model, charge density is always non-negative.

Table 4.2: Norm of the system state (positive, negative and total probability density) at $t_3 = 0.66$ ps when using the Hamiltonian eigenstates (H.E.) or the general states (G.S.) scattering to deal with the collision.

	Norm		
	Positive probability	Negative probability	Total probability
H.E. scattering	1.025	-0.025	1
G.S. scattering	1	0	1

The general states scattering approach based on the generalization of the Boltzmann collision operator as written in (4.23) will always avoid the unphysical features discussed here. In addition, it still retains the intuitiveness and the computational simplicity of the Boltzmann collision operator. It only require the knowledge of the states that conform the density matrix or Wigner distribution function. This detailed knowledge of the states that build the density matrix is trivially accessible in the Bohmian formulation mentioned in this thesis [42]. The collision process can be applied directly into the Hamiltonian of the time-evolution equation of the conditional wave function (just adding an additional term in the kinetic part of the Hamiltonian) [110, 111].

We remark also that this new algorithm for collision explained here is relevant for time-dependent modeling of quantum transport. In addition, since it requires a perfect knowledge of the states that built the density matrix, its practical implementation fits perfectly well with the BITLLES simulator developed with conditional wave functions [42, 110–114], which will be discussed in the following section 4.3.

4.3 Collisions with Conditional Wave Functions

In this section I will provide a more detailed discussion on how to treat quantum dissipative transport using the conditional wave functions. I will show why the conditional sates allow us to know the states that construct the density matrix associated to an open system, at all times. After, as a practical application of this procedure to deal with quantum dissipation, I will numerically compute the simulation of the current-voltage characteristic of a resonant tunneling device (RTD) with a parabolic-band structure.

As we have discussed previously, modeling dissipation in an open system requires important approximations. The physical soundness of these approximations have to avoid unphysical results as the negative charge mentioned in the previous sections. From a more technical point of view, this unphysical results and others can be eliminated if we ensure that the dynamical map associated to the open system is completely positive⁷

⁷For any state $|\psi\rangle$, if the operator, for instance, a density operator $\hat{\rho}$, satisfies $\langle\psi|\hat{\rho}|\psi\rangle \geq 0$, then, the operator $\hat{\rho}$ is a positive operator. During the evolution of a quantum system, if the density operator of

when including microscopic models for the collision operator. A dynamical map is just the equation of motion that determines the time-evolution of the reduced density matrix. That is, for an open system which is described by the density matrix, a proper equation of motion of the density matrix must obtain a dynamical map that satisfies complete positivity (CP) [115, 116], which guarantees that the density matrix is always a positive operator at any time. In the Section 4.2, the Wigner function formalism for collisions implemented with the Boltzmann collision operator is not CP dynamical map and unphysical results appear. In this part, I will show that the use of conditional wave functions to define the state of an open system, by construction, ensures that we are dealing with a CP map for either Markovian or non-Markovian dynamics.

Considering a closed system which is described by a full many-body wave function $\Psi(\vec{r}_1, \dots, \vec{r}_N, t) = \langle \vec{r}_1, \dots, \vec{r}_N | \Psi(t) \rangle$ solution of the Schrödinger equation (1.9). We decompose the total Hilbert space of N particles as $\hat{\mathcal{H}} = \hat{\mathcal{H}}_a \otimes \hat{\mathcal{H}}_b$ with $\vec{r} = \{\vec{r}_1, \dots, \vec{r}_N\} = \{\vec{r}_a, \vec{r}_b\}$ being \vec{r}_a the position of the a -particle and $\vec{r}_b = \{\vec{r}_1, \dots, \vec{r}_{a-1}, \vec{r}_{a+1}, \dots, \vec{r}_N\}$ the positions of the rest of particles. Let \hat{O}_a be an operator for $\hat{\mathcal{H}}_a$, its expectation values $\langle O_a \rangle = \langle \Psi | \hat{O}_a \otimes \mathbb{1}_b | \Psi \rangle$ being $\mathbb{1}_b$ the identity operator for $\hat{\mathcal{H}}_b$, can be computed as:

$$\langle O_a \rangle = \int d\vec{r}_a O_a \rho(\vec{r}_a, \vec{r}'_a, t) |_{\vec{r}'_a = \vec{r}_a} \quad (4.25)$$

where O_a is the position representation of \hat{O}_a and $\rho(\vec{r}_a, \vec{r}'_a, t)$ is the density matrix (of the open system in Hilbert space $\hat{\mathcal{H}}_a$), which is:

$$\rho(\vec{r}_a, \vec{r}'_a, t) = \int d\vec{r}_b \Psi^*(\vec{r}'_a, \vec{r}_b, t) \Psi(\vec{r}_a, \vec{r}_b, t) \quad (4.26)$$

Now, let us see how to describe the subsystem with the density matrix $\rho(\vec{r}_a, \vec{r}'_a, t)$ in the Hilbert space $\hat{\mathcal{H}}_a$ with the Bohmian theory. As we have discussed in the Appendix A, a Bohmian system state is completely defined by the same wave function $\Psi(\vec{r}_a, \vec{r}_b, t)$ plus a set of well-defined trajectories in physical space $\{\vec{r}_1^j[t], \vec{r}_b^j[t]\}$ in the j experiment. The trajectories move continuously under the guidance of the wave function with the velocity (see Appendix A) is:

$$\vec{v}_a^j[t] = \frac{d\vec{r}_a^j[t]}{dt} = \frac{\vec{J}_a(\vec{r}_a^j[t], \vec{r}_b^j[t], t)}{|\Psi(\vec{r}_a^j[t], \vec{r}_b^j[t], t)|^2} \quad (4.27)$$

where $\vec{J}_a = \hbar \text{Im}(\Psi^* \vec{\nabla}_a \Psi) / m_a$ is the ensemble value of the current density with m_a the mass of the a -th particle. Moreover, the set of N positions in an infinite ensemble

the system always guarantees positive, then, we call the linear dynamical map as a positive map. There is a sub-class of the linear dynamical map on the density matrix, called completely positive map. Here, “completely” is just a *technical* word. For example, given a Hilbert space \mathcal{H} which has N dimensionality, if a linear map $\Phi(\hat{\rho})$ is n -positive map, i.e., $\Phi \otimes \mathbb{1}_n$ is positive for all positive integers $n \leq N$, then, Φ is a completely positive map.

experiments $j = 1, \dots, W$ with $W \rightarrow \infty$ can be mathematically written as (quantum equilibrium hypothesis mentioned in Appendix A):

$$|\Psi(\vec{r}_a, \vec{r}_b, t)|^2 = \frac{1}{W} \sum_{j=1}^W \delta(\vec{r}_a - \vec{r}_a^j[t]) \delta(\vec{r}_b - \vec{r}_b^j[t]) \quad (4.28)$$

which guarantees empirical equivalence between Bohmian and orthodox quantum (non-relativistic) results in the closed system, which also implies empirical equivalence of any smaller portion, i.e., the open system. The mean value of the operator \hat{O}_a over the wave function $\Psi(\vec{r}_a, \vec{r}_b, t)$ is:

$$\langle O_a \rangle = \int \int d\vec{r}_a d\vec{r}_b \Psi^*(\vec{r}_a, \vec{r}_b, t) Q_a \Psi(\vec{r}_a, \vec{r}_b, t) \quad (4.29)$$

Putting the equation (4.28) into the mean value $\langle O_a \rangle$ in (4.29) and arrange it as:

$$\begin{aligned} \langle O_a \rangle &= \int \int d\vec{r}_a d\vec{r}_b \frac{1}{W} \sum_{j=1}^W \delta(\vec{r}_a - \vec{r}_a^j[t]) \delta(\vec{r}_b - \vec{r}_b^j[t]) \frac{\Psi^*(\vec{r}_a, \vec{r}_b, t) Q_a \Psi(\vec{r}_a, \vec{r}_b, t)}{|\Psi(\vec{r}_a, \vec{r}_b, t)|^2} \\ &= \sum_{j=1}^W \frac{1}{W} \int d\vec{r}_a \delta(\vec{r}_a - \vec{r}_a^j[t]) \frac{\Psi^*(\vec{r}_a, \vec{r}_b^j[t], t) Q_a \Psi(\vec{r}_a, \vec{r}_b^j[t], t)}{|\Psi(\vec{r}_a, \vec{r}_b^j[t], t)|^2} \\ &= \sum_{j=1}^W \frac{1}{W} \frac{\Psi^*(\vec{r}_a, \vec{r}_b^j[t], t) Q_a \Psi(\vec{r}_a, \vec{r}_b^j[t], t)}{|\Psi(\vec{r}_a^j[t], \vec{r}_b^j[t], t)|^2} \Big|_{\vec{r}_a = \vec{r}_a^j[t]} \end{aligned} \quad (4.30)$$

where $\Psi(\vec{r}_a, \vec{r}_b^j[t], t) = \phi_a^j(\vec{r}_a, t)$ is the conditional wave function, which can be thought of as the wave functions of the open system in Hilbert space $\hat{\mathcal{H}}_a$ conditioned to a continuous observable, i.e., the pointer position $\vec{r}_b^j[t]$. By comparing the mean value in equation (4.25) with that in equation (4.30), we can write the density matrix in equation (4.26) using the fundamental elements of the Bohmian theory—the (tilde) conditional wave function $\tilde{\phi}_a^j(\vec{r}_a, t) \equiv \Psi(\vec{r}_a, \vec{r}_b^j[t], t) / |\Psi(\vec{r}_a^j[t], \vec{r}_b^j[t], t)|$ of the a -th particle in the j experiment:

$$\rho(\vec{r}_a, \vec{r}'_a, t) = \sum_{j=1}^W p_j \tilde{\phi}_a^{j*}(\vec{r}'_a, t) \tilde{\phi}_a^j(\vec{r}_a, t) \quad (4.31)$$

where $p_j = 1/W$. The generalization of conditional wave functions with an arbitrary number of particles is straightforward. The time evolution of equation (4.31) ensures that the dynamical map associated with our approach is CP. For any state $|\phi_k\rangle$, we obtain $\langle \phi_k | \hat{\rho} | \phi_k \rangle = \sum_{j=1}^W p_j \langle \phi_k | \tilde{\phi}_a^j(t) \rangle \geq 0$ at any time. We remark here again that the information of the states that built the density matrix of the open system is known all the time by using the conditional wave functions. As we have discussed in the Section

4.2, the effect of the Boltzmann collision operator in the Wigner formalism is generally not a CP map. On the contrary, the density operator of the open system in (4.31), which is just expression (4.11), gives a positive operator at any time.

The conditional wave function $\phi_a^j(\vec{r}_a, t) = \langle \vec{r}_a, \vec{r}_b | \Psi(t) \rangle$ can be computed from the following single-particle pseudo-Schrödinger equation in physical space:

$$i\hbar \frac{d\langle \vec{r}_a, \vec{r}_b | \Psi(t) \rangle}{dt} \Big|_{\vec{r}_b = \vec{r}_b^j[t]} = \langle \vec{r}_a, \vec{r}_b | \hat{\mathcal{H}} | \Psi(t) \rangle \Big|_{\vec{r}_b = \vec{r}_b^j[t]} \quad (4.32)$$

where $\hat{\mathcal{H}}$ is the many-body Hamiltonian of the closed system. The equation (4.32) can also be written as:

$$i\hbar \frac{d\phi_a(\vec{r}_a, t)}{dt} = H \phi_a(\vec{r}_a, t) = (H_c + H_{eh, \vec{u}}) \phi_a(\vec{r}_a, t) \quad (4.33)$$

where $H_{eh, \vec{u}}$ is the interaction of electrons with the displacement of the ions and H_c includes all the kinetic energies and all interactions except $H_{eh, \vec{u}}$. The computation of $\langle \vec{r}_a, \vec{r}_b | \hat{\mathcal{H}} | \Psi(t) \rangle$ before conditioning depends on the full many-body wave function $\Psi(\vec{r}_a, \vec{r}_b, t)$ and requires educated guesses to get the *effective* conditional potentials H_c and $H_{eh, \vec{u}}$. More details can be found in the Appendix A. In the following, as an example, we compute the equation of motion of the conditional wave function to deal with electron-phonon interaction, i.e. we compute H_c and $H_{eh, \vec{u}}$.

4.3.1 Conditioned Hamiltonian for the Electron-Phonon Interaction

For a closed system, the Hamiltonian is given in equation (1.10). Let us give more details about the many-body Hamiltonian $\hat{\mathcal{H}}$. Assuming the closed system contains N_e electrons with positions $\vec{r} = \{\vec{r}_1, \dots, \vec{r}_{N_e}\}$, N_h ions with positions $\vec{R} = \{\vec{R}_1, \dots, \vec{R}_{N_h}\}$ and all the rest of the particles of the closed system not explicitly indicated here. We will usually use \vec{r}_a (\vec{r}_e) to refer to the a (or e) electron. We also defined $\vec{r} = \{\vec{r}_a, \vec{z}_a\}$ with $\vec{z}_a = \{\vec{r}_1, \dots, \vec{r}_{a-1}, \vec{r}_{a+1}, \dots, \vec{r}_{N_e}\}$.

In order to discuss how electron interact with the atoms, we refer to the term that contains electron and atoms (or ions) positions on the global Hamiltonian of the circuit discussed in (1.10). In particular, I will explicitly construct the equation of motion for the a -particle $\phi_a(\vec{r}_a, t)$ in equation (4.32) with special attention to the second term on the right of the equation (1.10)—what we have called here the electron ion Hamiltonian $\hat{\mathcal{H}}_{eh}$. Due to the perturbation, the electron ion Hamiltonian $\hat{\mathcal{H}}_{eh}$ is divided into the interaction of the electrons with the fixed (equilibrium) positions of the ions $\vec{R}_0 = \{\vec{R}_{1,0}, \dots, \vec{R}_{N_h,0}\}$ in $\hat{\mathcal{H}}_{eh, \vec{R}_0}$ and the interaction of the electrons with the displacement of the ions $\vec{u} =$

$\vec{R} - \vec{R}_0 = \{\vec{u}_1, \dots, \vec{u}_{N_h}\}$ in $\hat{\mathcal{H}}_{eh, \vec{u}}$. That is:

$$\begin{aligned} \hat{\mathcal{H}}_{eh} &= \hat{\mathcal{H}}_{eh, \vec{R}_0} + \hat{\mathcal{H}}_{eh, \vec{u}} = \sum_{e,h} V_{eh}(\vec{r}_e - \vec{R}_h) \\ &\approx \sum_{e,h} \left[V_{eh}(\vec{r}_e - \vec{R}_{h,0}) + (\vec{R}_h - \vec{R}_{h,0}) \cdot \nabla_h V_{eh}(\vec{r}_e - \vec{R}_h) \Big|_{\vec{R}_h = \vec{R}_{h,0}} \right] \\ &= \sum_{e,h} \left[V_{eh}(\vec{r}_e - \vec{R}_{h,0}) + \vec{u}_h \cdot \nabla_h V_{eh}(\vec{r}_e - \vec{R}_h) \Big|_{\vec{R}_h = \vec{R}_{h,0}} \right] \end{aligned} \quad (4.34)$$

where the potential $V_{eh}(\vec{r}_e - \vec{R}_h)$ is decomposed in a Taylor expansion around the fixed position $\vec{R}_{h,0}$. As we have discussed in Chapter 1, the term $\hat{\mathcal{H}}_{eh, \vec{R}_0}$ will become relevant to the electronic band structure of the material. Let us see what is the effect of $\hat{\mathcal{H}}_{eh, \vec{u}}$ on the conditional wave function $\phi_a(\vec{r}_a, t)$. Instead of dealing with individual displacement \vec{u}_h , we consider the normal coordinate $\vec{Q}_{\vec{q}_p}$ defined from the Fourier transform:

$$\vec{u}_h = \sum_{\vec{q}_p} \vec{Q}_{\vec{q}_p} e^{i \vec{q}_p \cdot \vec{R}_{h,0}} \quad (4.35)$$

where \vec{q}_p is a wave vector in the reciprocal space that labels each of the possible collective solutions of the movement of ions. The Fourier transform of the potential $V_{eh}(\vec{r}_e - \vec{R}_h)$ is:

$$V_{eh}(\vec{r}_e - \vec{R}_h) = \sum_{\vec{v}} e^{i \vec{v} \cdot (\vec{r}_e - \vec{R}_h)} U_{\vec{v}} \quad (4.36)$$

where \vec{v} is another wave vector in the reciprocal space and $U_{\vec{v}}$ is the Fourier coefficient of the potential. Then, we can write the Hamiltonian $\hat{\mathcal{H}}_{eh, \vec{u}}$ in the position representation, which is:

$$H_{eh, \vec{u}} = \sum_{e,h} \vec{u}_h \cdot \nabla_h V_{eh}(\vec{r}_e - \vec{R}_h) \Big|_{\vec{R}_h = \vec{R}_{h,0}} = \sum_e \sum_h \sum_{\vec{q}_p} \vec{Q}_{\vec{q}_p} e^{i \vec{q}_p \cdot \vec{R}_{h,0}} \sum_{\vec{v}} (-i \vec{v}) e^{i \vec{v} \cdot (\vec{r}_e - \vec{R}_{h,0})} U_{\vec{v}} \quad (4.37)$$

Let us define the fully many-body wave function $\Psi(\vec{r}, \vec{R}, t) = \Psi(\vec{r}_a, \vec{z}_a, \vec{R}, t)$ as:

$$\begin{aligned} \Psi(\vec{r}_a, \vec{z}_a, \vec{R}, t) &= \sum_{\vec{k}, \vec{q}} a(\vec{k}, \vec{q}, t) \Phi_{\vec{k}}(\vec{r}) \Phi_{\vec{q}}(\vec{R}) \\ &= \sum_{\vec{k}, \vec{q}} a(\vec{k}, \vec{q}, t) \Phi_{\vec{q}}(\vec{R}) \sum_{\vec{k}_w} \varphi_{\vec{k}_w}(\vec{r}_a) s_{a,w} \langle \vec{r}_a | \hat{c}_{\vec{k}_1}^\dagger \cdots \hat{c}_{\vec{k}_{w-1}}^\dagger \hat{c}_{\vec{k}_{w+1}}^\dagger \cdots \hat{c}_{\vec{k}_{N_e}}^\dagger | 0 \rangle \end{aligned} \quad (4.38)$$

where $a(\vec{k}, \vec{q}, t)$ accounts for an arbitrary superposition of the many-body electron base $\Phi_{\vec{k}}(\vec{r})$ and the many-body phonon base $\Phi_{\vec{q}}(\vec{R})$, the vector $\vec{k} = \{\vec{k}_1, \dots, \vec{k}_{N_e}\}$ represents the index of the electronic (Bloch) base and $\vec{q} = \{\vec{q}_1, \dots, \vec{q}_{N_h}\}$ is the index of the ionic base, the $\hat{c}_{\vec{k}_w}^\dagger$ is a operator of the (Bloch) eigenstate $\langle \vec{r}_a | \hat{c}_{\vec{k}_w}^\dagger | 0 \rangle = \varphi_{\vec{k}_w}(\vec{r}_a)$ and $s_{a,w}$ is the

sign of the (a, w) cofactor. The Bloch eigenstate is:

$$\varphi_{\vec{k}_w}(\vec{r}_a) = \langle \vec{r}_a | \hat{c}_{\vec{k}_w}^\dagger | 0 \rangle = \langle \vec{r}_a | \vec{k}_w \rangle = e^{i\vec{k}_w \vec{r}_a} u_{\vec{k}_w}(\vec{r}_a) \quad (4.39)$$

where $u_{\vec{k}_w}(\vec{r}_a)$ is periodic with respect to lattice translations including the appropriate normalizing constant and \vec{k}_w is the electron (quasi) wave vector related to the quasi momentum $\vec{p}_w = \hbar \vec{k}_w$. The conditional wave function $\phi_a(\vec{r}_a, t)$ before the collision can be obtained from equation (4.38) by fixing $\vec{z}_a = \vec{z}_a^j[t]$ and $\vec{R} = \vec{R}^j[t]$ which are obtained from j experiment, as:

$$\begin{aligned} \phi_a^j(\vec{r}_a, t) &= \Psi(\vec{r}_a, \vec{z}_a^j[t], \vec{R}^j[t], t) \\ &= \sum_{\vec{k}, \vec{q}} a(\vec{k}, \vec{q}, t) \Phi_{\vec{q}}(\vec{R}^j[t]) \sum_{\vec{k}_w} \varphi_{\vec{k}_w}(\vec{r}_a) s_{a,w} \langle \vec{z}_a^j[t] | \hat{c}_{\vec{k}_1}^\dagger \cdots \hat{c}_{\vec{k}_{w-1}}^\dagger \hat{c}_{\vec{k}_{w+1}}^\dagger \cdots \hat{c}_{\vec{k}_{N_e}}^\dagger | 0 \rangle \\ &= \sum_{\vec{k}_w} \varphi_{\vec{k}_w}(\vec{r}_a) f_a(\vec{k}_w, t) \end{aligned} \quad (4.40)$$

with $f_a(\vec{k}_w, t)$ defined as:

$$f_a(\vec{k}_w, t) = \sum_{\vec{q}} \sum_{\dots, \vec{k}_{w-1}, \vec{k}_{w+1}, \dots} a(\vec{k}, \vec{q}, t) \Phi_{\vec{q}}(\vec{R}^j[t]) s_{a,w} \langle \vec{z}_a^j[t] | \hat{c}_{\vec{k}_1}^\dagger \cdots \hat{c}_{\vec{k}_{w-1}}^\dagger \hat{c}_{\vec{k}_{w+1}}^\dagger \cdots \hat{c}_{\vec{k}_{N_e}}^\dagger | 0 \rangle \quad (4.41)$$

Under the standard envelop approximation that the wave packet is centered around $\vec{k}_w \approx \vec{k}_{0w}$, we can rewrite the Bloch states as $\varphi_{\vec{k}_w}(\vec{r}_a) \approx e^{i\vec{k}_w \vec{r}_a} u_{\vec{k}_{0w}}(\vec{r}_a)$ and substitute it into the equation (4.40), finally, the $\phi_a^j(\vec{r}_a, t)$ is:

$$\phi_a^j(\vec{r}_a, t) = u_{\vec{k}_{0w}}(\vec{r}_a) \sum_{\vec{k}_w} e^{i\vec{k}_w \vec{r}_a} f_a(\vec{k}_w, t) \approx \sum_{\vec{k}_w} e^{i\vec{k}_w \vec{r}_a} f_a(\vec{k}_w, t) \quad (4.42)$$

where we ignore the atomic periodicity $u_{\vec{k}_{0w}}(\vec{r}_a)$. The mean value of the momentum of the initial envelop wave packet $\phi_a^j(\vec{r}_a, t)$ at time $t = t_{c1}$ before the collision is:

$$\langle \vec{p}_a \rangle_{t_{c1}} = \sum_{\vec{k}_w} \hbar \vec{k}_w |f_a(\vec{k}_w, t)|^2 \quad (4.43)$$

Next, we will evaluate the effect of the $\hat{\mathcal{H}}_{eh, \vec{u}}$ on the wave function $\Psi(\vec{r}_a, \vec{z}_a, \vec{R}, t)$ and then conditioned the result to the fixed positions $\vec{z}_a^j[t]$ and $\vec{R}^j[t]$. The evolution of the term

$H_{eh,\vec{u}}(\vec{r}, \vec{R}, t)\Psi(\vec{r}_a, \vec{z}_a, \vec{R}, t)$ is:

$$H_{eh,\vec{u}}(\vec{r}, \vec{R}, t)\Psi(\vec{r}_a, \vec{z}_a, \vec{R}, t) = \left[\sum_{e \neq a} H_{eh,\vec{u},\vec{r}_e}(\vec{r}_e, \vec{R}, t)\Psi(\vec{r}_a, \vec{z}_a, \vec{R}, t) \right] + H_{eh,\vec{u},\vec{r}_a}(\vec{r}_a, \vec{R}, t)\Psi(\vec{r}_a, \vec{z}_a, \vec{R}, t) \quad (4.44)$$

The first term $\sum_{e \neq a} H_{eh,\vec{u},\vec{r}_e}(\vec{r}_e, \vec{R}, t)$ does not depend on \vec{r}_a , which only provide a global phase on the conditional wave function $\phi_a^j(\vec{r}_a, t)$ when conditioned to $\vec{z}_a^j[t]$ and $\vec{R}^j[t]$. Therefore, we can only concentrate on the second term, which is:

$$\begin{aligned} H_{eh,\vec{u},\vec{r}_a}(\vec{r}_a, \vec{R}, t)\Psi(\vec{r}_a, \vec{z}_a, \vec{R}, t) &= \langle \vec{r}, \vec{R} | \hat{\mathcal{H}}_{eh,\vec{u},\vec{r}_a} | \Psi(t) \rangle \\ &= \sum_{\vec{k}_w} \sum_{\vec{k}_w''} \langle \vec{r}_a | \vec{k}_w'' \rangle \langle \vec{k}_w'', \vec{z}_a, \vec{R} | \hat{\mathcal{H}}_{eh,\vec{u},\vec{r}_a} | \vec{k}_a, \vec{z}_a, \vec{R} \rangle \langle \vec{k}_a, \vec{z}_a, \vec{R} | \Psi(t) \rangle \end{aligned} \quad (4.45)$$

where we have used the identities $\int_{\vec{r}} d\vec{r}' |\vec{r}'\rangle \langle \vec{r}'|$, $\int_{\vec{R}} d\vec{R}' |\vec{R}'\rangle \langle \vec{R}'|$ and $\sum_{\vec{k}_w} |\vec{k}_w\rangle \langle \vec{k}_w|$ and the fact that $\hat{\mathcal{H}}_{eh,\vec{u},\vec{r}_a}$ is diagonal in the position representation. Let us define $T(\vec{k}_w'', \hat{\mathcal{H}}_{eh,\vec{u},\vec{r}_a}, \vec{k}_w) = \langle \vec{k}_w'', \vec{z}_a, \vec{R} | \hat{\mathcal{H}}_{eh,\vec{u},\vec{r}_a} | \vec{k}_a, \vec{z}_a, \vec{R} \rangle$ as the electron-phonon Hamiltonian in the momentum (Bloch state) representation, and rewrite it as:

$$T(\vec{k}_w'', \hat{\mathcal{H}}_{eh,\vec{u},\vec{r}_a}, \vec{k}_w) = \int_{\vec{r}_a} d\vec{r}'_a \langle \vec{k}_w'' | \vec{r}'_a \rangle \langle \vec{r}'_a, \vec{z}_a, \vec{R} | \hat{\mathcal{H}}_{eh,\vec{u},\vec{r}_a} | \vec{r}'_a, \vec{z}_a, \vec{R} \rangle \langle \vec{r}'_a | \vec{k}_w \rangle \quad (4.46)$$

Substituting the expressions (4.37) and the Bloch states into the electron-phonon Hamiltonian, assuming the change of variable $\vec{r}'_a = \vec{r}'_a - \vec{R}_{m,0}$ with \vec{r}'_a integrates only inside the first Brillouin zone, we obtains:

$$\begin{aligned} T(\vec{k}_w'', \hat{\mathcal{H}}_{eh,\vec{u},\vec{r}_a}, \vec{k}_w) &= \int_{\vec{r}_a} d\vec{r}'_a e^{-i\vec{k}_w'' \vec{r}'_a} u_{\vec{k}_w''}(\vec{r}'_a) e^{i\vec{k}_w \vec{r}'_a} u_{\vec{k}_w}(\vec{r}'_a) \sum_h \sum_{\vec{q}_p} \vec{Q}_{\vec{q}_p} e^{i\vec{q}_p \vec{R}_{h,0}} \sum_{\vec{v}} (-i\vec{v}) e^{i\vec{v}(\vec{r}'_a - \vec{R}_{h,0})} U_{\vec{v}} \\ &= \sum_h \sum_{\vec{q}_p} \vec{Q}_{\vec{q}_p} \sum_{\vec{v}} (-i\vec{v}) e^{i\vec{R}_{h,0}(\vec{q}_p - \vec{v})} U_{\vec{v}} \left(\sum_m e^{i\vec{R}_{m,0}(-\vec{k}_w'' + \vec{v} + \vec{k}_w)} \right) \\ &\quad \int_{\vec{r}'_a} d\vec{r}'_a e^{-i\vec{k}_w'' \vec{r}'_a} u_{\vec{k}_w''}(\vec{r}'_a) e^{i\vec{k}_w \vec{r}'_a} u_{\vec{k}_w}(\vec{r}'_a) \end{aligned} \quad (4.47)$$

The sum over $\vec{R}_{h,0}$ in $e^{i\vec{R}_{h,0}(\vec{q}_p - \vec{v})}$ imposes the condition $\vec{G} = \vec{q}_p - \vec{v}$ and the sum over $\vec{R}_{m,0}$ in $e^{i\vec{R}_{m,0}(-\vec{k}_w'' + \vec{v} + \vec{k}_w)}$ imposes that $\vec{G}' = -\vec{k}_w'' + \vec{v} + \vec{k}_w$ being \vec{G} and \vec{G}' two vectors of the reciprocal lattice. We assume that all momentum vectors are in the first Brillouin zone, $\vec{G} = 0$ and $\vec{G}' = 0$, so that $\vec{k}_w'' = \vec{k}_w + \vec{q}_p$, and the electron-phonon Hamiltonian is:

$$T(\vec{k}_w'', \hat{\mathcal{H}}_{eh,\vec{u},\vec{r}_a}, \vec{k}_w) = \sum_{\vec{q}_p} \delta(\vec{k}_w'' - \vec{k}_w - \vec{q}_p) g_{\vec{k}_w}^{\vec{q}_p} \quad (4.48)$$

where the coupling constant $g_{\vec{k}_w}^{\vec{q}_p}$ is defined as:

$$g_{\vec{k}_w}^{\vec{q}_p} = -i\vec{Q}_{\vec{q}_p}\vec{q}_p U_{\vec{q}_p} \int_{\vec{r}'_a} d\vec{r}'_a e^{-i(\vec{k}_w+\vec{q}_p)\vec{r}'_a} u_{\vec{k}_w+\vec{q}_p}(\vec{r}'_a) e^{i\vec{k}_w\vec{r}'_a} u_{\vec{k}_w}(\vec{r}'_a) \quad (4.49)$$

Here, we do not include any dependence on the n band structure. Therefore, the evolution of $H_{eh,\vec{u},\vec{r}_a}(\vec{r}_a, \vec{R}, t)\Psi(\vec{r}_a, \vec{z}_a, \vec{R}, t)$ is:

$$\begin{aligned} H_{eh,\vec{u},\vec{r}_a}(\vec{r}_a, \vec{R}, t)\Psi(\vec{r}_a, \vec{z}_a, \vec{R}, t) &= \sum_{\vec{k}_w} \sum_{\vec{k}_w''} \langle \vec{r}_a | \vec{k}_w'' \rangle T(\vec{k}_w'', \hat{\mathcal{H}}_{eh,\vec{u},\vec{r}_a}, \vec{k}_w) \langle \vec{k}_a, \vec{z}_a, \vec{R} | \Psi(t) \rangle \\ &= \sum_{\vec{q}_p} \sum_{\vec{k}_w} g_{\vec{k}_w}^{\vec{q}_p} \langle \vec{r}_a | \vec{k}_w + \vec{q}_p \rangle \langle \vec{k}_w, \vec{z}_a, \vec{R} | \Psi(t) \rangle \end{aligned} \quad (4.50)$$

Once we know the effect of the electron-phonon Hamiltonian on the conditional wave packet, let us see what is the wave function of the a -particle after the collision. We consider that the collision starts at t_{c1} and ends at t_{c2} . Assuming that the a wave packet is narrow enough in momentum space so that $g_{\vec{k}_w}^{\vec{q}_p}[t] \approx g_{\vec{k}_{0w}}^{\vec{q}_p,j}[t]$ in the j experiment. The conditional wave function just after the collision at time $t = t_{c2}$ is:

$$\begin{aligned} \phi_a^j(\vec{r}_a, t_{c2}) &= \langle \vec{r}_a, \vec{r}_z^j[t_{c2}], \vec{R}^j[t_{c2}] | \hat{\mathcal{H}}_{eh,\vec{u},\vec{r}_a} | \Psi(t_{c2}) \rangle = g_{\vec{k}_{0w}}^{\vec{q}_p,j}[t_{c2}] \sum_{\vec{k}_w} \langle \vec{r}_a | \vec{k}_w + \vec{q}_p \rangle \langle \vec{k}_w, \vec{z}_a, \vec{R} | \Psi(t_{c2}) \rangle \\ &= g_{\vec{k}_{0w}}^{\vec{q}_p,j}[t_{c2}] \sum_{\vec{k}_w} \varphi_{\vec{k}_w+\vec{q}_p}^{\vec{q}_p}(\vec{r}_a) f(\vec{k}_w, t_{c2}) \approx e^{i\vec{q}_p\vec{r}_a} \phi_a^j(\vec{r}_a, t_{c1}) \end{aligned} \quad (4.51)$$

In one experiment j , the coupling constant $g_{\vec{k}_{0w}}^{\vec{q}_p,j}[t_{c2}]$ has no big role in the dynamical of a conditional wave function. It becomes relevant in the full many-body wave function $\Psi(\vec{r}, \vec{R}, t)$ in determining the different transition probabilities between different initial and final wave packets in different experiments. Such transition rates $g_{\vec{k}_{0w}}^{\vec{q}_p}$ and the distribution of the collision time t_c are precomputed from typical expressions of transition rates [117].

As an example, the figure 4.3.1 is the energy-dependent scattering rates for the GaAs at 300 K. In the numerical example, we will use these precomputed values to implement the elastic and inelastic collisions in the simulation. The fact that emission of a phonon is more probable than absorption of a phonon is directly given by precomputed scattering rates. In such asymmetry, they introduce time-irreversibility into the simulation. As time goes by, quantum dissipation appears in the open system, not the contrary. The ensemble momentum of the a -particle is:

$$\langle \vec{p}_a \rangle_{t_{c2}} = \sum_{\vec{k}_w} \hbar(\vec{k}_w + \vec{q}_p^j) |f_a(\vec{k}_w, t)|^2 = \langle \vec{p}_a \rangle_{t_{c1}} + \hbar\vec{q}_p^j \quad (4.52)$$

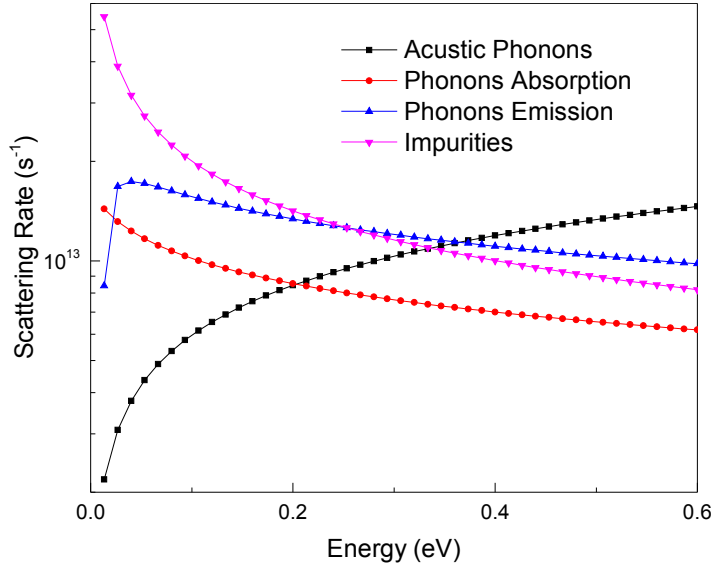


Figure 4.3.1: Energy dependence of scattering rates for the Γ valley of GaAs at 300 K.

That is to say, after the collision, the (Bloch state) quasi-momentum eigenstates that built the wave packet superposition change from $|\vec{k}_w\rangle$ to $|\vec{k}_w + \vec{q}_p^j\rangle$, while its weight $f(\vec{k}_w, t)$ remains unchanged.

4.3.2 Equation of motion of the conditional wave functions

Once we know the effect of the electron-phonon Hamiltonian on the wave function $\phi_a(\vec{r}, t)$, let us present the equation of motion of the conditional wave function that provides such effect. From ref. [42], for a parabolic band structure, the single-particle pseudo-Schrödinger equation can be written as:

$$i\hbar \frac{\partial \phi_a^j(\vec{r}_a, t)}{\partial t} = \left[\frac{1}{2m^*} (\vec{p}_a)^2 + V_a + A_a + iB_a \right] \phi_a^j(\vec{r}_a, t) \quad (4.53)$$

where V_a is the Coulomb interaction of the a -particle with the rest of electrons which can be easily known once the set of the $\vec{z}_a^j[t]$ trajectories are known. The details of other terms A_a and B_a can be found in the paper [42].

We have known the equation of motion of $\phi_a(\vec{r}_a, t)$ before the collision in equation (4.53). Next, we will combine the time evolution of the conditional wave function $\phi_a(\vec{r}_a, t)$ before and after the collision in a unique equation of motion. The time evolution operator from initial time $t = t_0$ until a time $t < t_{c1}$ is:

$$\hat{U}_a(t, t_0) = e^{-\frac{i}{\hbar} \int_{t_0}^t \hat{\mathcal{H}}_a(t') dt'} \quad (4.54)$$

with $\hat{\mathcal{H}}_a = \frac{1}{m^*} (\vec{p}_a)^2 + V_a$. Assuming the electron-phonon interaction is $\hat{\mathcal{H}}_{eha} = -\hbar \vec{\lambda}_a \vec{r}_a \delta(t -$

t_c). The time evolution operator from initial time $t = t_0$ until a time $t > t_{c1}$ after the collision is:

$$\begin{aligned}\hat{U}_a(t, t_0) &= e^{-\frac{i}{\hbar} \int_{t_{c2}}^t \hat{H}_a(t') dt'} e^{-\frac{i}{\hbar} \int_{t_{c1}}^{t_{c2}} \hat{H}_{cha}(t') dt'} e^{-\frac{i}{\hbar} \int_{t_0}^{t_{c1}} \hat{H}_a(t') dt'} \\ &= e^{-\frac{i}{\hbar} \int_{t_{c2}}^t \hat{H}_a(t') dt'} e^{i \frac{\vec{\lambda}_a \vec{r}_a}{\hbar}} e^{-\frac{i}{\hbar} \int_{t_0}^{t_{c1}} \hat{H}_a(t') dt'}\end{aligned}\quad (4.55)$$

For a small time interval Δt , we have $\hat{U}_a(t + \Delta t, t) = 1 - \frac{i}{\hbar} \Delta t \hat{H}_a$, and $(1 - \frac{i}{\hbar} \Delta t H_a) e^{i \frac{\vec{\lambda}_a \vec{r}_a}{\hbar}} \phi_a(\vec{r}_a, t_{c1}) = e^{i \frac{\vec{\lambda}_a \vec{r}_a}{\hbar}} (1 - \frac{i}{\hbar} \Delta t H_{a+\lambda}) \phi_a(\vec{r}_a, t_{c1})$ being $H_{a+\lambda} = \frac{(\vec{p}_a + \vec{\lambda})^2}{2m^*} + V_a$. Then, the operator $\hat{U}_a(t, t_0)$ in equation (4.55) can be understood as until time $t = t_0 + n\Delta t$. And the time evolution of the $\phi_a(\vec{r}_a, t)$ at time $t = t_0 + n\Delta t$ is:

$$(1 - \frac{i}{\hbar} \Delta t H_a) \cdots (1 - \frac{i}{\hbar} \Delta t H_a) e^{i \frac{\vec{\lambda}_a \vec{r}_a}{\hbar}} \phi_a(\vec{r}_a, t_{c1}) = e^{i \frac{\vec{\lambda}_a \vec{r}_a}{\hbar}} (1 - \frac{i}{\hbar} \Delta t H_{a+\lambda}) \cdots (1 - \frac{i}{\hbar} \Delta t H_{a+\lambda}) \phi_a(\vec{r}_a, t_{c1})\quad (4.56)$$

Finally, the time evolution of the conditional wave function $\phi_a(\vec{r}_a, t)$ before and after the collision is:

$$i\hbar \frac{\partial \phi_a^j(\vec{r}_a, t)}{\partial t} = \left[\frac{1}{2m^*} (\vec{p}_a + \vec{\lambda}_a \Theta_{t_c})^2 + V_a \right] \phi_a^j(\vec{r}_a, t)\quad (4.57)$$

where $\Theta_{t_c} = \Theta(t - t_c)$ is the step Heaviside function. For simplicity, we have assume that the collision process take a time interval equal to zero. We define $t_c = t_{c1} = t_{c2}$. This equation of motion exactly reproduces the transition of ϕ_a from equation (4.42) before the collision to the equation (4.51) after the scattering is completed. The selection of the collision times t_c and the type of collision is done following the traditional procedure in the semi-classical Monte Carlo simulation of Boltzmann equation for transport with the energy-dependent scattering rates plotted in figure 4.3.1. The only difference is that the dynamics of each particle is given by (4.57), not by Newtons law.

4.3.3 Example of Collisions in a Resonant Tunneling Device

As an example, we apply the new approach for the simulation of quantum dissipation with conditional wave functions solution of equation (4.57) for the simulation of a GaAs/AlGaAs RTD. The numerical result of the current-voltage characteristic are plotted in figure 4.3.2. We consider elastic (acoustic phonons and impurities) and inelastic (optical phonons) collisions. Each electron is associated to a conditional wave function plus a Bohmian trajectories. The number of injected electrons, and its properties, are determined by the injection model described in the previous Chapter 3. The time evolution of the conditional wave function ϕ_a interacting with a phonon \vec{q}_p in a material with parabolic band structure is obtained from equation (4.57). The electron effective mass is $m^* = 0.067 m_e$ being m_e the free electron mass and $\vec{\lambda}_a = \hbar \vec{q}_p$ accounts for the momentum exchange. Each electron $a = \{a, \dots, N_e\}$ has its own dynamical equation (4.57) to

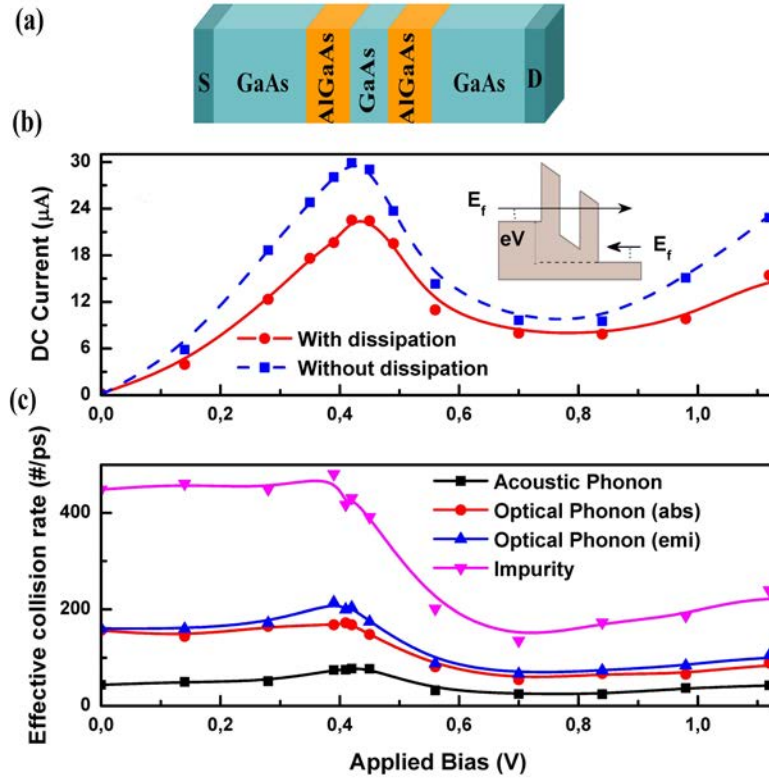


Figure 4.3.2: (a) Schematic representation of a typical GaAs/AlGaAs resonant tunneling device realized in the BITLLES simulator. (b) Current-voltage characteristic for a RTD with (solid red line) and without (blue dashed line) dissipation. (c) Effective collision rate as a function of the source-drain bias. The parameters in the simulation are: the barrier height is 0.5 eV, the width is 1.6 nm and the well width is 2.4 nm. In the contacts, a N -type doping with the Fermi level of $E_f = 0.15$ eV above the conduction band is considered. The optical phonons lead to an inelastic change of the electron energy of ± 0.036 eV. Here we consider the acoustic phonons, optical phonons and impurities collisions.

compute the wave function and trajectory $\vec{r}_a^j[t]$ which is computed by time integrating the Bohmian velocity in equation (4.27). We inject the Gaussian wave packet with a dispersion $\sigma = 40$ nm, which is initially located outside the simulation box.

The current collected on the drain contact is computed as the net number of trajectories $\vec{r}_a^j[t]$ transmitted from the source to the drain, divided by the total time (5 ps). As a test, the average current is also computed from the total (particle plus displacement) current as indicated in Section 2.4. Both computations of the average current provides the same results, indicating the numerical accuracy of the computations and the effective zero average value of the displacement current. The number and type of collisions are obtain from the Fermi-Golden rule for GaAs material with the scattering rates plotted in figure 4.3.1. In figure 4.3.2, the reduction of the transmission is due to the acoustic

phonons and to the emission of optical phonons (energy dissipation). Moreover, we can have the information of all sources of collisions in figure 4.3.2(c), where the number of optical phonon emission is always larger than that of optical phonon absorption. The number of collisions at resonance energy is three times larger than that of outside the resource, showing that the ballisticity of RTD depends on the electron transit time, which changes with the applied drain bias.

CHAPTER 5

High-Frequency Behaviour of FETs: Practical Computations of Graphene Devices

5.1 The Theoretical Discussion

In the computations of high-frequency performances of electron devices, while most of the predictions have been obtained from the quasi-static approximation with time-independent models, enriched information would be obtained by going beyond the quasi-static approximation. At the beginning of this chapter, some theoretical discussions about the non-quasi-static formalism and about what kind of new results can be accessible with this time-dependent (dynamic) simulation of particle plus displacement currents will be discussed. Then, I will provide some numerical results about the high-frequency noise of Graphene devices.

5.1.1 The Ramo-Shockley-Pellegrini Theorem

In Chapter 1.2, I have discussed the role of the displacement current on the measured current obtained in a laboratory. The total current (not only the particle current) on a surface has to be computed to be sure that the simulated result is equal to the measured one in the laboratory. Generally, the displacement current $I_d(t)$ and the particle current $I_p(t)$ on a particular surface S_i can be computed from the standard expressions (2.31) and (2.32) mentioned in Chapter 2.

In order to discuss in details the relation between the total (particle plus displacement) current and the dynamics of electrons inside a semiconductor device, using Green's second identity to create another electrokinematics equations, we provide an alternative expression (named Ramo-Shockley-Pellegrini (RSP) theorem [31]) for computing the

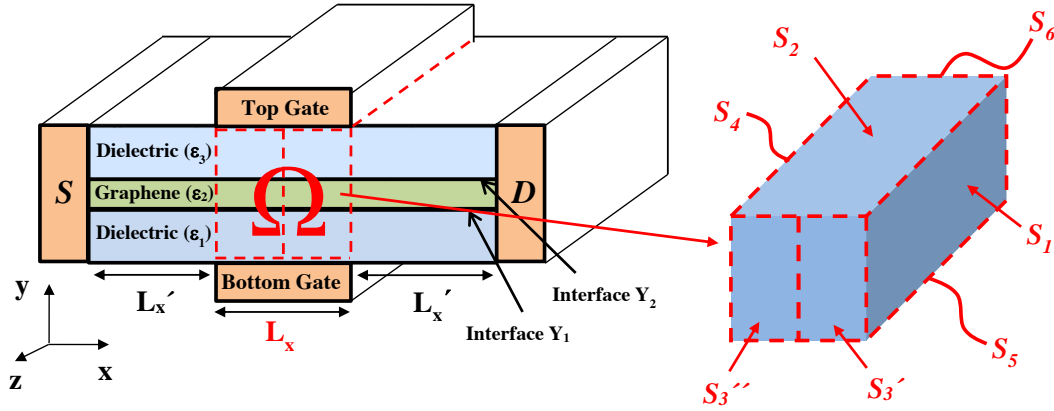


Figure 5.1.1: Schematic representation of a 2D material device (the 2D material channel is sandwiched between two dielectrics) in BITLLES simulator, whose volume Ω (with 3D structure plotted by dashed red lines) is limited by a closed surface $S = \{S_1, S_2, \dots, S_6\}$. In volume Ω , the channel length is L_x , the surface S_3 (and S_6) are divided into S_3' (S_6') and S_3'' (S_6''). A spacer length is L_x' .

time-dependent total current different from direct definitions of displacement and particle currents. As illustrated in figure 5.1.1, a parallelepiped of volume $\Omega = L_x \times L_y \times L_z$ is considered as the device active region. The volume Ω is limited by a closed surface S which is composed of six rectangular surfaces $S = \{S_1, S_2, \dots, S_6\}$. The total time-dependent current on a surface S_j is defined by the RSP theorem as $I_T(t) = \Gamma_j^q(t) + \Gamma_j^e(t)$ with the volume expression $\Gamma_j^q(t)$ gives [31]:

$$\Gamma_j^q(t) = - \int_{\Omega} \vec{F}_j(\vec{r}) \cdot \vec{J}_c(\vec{r}, t) d\nu = - \sum_{m=1}^N \text{sign}(\vec{v}_m) q \vec{F}_j(\vec{r}_m) \cdot \vec{v}_m(\vec{r}_m) \quad (5.1)$$

and the surface expression $\Gamma_j^e(t)$ as:

$$\Gamma_j^e(t) = \int_{S_j} \epsilon(\vec{r}) \frac{dV(\vec{r}, t)}{dt} \vec{F}_j(\vec{r}) \cdot d\vec{s} \quad (5.2)$$

where $\vec{J}_c(\vec{r}, t)$ is the particle current density at the position \vec{r} at time t , $\vec{v}_m(\vec{r}_m)$ is the m -electron velocity, \vec{r}_m is the m -electron position, q is the electron charge without sign, N is the total number of electrons in the simulation box, $V(\vec{r}, t)$ is the scalar potential at position \vec{r} and time t . The vector function $\vec{F}_j(\vec{r})$ is defined through an expression $\vec{F}_j(\vec{r}) = -\nabla\phi_j(\vec{r})$, where $\phi_j(\vec{r})$ is its scalar potential. The function $\text{sign}(\vec{v}_m)$ is equal to 1 when one electron leaves the volume Ω through the surface S_j , while $\text{sign}(\vec{v}_m) = -1$ when the electron enters. Let us note that the terms $\Gamma_j^q(t)$ and $\Gamma_j^e(t)$ cannot be interpreted as particle current and displacement current, respectively. In fact, the term $\Gamma_j^q(t)$ includes itself the particle current and part of the displacement current altogether. For example,

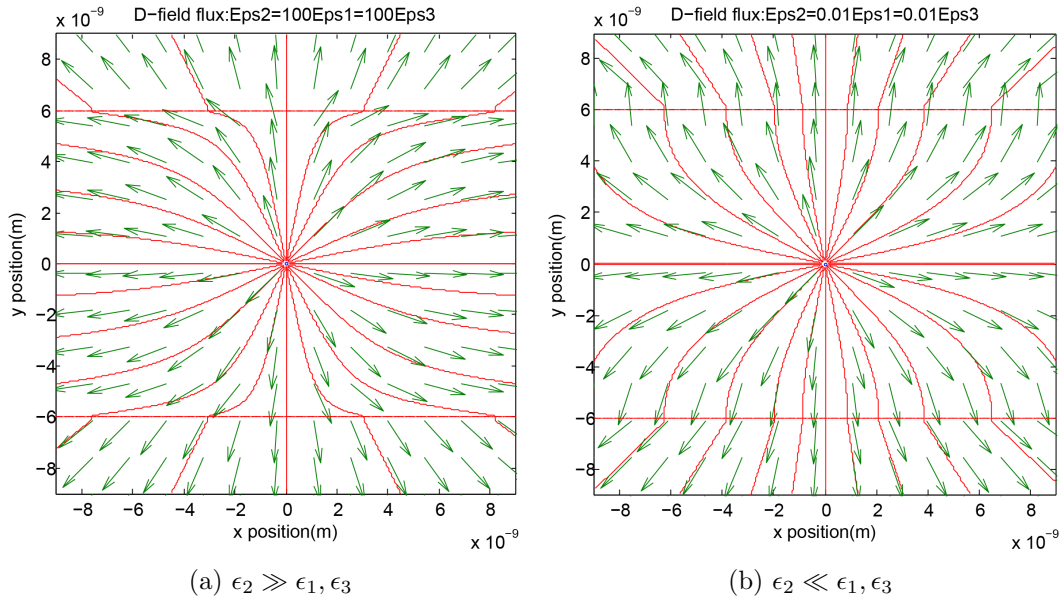


Figure 5.1.2: Lines of electric displacement in the cross-section of volume Ω due to a point charge q inside the graphene channel (with electric permittivity ϵ_2 and is located between top-dielectric (ϵ_3) and bottom-dielectric (ϵ_1)) (a) in case $\epsilon_2 \gg \epsilon_1, \epsilon_3$ and (b) in case $\epsilon_2 \ll \epsilon_1, \epsilon_3$.

when an electron is not crossing a surface, say S_j , $\Gamma_j^q(t) \neq 0$ while $I_p(t) = 0$. From the RSP theorem (5.1) and (5.2), it is obvious that the electric permittivity ϵ and the device geometry affect the time-dependent total current. As a consequence, in the following two subsections, I will explicitly analyze how the ϵ and device geometry effectively affect the total current.

5.1.2 The Role of Different Dielectric Constants on the Total Current Behaviour

In this part, the 3D Poisson's equation will be solved for a moving electron within an arbitrary three-layer structure of figure 5.1.1, a 2D material (with electric permittivity ϵ_2) channel is located between the first (bottom dielectric, electric permittivity ϵ_1) and third (top dielectric, electric permittivity ϵ_3) layers. More details about the solution of the 3D poisson's equation are provided in Appendix B. The electric displacement lines in the 2D plane X-Y of volume Ω due to a point charge q inside the channel are plotted in figure 5.1.2.

In the case $\epsilon_2 \gg \epsilon_1, \epsilon_3$, shown in figure 5.1.2 (a), the lines start from the point charge and tend to reach the bottom/top regions. However, the difference on the values of the dielectrics in the three regions implies a tendency of the electric lines to keep in region ϵ_2 .

A moving electron inside the channel has a strong influence on surfaces S_1 or S_4 (right and left in the figure) and leads to a non-negligible displacement current there. On the contrary, displacement current on surface S_2 and surface S_5 in volume Ω , top and bottom in the figure 5.1.2 (a), can be somehow neglected. Thus, in conclusion, although dealing with a 3-terminal device, the different dielectrics tend to provide an electric field similar to that found in a 2-terminal device.

On the contrary, when $\epsilon_2 \ll \epsilon_1, \epsilon_3$, most lines of the electric field tend to reach surface S_2 and surface S_5 in volume Ω , top and bottom in the figure 5.1.2 (b), providing a non-negligible current on the gates in a 3-terminal device. Thus, the instantaneous current on S_4 do not need to be equal to that on S_1 , while still satisfying instantaneous current conservation.

From this simple results, we conclude that a proper engineering design of the different electric permittivity allows to maximize/minimize the displacement current collected on the gates. In the next subsection, I will show that this type of manipulation of the source, drain and gate currents can be also realized by modifying the lateral areas of the FETs.

5.1.3 The Role of Device Geometry on the Total Current Behaviour

After the general discussion presented in the previous part, now I provide some simple results focus on the 2D material transistor and study the dependence of the total current (for an electron traversing the graphene transistor) on the device geometry. In order to compute the current due to an electron with a trajectory $\vec{r}(t) = \{v_x \cdot t, 0, 0\}$ with velocity $v_x = 5 \times 10^5$ m/s moving in FETs based on 2D material (the active region is volume Ω), as depicted in figure 5.1.1, we define the time-dependent drain current as $I_D(t) = I_{S_1} + I_{S'_3} + I_{S''_6}$, source current $I_S(t) = I_{S_4} + I_{S'_3} + I_{S''_6}$, gate current $I_G(t) = I_{S_2} + I_{S_5}$. These definitions of the gate, source and drain currents satisfy the requirement of $I_D(t) + I_S(t) + I_G(t) = 0$, at any time, because the sum $\sum_{j=1}^6 I_{S_j}(t) = 0$. Here S'_3 and S''_6 are the right half parts of S_3 and S_6 , respectively. S''_3 and S''_6 are respectively the rest part of S_3 and S_6 to ensure that $S'_3 + S''_3 = S_3$ (indicated in figure 5.1.1) and $S'_6 + S''_6 = S_6$.

An electron moving inside the channel generates a time-dependent electric field $\vec{E}(\vec{r}, t)$ on surface S_1 , which finally affects the drain current $I_D(t)$. The value of $I_D(t)$ plotted in figure 5.1.3 (a) shows the dependence of the duration of the total current peak τ_i (illustrated in the figure) on the lateral area $L_y \times L_z$. Let us emphasize that a unique trajectory, meaning a unique electron transit time $\tau_e = L_x/v_x$, with a fixed length $L_x = 20$ nm, is used in all computations where only the lateral dimension L_y is modified. In summery, from figure 5.1.3, the shape of the current pulse (transient current) is strongly

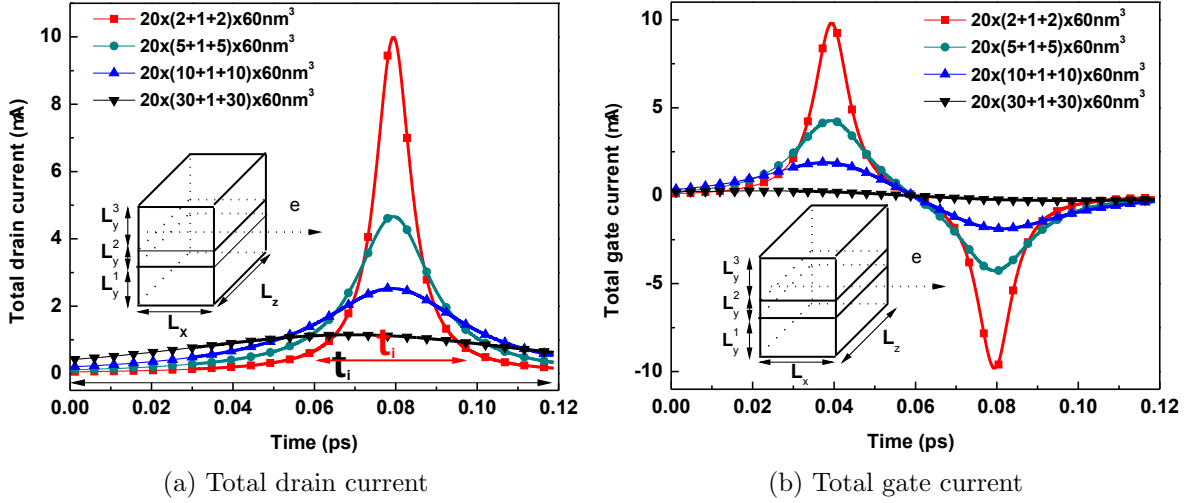


Figure 5.1.3: Total current (a) $I_D(t)$ and (b) $I_G(t)$ due to an electron traversing the volume $\Omega = L_x \times (L_y^1 + L_y^2 + L_y^3) \times L_z$. A fixed length $L_x = 20 \text{ nm}$ and several lateral areas by changing height L_y but constant width $L_z = 60 \text{ nm}$, are considered.

dependent on the lateral surface $L_y \times L_z$. Due to the symmetry, the dependence of the source current (not plotted) on the geometry is exactly the same as that for the drain current (with a negative sign).

A quite different behavior for the gate current is observed. There are two peaks, one positive and one negative, in the gate current. The positive part corresponds to increasing the electric field collected in the gate when the electron is approaching the center of the volume Ω , while the negative values correspond to decreasing the electric field on the gate surface when the electron is leaving. Between positive and negative parts the gate current has to cross the zero. Interestingly, the temporal distance between the maximum and minimum values of the gate current increases for larger lateral areas. Let us mention that a lot of information about the frequency spectrum of the current fluctuations can be anticipated from these simple results. On one hand, the Fourier transform of these currents provides direct information on the maximum frequencies of the corresponding spectrum. For example, as a general rule, higher frequencies are required to build sharp peaks associated to the currents of small lateral areas, while lower frequencies are required for the soft peaks associated to the current with large lateral areas. Up to now, we have provided numerical results how the device geometry affect the total current. As we know, the vector function $\vec{F}_j(\vec{r})$ in expressions (5.1) and (5.2) depends on the volume Ω . Next, let us see how to explain the results in figure 5.1.3 with the RSP theorem.

The 2-terminal Device

For the structure $20 \times (30 + 1 + 30) \times 60 \text{ nm}^3$ with $\Omega = L_x \times (L_y^1 + L_y^2 + L_y^3) \times L_z$, the drain current remains constant when the electron is traversing the device channel, which recovered the old result of Ramo [27] and of Shockley [28], i.e. a current constant in time. The gate current is almost zero. Therefore, this device behaves as a 2-terminal device. In the following, let us see how to explain the total current behaviour of a 2-terminal device with the RSP expressions (5.1) and (5.2).

The first version of the RSP theorem was presented by the work of Shockley [28] in 1938 and of Ramo [27] in 1939. They, separately, provided a simple expression for the computation of the total (particle plus displacement) current flowing through a vacuum tube, i.e. a typical electron device at that time. A vacuum tube can be roughly modeled as two infinite metallic plates separated by air—a 2-terminal device. According to the figure 5.1.4(a), let us name S_4 the left plate, S_1 the right plate and assume that an electron is moving inside volume Ω . It can be demonstrated that one gets $\vec{F}_4(\vec{r}) \approx -(1/L_x) \cdot \vec{x}$ when considering the volume Ω' (the bottom and upper surfaces are much smaller than the lateral ones) which captures all the lines of the electric field generated in the active region by the moving electron [118], where L_x is the distance between plates and \vec{x} is the unit vector in the transport direction perpendicular to the plates. Then, using equations (5.1) and (5.2) for just one electron moving with velocity $\vec{v} = \{v_x, 0, 0\}$ in the transport direction, the total current on S_4 during $0 < t < \tau_e$ can be written as:

$$I_4(t) \approx \Gamma_4^q(t) \approx -q \frac{v_x(t)}{L_x}, \quad (5.3)$$

The current value is a constant while the electron is inside the Ω and its time-integral during $\tau_e = L_x/v_x$ gives the expected transmitted charge $-q$. In addition, the currents on S_1 and S_4 are equal at any time. In this particular case, the relevant time for the peak current τ_i is roughly equal to the electron transit time $\tau_e = L_x/v_x$.

The 3-terminal Device

For the other structures, for instance $\Omega = 20 \times (2 + 1 + 2) \times 60 \text{ nm}^3$, the devices behave beyond the previous Ramo-Shockley result. In fact, these devices behave as a 3-terminal device where the instantaneous current $I_S(t)$ in the source S is not equal to the $I_D(t)$ in the drain D , while still satisfying the instantaneous current conservation. As a general 3-terminal device Ω plotted in 5.1.4(b), the top and bottom surfaces are no longer smaller than the lateral surfaces. For that geometry of the volume Ω , we get the expression $\vec{F}_4(\vec{r}) \approx -\alpha_x \cdot \exp(\alpha_x(x - L_x)) \cdot \vec{x}$ [118], where $\alpha_x = \sqrt{(\frac{1}{L_y})^2 + (\frac{1}{L_z})^2}$ (being L_y the vertical height and L_z the width indicated in figure 5.1.1. the vector function $\vec{F}_4(\vec{r})$ is

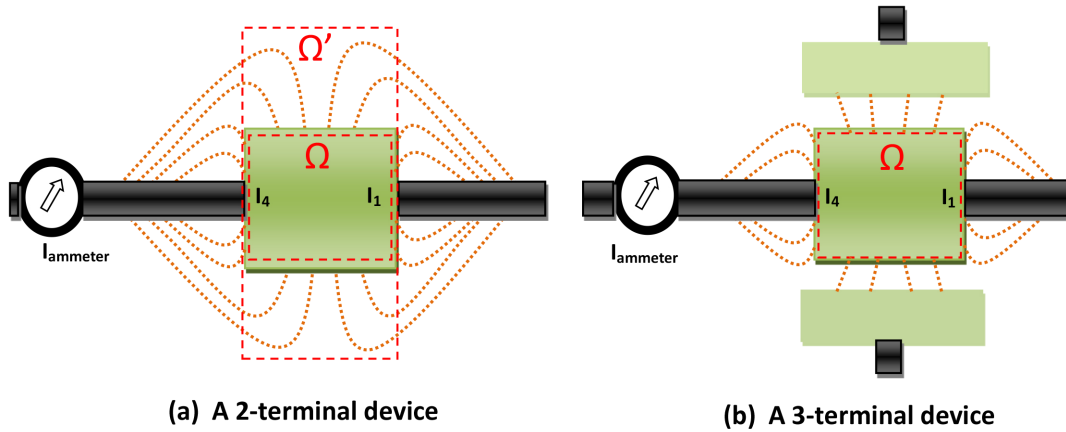


Figure 5.1.4: (a) A 2-terminal device, a very large simulation box Ω' is used to compute the total current, i.e. I_4 on surface S_4 , which is equal to the current $I_{ammeter}$ in the ammeter. (b) A 3-terminal device. The dashed lines represent the variational electric field lines.

not constant neither in modulus nor in direction. The current on S_4 due to one electron moving in x direction with velocity v_x is directly written from equations (5.1) and (5.2) as,

$$I_4(t) \approx \Gamma_4^q(t) \approx -q v_x \alpha_x e^{v_x \alpha_x (t - \tau_e)}. \quad (5.4)$$

It is seen clearly that the geometry of Ω has a clear influence on $\vec{F}_4(\vec{r})$, which, in turn, affects the current $I_4(t)$. Here, the electron transit time is different from the current peak duration, $\tau_e > \tau_i$.

Up to here, we have a better understanding how the device geometry affect the total current. Then, I will analysis the high-frequency behaviours of FETs based on 2D materials, in particular, the high-frequency noise of graphene FETs in Section 5.2.

5.2 Practical Computations for Graphene FETs

In this section, I will study the high-frequency noise of the graphene FETs. The introduction of graphene has been explained in Chapter 1. Before the discussion, let me mention shortly the theoretical work done in the prediction of the graphene transistor. A very simple estimation of the intrinsic cut-off frequency as the inverse of electron transit time shows that one can easily reach frequencies higher than 1 THz (active region shorter than 10^{-6} m with electron velocity on the order of 10^6 m/s). *Are such simple intrinsic high-frequency predictions really achievable? What noise is expected at such frequencies?*

The intrinsic THz performance of graphene transistors beyond the quasi-static approximation will be carefully studied, by explicitly simulating the time-dependent dis-

placement and particle currents in the active region of graphene transistors. In previous work, an original strategy has been presented to optimize radio frequency performance of gate-all around (GAA) quantum-wire Silicon FETs by modifying their lateral areas, without length scaling or mobility improvement [119]. In the definition of the duration of the total current peak due to an electron traveling along the device, there are scenarios where the exact transit time of the electron is not at all a relevant parameter for f_T estimations. It has been proved [119] that, for GAA quantum-wire Silicon FETs, the ultimate responsible of the high-frequency noise is not the electron transit time τ_e , but a different time related to the duration of the total current peak τ_i , while the electron is crossing the device. Hereafter, I will show that similar arguments can be also applied to the intrinsic THz performance of graphene transistors. Along this work I refer to intrinsic modeling in order to emphasize that spurious effects (like the important drawbacks occasioned by the contact resistance mentioned above) are not considered in this work. I only deal with electron dynamics inside the device active region. The intrinsic Klein (Band-to-Band) tunneling and positive-negative energy injection on graphene transistors are carefully analyzed and predictions on their effect on the graphene high-frequency performance are provided.

Before computing the high-frequency noise of graphene FETs, let us discuss some peculiarities of graphene material. Due to the 2D nature of graphene, only two degrees of freedom specify the electron position, $\{x, z\}$. Equivalently, only two wave vectors $\{k_x, k_z\}$ are needed. As a consequence of the honeycomb graphene structure, the relationship between the energy of electrons, E_k and its wave vector $|\mathbf{k}| = \sqrt{k_x^2 + k_z^2}$ is:

$$E_k = \pm \hbar v_f |\mathbf{k}|, \quad (5.5)$$

where $v_f = 5 \times 10^5$ m/s is the Fermi velocity. This linear $E_k - k$ dispersion has several relevant differences with typical parabolic $E_k - k$ dispersion in Silicon that, at the end of the day, implies important differences with the typical Monte Carlo tools:

- Electrons with positive and negative (kinetic) energy in a gapless material: From the \pm signs in equation (5.5), we notice that there are two possible energies for an electron with momentum $|\mathbf{k}|$. In the literature, usually those electrons with negative energy are called holes and with positive energy called electrons. We do not use the name hole because here we simulate explicitly electrons in the conduction band (CB, positive kinetic energy) and electrons in the valence band (VB, negative kinetic energy). The graphene (kinetic) energy band structure has a zero (kinetic) energy at the Dirac point. Contrary to Silicon semiconductors, there is no energy gap between electrons with positive energy and electrons with negative energy. Injections from the contact have to consider electrons above and below the Dirac

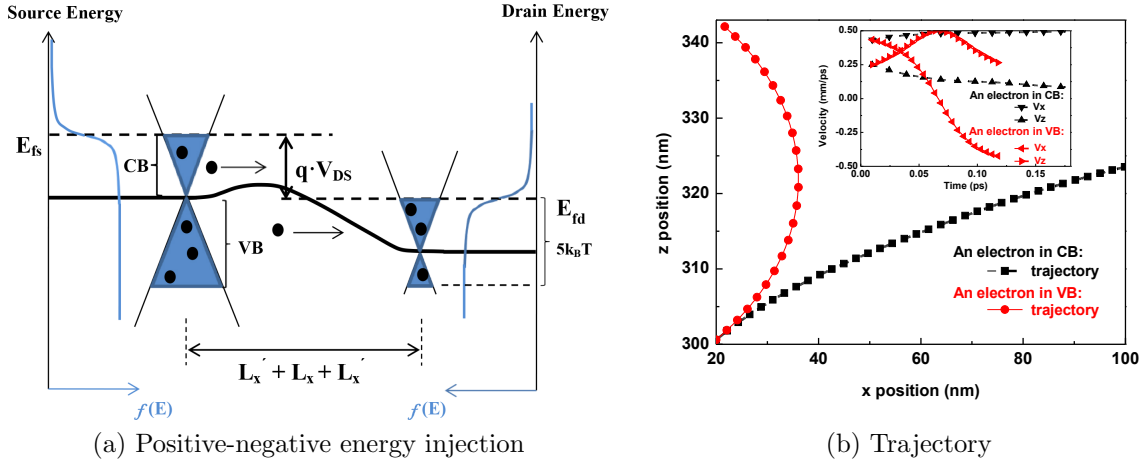


Figure 5.2.1: (a) Schematic representation of an energy profile in the transport direction of graphene transistors in BITLLES simulator. The applied drain-source bias, V_{DS} , provides a different source, E_{fs} , and drain, E_{fd} , Fermi levels, the Fermi-Dirac distribution function at each contact are indicated. (b) The trajectory for one electron above the Dirac point and one below with the same absolute kinetic energy injected from the source approaching the drain.

point, as illustrated in figure 5.2.1(a). The details of the particular positive-negative (kinetic) energy injection model in the BITLLES simulator have been explained in Chapter 3.

- Transport equation in graphene: From equation (5.5) one can easily find the semi-classical equations of motion for electrons in graphene. Their dynamical behavior is similar to massless relativistic particles. However, their maximum velocity is not the speed of light, but v_f . A simple understanding of graphene electrons under an applied bias (from drain to source) can be achieved by using the conservation of the total energy E and of the momentum k_z in the z direction (no applied bias in that direction). If we define θ as the angle between \mathbf{k} and k_x , i.e. $\sin(\theta) = k_z/|\mathbf{k}|$, then the conservation of E and of z -momentum imply that an electron of total energy E moving from a location with potential energy U_o till another point with U_f has to satisfy the relation:

$$(E - U_o)\sin(\theta_o) = \pm(E - U_f)\sin(\theta_f) \quad (5.6)$$

When an electron with positive kinetic energy E_k moves with $U_o > U_f$ (and with both $U_o < E$ and $U_f < E$), then, it tends to reach the maximum velocity in the x direction and minimum in the z direction (dashed lines in the inset of figure 5.2.1(b))

and the contrary if $U_o < U_f$. The opposite behavior (solid lines in the inset of figure 5.2.1(b)) is found for an electron with negative kinetic energy E_k (with both $U_o > E$ and $U_f > E$). All previous trajectories are compatible with using the sign + in equation (5.6). On the contrary, if the electron trajectory involves changing from positive to negative kinetic energies because of Klein tunneling (either $U_o < E$ and $U_f > E$ or $U_o > E$ and $U_f < E$), then, the sign – has to be used in equation (5.6).

- Because of the energies available above and below the Fermi point, the typical gap barrier with forbidden energies found in Silicon is unachievable in graphene. This exotic phenomenon leads to a particular effect called Klein tunneling [120, 121]. When an electron impinges with sharp variations of the potential energies, there is a large probability that the electron tunnels from one band to another [120, 121]. This kind of band-to-band tunneling implies that the tunneling current is always relevant, resulting in a failure to get saturation near the pinchoff [122, 123]. The tunneling probability in the x direction is given by [81]:

$$T = \exp\left(-\pi\hbar v_f k_z^2 / (e|F|)\right), \quad (5.7)$$

where $|F|$ is the magnitude of the local electric field in the x direction, and k_z is the wave vector in z component. Similar probability expression is used for the tunneling in the z direction.

The simulation of high-frequency graphene FETs is performed by using the BITLLES simulator solving the Monte Carlo solutions of the Boltzmann equation (adapted for graphene structures). The peculiarity in graphene, for instance, the Klein tunneling, linear band-structure and the positive-negative injection, are also taken into account in the simulation. An ideal Ohmic contact is assumed in the drain and source contacts to ensure that the applied V_{DS} directly translates into a difference of the source and drain Fermi levels, i.e. $E_{fd} = E_{fs} - qV_{DS}$, being E_{fs} and E_{fd} the source and drain Fermi levels, respectively. The extrinsic role of the contact resistance mentioned previously is directly disregarded in all the intrinsic results discussed in this work. All simulations of the graphene devices are performed with a DC polarization for the gate, source and drain bias. In particular, I define $E_{fs} = 0.05$ eV with $V_{TG} = V_{BG} = 0.05$ V (being V_{TG} top gate voltage and V_{BG} bottom gate voltage), $V_S = 0$ V and $V_D = 0.1$ V.

In any case, by dealing with an explicit time-dependent formalism, the intrinsic dynamics of the electrons in the active device region will be captured. Each bias point is simulated during $T = 1000$ ps, with a time step of $\Delta t = 0.7$ fs. The Poisson equation is solved in the whole simulation box depicted in figure 5.1.1 including external spacer L'_x , larger than the device active region Ω , with Dirichlet boundary conditions on the gates, source and drain surfaces and Dirichlet in the rest of boundaries. At each time step of

the Monte Carlo simulation, Δt , the total current $I(t)$ in all surfaces of the volume Ω are computed, following the direct expressions (2.31) and (2.32), or the RSP theorem (5.1) and (5.2). From these currents on the six faces of the volume Ω , the source, gate and drain currents are computed following the definitions given in Subsection 5.1.3. Once the time-dependent currents are known, autocorrelation function $\Delta R(\tau)$ and the power spectral density (PSD) can be computed from expressions (2.2) and (2.3) in Chapter 2, respectively [124].

Two different geometries for the graphene FET depicted in figure 5.1.1 are considered. The device A has a volume $\Omega_A = 20 \times (2 + 1 + 2) \times 60 \text{ nm}^3$ and device B is $\Omega_B = 20 \times (30 + 1 + 30) \times 60 \text{ nm}^3$ with $\Omega = L_x \times (L_y^1 + L_y^2 + L_y^3) \times L_z$. In both geometries, the length in the transport direction is $L_x = 20 \text{ nm}$ (identical transit times), the height in the y direction of the 2D graphene sheet is 1 nm and width in the z direction is $L_z = 60 \text{ nm}$. The only difference is the height of the dielectrics. All the rest physical parameters discussed in the previous section are identical for both structures. In order to test the effect of the Klein tunneling and positive-negative (kinetic) energy injection discussed, we consider high-frequency performance for three types of simulations for both structures. The results of the DC currents and low-frequency noise with or without Klein tunneling and with or without negative energy injection are summarized in table 5.1.

5.2.1 PSD without Klein Tunneling and only Positive Energy Injection

First of all, a simulation without Klein-tunneling and only positive kinetic energy injection is considered. This is a type of simulation similar to the one done for Silicon FETs. The PSD of current fluctuations for the two different geometries is plotted in figure 5.2.2. First, from the figure, it is easy to realize that the (maximum) frequencies where the PSD of the drain and source current fluctuations drops down to zero become different and with a difference of almost one order of the magnitude. Let us emphasize that, in principle, both geometries in devices A and B have roughly the same electron transit time $\tau_e = L_x/v_x$. A displacement of the noise spectrum to the higher frequency range can be achieved without changing the device active region $L_x = 20 \text{ nm}$ nor its (average) velocity v_x . The physical reason of this effect can be easily understood from the results of figure 5.1.3 for the drain and source currents and the explanation there. Sharp temporal peaks of the displacement currents requires higher frequencies, and vice versa. This very relevant effect will also appear in all the rest of simulations and its consequences in the cut-off frequencies will be mentioned in the conclusions.

In addition, in figure 5.2.2, a large peak of the gate current for device A at frequency $f = 10 \text{ THz}$ is observed, which is much larger than that of device B. This effect can also

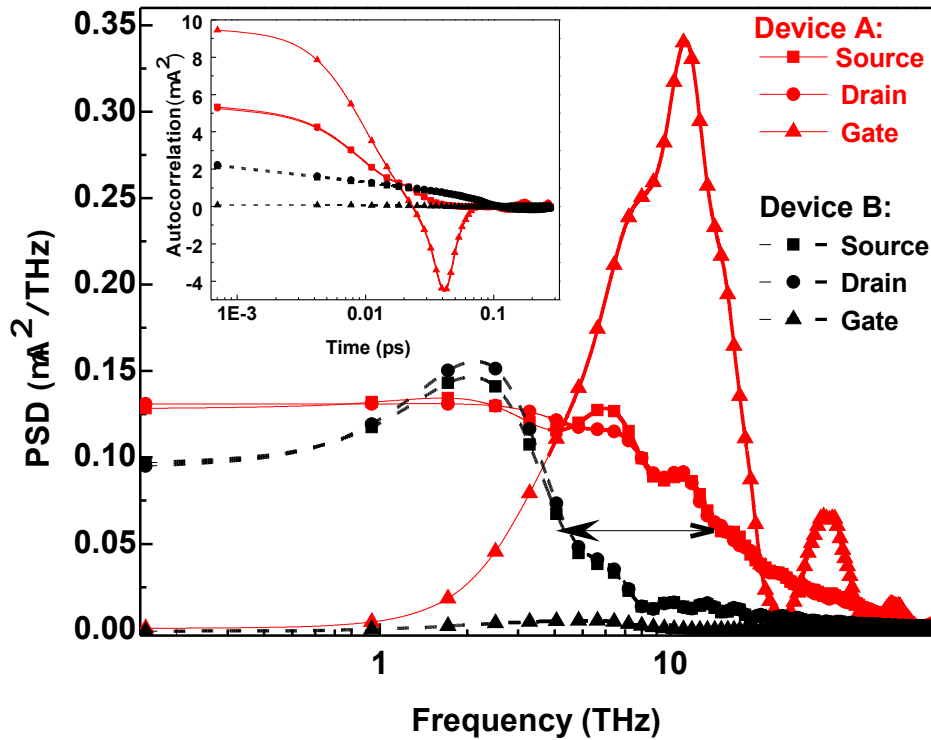


Figure 5.2.2: PSD of the current fluctuations as a function of frequency for graphene FETs with two different geometries (but identical channel length $L_x = 20$ nm) in device A and B, operating under DC conditions: double gates $V_{TG} = V_{BG} = 0.05$ V, applied bias $V_{DS} = 0.1$ V, without Klein tunneling and only positive kinetic energy injection.

be clearly seen in the autocorrelation plotted in the inset of the figure. The sample B has a much lower value of the PSD of the gate current peak and its peak appears at a lower frequency $f = 4$ THz. The basic features of these peaks of the gate current again can be straightforwardly understood from the results of figure 5.1.3. The Fourier transform of the gate current drawn in figure 5.1.3 is basically a delta in the frequency of the oscillatory signal for device B and several deltas in the case of sample A. Notice the tendency to a multi peak spectrum in the PSD of device A. In both cases, no PSD appears at zero frequency because there is no particle current in the gate, but only displacement current that goes to zero when averaged in a long period of time [125].

5.2.2 PSD with Klein Tunneling and only Positive Energy Injection

When the Klein tunneling is considered, but still only electron injection from above the Fermi Dirac point, the results in figure 5.2.3 are qualitatively very similar to the ones plotted in figure 5.2.2. However, let us emphasize that the PSD is basically one order

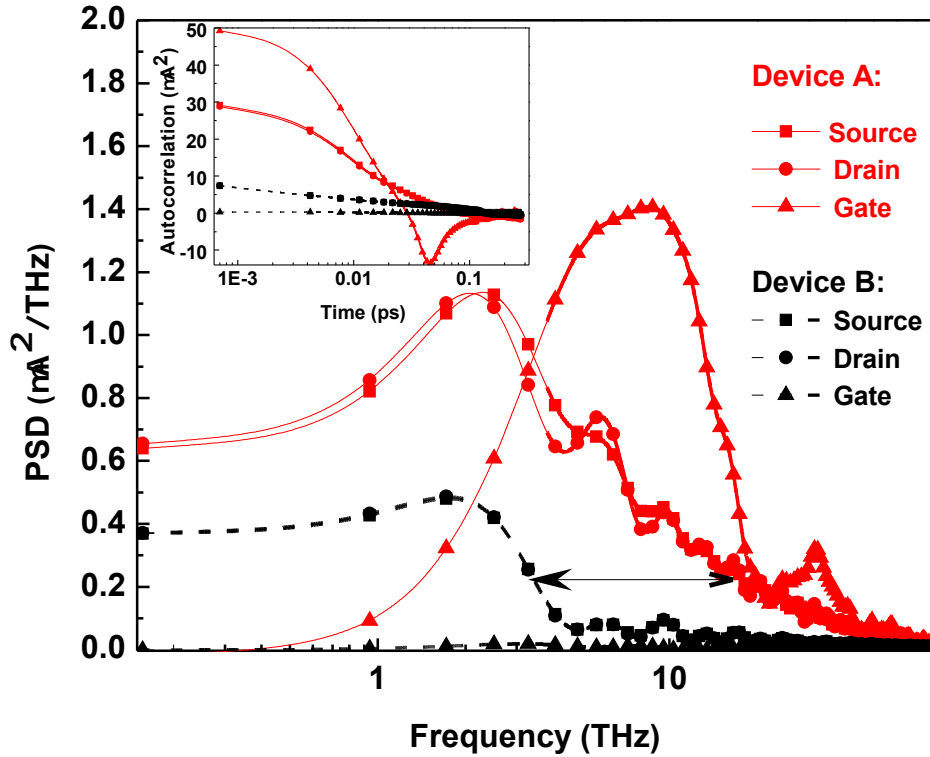


Figure 5.2.3: PSD of the current fluctuations as a function of frequency for graphene FETs with two different geometries (but identical channel length $L_x = 20$ nm) in device A and B, operating under DC conditions: double gates $V_{TG} = V_{BG} = 0.05$ V, applied bias $V_{DS} = 0.1$ V, with Klein tunneling and only electron injection from above the Dirac point.

of magnitude larger now as written in table 5.1. The Klein tunneling with a “random” tunneling probability of being reflected or transmitted given by equation (5.7) (with the change from positive kinetic energy to negative kinetic energy or vice versa) introduces an important source of noise. These new source of noise cannot be avoided in graphene and is present even in the “ballistic” regime (no phonon or impurity scattering) considered in this work.

Looking at the DC currents in table 5.1, this noise increment is obtained, in fact, with a reduction of the DC current (the signal). The physical reason of the reduction is quite simple. Now, electrons from the drain are able to reach the source, even with an applied bias $V_{DS} = 0.1$ V, because of the Klein tunneling. This new addition of flux of electrons has an opposite sign when compared to the conventional source-to-drain current. Certainly, the signal-to-noise ratio is greatly degraded because of the Klein tunneling. This is an important and unavoidable drawback for high-frequency applications of graphene, not usually noticed in the literature.

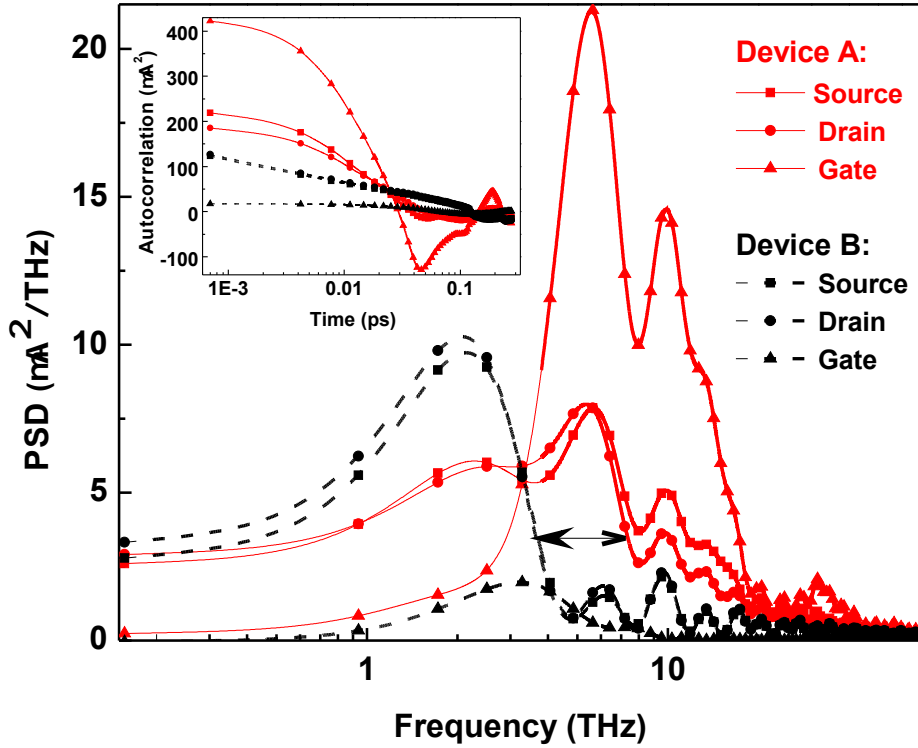


Figure 5.2.4: PSD of the current fluctuations as a function of frequency for graphene FETs with two different geometries (but identical channel length $L_x = 20$ nm) in device A and B, operating under DC conditions: double gates $V_{TG} = V_{BG} = 0.05$ V, applied bias $V_{DS} = 0.1$ V, with Klein tunneling and positive-negative energy injection.

5.2.3 PSD with Klein Tunneling and Positive-Negative Energy Injection

Finally, in figure 5.2.4, the PSD are plotted for device A and B when, both, Klein tunneling and positive-negative energy injection are considered. The main features discussed for figures 5.2.2 and 5.2.3 are also present in these new results. Again, let me emphasize that the PSD increases two orders of magnitude, while the DC current is roughly a factor of 10 greater than that in the first case. For the noise, the new thermal injections from below the Fermi point implies larger noise. For the DC current, now, there is a combination of a decrement of the DC current due to Klein tunneling and an increment due to the source-to-drain injection from below of the Fermi Dirac point (greater than the drain-to-source injection). Note that I consider the effect of the Pauli principle in the injection model, but do not consider it during the dynamics of electrons in the device active region. Therefore, the DC current is a little overestimated. In any case, the important degradation of the signal-to-noise ratio mentioned for the results of figure 5.2.3

Table 5.1: DC current and zero-frequency noise (i.e. $S(\omega \rightarrow 0)$) for three types of simulations for both device A and device B. In the table, KT means simulation with Klein tunneling, PI with positive (kinetic) energy injection and NI with negative kinetic energy injection.

			Device A		Device B	
			DC current	noise	DC current	noise
			(μA)	($\mu\text{A}^2/\text{THz}$)	(μA)	($\mu\text{A}^2/\text{THz}$)
	PI		0.68	0.130	1.50	0.095
KT	PI		0.21	0.641	0.31	0.368
KT	PI	NI	10.2	2.711	8.14	2.956

is also present here.

In conclusion, a new path is opened to study the announced THz behavior of graphene transistors. Instead of using the extended strategy of providing high-frequency predictions from quasi-static simulations, I directly simulate the time-dependent particle and displacement currents in an intrinsic graphene FET. Only the device active region is explicitly simulated, thus, all extrinsic effects due to (parasitic) resistances in the source, drain or gate contacts are directly ignored in this work. A Monte Carlo solution of the Boltzmann equation is fully adapted to graphene FETs. In particular, the semi-classical transport equations for electrons above and below the Dirac (zero energy) point are adapted accordingly. In addition, the Klein tunneling is explicitly considered allowing electrons to transit from above to below the Dirac point, or vice versa. A novel electron injection model for electrons with positive and negative kinetic energies are developed for graphene (including the thermal noise and Fermi Dirac statistic). From the simulations of the dynamics of the electrons inside the active region (under constant DC polarization in the gate, source and drain contact), I compute the *measured* total currents in the three FET terminals. From such time-dependent currents, the PSD of their fluctuations is computed as a Fourier transform of the current autocorrelation.

Particular features of high frequency behavior of graphene FETs are predicted from such PSD. I perform simulation with and without Klein tunneling, and injection from positive or both positive and negative (graphene injection) kinetic energies. From such simulations, we conclude that the unavoidable Klein tunneling and graphene injection provide an increment of noise at THz frequencies (and also at lower frequencies) when compared to simulations without Klein tunneling or graphene injection. Such increment of the noise is not compensated by a similar increment on the average DC current (interpreted here as the signal), providing an unavoidable degradation of the signal-to-noise ratio. Certainly, the use of a semi-classical simulation tool is an approximation, however, a test with (Bohmian) quantum solutions of the Dirac equation that the extension to-

wards quantum simulations tools will not provide important variations [42, 69, 70, 114]. The main approximation in this present work (common in most Monte Carlo simulations) is the fact that the Pauli principle (the exchange interaction between electrons) is not explicitly considered during the dynamics of electrons in the device active region.

The two geometries of the graphene FET studied in this work, device A and device B, have exactly the same length in the x (drain-source transport) direction. Therefore, both geometries imply the same transit time, τ_e , but they have different temporal width of the peak current τ_i , see figure 5.1.3. However, the shorter the vertical height (in comparison with the length of the active region in the transport direction), the larger the maximum frequency of the PSD. This can be seen in figures 5.2.2, 5.2.3 and 5.2.4. From this result, an alternative strategy (without length scaling) is envisioned to optimize the intrinsic cut-off frequency of graphene transistors. It is argued from the usual (quasi-static approximation) predictions of the cut-off frequency, f_T , that its value is inversely proportional to the transit time, $f_T \approx 1/(2\pi\tau_e)$, pointing out that the electron transit time as the ultimate limiting factor [4, 126]. This last result suggests to improve the material mobility and shorten the x transport direction when optimizing f_T . However, in this work, I have shown that in fact a careful time-dependent analysis of the displacement current generated by a moving electron shows that, for some particular graphene FETs named here as device A (with lateral dimensions much shorter than their gate length), the limiting effective time is the current peak, τ_i , which can be much smaller than τ_e . This can be seen in figures 5.2.2, 5.2.3 and 5.2.4. The same result can be anticipated from figure 5.1.3.

CHAPTER 6

Limitations of f_T to Correctly Quantify the Speed of Nanoscale Transistors: Practical Computations of 2D Devices

The development of faster electron devices for digital and analog applications is a constant demand in the electronics industry [4, 5]. The scientific community tries to quantify how fast the field effect transistors (FETs) work through some figures of merit (FoMs). In this chapter, I will discuss with theoretical and numerical results to test if the intrinsic cut-off frequency (f_T) can be an appropriate FoM to quantify the intrinsic speed of these nanoscale FETs with dimensions of few nanometers for digital or analog TeraHertz (THz) applications.

6.1 The Theoretical Discussion

There is no such a unique FoM that unequivocally quantifies how fast an electron device works. Some definitions are linked to a particular circuit or application, others to the intrinsic device itself. Some FoMs are redefined to make them more easily accessible from simulations, or from measurements. Usually, the FoMs in digital FET applications are related with times, while that in analog ones are commonly described with frequencies.

In digital FET applications, for example, an important FoM is the intrinsic delay time τ_d . The idea of this FoM is to quantify the time needed for an output signal to respond to an input signal[127]. Many times, a simpler quasi-static (QS) definition of the intrinsic delay time, $\tau_d^{QS} \approx C \cdot V_{gs}/I_{ds}$, is preferred because it is easily accessible from DC (time-independent) simulations [4]. Such expression can be interpreted as the time needed to charge the next gate capacitor C , until the gate voltage associated to

the ON state V_{gs} , with a constant drain-source current I_{ds} . From an experimental point of view, however, a new definition of the intrinsic delay time from a ring oscillator of N (odd) CMOS inverters is used. By taking the inverse of the frequency at which the ring oscillator runs and dividing it by N , such intrinsic delay time can be easily obtained [128].

In analog applications, the cut-off frequency f_T and the maximum oscillation frequency f_{max} are the main FoMs. The f_T is defined as the frequency at which the drain and gate current phasors become equal (that is a current gain of 0 dB) [129, 130]. Equivalently, the f_{max} is the frequency at which the power gain is 0 dB [4]. Both frequencies are easily accessible from the measurement of S -parameters and even their intrinsic values (when all parasitic elements of the circuit are eliminated using de-embedding techniques) are measurable. Needless to say, f_{max} , based on Mason's identities [131], becomes a more relevant FoM in high-frequency analog applications [5].

It is accepted that, although the intrinsic f_T is not the relevant FoM in high frequency analog applications, it is a meritorious FoM providing useful information on the speed of FETs. In order to provide an expression of the cut-off frequency accessible from DC (time-independent) simulations, the so-called QS approximation $f_T^{QS} \approx g_m/(2\pi C)$ is presented in the literature [6, 132–135]. It is based on assuming that the drain current is only the DC component related to the (linear) transconductance $g_m = dI_{ds}/dV_{gs} \approx I_{ds}/V_{gs}$, while the gate current is the displacement component proportional to the capacitor C and frequency. From the previous QS definition of the intrinsic delay time $\tau_d^{QS} \approx C \cdot V_{gs}/I_{ds}$ in digital applications, we easily arrive to the approximation $f_T^{QS} \approx 1/(2\pi\tau_d^{QS})$ [136, 137]. This last expression supposedly justifies why the cut-off frequency is a good FoM to quantify the intrinsic switching speed in digital applications. Alternatively, several non-quasi-static (NQS) approximations are also proposed for more accurate predictions of f_T [130, 133, 138, 139].

In this chapter, we discuss if f_T can be an appropriate FoM to quantify the intrinsic speed of these nanoscale FETs with dimensions of few nanometers for digital or analog TeraHertz (THz) applications. In such FETs, the electric field generated by an electron crossing the channel is not properly screened and it induces displacement current on the terminals. We will construct a condition for the validity of the QS estimation of f_T^{QS} and prove that f_T far from this condition can be a quite misleading estimator (with or without approximations) for the speed of ballistic FETs.

We summarize here four relevant time intervals that will be used along the paper. The intrinsic delay time τ_d quantifies the temporal difference between the time when a gate voltage perturbation starts and the time when the gate, drain and source currents reach steady-state values. The τ_d^{QS} and τ_d^{NQS} are the intrinsic delay time mentioned above under the QS approximation and under the zero-order NQS approximation, respectively.

Due to the displacement current, one electron traversing the channel length generates a current pulse¹. The temporal width of such pulse is defined as τ_p . The value of τ_p is influenced by the device geometry and the dielectric relaxation time needed for the background charge to neutralize (screen) the electric field generated by the single electron. We also define f_T^d , f_T^{QS} and f_T^{NQS} as the cut-off frequencies associated to τ_d , τ_d^{QS} and τ_d^{NQS} , respectively. Finally, f_T is the exact definition of the cut-off frequency from the condition of the current gain equals to one. We will see in this chapter that f_T can dramatically differ from f_T^d .

6.1.1 Fourier Analysis of f_T

In this subsection, a Fourier analysis of the definition of f_T from the condition of the current gain equals to one will be discussed, with special attention to the role played by the particle and displacement currents on it. This complete discussion is valid for any type of (ballistic or non-ballistic) FET.

We consider a dual-gate FET depicted in figure 6.1.1(a) with three terminals. The three relevant total (displacement plus particle) currents, named $I_1(t)$, $I_2(t)$ and $I_3(t)$ are respectively associated to the gate, drain and source terminals (more details about the definition and computation of these three terminal total currents with the BITLLES simulator can be found in Chapter 5), as:

$$I_m(t) = \int_{S_m} \epsilon(\vec{r}) \frac{d\vec{E}(\vec{r}, t)}{dt} \cdot d\vec{s} + \int_{S_m} \vec{J}(\vec{r}, t) \cdot d\vec{s}, \quad (6.1)$$

being $\epsilon(\vec{r})$ the electric permittivity, $\vec{E}(\vec{r}, t)$ the electric field and $\vec{J}(\vec{r}, t)$ the particle current density. We consider $d\vec{s}$ outwards. The three surfaces in equation (6.1) construct a surface $S = S_1 + S_2 + S_3$ that totally enclose an arbitrary volume Ω . Then, by construction, at any time t , the three currents satisfy:

$$I_1(t) + I_2(t) + I_3(t) = 0. \quad (6.2)$$

which is just the conservation of the total current in the active region Ω due to the application of Gauss's law in S .

In the evaluation of f_T , we are interested in a transient simulation. Initially, the three currents have steady-state values $I_m(0)$. At $t = 0$, a (small-signal) voltage perturbation is applied on one of the three FET terminals. Then, during a time interval τ_d (we will

¹In the case of an electron with charge q and velocity v moving between two infinite parallel metals separated with a distance L , it is well known from the Ramo-Shockley-Pellegrini theorem [119] that the square pulse current has a temporal width of $\tau_p = L/v$ and a height equals to qv/L . The total charge of the current pulse is $(qv/L) \times (L/v) = q$.

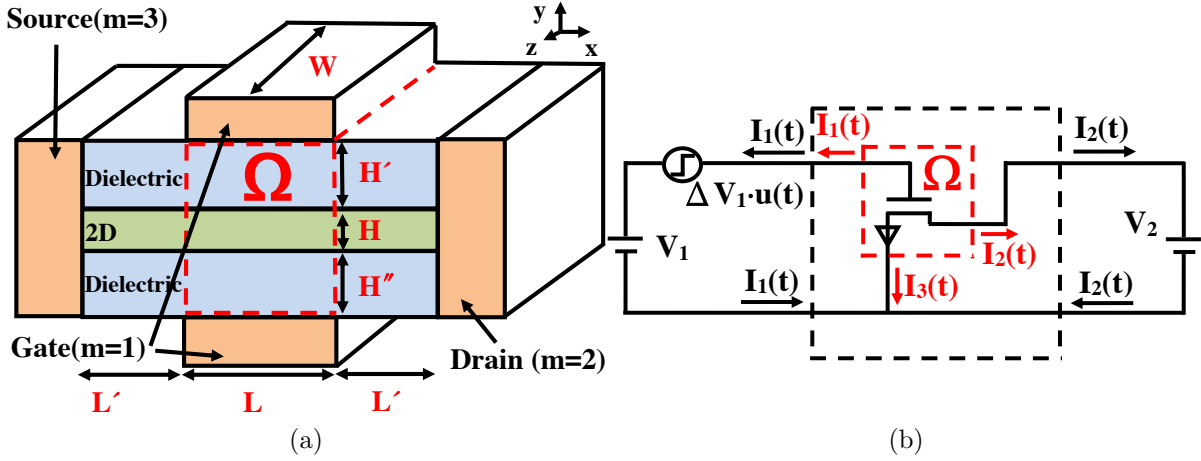


Figure 6.1.1: (a) Cross-section of the active region $\Omega = L \times (H' + H + H'') \times W$ in a dual-gate 2D FET being L the gate length. (b) A two-port network of the intrinsic device.

see later that this time is indeed the intrinsic delay time), the three output currents oscillate. Finally, new steady-state values $I_m(\tau_d)$ for the three currents are achieved with $I_m(t) = I_m(\tau_d)$ for $t \geq \tau_d$. For each contact m , we define the incremental charge during τ_d as:

$$\Delta Q_m \equiv \int_0^{\tau_d} (I_m(t) - I_m(\tau_d)) dt. \quad (6.3)$$

Instituting the total current expression (6.1) into the incremental charge, we get:

$$\begin{aligned} \Delta Q_m &= \int_0^{\tau_d} \left[\int_{S_m} \epsilon(\vec{r}) \frac{d\vec{E}(\vec{r}, t)}{dt} \cdot d\vec{s} + \int_{S_m} \vec{J}(\vec{r}, t) \cdot d\vec{s} \right] dt + \int_0^{\tau_d} I_m(\tau_d) dt \\ &= \int_{S_m} \epsilon(\vec{r}) [\vec{E}(\vec{r}, \tau_d) - \vec{E}(\vec{r}, 0)] \cdot d\vec{s} + \int_0^{\tau_d} \int_{S_m} \vec{J}(\vec{r}, t) \cdot d\vec{s} dt + I_m(\tau_d) \cdot \tau_d \\ &= \Delta \Phi_{D,m} + \sum_{j=1}^{N_m} \text{sign}(\vec{v}_j) \cdot q + I_m(\tau_d) \cdot \tau_d, \end{aligned} \quad (6.4)$$

where we define the incremental D -field flux on surface m as $\Delta \Phi_{D,m} = \Phi_{D,m}(\tau_d) - \Phi_{D,m}(0)$ with $\Phi_{D,m}(t) = \int_{S_m} \epsilon(\vec{r}) \vec{E}(\vec{r}, t) \cdot d\vec{s}$. The sum N_m is the number of electrons that have crossed the surface S_m during the time from 0 till τ_d . The function $\text{sign}(\vec{v}_j)$ is equal to 1 when one electron leaves the volume Ω through the surface S_m , while that the $\text{sign}(\vec{v}_j)$ is -1 when the electron enters, \vec{v}_j represents the velocity of the j -th electron and q is the electron charge without sign. Using (6.2) that ensures $I_1(t) + I_2(t) + I_3(t) - I_1(\tau_d) - I_2(\tau_d) - I_3(\tau_d) = 0$ at any time for the volume Ω , we easily get:

$$\Delta Q_1 + \Delta Q_2 + \Delta Q_3 = 0. \quad (6.5)$$

The equation (6.5) is rewritten by replacing the incremental charge ΔQ_m with the expression (6.4), as:

$$\begin{aligned}
& \Delta\Phi_{D,1} + \sum_{j=1}^{N_1} \text{sign}(\vec{v}_j) \cdot q + I_1(\tau_d) \cdot \tau_d + \Delta\Phi_{D,2} + \sum_{j=1}^{N_2} \text{sign}(\vec{v}_j) \cdot q + I_2(\tau_d) \cdot \tau_d \\
& \qquad \qquad \qquad + \Delta\Phi_{D,3} + \sum_{j=1}^{N_3} \text{sign}(\vec{v}_j) \cdot q + I_3(\tau_d) \cdot \tau_d \\
& = \Delta\Phi_{D,1} + \Delta\Phi_{D,2} + \Delta\Phi_{D,3} + \sum_{j=1}^N \text{sign}(\vec{v}_j) \cdot q + (I_1(\tau_d) + I_2(\tau_d) + I_2(\tau_d)) \cdot \tau_d \\
& = \Delta\Phi_{D,1} + \Delta\Phi_{D,2} + \Delta\Phi_{D,3} + \sum_{j=1}^N \text{sign}(\vec{v}_j) \cdot q = 0, \tag{6.6}
\end{aligned}$$

where we have used the current conservation law $(I_1(\tau_d) + I_2(\tau_d) + I_2(\tau_d)) \cdot \tau_d = 0$ and the total number of electrons cross the surface S is $N = N_1 + N_2 + N_3$. This equation just states that the variation of electron charge from 0 till τ_d in the volume Ω is compensated by the variations of the electric flux during this time interval on the surface S .

The All-order Definition of f_T

The usual definition of f_T comes from a FET in common source configuration as plotted in figure 6.1.1(b). Following the signs of the currents assigned to the FET of figure 6.1.1(a), the currents on the gate and drain terminals of the two-port network are positive when leaving the network. In the model of figure 6.1.1(b), the relationship between the phasor voltages $\tilde{V}_m(\omega) \equiv \mathcal{F}\{V_m(t) - V_m(0)\}$, the phasor currents $\tilde{I}_m(\omega) \equiv \mathcal{F}\{I_m(t) - I_m(0)\}$ and the Y -parameter matrix is:

$$\begin{bmatrix} \tilde{I}_1(\omega) \\ \tilde{I}_2(\omega) \end{bmatrix} = \begin{bmatrix} Y_{11}(\omega) & Y_{12}(\omega) \\ Y_{21}(\omega) & Y_{22}(\omega) \end{bmatrix} \begin{bmatrix} \tilde{V}_1(\omega) \\ \tilde{V}_2(\omega) \end{bmatrix}. \tag{6.7}$$

where ω is the angular frequency and $\mathcal{F}\{..\}$ is the Fourier transform. The individual matrix elements is computed by exciting the device with a single voltage perturbation [129, 140]:

$$Y_{mn} = \left. \frac{\tilde{I}_m}{\tilde{V}_n} \right|_{\tilde{V}_k=0, k \neq n} = \frac{\mathcal{F}\{I_m(t) - I_m(0)\}}{\mathcal{F}\{V_n(t) - V_n(0)\}}. \tag{6.8}$$

When a step perturbation $V_n(t) = V_n(0) + \Delta V_n \cdot u(t)$ (with u stands for the Heaviside step function) is applied on contact n and zero volts on the rest of terminals, the Y_{mn}

can be simplified by substituting the step perturbation in equation (6.8), as:

$$\begin{aligned}
 Y_{mn} &= \frac{\int_{-\infty}^{\infty} (I_m(t) - I_m(0)) e^{-j\omega t} dt}{\int_{-\infty}^{\infty} (V_n(t) - V_n(0)) e^{-j\omega t} dt} = \frac{\int_0^{\infty} (I_m(t) - I_m(\tau_d) + I_m(\tau_d) - I_m(0)) e^{-j\omega t} dt}{\Delta V_n \cdot \int_{-\infty}^{\infty} u(t) e^{-j\omega t} dt} \\
 &= \frac{(I_m(\tau_d) - I_m(0)) \cdot \int_0^{\infty} e^{-j\omega t} dt}{\Delta V_n \cdot \int_{-\infty}^{\infty} u(t) e^{-j\omega t} dt} + \frac{\int_0^{\infty} (I_m(t) - I_m(\tau_d)) e^{-j\omega t} dt}{\Delta V_n \cdot (\pi\delta(\omega) + \frac{1}{j\omega})} \\
 &= \frac{(I_m(\tau_d) - I_m(0)) \cdot \int_{-\infty}^{\infty} u(t) e^{-j\omega t} dt}{\Delta V_n \cdot \int_{-\infty}^{\infty} u(t) e^{-j\omega t} dt} + \frac{\int_0^{\infty} (I_m(t) - I_m(\tau_d)) e^{-j\omega t} dt}{\Delta V_n \cdot (\pi\delta(\omega) + \frac{1}{j\omega})} \\
 &\approx \frac{\Delta I_m}{\Delta V_n} + \frac{j\omega}{\Delta V_n} \int_0^{\tau_d} (I_m(t) - I_m(\tau_d)) e^{-j\omega t} dt \quad (\omega \neq 0), \tag{6.9}
 \end{aligned}$$

where the Fourier transform of the Heaviside step function is $\mathcal{F}\{u(t)\} = \pi\delta(\omega) + \frac{1}{j\omega}$ and $\Delta I_m = I_m(\tau_d) - I_m(0)$. In expression (6.9), the results $I_m(t) = I_m(\tau_d)$ for $t \geq \tau_d$ and $I_m(t) = I_m(0)$ for $t \leq 0$ are also considered.

The intrinsic cut-off frequency f_T computed from the Y -parameter is the linear frequency at which the current gain magnitude drops to unity (0 dB) [129]:

$$|h_{21}(\omega = 2\pi f_T)| \equiv \frac{|Y_{21}^{All}|}{|Y_{11}^{All}|} \equiv \frac{\mathcal{F}\{I_2(t) - I_2(0)\}}{\mathcal{F}\{I_1(t) - I_1(0)\}} = 1. \tag{6.10}$$

The superindex *All* means that all orders of the Taylor expansions of the Fourier transform in (6.9) are taken into account (without approximations).

The Quasi-static Definition of f_T^{QS}

The expression of f_T^{QS} within the QS approximation is obtained by computing the term Y_{21} from (6.9) without any frequency dependence, $e^{-j\omega t} \approx 0$, as:

$$Y_{21}^{QS}(\omega) \approx \frac{\Delta I_2}{\Delta V_1} \equiv \frac{dI_2}{dV_1} \equiv g_m. \tag{6.11}$$

The term Y_{11} is computed with a zero-order approximation, $e^{-j\omega t} \approx 1$, from (6.9) as:

$$Y_{11}^{QS}(\omega) \approx \frac{j\omega}{\Delta V_1} \int_0^{\tau_d} (I_1(t) - I_1(\tau_d)) dt = j\omega \frac{\Delta Q_1}{\Delta V_1}, \tag{6.12}$$

where ΔQ_1 is defined in (6.3). The approximation in (6.11) is based on the assumption that the current pulse τ_p is short enough to neglect any displacement component of the drain current. Expression (6.12) assumes that the gate current is the displacement component. As indicated in the Introduction, from (6.10), using (6.11) and (6.12), we get:

$$f_T^{QS} = \frac{g_m}{2\pi \Delta Q_1 / \Delta V_1} = \frac{g_m}{2\pi C_1}, \tag{6.13}$$

where the term $\Delta Q_1/\Delta V_1 \equiv C_1$ is usually associated to the gate capacitor [141].

The Zero-Order Non-Quasi-Static Definition of f_T^{NQS}

In order to better include the drain displacement current, it seems more appropriate to use the same zero-order approximation of the exponential term, $e^{-j\omega t} \approx 1$, that we have used for Y_{11} in (6.12), in the computation of Y_{21} from (6.9):

$$\begin{aligned} Y_{21}^{NQS}(\omega) &\approx g_m + \frac{j\omega}{\Delta V_1} \int_0^{\tau_d} (I_2(t) - I_2(\tau_d)) dt \\ &= g_m - j\omega |\Delta Q_2| / \Delta V_1, \end{aligned} \quad (6.14)$$

where ΔQ_2 is also defined in (6.3). Consequently, from (6.10), a NQS estimation of f_T gives [142]:

$$f_T^{NQS} = \frac{g_m}{2\pi \sqrt{\Delta Q_1^2 - \Delta Q_2^2} / \Delta V_1}. \quad (6.15)$$

This is a first step (zero-order Taylor approximation) in the evaluation of f_T^{NQS} beyond the quasi-static approximation.

6.1.2 Conditions for the Validity of the Quasi-Static Estimation of f_T

In the QS approximation, assuming that $\Delta Q_1 \approx \Delta Q_2$ during the transient evolution:

$$\Delta Q_1 \approx \Delta Q_2 \equiv \int_0^{\tau_d} (I_2(t) - I_2(\tau_d)) dt \approx \Delta I_2 \tau_d^{QS}, \quad (6.16)$$

we get the condition $C_1 \Delta V_1 = \Delta Q_1 \approx \Delta Q_2 \approx \Delta I_2 \tau_d^{QS}$ where $\tau_d^{QS} \approx C_1 \Delta V_1 / \Delta I_2$ is the typical QS definition of the intrinsic delay time mentioned in the Section 6.1 when $\Delta V_1 \approx V_{gs}$ giving $\Delta I_2 \approx I_{ds}$. Then, the definition of the (small-signal) transconductance in equation (6.11), with expression (6.16), can be redefined as [136]:

$$g_m \equiv \frac{dI_2}{dV_1} \approx \frac{\Delta I_2}{\Delta V_1} = \frac{\Delta I_2}{\Delta Q_1} \frac{\Delta Q_1}{\Delta V_1} = \frac{1}{\tau_d^{QS}} C_1. \quad (6.17)$$

Putting (6.17) into (6.13), one arrives to the final result:

$$f_T^{QS} = 1 / (2\pi \tau_d^{QS}), \quad (6.18)$$

which is one of the main reasons why f_T^{QS} is interpreted as a relevant FoM on how fast a digital FET works. In summary, the QS approximation is valid whenever the condition $\Delta Q_1 \approx \Delta Q_2$ is satisfied. From (6.5), such condition can be equivalently written as

$\Delta Q_3 \approx 0$. From (6.3), the previous conditions in a transient evolution means that the source current rapidly becomes equivalent to its high value $I_3(t) \approx I_3(\tau_d)$ while the drain current remains low $I_2(t) \approx I_2(0)$ during the intrinsic delay time interval $0 < t < \tau_d$. These conditions are typical in many FETs with a large channel length L where the intrinsic delay time τ_d is much larger than the temporal width of the current pulse generated by one electron τ_p , i.e. $\tau_d > \tau_p$. Then, the total (particle and displacement) current in the drain and source contacts are detected only when electrons cross the surfaces S_2 and S_3 , respectively. However, in FET devices with a short channel length L , one can easily get scenarios with $\tau_d \approx \tau_p$ where an electron moving along the channel generates a time-dependent electric field that is detected as displacement current on the source and drain contacts without even crossing the surfaces S_2 (drain contact) and S_3 (source contact).

In a typical n-type FET, when ΔV_1 is positive, we can expect a positive transient current $I_2(t)$ satisfying $I_2(0) \leq I_2(t) \leq I_2(\tau_d)$, while the current on the source is negative and decreases $I_3(0) \geq I_3(t) \geq I_3(\tau_d)$ because of the signs selected in figure 6.1.1(b). Since we deal with an increment of electrons (negative charge) in the channel, we expect $I_1(t) \geq 0$ in the metal. From (6.3) we get positive ΔQ_1 and ΔQ_3 , while negative ΔQ_2 . Therefore, the expression $\Delta Q_1 + \Delta Q_3 = |\Delta Q_2|$ is achieved, which means $|\Delta Q_1| < |\Delta Q_2|$. This condition will be numerically tested later. Therefore, in the NQS approximation, the definition of f_T^{NQS} in (6.15) can be ill-defined because it deals with a square root of a negative number, that is, the condition $|h_{21}| = 1$ cannot be reached with this zero-order NQS approximation.

We arrive now to a relevant question about the adequacy of f_T as a proper FoM for testing FET speed. *Is it possible to find FETs where the gate phasor current is always smaller than the drain one, even with the exact definition of the Y parameters in (6.10)? This would imply that, contrarily to what it is assumed in the own definition of f_T , the current gain never drops to 0 dB at any frequency.*

6.2 Practical Computations for 2D FETs

In Section 6.1.1, the conditions of validity of f_T^{QS} were discussed. We also pointed out the possibility that the own definition of f_T is ill-defined because there is no guarantee that the gate phasor current becomes higher than the drain phasor current as frequency grows. Next, we provide numerical confirmation of these drawbacks for ballistic nanoscale FETs. First of all, I will give some details about the device structure and the time-dependent simulation performed in the BITLLES simulator.

We will consider dual-gate FETs schematically drawn in figure 6.1.1(a) with a 2D channel material. These 2D materials are expected to improve electron mobility and to

suppress the short channel effect for ultra-scaled devices. In order to simplify the numerical simulations (avoiding extra complications, like Klein tunneling or hole transport, that will obscure the interpretations of our numerical results), we will consider only electron transport in the conduction band of a n-type graphene-like material with a linear energy band $E_{\vec{k}} = \pm \hbar v_f |\vec{k}|$ being $v_f = 5 \times 10^5$ m/s the Fermi velocity and \vec{k} the wave vector which contains the two degrees of freedom $\{k_x, k_z\}$. The permittivity is $\epsilon = 4\epsilon_0$ in the 2D material and $\epsilon = 3.9\epsilon_0$ in dielectrics with ϵ_0 represents the vacuum permittivity. Electron transport will be assumed ballistic (without phonon or impurity scattering) and only the electron-electron interaction through the time-dependent solution of the Poisson equation will be considered. The simulation box will not include the 3D-2D contact resistances and other parasitic elements (which are the well-known frequency bottleneck [4]). Thus, we only simulate the intrinsic performance of FETs.

We will consider FET devices with a width of the current pulse associated to one electron comparable to the intrinsic delay time along the channel, i.e. $\tau_p \approx \tau_d$. These conditions just mean that the channel is short enough and the dielectric relaxation time² large enough so that the displacement current of an electron crossing the channel has to be considered in each terminal even when the electron is in the middle of the channel. The extension L' depicted in figure 6.1.1(a) is present to ensure the proper computation of such displacement current, even when the electrons are outside of the volume Ω . The time-dependent total currents in equation (6.1) are computed with the BITLLES simulator from self-consistent Monte Carlo solutions of the Boltzmann and Poisson equations. The temporal step of the simulations is $\Delta t = 7 \times 10^{-16}$ s. Finally, we notice that all the transient simulations have been repeated many times and the results properly averaged in order to minimize the presence of physical noise [144] (random fluctuations) in the current values. The reasons are to avoid extra non-pertinent complexities in the discussions of the results and to approach experimental S -parameters setups which provide measurements through several periods of the oscillating signals.

6.2.1 Example 1 (Device A): Conditions for the Validity of the Quasi-Static Approximation

As a first example, let us confirm the condition for the validity of the QS approximation. We try to design a device which has the incremental charge $\Delta Q_1 \approx \Delta Q_2$, and check

²The dielectric relaxation time indicates the time needed for a charge to become neutrality in a medium. In electron device modeling, the electron current assigned to metals and semiconductors is the particle component (through drift or diffusion terms), while to dielectrics is the displacement current. Such assignments are justified in terms of the dielectric relaxation time τ_{die} . Each electron moving along the channel generates a time-dependent electric field that can be detected as displacement current in the contacts. In general, electrons try to achieve charge neutrality by screening non-zero electric fields. Therefore, such electric fields are detectable at the contacts during time intervals shorter than τ_{die} [143].

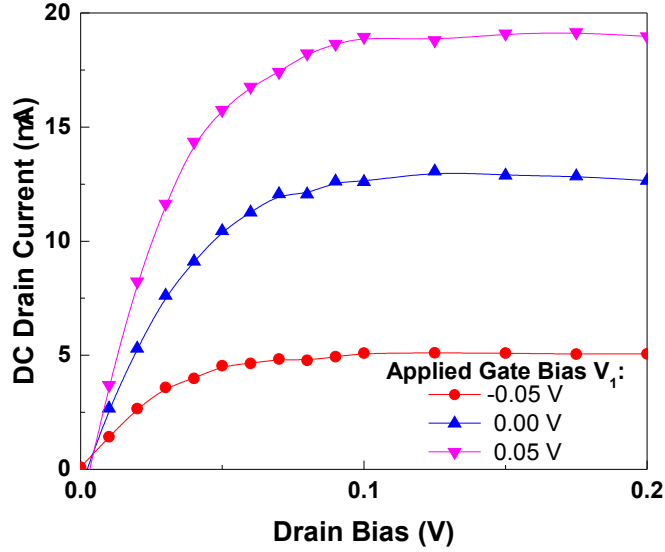


Figure 6.2.1: The output characteristic of device A for different V_1 .

if the cut-off frequency computed from the all-order, QS and NQS approximations are equivalent.

Considering a device A with the volume $\Omega_A = 300 \times (45 + 1 + 45) \times 1125 \text{ nm}^3$ in figure 6.1.1(a) with the 2D material thickness $H = 1 \text{ nm}$ and the gate length $L = 300 \text{ nm}$. In the simulation box, we set spatial steps $\Delta x = 30 \text{ nm}$, $\Delta y = 11.25 \text{ nm}$ and $\Delta z = 225 \text{ nm}$ resulting $22 \times 11 \times 7$ cells. The DC characteristic plotted in figure 6.2.1 is computed by time-averaging the total drain current in (6.1) and by summing the net number of electrons transmitted through the drain surface. Both DC values coincide because the time-averaged displacement current is zero. In any case, such double computation of the drain DC value certifies the correct simulation of the displacement current.

The transient currents in response to a square voltage pulses on the gate contact are indicated in figure 6.2.2. As illustrated in figure 6.1.1(b), since we deal with a small-signal formalism, the evaluation of Y_{21} and Y_{11} is done with a DC bias, $V_2 = 0.1 \text{ V}$, applied between drain and source contacts, and a DC voltage $V_1 = -0.05 \text{ V}$ plus the transient perturbation $\Delta V_1 = 0.1 \text{ V}$ on the gate. In figure 6.2.2, the sum of the total currents on the drain, gate and source contacts of device A maintains consistency with the continuity equation (6.2). The incremental charges (red dashed area in figure 6.2.2) are $\Delta Q_1 = 69.17 \times 10^{-19} \text{ C}$, $\Delta Q_2 = -80.05 \times 10^{-19} \text{ C}$ and $\Delta Q_3 = 17.82 \times 10^{-19} \text{ C}$. Note that, in device A, the incremental charge $\Delta Q_3 \approx 0$ and the $\Delta Q_1 \approx |\Delta Q_2|$, which satisfy the conditions of validity of the QS approximation. Then, let us check if the f_T predicted from the QS approximation is equivalent to that from the all orders and the NQS ones.

The Y parameters changing with frequency in all-order (solid lines), NSQ and QS

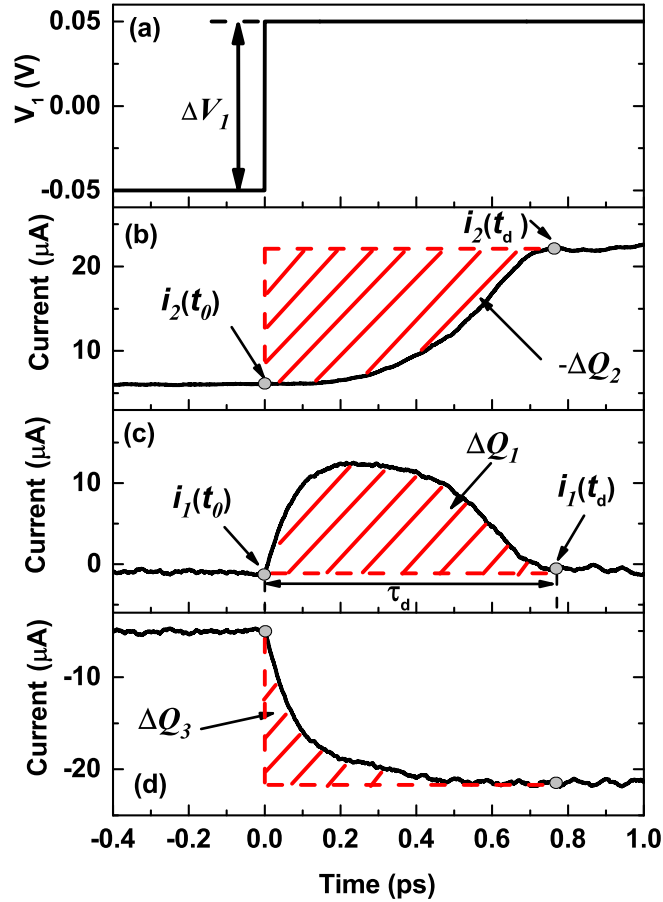


Figure 6.2.2: Total (particle plus displacement) transient currents on the drain (b), gate (c) and source (d) contacts of device A when a square voltage pulses (a) is applied on the gate contacts. $V_2 = 0.1$ V.

models (dashed lines) for device A are plotted in figure 6.2.3. In the all-order model, for frequencies high enough, the absolute value of Y_{21}^{All} shows strong frequency dependency and the $|Y_{11}^{All}|$ is no longer linearly increasing with the frequency, which is qualitatively identical to the experimental observations [141]. The lines of $|Y_{21}^{All}|$ and $|Y_{11}^{All}|$ cross at $f_T = 0.39$ THz. Using the QS approximation in expression (6.13), we get $f_T^{QS} = 0.39$ THz, which is exactly the same value as $f_T = 0.39$ THz. In the NQS approximation, since $\Delta Q_1^2 < \Delta Q_2^2$, there is no solution to the f_T in non-quasi-static case. This result can also be understood from (6.14) indicating that $|\Delta Q_2|$ controls the frequency slope of Y_{21}^{NQS} at high enough frequencies. Similarly, from (6.12), the slope of Y_{11}^{QS} is controlled by the ΔQ_1 . Since $\Delta Q_1 < |\Delta Q_2|$, the terms Y_{21}^{NQS} and Y_{11}^{QS} never cross as can be seen in figure 6.2.3. Surprisingly, the (zero-order) NQS model is even worse than the QS one.

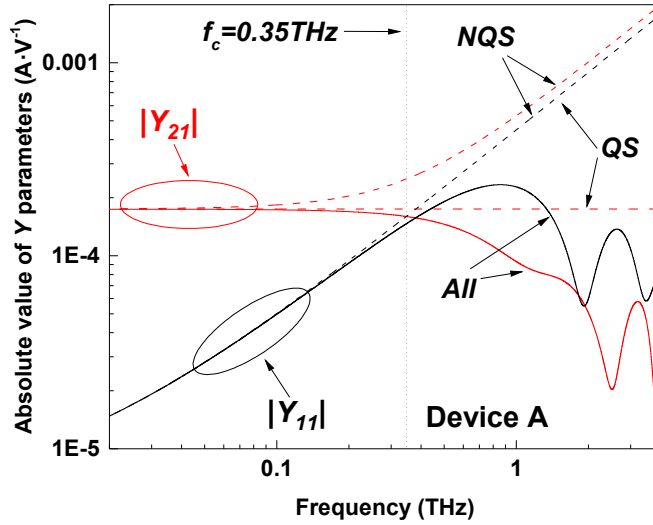


Figure 6.2.3: The Y parameters computed from the time-dependent simulation of the total (particle plus displacement) currents in device A using three different expressions. In solid lines, taken into account all orders (*All*) and in dashed lines with the NQS or the QS approximations.

6.2.2 Example 2 (Device B and Device C): Limitations of the Quasi-Static Approximation

Device B

We consider device B with a volume $\Omega_B = 100 \times (45 + 1 + 45) \times 1125 \text{ nm}^3$ in figure 6.1.1(a) with the 2D material thickness $H = 1 \text{ nm}$ and the gate length $L = 100 \text{ nm}$. In the simulation box, we set spatial steps $\Delta x = 10 \text{ nm}$, $\Delta y = 11.25 \text{ nm}$ and $\Delta z = 225 \text{ nm}$ resulting $22 \times 11 \times 7$ cells. The DC characteristic is plotted in figure 6.2.4 where no short channel effects appear. The transient currents in response to two square voltage pulses on the gate contact are indicated in figure 6.2.5. In this simulation, a DC bias, $V_2 = 0.1 \text{ V}$, is applied between drain and source contacts, and a DC voltage $V_1 = -0.05 \text{ V}$ plus the transient perturbation $\Delta V_1 = 0.1 \text{ V}$ is applied on the gate. The sum of the total currents in figure 6.2.5 maintains consistency with the continuity equation (6.2).

In figure 6.2.6, the solid lines are the $|Y_{21}^{All}|$ and $|Y_{11}^{All}|$ computed exactly from (6.9) as a function of frequency. For frequencies higher enough, the absolute value of Y_{21}^{All} shows strong frequency dependency and the $|Y_{11}^{All}|$ is no longer linearly increasing with the frequency. The values of $|Y_{21}^{All}|$ and $|Y_{11}^{All}|$ become equal at $f_T = 1.31 \text{ THz}$. Using the QS approximation in expression (6.13), we get $f_T^{QS} = 1.45 \text{ THz}$, which is similar to the previous value $f_T = 1.31 \text{ THz}$. In the NQS approximation, the formula (6.15) requires the restriction $|\Delta Q_1| > |\Delta Q_2|$. As illustrated in figure 6.2.5 (red dashed area),

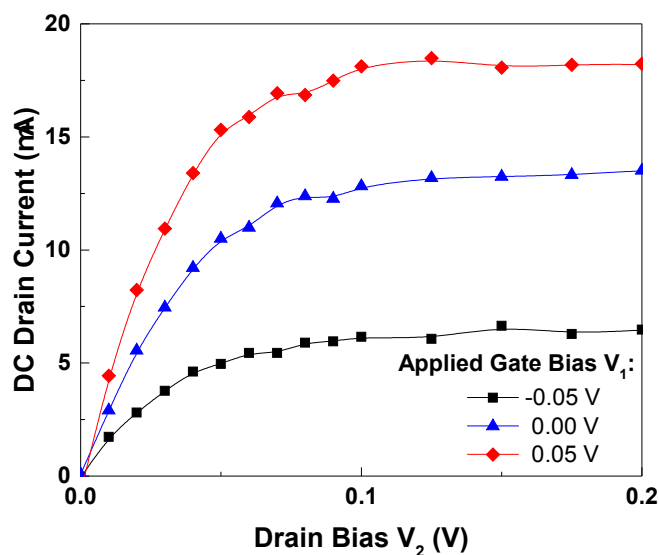


Figure 6.2.4: The output characteristic of device B for different V_1 .

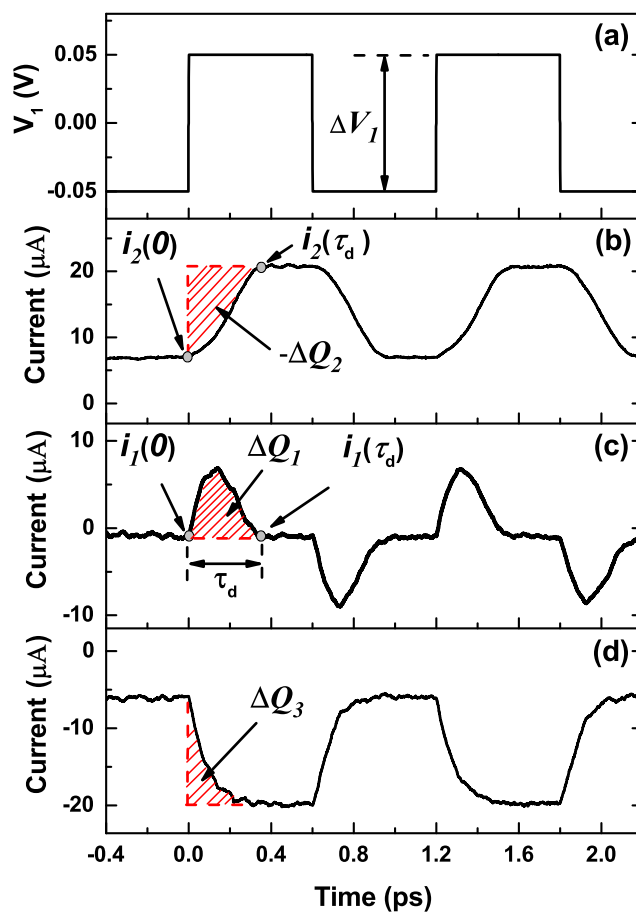


Figure 6.2.5: Total (particle plus displacement) transient currents on the drain (b), gate (c) and source (d) contacts of device B when a sequence of square voltage pulses (a) is applied on the gate contacts. $V_2 = 0.1$ V.

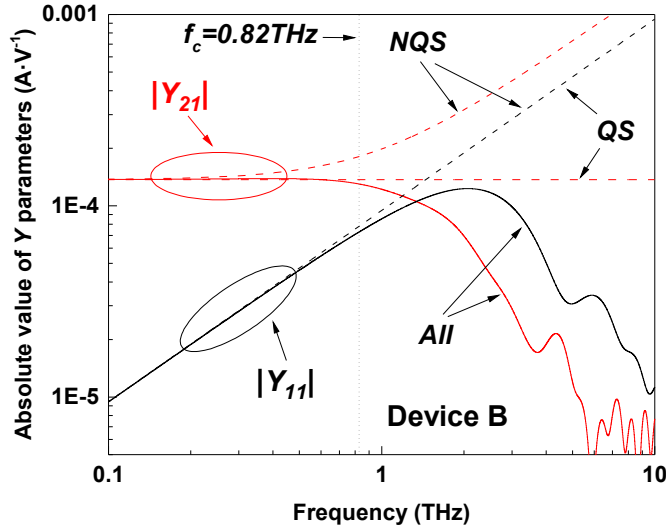


Figure 6.2.6: The Y parameters computed from the time-dependent simulation of the total (particle plus displacement) currents in device B using three different expressions. In solid lines, taken into account all orders (*All*) and in dashed lines with the NQS or the QS approximations.

$\Delta Q_1 = 11.62 \times 10^{-19}$ C, $\Delta Q_2 = -26.53 \times 10^{-19}$ C and $\Delta Q_3 = 14.91 \times 10^{-19}$ C. The result $\Delta Q_1 < |\Delta Q_2|$ is coincident with what we anticipated in Section 6.1.1 that no solution is obtained for the f_T in NQS case.

The errors when neglecting the displacement current in the computation of f_T^{QS} can be quantified from expression (6.14). The elimination of the drain displacement current can be justified for those frequencies satisfying that g_m is larger or equal than the $\omega|\Delta Q_2|/\Delta V_1$. By imposing the previous condition, $g_m \approx 2\pi f_c|\Delta Q_2|/\Delta V_1$, we get a definition of the maximum frequency f_c where the drain displacement current can be reasonably neglected:

$$f_c = \frac{g_m}{2\pi|\Delta Q_2|/\Delta V_1}. \quad (6.19)$$

However, since we have demonstrated in equation (6.5) that $|\Delta Q_2| > \Delta Q_1$, we always get $f_c < f_T^{QS}$ which can be seen in figure 6.2.6 where solid lines (*All*) start to deviate from dashed lines (*QS*) at $f_c = 0.82$ THz $< f_T^{QS} = 1.45$ THz. Notice that the condition $\Delta Q_1 \approx \Delta Q_2$ in (6.19) implies that $f_c \approx f_T^{QS}$ justifying the arguments on the range of validity of f_T^{QS} mentioned in Section 6.1.1.

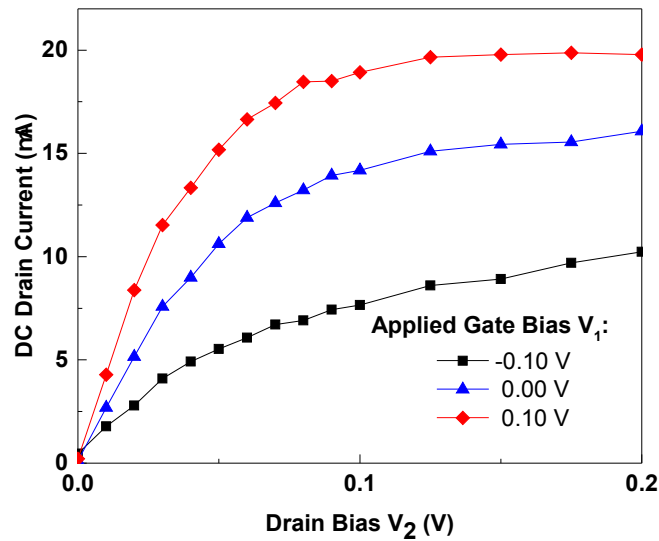


Figure 6.2.7: The current-voltage characteristic of device C for different V_1 .

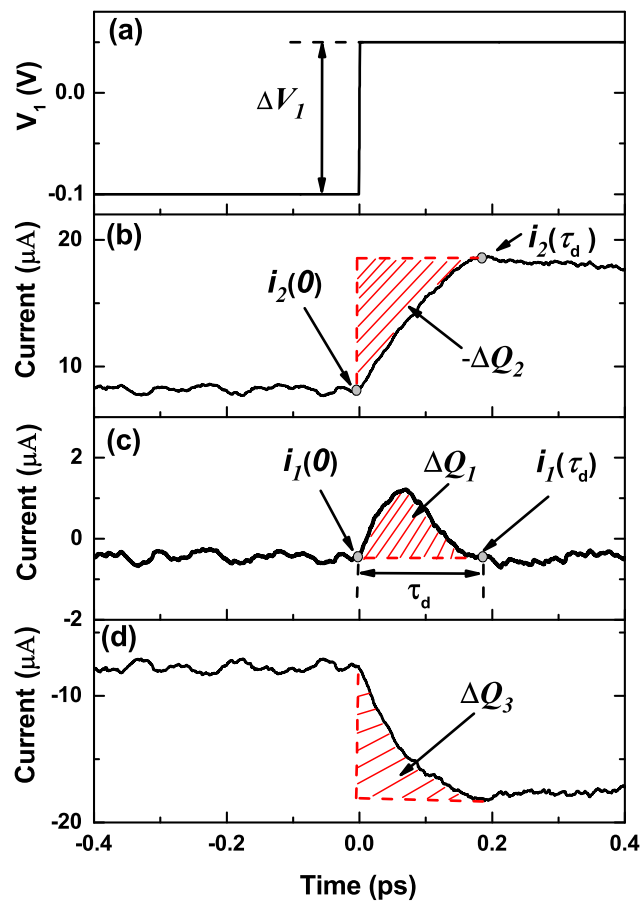


Figure 6.2.8: The total (particle plus displacement) transient currents on the drain (b), gate (c) and source (d) contacts of device C in response to a step voltage perturbation (a) on the gate contacts. $V_2 = 0.1$ V.

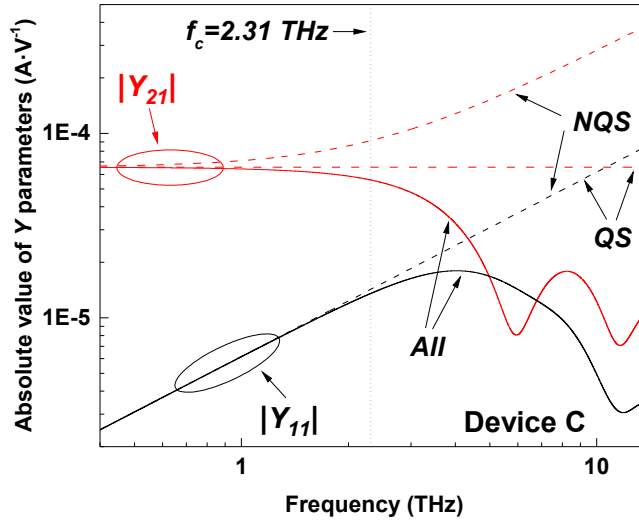


Figure 6.2.9: The Y parameters computed from time-dependent simulation of the total currents in device C using three different expressions (as in figure 6.2.6).

Device C

The QS approximation seems to imply that a desired condition for a fast FET is $\Delta Q_1 \rightarrow 0$ ($C_1 \rightarrow 0$) if short channel effects are still under control. Such condition would imply that $f_T^{QS} = g_m / (2\pi\Delta Q_1 / \Delta V_1) = g_m / (2\pi C_1) \rightarrow \infty$ in equation (6.13) and $\tau_d^{QS} \approx C_1 \Delta V_1 / \Delta I_2 \approx \Delta Q_1 / \Delta I_2 \rightarrow 0$. We consider a new design (device C) with the goal of getting $C_1 \rightarrow 0$. In particular we consider the same FET of figure 6.1.1(a) with the geometry $\Omega_C = 20 \times (45 + 1 + 45) \times 700 \text{ nm}^3$ (gate length $L = 20 \text{ nm}$) under the same type of simulation as in device A. In the simulation box, we set spatial steps $\Delta x = 2 \text{ nm}$, $\Delta y = 11.25 \text{ nm}$ and $\Delta z = 140 \text{ nm}$ resulting $22 \times 11 \times 7$ cells. We plot the DC current-voltage characteristic of device C in Fig 6.2.7. In spite of the small capacitance, the short channel effects are reasonably under control. We use $V_2 = 0.1 \text{ V}$, applied between drain and source contacts, and $V_1 = -0.1 \text{ V}$ plus the transient perturbation $\Delta V_1 = 0.15 \text{ V}$ on the gate. The total transient currents on the drain, gate and source contacts of device C due to a step voltage perturbation in the gate are plotted in figure 6.2.8, where the sum of the total currents also maintains consistency with the continuity equation (6.2). Moreover, the incremental charge $\Delta Q_1 = 1.54 \times 10^{-19} \text{ C}$, $\Delta Q_2 = -6.76 \times 10^{-19} \text{ C}$ and $\Delta Q_3 = 5.24 \times 10^{-19} \text{ C}$.

The Y parameters changing with frequency in all orders (solid lines), NQS and QS models (dashed lines) for device C are plotted in figure 6.2.9. In the QS estimation, because the $|\Delta Q_1|$ in device C becomes smaller than that of device B, the Y_{11}^{QS} is shifted towards the horizontal axis, therefore, the QS value of the cut-off frequency increases giving $f_T^{QS} = 10.64 \text{ THz}$. The behaviors of NQS for device C and device B are similar. In the all orders model, the condition $|h_{21}| = 1$ is satisfied at $f_T = 4.97 \text{ THz}$. The

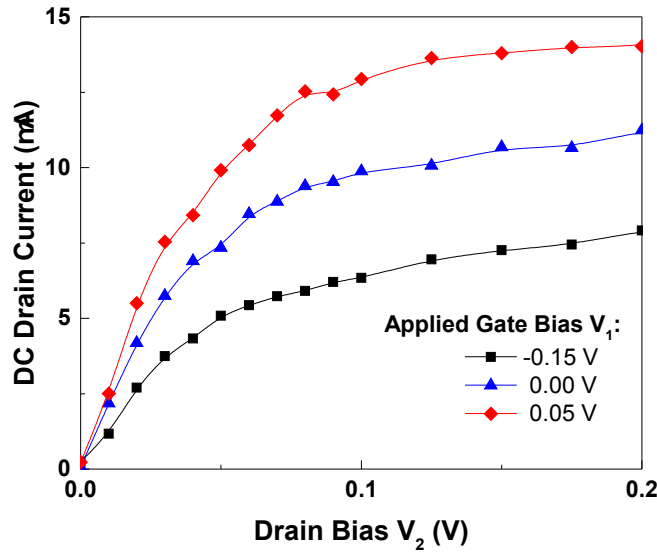


Figure 6.2.10: The current-voltage characteristic of device D for different V_1 .

oscillations of Y_{11}^{All} and Y_{21}^{All} at higher frequencies are the Fourier transform of time-dependent variations of the total currents in figure 6.2.8, which can be associated to plasmonic oscillations with shorter periods than the value of τ_d plotted there. So the exact value of the f_T is randomly influenced by such oscillations. We have assumed an ideal metallic contact (dielectric relaxation time equals to zero) in all simulations. One can expect significantly different randomness in the oscillations of the Y parameters at high frequency for heavily doped contacts [145]. The problem present in device C is that the real frequency where the device stops working properly is much lower than $f_T^{QS} = 10.64$ THz and $f_T = 4.97$ THz.

6.2.3 Example 3 (Device D): the Infinite Value of f_T

To go a step further, we design a device D which has volume $\Omega_D = 20 \times (45 + 1 + 45) \times 200$ nm³ (gate length $L = 20$ nm). The DC current is plotted in figure 6.2.10, which indicates the ability of the gate to control the channel. In the transient current plotted in figure 6.2.11 in response to a step voltage perturbation, we get the incremental charge $\Delta Q_2 = -4.33 \times 10^{-19}$ C, $\Delta Q_3 = 3.45 \times 10^{-19}$ C and $\Delta Q_1 = 0.9 \times 10^{-19}$ C. The ΔQ_1 approaches to 0. The Y parameters are plotted in figure 6.2.12. The QS result $f_T^{QS} = 13.43$ THz is quite far from the maximum frequency $f_c = 2.68$ THz. It is relevant to emphasize that the condition $|h_{21}| = 1$ is never satisfied in the whole THz window for the all orders model, i.e. the $|Y_{21}^{All}|$ and $|Y_{11}^{All}|$ never cross, showing a misleading result $f_T = \infty$. Certainly, the real nano FET stops working properly at some frequency.

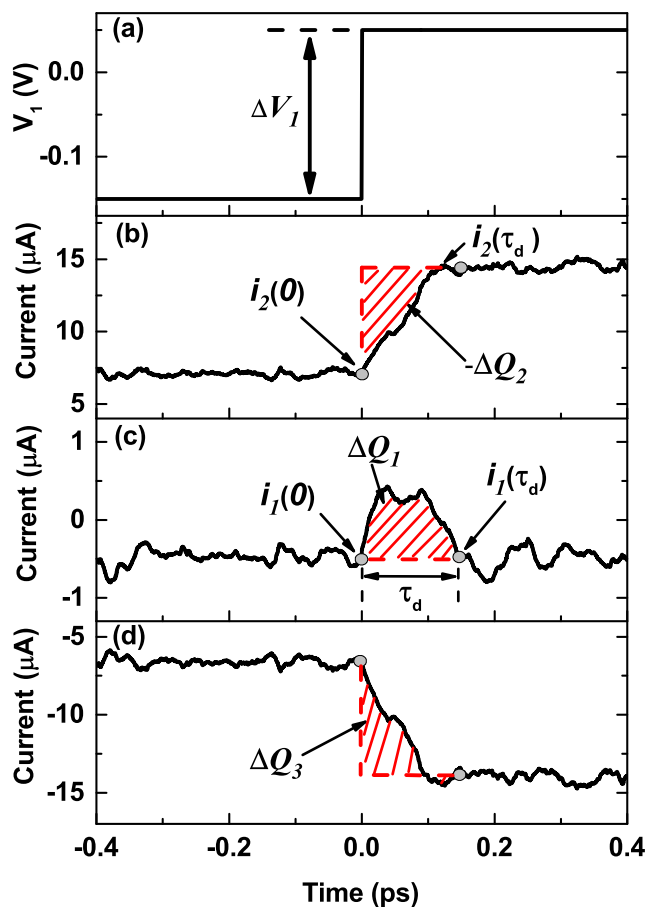


Figure 6.2.11: The total (particle plus displacement) transient currents on the drain (b), gate (c) and source (d) contacts of device D in response to a step voltage perturbation (a) on the gate contacts. $V_2 = 0.1$ V.

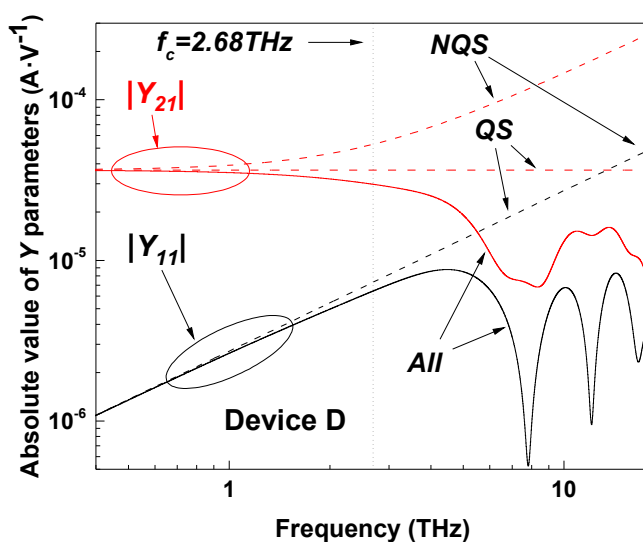


Figure 6.2.12: The Y parameters computed from time-dependent simulation of the total currents in device D using three different expressions (as in figure 6.2.6).

To understand the real speed limitation of devices C and D, let us notice that the simulations in figures 6.2.5, 6.2.8 and 6.2.11 can be interpreted in two different ways. First, as we have done up to here, the currents are the FET response to a step voltage perturbation needed for computing the small-signal Y -parameter in a linear system. Second, they can be identically interpreted as the current response when the gate change from the digital voltage ‘0’ to ‘1’. Then, the time τ_d defined in expression (6.3) is directly related to the intrinsic delay time τ_d discussed in the Introduction as a FoM for digital electronics. In other words, the two pulses in Figs. 6.2.5(a) can be understood as the input digital signal and the drain currents as the output digital signals. Certainly, the FETs are not properly switched-off in our small-signal simulations, and a large-signal simulation will be needed, in principle. However, the present simulations are enough to compare the different FET speed estimators. The relation between the input and output signals in figures 6.2.5, 6.2.8 and 6.2.11 can be modeled from linear system theory. It is clear that the relevant frequencies are inversely proportional to the time interval τ_d . A reasonable expression could be $f_T^d \approx 1/(2\tau_d)$ [146] [147].

In device B, from figure 6.2.5, we get a value of the intrinsic delay time $\tau_d = 0.352$ ps, resulting $f_T^d = 1.42$ THz, which is similar to the QS cut-off frequencies $f_T^{QS} = 1.45$ THz. However, in device C, from figure 6.2.8, we get a simulated $\tau_d = 0.185$ ps giving $f_T^d = 2.70$ THz, which is much smaller than the value $f_T^{QS} = 10.64$ THz. In device D, the result is even worse where the intrinsic delay time is $\tau_d = 0.138$ ps providing $f_T^d = 3.62$ THz. The reason why the QS expression (6.13) does not capture the real intrinsic delay time in devices C and D is because the approximation $\Delta Q_2 \approx \Delta Q_1$ is no longer true. In fact, since we looked for $\Delta Q_1 \rightarrow 0$, the result $\Delta Q_2 \gg \Delta Q_1$ gives f_T^{QS} in (6.13) much larger than f_c in (6.19). Let us notice that the QS estimation of the intrinsic delay time is again clearly misleading. In device C, we get $\tau_d^{QS} \approx C_1 \Delta V_1 / \Delta I_2 \approx 0.015$ ps, which is more than one order of magnitude larger than our simulated value $\tau_d = 0.185$ ps (the ratio τ_d / τ_d^{QS} is different from f_T^d / f_T^{QS} because of the factor π in (6.18)). In device D, the $\tau_d^{QS} \approx 0.012$ ps is also more than one order of magnitude larger than the simulated value $\tau_d = 0.138$ ps. The reason of this discrepancy is also the condition $\Delta Q_2 \gg \Delta Q_1$, which invalidates the QS estimation discussed in Section 6.1.1.

In conclusion, we have established the condition for the validity of the QS approximation of f_T^{QS} in terms of the electrical current and electrical flux on the gate, drain and source FET terminals defined in expressions (6.1) and (6.3). Such approximation is applicable when $\Delta Q_1 \approx \Delta Q_2$ which means that we are dealing with FETs where the intrinsic delay time is much larger than the temporal width of the current pulse generated by one electron, i.e. $\tau_d > \tau_p$ (with large channel length L as in device A). On the contrary, in devices where $\tau_d \approx \tau_p$ (i.e. as in devices C and D with short channel

length L), the QS approximation is not applicable because the electric field generated by electrons are not screened inside the device active region, and its associated displacement current becomes relevant during all the time while the electron is traversing the channel. We have shown through analytical arguments supported by numerical simulations that the estimations of the intrinsic cut-off frequency based on $|h_{21}| = 1$ (with the QS f_T^{QS} , zero-order NQS f_T^{NQS} or without approximations f_T) can provide misleading results for the speed of FETs. This problem is specially severe for nanoscale FETs which are routinely modeled from quantum transport simulators. The explicit quantum simulation of the time-dependent displacement current and τ_d demand such huge amount of computational resources [42, 119, 145] that the intrinsic FoM of the speed of such ballistic FET are routinely taken from QS estimations. As shown in some examples in this work, such type of QS estimations can erroneously predict the FET speed by one order of magnitude. Other examples show no finite value of f_T underlying an important limitation of the traditional definition of f_T to properly quantify the speed of FETs. When parasitic elements are included in the simulation, one can expect a tendency to recover the validity of the QS approximation (τ_d grows and τ_p remains the same) at the price of getting lower FET speed than its intrinsic value.

CHAPTER 7

Conclusions

In this dissertation, I have presented a simulation model (by tackling the fundamental issue of the measurement problem and the practical issue of the many-body problem) for the quantum nanodevices working at THz frequencies in term of accurate computation of the displacement current. As practical examples, this model has been utilized to compute the high frequency behaviors of transistors based on graphene and other 2D materials.

In the first **Chapter 1**, firstly, I have briefly mentioned some important milestones of the evolution of electronics since its birth at the beginning of the twentieth century. Nowadays, transistors have reached nanoscale range with their working frequencies extended to THz range. Electron transport in the nanoelectronics has approached the regime of quantum transport, at which some relevant quantum effects have to be taken into account, for instance, the many-body problem, the measurement problem and the dissipative transport. Thus, in the next Section 1.2, I have presented the importance of the displacement current in the proper prediction of electron transport behaviour in high-frequency regime from a computational point of view. In Section 1.3, the fundamental issue in the quantum simulation—the many-body problem—has been discussed. In particular, some approaches (for example, the open system, the stochastic injection, the collisions) are briefly mentioned in solving the many-particle Schrödinger equation for the application to quantum transport (i.e., the computation of the current in an electronic device) in the following.

Up to here, it is mandatory to mention another fundamental issue in the computation of quantum transport—the measurement problem. In fact, the measurement problem is an *intrinsic* issue since the beginning of the quantum theory. This problem can be relax in the computation of DC current where only one measurement is enough. Since I deal with the quantum transport in the THz range where more than twice measurements of the system during the whole evolution are required, the measurement problem which has been explicitly discussed in **Chapter 2**, becomes a relevant part in this dissertation. The prediction of the DC and AC current behaviours of an electronic device has been discussed with the orthodox and Bohmian approaches.

In this **Chapter 3**, the literature relating to the irreversible boundary conditions for open system has been considered. First of all, the explanation of the irreversible boundary conditions has been explicitly presented. The picture of particles entering into the open system depends on the reservoir and of particles flowing out of the system depends on the dynamical evolution of the system itself, is relevant for the open system, which requires the dissipative scatterings to make a proper prediction. However, the irreversible boundary conditions have limitations (i.e., non-diagonal injection, uniqueness solutions) in the time-independent scenario. On the contrary, all the problems disappear when we inject wave packet into the open system in time-dependent picture. Such wave packet is described by the conditional wave function—wave function used to describe states in open system. Furthermore, the effect of the energy spectrum (linear band and parabolic band structures) on the injection has been discussed. As a last step, the implementation of the irreversible boundary conditions to the BITLLES simulator has been presented.

In **Chapter 4**, firstly, the use of the Boltzmann collision operator for dissipative quantum transport has been analyzed. Its mathematical role on the description of the time-evolution of the density matrix during a collision can be understood as processes of adding and subtracting states. We have shown that unphysical results (i.e., negative values of the charge density) can be present in quantum simulations when the old states (that built the density matrix associated to an open system before the collision) are different from the additional states generated by the Boltzmann collision operator. This unphysical feature disappears when the Boltzmann collision operator generates states that were already present in the density matrix of the quantum system before the collision, which only requires the exact knowledge, at all times, of the states that build the density matrix of the open system. As a practical application, I have discussed how to compute the dissipative transport with conditional wave functions and its application to a resonant tunneling device. With our scattering approach, we can have an exact description of realistic stochastic sources of dissipation (effective collision rates of acoustic phonon, optical phonon and impurities).

A practical computation of high-frequency behaviour of FETs, in particular, graphene devices, has been analyzed from a careful simulation of the time-dependent particle and displacement currents in **Chapter 5**. From such currents, the power spectral density of the total current fluctuations has been computed at the source, drain and gate contacts. The roles of the lateral dimensions of the transistors, the Klein tunneling and the positive-negative energy injection on the PSD have been carefully analyzed. Through the comparison of the PSD with and without Band-to-Band tunneling and graphene injection, we have shown that the unavoidable Klein tunneling and positive-negative energy injection in graphene structures imply an increment of noise without similar increment on the current, degrading the (either low or high frequency) signal-to-noise ratio. Finally,

we have proved that the shorter the vertical height (in comparison with the length of the active region in the transport direction), the larger the maximum frequency of the PSD. As a byproduct of this result, an alternative strategy (without length scaling) to optimize the intrinsic cut-off frequency of graphene transistors will be envisioned

Finally, in **Chapter 6**, the definition of the intrinsic cut-off frequency (f_T) based on the current gain equals to one (0 dB) has been critically analyzed. A condition for the validity of the quasi-static estimation of f_T has been established in terms of the temporal variations of the electric charge and electric flux on the drain, source and gate terminals. Due to the displacement current, an electron traversing the channel length generates a current pulse of finite temporal width. For electron devices where the intrinsic delay time of the current after a transient perturbation is comparable to such width, the displacement currents cannot be neglected and the quasi-static approximation becomes inaccurate. As the first example, we have performed some simulations to conform the validity of the quasi-static approximation. Then, We have presented numerical results for some ballistic transistors where the estimation of f_T under the quasi-static approximation can be one order of magnitude larger than predictions obtained from a time-dependent numerical simulations of the intrinsic delay time (including particle and displacement currents). In other ballistic transistors, we have shown that the gate current phasor can be smaller than the drain one at all frequencies, giving no finite value for f_T .

Finally, let us complete the thesis with some further investigations. As we have mentioned in Chapter 6, the maximum oscillation frequency f_{max} is a more relevant figure of merit in high-frequency analogy applications. Following the work done in Chapter 6, an investigation of the f_{max} of nanodevices based on 2D materials will be performed. We envision that similar arguments in Chapter 6 will be achieved in the f_{max} when including the input and output resistances in the simulated transistors. In addition, the accurate inclusion of the quantum dissipation (in Chapter 4), irreversible spatial boundary conditions (in Chapter 3), noise computation and high-frequency displacement currents (in Chapter 2) into the time-dependent BITLLES simulator (compatible with electron-electron interaction beyond mean field [148], exchange (fermion) interactions [114, 149]) provides a complete quantum simulation framework for the electron transport at all frequencies. Based on such versatile and powerful simulator, simulations of realistic devices based on 2D materials will be performed to understand experiment results and to optimize device performance.

Bibliography

- [1] F. Schwierz, J. Pezoldt, and R. Granzner, “Two-dimensional materials and their prospects in transistor electronics,” *Nanoscale*, vol. 7, no. 18, pp. 8261–8283, 2015.
- [2] G. E. Moore, “Cramming more components onto integrated circuits,” *Proceedings of the IEEE*, vol. 86, no. 1, pp. 82–85, 1998.
- [3] F. Schwierz, “Graphene transistors: status, prospects, and problems,” *Proceedings of the IEEE*, vol. 101, no. 7, pp. 1567–1584, 2013.
- [4] F. Schwierz, “Graphene transistors,” *Nature nanotechnology*, vol. 5, no. 7, pp. 487–496, 2010.
- [5] G. Fiori, F. Bonaccorso, G. Iannaccone, T. Palacios, D. Neumaier, A. Seabaugh, S. K. Banerjee, and L. Colombo, “Electronics based on two-dimensional materials,” *Nature nanotechnology*, vol. 9, no. 10, pp. 768–779, 2014.
- [6] D. Logoteta, G. Fiori, and G. Iannaccone, “Graphene-based lateral heterostructure transistors exhibit better intrinsic performance than graphene-based vertical transistors as post-CMOS devices,” *Scientific reports*, vol. 4, 2014.
- [7] D. K. Ferry, M. J. Gilbert, and R. Akis, “Some considerations on nanowires in nanoelectronics,” *IEEE Transactions on Electron Devices*, vol. 55, no. 11, pp. 2820–2826, 2008.
- [8] A. H. C. Neto, F. Guinea, N. M. R. Peres, K. S. Novoselov, and A. K. Geim, “The electronic properties of graphene,” *Reviews of modern physics*, vol. 81, no. 1, pp. 109, 2009.
- [9] A. K. Geim, “Graphene: status and prospects,” *science*, vol. 324, no. 5934, pp. 1530–1534, 2009.
- [10] F. Schwierz, “Electronics: Industry-compatible graphene transistors,” *Nature*, vol. 472, no. 7341, pp. 41–42, 2011.

- [11] R. Sordan and A. C. Ferrari, "Gigahertz multi-transistor graphene integrated circuits," in *Electron Devices Meeting (IEDM), 2013 IEEE International*. IEEE, 2013, pp. 1–1.
- [12] I. Meric, N. Baklitskaya, P. Kim, and K. L. Shepard, "RF performance of top-gated, zero-bandgap graphene field-effect transistors," in *Electron Devices Meeting, 2008. IEDM 2008. IEEE International*. IEEE, 2008, pp. 1–4.
- [13] Y.-M. Lin, C. Dimitrakopoulos, K. A. Jenkins, D. B. Farmer, H.-Y. Chiu, A. Grill, and Ph. Avouris, "100-GHz transistors from wafer-scale epitaxial graphene," *Science*, vol. 327, no. 5966, pp. 662–662, 2010.
- [14] L. Liao, Y.-C. Lin, M. Bao, R. Cheng, J. Bai, Y. Liu, Y. Qu, K. L. Wang, Y. Huang, and X. Duan, "High-speed graphene transistors with a self-aligned nanowire gate," *Nature*, vol. 467, no. 7313, pp. 305–308, 2010.
- [15] R. Cheng, J. Bai, L. Liao, H. Zhou, Y. Chen, L. Liu, Y.-C. Lin, S. Jiang, Y. Huang, and X. Duan, "High-frequency self-aligned graphene transistors with transferred gate stacks," *Proceedings of the National Academy of Sciences*, vol. 109, no. 29, pp. 11588–11592, 2012.
- [16] B. Radisavljevic, A. Radenovic, J. Brivio, V. Giacometti, and A. Kis, "Single-layer MoS₂ transistors," *Nature nanotechnology*, vol. 6, no. 3, pp. 147–150, 2011.
- [17] "The International Technology Roadmap for Semiconductors, <http://www.itrs.net>," .
- [18] K. S. Novoselov, D. Jiang, F. Schedin, T. J. Booth, V. V. Khotkevich, S. V. Morozov, and A. K. Geim, "Two-dimensional atomic crystals," *Proceedings of the National Academy of Sciences of the United States of America*, vol. 102, no. 30, pp. 10451–10453, 2005.
- [19] H. Liu and D. Y. Peide, "MoS₂ Dual-Gate MOSFET with Atomic-Layer-Deposited Al₂O₃ as Top-Gate Dielectric," *IEEE Electron Device Letters*, vol. 33, no. 4, pp. 546–548, 2012.
- [20] L. Liu, S. B. Kumar, Y. Ouyang, and J. Guo, "Performance limits of monolayer transition metal dichalcogenide transistors," *IEEE Transactions on Electron Devices*, vol. 58, no. 9, pp. 3042–3047, 2011.
- [21] Y. Yoon, K. Ganapathi, and S. Salahuddin, "How good can monolayer MoS₂ transistors be?," *Nano letters*, vol. 11, no. 9, pp. 3768–3773, 2011.

- [22] V. Sverdlov, E. Ungersboeck, H. Kosina, and S. Selberherr, “Current transport models for nanoscale semiconductor devices,” *Materials Science and Engineering: R: Reports*, vol. 58, no. 6, pp. 228–270, 2008.
- [23] S. G. Kim, M. Luisier, A. Paul, T. B. Boykin, and G. Klimeck, “Full three-dimensional quantum transport simulation of atomistic interface roughness in silicon nanowire FETs,” *IEEE Transactions on Electron Devices*, vol. 58, no. 5, pp. 1371–1380, 2011.
- [24] J. Zheng, L. Wang, R. Quhe, Q. Liu, H. Li, D. Yu, W.-N. Mei, J. Shi, Z. Gao, and J. Lu, “Sub-10 nm gate length graphene transistors: operating at terahertz frequencies with current saturation,” *Scientific reports*, vol. 3, pp. 1314, 2013.
- [25] A. Chanana, A. Sengupta, and S. Mahapatra, “Performance analysis of boron nitride embedded armchair graphene nanoribbon metal–oxide–semiconductor field effect transistor with stone wales defects,” *Journal of Applied Physics*, vol. 115, no. 3, pp. 034501, 2014.
- [26] F. Xia, V. Perebeinos, Y.-M. Lin, Y. Wu, and P. Avouris, “The origins and limits of metal-graphene junction resistance,” *Nature nanotechnology*, vol. 6, no. 3, pp. 179–184, 2011.
- [27] S. Ramo, “Currents induced by electron motion,” *Proceedings of the IRE*, vol. 27, no. 9, pp. 584–585, 1939.
- [28] W. Shockley, “Currents to conductors induced by a moving point charge,” *Journal of applied physics*, vol. 9, no. 10, pp. 635–636, 1938.
- [29] G. Cavalleri, E. Gatti, G. Fabri, and V. Svelto, “Extension of Ramo’s theorem as applied to induced charge in semiconductor detectors,” *Nuclear Instruments and Methods*, vol. 92, no. 1, pp. 137–140, 1971.
- [30] P. O. Lauritzen, “Noise due to generation and recombination of carriers in p-n junction transition regions,” *IEEE Transactions on Electron Devices*, vol. 15, no. 10, pp. 770–776, 1968.
- [31] B. Pellegrini, “Electric charge motion, induced current, energy balance, and noise,” *Physical Review B*, vol. 34, no. 8, pp. 5921, 1986.
- [32] C. Cohen-Tannoudji and B. Diu, “Quantum mechanics, vol. I,” 1977.
- [33] D. Querlioz and P. Dollfus, *The Wigner Monte-Carlo Method for Nanoelectronic Devices: A Particle Description of Quantum Transport and Decoherence*, John Wiley & Sons, 2013.

- [34] P. A. M. Dirac, “Quantum mechanics of many-electron systems,” in *Proceedings of the Royal Society of London A: Mathematical, Physical and Engineering Sciences*. The Royal Society, 1929, vol. 123, pp. 714–733.
- [35] M. Born and R. Oppenheimer, “Zur quantentheorie der molekeln,” *Annalen der Physik*, vol. 389, no. 20, pp. 457–484, 1927.
- [36] C. Kittel, *Introduction to solid state*, vol. 162, John Wiley & Sons, 1966.
- [37] P. Hohenberg and W. Kohn, “Inhomogeneous electron gas,” *Physical review*, vol. 136, no. 3B, pp. B864, 1964.
- [38] W. Kohn and L. J. Sham, “Self-consistent equations including exchange and correlation effects,” *Physical review*, vol. 140, no. 4A, pp. A1133, 1965.
- [39] D. R. Hartree, “The wave mechanics of an atom with a non-Coulomb central field. part I. theory and methods,” in *Mathematical Proceedings of the Cambridge Philosophical Society*. Cambridge Univ Press, 1928, vol. 24, pp. 89–110.
- [40] D. R. Hartree, “The wave mechanics of an atom with a non-Coulomb central field. part II. some results and discussion,” in *Mathematical Proceedings of the Cambridge Philosophical Society*. Cambridge Univ Press, 1928, vol. 24, pp. 111–132.
- [41] V. Fock, “Näherungsmethode zur lösung des quantenmechanischen mehrkörperproblems,” *Zeitschrift für Physik*, vol. 61, no. 1-2, pp. 126–148, 1930.
- [42] X. Oriols, “Quantum-trajectory approach to time-dependent transport in mesoscopic systems with electron-electron interactions,” *Physical review letters*, vol. 98, no. 6, pp. 066803, 2007.
- [43] T González, J Mateos, D Pardo, L Varani, and L Reggiani, “Injection statistics simulator for dynamic analysis of noise in mesoscopic devices,” *Semiconductor science and technology*, vol. 14, no. 11, pp. L37, 1999.
- [44] M. Planck, *Treatise on thermodynamics*, Courier Corporation, 2013.
- [45] W. R. Frensley, “Boundary conditions for open quantum systems driven far from equilibrium,” *Reviews of Modern Physics*, vol. 62, no. 3, pp. 745, 1990.
- [46] R. P. Zaccaria and F. Rossi, “On the problem of generalizing the semiconductor Bloch equation from a closed to an open system,” *Physical Review B*, vol. 67, no. 11, pp. 113311, 2003.

- [47] E. Schrödinger, “Die gegenwärtige situation in der quantenmechanik,” *Naturwissenschaften*, vol. 23, no. 48, pp. 807–812, 1935.
- [48] T. Maudlin, “Three measurement problems,” *topoi*, vol. 14, no. 1, pp. 7–15, 1995.
- [49] D. Bohm and J. Bub, “A proposed solution of the measurement problem in quantum mechanics by a hidden variable theory,” *Reviews of Modern Physics*, vol. 38, no. 3, pp. 453, 1966.
- [50] E. P. Wigner, “The problem of measurement,” *American Journal of Physics*, vol. 31, no. 1, pp. 6–15, 1963.
- [51] A. J. Leggett, “The quantum measurement problem,” *science*, vol. 307, no. 5711, pp. 871–872, 2005.
- [52] J. Neumann, *Mathematische grundlagen der quantenmechanik*, Verlag von Julius Springer Berlin, 1932.
- [53] J. Bell, “Against measurement,” *Physics world*, vol. 3, no. 8, pp. 33, 1990.
- [54] D. Dürr and S. Teufel, *Bohmian mechanics: the physics and mathematics of quantum theory*, Springer Science & Business Media, 2009.
- [55] M. Daumer, D. Dürr, S. Goldstein, and N. Zanghì, “Naive realism about operators,” *Erkenntnis*, vol. 45, no. 2-3, pp. 379–397, 1996.
- [56] D. Dürr, S. Goldstein, and N. Zanghì, “Quantum equilibrium and the role of operators as observables in quantum theory,” *Journal of Statistical Physics*, vol. 116, no. 1, pp. 959–1055, 2004.
- [57] J. Bell, *Speakable and unspeakable in quantum mechanics: Collected papers on quantum philosophy*, Cambridge university press, 2004.
- [58] B. S. DeWitt, “Quantum mechanics and reality,” *Physics today*, vol. 23, no. 9, pp. 30–35, 1970.
- [59] L Reggiani, E Starikov, P Shiktorov, V Gruzinskis, and L Varani, “Modelling of small-signal response and electronic noise in semiconductor high-field transport,” *Semiconductor science and technology*, vol. 12, no. 2, pp. 141, 1997.
- [60] L Varani, T Kuhn, L Reggiani, Y Perles, JC Vaissiere, and JP Nougier, “Monte carlo analysis of fluctuations in submicron n+ nn+ structures,” *Semiconductor Science and Technology*, vol. 7, no. 3B, pp. B552, 1992.

- [61] S. Goldstein, J. L. Lebowitz, C. Mastrodonato, R. Tumulka, and N. Zanghì, “Normal typicality and von Neumanns quantum ergodic theorem,” in *Proceedings of the Royal Society of London A: Mathematical, Physical and Engineering Sciences*. The Royal Society, 2010, vol. 466, pp. 3203–3224.
- [62] R. Landauer, “Condensed-matter physics: The noise is the signal,” *Nature*, vol. 392, no. 6677, pp. 658–659, 1998.
- [63] C. Beenakker and C. Schönberger, “Quantum shot noise,” *Physics Today*, vol. 56, no. 5, pp. 37–42, 2003.
- [64] M. Büttiker, “Scattering theory of current and intensity noise correlations in conductors and wave guides,” *Physical Review B*, vol. 46, no. 19, pp. 12485, 1992.
- [65] M. Büttiker, “Scattering theory of thermal and excess noise in open conductors,” *Physical review letters*, vol. 65, no. 23, pp. 2901, 1990.
- [66] T. Martin and R. Landauer, “Wave-packet approach to noise in multichannel mesoscopic systems,” *Physical Review B*, vol. 45, no. 4, pp. 1742, 1992.
- [67] D. Marian, E. Colomé, Z. Zhan, and X. Oriols, “Quantum noise from a bohmian perspective: fundamental understanding and practical computation in electron devices,” *Journal of Computational Electronics*, vol. 14, no. 1, pp. 114–128, 2015.
- [68] G. Albareda, D. Marian, A. Benali, S. Yaro, N. Zanghì, and X. Oriols, “Time-resolved electron transport with quantum trajectories,” *Journal of Computational Electronics*, vol. 12, no. 3, pp. 405–419, 2013.
- [69] G. Albareda, F. L. Traversa, A. Benali, and X. Oriols, “Computation of quantum electrical currents through the Ramo–Shockley–Pellegrini theorem with trajectories,” *Fluctuation and Noise Letters*, vol. 11, no. 03, pp. 1242008, 2012.
- [70] A Alarcón and X Oriols, “Computation of quantum electron transport with local current conservation using quantum trajectories,” *Journal of Statistical Mechanics: Theory and Experiment*, vol. 2009, no. 01, pp. P01051, 2009.
- [71] F. Rossi, *Theory of semiconductor quantum devices: microscopic modeling and simulation strategies*, Springer Science & Business Media, 2011.
- [72] W. R. Frensley, “Wigner-function model of a resonant-tunneling semiconductor device,” *Physical Review B*, vol. 36, no. 3, pp. 1570, 1987.

- [73] A. M. Kriman, N. C. Kluksdahl, and D. K. Ferry, “Scattering states and distribution functions for microstructures,” *Physical Review B*, vol. 36, no. 11, pp. 5953, 1987.
- [74] N. C. Kluksdahl, A. M. Kriman, D. K. Ferry, and C. Ringhofer, “Self-consistent study of the resonant-tunneling diode,” *Physical Review B*, vol. 39, no. 11, pp. 7720, 1989.
- [75] F. Rossi, A. Di Carlo, and P. Lugli, “Microscopic theory of quantum-transport phenomena in mesoscopic systems: a Monte Carlo approach,” *Physical review letters*, vol. 80, no. 15, pp. 3348, 1998.
- [76] R. Rosati, F. Dolcini, R. C. Iotti, and F. Rossi, “Wigner-function formalism applied to semiconductor quantum devices: failure of the conventional boundary condition scheme,” *Physical Review B*, vol. 88, no. 3, pp. 035401, 2013.
- [77] E. Wigner, “On the quantum correction for thermodynamic equilibrium,” *Physical review*, vol. 40, no. 5, pp. 749, 1932.
- [78] X. Oriols and J. Suñé, “Study of electronic transport in tunneling devices using an incoherent superposition of time dependent wave packets,” *VLSI Design*, vol. 13, no. 1-4, pp. 145–148, 2001.
- [79] X. Oriols, E. Fernandez-Diaz, A. Alvarez, and A. Alarcón, “An electron injection model for time-dependent simulators of nanoscale devices with electron confinement: Application to the comparison of the intrinsic noise of 3d-, 2d-and 1d-ballistic transistors,” *Solid-State Electronics*, vol. 51, no. 2, pp. 306–319, 2007.
- [80] X. Du, I. Skachko, A. Barker, and E. Y. Andrei, “Approaching ballistic transport in suspended graphene,” *Nature nanotechnology*, vol. 3, no. 8, pp. 491–495, 2008.
- [81] L. M. Zhang and M. M. Fogler, “Nonlinear screening and ballistic transport in a graphene p-n junction,” *Physical review letters*, vol. 100, no. 11, pp. 116804, 2008.
- [82] M. V. Fischetti, “Master-equation approach to the study of electronic transport in small semiconductor devices,” *Physical Review B*, vol. 59, no. 7, pp. 4901, 1999.
- [83] H. Mizuta and C. J. Goodings, “Transient quantum transport simulation based on the statistical density matrix,” *Journal of Physics: Condensed Matter*, vol. 3, no. 21, pp. 3739, 1991.
- [84] M. Nedjalkov, D. Querlioz, P. Dollfus, and H. Kosina, “Wigner function approach,” in *Nano-Electronic Devices*, pp. 289–358. Springer, 2011.

- [85] M. Nedjalkov, “Wigner transport in the presence of phonons: Particle models of electron kinetics,” in *Proceedings-International School of Physics Enrico Fermi*. IOS Press; Ohmsha, 2005, vol. 160, p. 55.
- [86] D. Querlioz, H.-N. Nguyen, J. Saint-Martin, A. Bournel, S. Galdin-Retailleau, and P. Dollfus, “Wigner-Boltzmann Monte Carlo approach to nanodevice simulation: from quantum to semiclassical transport,” *Journal of computational electronics*, vol. 8, no. 3, pp. 324–335, 2009.
- [87] J. García-García, X. Oriols, F. Martin, and J. Suñé, “Comparison between the relaxation time approximation and the Boltzmann collision operator for simulation of dissipative electron transport in resonant tunnelling diodes,” *Solid-State Electronics*, vol. 39, no. 12, pp. 1795–1804, 1996.
- [88] M. Buttiker, “Coherent and sequential tunneling in series barriers,” *IBM Journal of Research and Development*, vol. 32, no. 1, pp. 63–75, 1988.
- [89] J. Wang, E. Polizzi, and M. Lundstrom, “A three-dimensional quantum simulation of silicon nanowire transistors with the effective-mass approximation,” *Journal of Applied Physics*, vol. 96, no. 4, pp. 2192–2203, 2004.
- [90] L. Diosi, “Quantum master equation of a particle in a gas environment,” *EPL (Europhysics Letters)*, vol. 30, no. 2, pp. 63, 1995.
- [91] D. Querlioz, P. Dollfus, V.-N. Do, and A. Bournel, “An improved Wigner Monte-Carlo technique for the self-consistent simulation of RTDs,” *Journal of Computational Electronics*, vol. 5, no. 4, pp. 443–446, 2006.
- [92] W. R. Frensley, “Transient response of a tunneling device obtained from the Wigner function,” *Physical review letters*, vol. 57, no. 22, pp. 2853, 1986.
- [93] D. Querlioz, J. Saint-Martin, A. Bournel, and P. Dollfus, “Wigner Monte Carlo simulation of phonon-induced electron decoherence in semiconductor nanodevices,” *Physical Review B*, vol. 78, no. 16, pp. 165306, 2008.
- [94] M. Nedjalkov, H. Kosina, S. Selberherr, C. Ringhofer, and D. K. Ferry, “Unified particle approach to Wigner-Boltzmann transport in small semiconductor devices,” *Physical Review B*, vol. 70, no. 11, pp. 115319, 2004.
- [95] J. L. dAmato and H. M. Pastawski, “Conductance of a disordered linear chain including inelastic scattering events,” *Physical Review B*, vol. 41, no. 11, pp. 7411, 1990.

- [96] L. Shifren, C. Ringhofer, and D. K. Ferry, “A Wigner function-based quantum ensemble Monte Carlo study of a resonant tunneling diode,” *IEEE Transactions on Electron Devices*, vol. 50, no. 3, pp. 769–773, 2003.
- [97] O. Jonasson and I. Knezevic, “Coulomb-driven terahertz-frequency intrinsic current oscillations in a double-barrier tunneling structure,” *Physical Review B*, vol. 90, no. 16, pp. 165415, 2014.
- [98] A. Polkovnikov, “Phase space representation of quantum dynamics,” *Annals of Physics*, vol. 325, no. 8, pp. 1790–1852, 2010.
- [99] M. Nedjalkov, S. Selberherr, D. K. Ferry, D. Vasileska, P. Dollfus, D. Querlioz, I. Dimov, and P. Schwaha, “Physical scales in the Wigner–Boltzmann equation,” *Annals of physics*, vol. 328, pp. 220–237, 2013.
- [100] R. C. Iotti and F. Rossi, “Electronic phase coherence vs dissipation in solid-state quantum devices: Two approximations are better than one,” *EPL (Europhysics Letters)*, vol. 112, no. 6, pp. 67005, 2016.
- [101] M. Nedjalkov, D. Vasileska, D. K. Ferry, C. Jacoboni, Ch. Ringhofer, I. Dimov, and V. Palankovski, “Wigner transport models of the electron-phonon kinetics in quantum wires,” *Physical Review B*, vol. 74, no. 3, pp. 035311, 2006.
- [102] O. Jonasson and I. Knezevic, “Dissipative transport in superlattices within the Wigner function formalism,” *Journal of Computational Electronics*, vol. 14, no. 4, pp. 879–887, 2015.
- [103] S. Barraud, “Dissipative quantum transport in silicon nanowires based on Wigner transport equation,” *Journal of Applied Physics*, vol. 110, no. 9, pp. 093710, 2011.
- [104] L. Boltzmann, “Weitere studien über das wärmeleichgewicht unter gasmolekülen,” in *Kinetische Theorie II*, pp. 115–225. Springer, 1970.
- [105] Z. Zhan, E. Colomés, and X. Oriols, “Unphysical features in the application of the Boltzmann collision operator in the time-dependent modeling of quantum transport,” *Journal of Computational Electronics*, vol. 15, no. 4, pp. 1206–1218, 2016.
- [106] B. R. Nag, *Electron transport in compound semiconductors*, vol. 11, Springer Science & Business Media, 2012.
- [107] R. Shankar, *Principles of quantum mechanics*, Springer Science & Business Media, 2012.

- [108] W. B. Case, “Wigner functions and Weyl transforms for pedestrians,” *American Journal of Physics*, vol. 76, no. 10, pp. 937–946, 2008.
- [109] E. Colomés, Z. Zhan, and X. Oriols, “Comparing Wigner, Husimi and Bohmian distributions: which one is a true probability distribution in phase space?,” *Journal of Computational Electronics*, vol. 14, no. 4, pp. 894–906, 2015.
- [110] X. Oriols, Z. Zhan, E. Colomés, and D. Marian, “Dissipative quantum transport using one-particle time-dependent (conditional) wave functions,” in *Computational Electronics (IWCE), 2015 International Workshop on*. IEEE, 2015, pp. 1–4.
- [111] X. Oriols, “Can decoherence make quantum theories unfalsifiable? understanding the quantum-to-classical transition without it,” in *Journal of Physics: Conference Series*, 2016, vol. 701, pp. 12004–12019.
- [112] X. Oriols and J. Mompert, *Applied Bohmian mechanics: From nanoscale systems to cosmology*, Pan Stanford Publishing, 2012.
- [113] A. Alarcón, X. Cartoixa, and X. Oriols, “Towards the explicit computation of Bohm velocities associated to N-electron wave-functions with arbitrary spin-orientations,” *physica status solidi (c)*, vol. 7, no. 11-12, pp. 2636–2639, 2010.
- [114] A. Alarcón, S. Yaro, X. Cartoixà, and X. Oriols, “Computation of many-particle quantum trajectories with exchange interaction: application to the simulation of nanoelectronic devices,” *Journal of Physics: Condensed Matter*, vol. 25, no. 32, pp. 325601, 2013.
- [115] B. Vacchini, “Completely positive quantum dissipation,” *Physical review letters*, vol. 84, no. 7, pp. 1374, 2000.
- [116] J. M. Dominy, A. Shabani, and D. A. Lidar, “A general framework for complete positivity,” *Quantum Information Processing*, vol. 15, no. 1, pp. 465–494, 2016.
- [117] C. Jacoboni and P. Lugli, *The Monte Carlo method for semiconductor device simulation*, Springer Science & Business Media, 2012.
- [118] A. Benali, F. L. Traversa, G. Albareda, A. Alarcon, M. Aghoutane, and X. Oriols, “Effect of gate-all-around transistor geometry on the high-frequency noise: analytical discussion,” *Fluctuation and Noise Letters*, vol. 11, no. 03, pp. 1241002, 2012.
- [119] A. Benali, F. L. Traversa, G. Albareda, M. Aghoutane, and X. Oriols, “Improving the intrinsic cut-off frequency of gate-all-around quantum-wire transistors without channel length scaling,” *Applied Physics Letters*, vol. 102, no. 17, pp. 173506, 2013.

- [120] M. I. Katsnelson, K. S. Novoselov, and A. K. Geim, “Chiral tunnelling and the Klein paradox in graphene,” *Nature physics*, vol. 2, no. 9, pp. 620–625, 2006.
- [121] D. Jena, T. Fang, Q. Zhang, and H. Xing, “Zener tunneling in semiconducting nanotube and graphene nanoribbon p-n junctions,” *Applied Physics Letters*, vol. 93, no. 11, pp. 112106, 2008.
- [122] J. K. David, L. F. Register, and S. K. Banerjee, “Semiclassical Monte Carlo analysis of graphene FETs,” *IEEE Transactions on Electron Devices*, vol. 59, no. 4, pp. 976–982, 2012.
- [123] A. Paussa, G. Fiori, P. Palestri, M. Geromel, D. Esseni, G. Iannaccone, and L. Selmi, “Simulation of the performance of graphene FETs with a semiclassical model, including band-to-band tunneling,” *IEEE Transactions on Electron Devices*, vol. 61, no. 5, pp. 1567–1574, 2014.
- [124] Luca Varani, Lino Reggiani, Tilmann Kuhn, Tomas Gonzalez, and Daniel Pardo, “Microscopic simulation of electronic noise in semiconductor materials and devices,” *IEEE Transactions on Electron Devices*, vol. 41, no. 11, pp. 1916–1925, 1994.
- [125] Tomas Gonzalez, Daniel Pardo, Luca Varani, and Lino Reggiani, “Monte carlo analysis of the behavior and spatial origin of electronic noise in gaas mesfet’s,” *IEEE Transactions on Electron Devices*, vol. 42, no. 5, pp. 991–998, 1995.
- [126] D. V. Morgan and M. J. Howes, “Microwave solid state devices and applications,” *Microwave Solid State Devices and Applications*, vol. 1, 1980.
- [127] Y. Taur and T. H. Ning, *Fundamentals of modern VLSI devices*, Cambridge university press, 2013.
- [128] K. Shohno, K. J. Callanan, and M. Hirayama, “47-stage P-MOS ring oscillator circuit using the two-photomask fabrication process,” *Japanese Journal of Applied Physics*, vol. 17, no. 6, pp. 1133, 1978.
- [129] S. E. Laux, “Techniques for small-signal analysis of semiconductor devices,” *IEEE Transactions on Electron Devices*, vol. 32, no. 10, pp. 2028–2037, 1985.
- [130] L. Wang, L. Li, N. Lu, Z. Ji, W. Wang, Z. Zong, G. Xu, and M. Liu, “An improved cut-off frequency model with a modified small-signal equivalent circuit in graphene field-effect transistors,” *IEEE Electron Device Letters*, vol. 36, no. 12, pp. 1351–1354, 2015.

- [131] S. Mason, "Power gain in feedback amplifier," *Transactions of the IRE Professional Group on Circuit Theory*, vol. 1, no. 2, pp. 20–25, 1954.
- [132] S. Venica, F. Driussi, P. Palestri, D. Esseni, S. Vaziri, and L. Selmi, "Simulation of DC and RF performance of the graphene base transistor," *IEEE Transactions on Electron Devices*, vol. 61, no. 7, pp. 2570–2576, 2014.
- [133] S. Cho, K. R. Kim, B.-G. Park, and I. M. Kang, "RF performance and small-signal parameter extraction of junctionless silicon nanowire MOSFETs," *IEEE Transactions on Electron Devices*, vol. 58, no. 5, pp. 1388–1396, 2011.
- [134] X. Zheng, M. Guidry, H. Li, E. Ahmadi, K. Hestroffer, B. Romanczyk, S. Wienecke, S. Keller, and U. K. Mishra, "N-polar GaN MIS-HEMTs on sapphire with high combination of power gain cutoff frequency and three-terminal breakdown voltage," *IEEE Electron Device Letters*, vol. 37, no. 1, pp. 77–80, 2016.
- [135] Z. Dong and J. Guo, "Assessment of 2-D transition metal dichalcogenide FETs at sub-5-nm gate length scale," *IEEE Transactions on Electron Devices*, vol. 64, no. 2, pp. 622–628, 2017.
- [136] J. Singh, *Semiconductor devices: basic principles*, John Wiley & Sons, 2007.
- [137] C. Rutherglen, D. Jain, and P. Burke, "Nanotube electronics for radiofrequency applications," *Nature Nanotechnology*, vol. 4, no. 12, pp. 811–819, 2009.
- [138] V. Teppati, S. Tirelli, R. Lovblom, R. Fluckiger, M. Alexandrova, and C. R. Bolognesi, "Accuracy of microwave transistor f_T and f_{MAX} extractions," *IEEE Transactions on Electron Devices*, vol. 61, no. 4, pp. 984–990, 2014.
- [139] H. Cuchillo-Sánchez, F. Zárate-Rincón, and R. Torres-Torres, "Alternative determination of the intrinsic cut-off frequency applied to a degraded MOSFET," *IEEE Microwave and Wireless Components Letters*, vol. 26, no. 9, pp. 693–695, 2016.
- [140] R. W. Hockney and J. W. Eastwood, *Computer simulation using particles*, crc Press, 1988.
- [141] Y. Cheng and M. Matloubian, "Frequency-dependent resistive and capacitive components in RF MOSFETs," *IEEE Electron Device Letters*, vol. 22, no. 7, pp. 333–335, 2001.
- [142] H. M. J. Boots, G. Doornbos, and A. Heringa, "Scaling of characteristic frequencies in RF CMOS," *IEEE Transactions on Electron Devices*, vol. 51, no. 12, pp. 2102–2108, 2004.

- [143] C. Leroy and P.-G. Rancoita, *Silicon solid state devices and radiation detection*, World Scientific, 2012.
- [144] Z. Zhan, E. Colomés, A. Benali, D. Marian, and X. Oriols, “Time-dependent simulation of particle and displacement currents in THz graphene transistors,” *Journal of Statistical Mechanics: Theory and Experiment*, vol. 2016, no. 5, pp. 054019, 2016.
- [145] D. Marian, N. Zanghì, and X. Oriols, “Weak values from displacement currents in multiterminal electron devices,” *Physical review letters*, vol. 116, no. 11, pp. 110404, 2016.
- [146] A. B. Carlson and P. B. Crilly, “Communication systems,” 2010.
- [147] Y. Tsvividis and C. McAndrew, *The MOS transistor*, Oxford University Press, 2012.
- [148] G Albareda, Jordi Suñé, and X Oriols, “Many-particle hamiltonian for open systems with full coulomb interaction: Application to classical and quantum time-dependent simulations of nanoscale electron devices,” *Physical Review B*, vol. 79, no. 7, pp. 075315, 2009.
- [149] D Marian, E Colomés, and X Oriols, “Time-dependent exchange and tunneling: detection at the same place of two electrons emitted simultaneously from different sources,” *Journal of Physics: Condensed Matter*, vol. 27, no. 24, pp. 245302, 2015.
- [150] M. Planck, “On the law of distribution of energy in the normal spectrum,” *Annalen der Physik*, vol. 4, no. 553, pp. 1, 1901.
- [151] A. Einstein, “Über einen die erzeugung und verwandlung des liches betreffenden heuristischen gesichtspunkt,” *Annalen der physik*, vol. 322, no. 6, pp. 132–148, 1905.
- [152] L. De Broglie, “Recherches sur la théorie des quanta,” *Annalen der Physik*, vol. 3, no. 22, 1925.
- [153] L. De Broglie, “La mécanique ondulatoire et la structure atomique de la matière et du rayonnement,” *Journal de Physique et le Radium*, vol. 8, no. 5, pp. 225–241, 1927.
- [154] D. Bohm, “A suggested interpretation of the quantum theory in terms of “hidden” variables. I,” *Physical Review*, vol. 85, no. 2, pp. 166, 1952.
- [155] D. Bohm, “A suggested interpretation of the quantum theory in terms of “hidden” variables. II,” *Physical Review*, vol. 85, no. 2, pp. 180, 1952.

-
- [156] J. S. Bell, “On the einstein podolsky rosen paradox,” 1964.
- [157] H. P. Stapp, “Bell’s theorem and world process,” *Il Nuovo Cimento B (1971-1996)*, vol. 29, no. 2, pp. 270–276, 1975.
- [158] T. Norsen, “The theory of (exclusively) local beables,” *Foundations of Physics*, vol. 40, no. 12, pp. 1858–1884, 2010.
- [159] H.-W. Lee, “Theory and application of the quantum phase-space distribution functions,” *Physics Reports*, vol. 259, no. 3, pp. 147–211, 1995.
- [160] L. E. Ballentine, *Quantum mechanics: A modern development*, World scientific, 1998.
- [161] F. L. Traversa, E. Buccafurri, A. Alarcon, G. Albareda, R. Clerc, F. Calmon, A. Poncet, and X. Oriols, “Time-dependent many-particle simulation for resonant tunneling diodes: interpretation of an analytical small-signal equivalent circuit,” *IEEE Transactions on Electron Devices*, vol. 58, no. 7, pp. 2104–2112, 2011.
- [162] R. G. Barrera, O. Guzman, and B. Balaguer, “Point charge in a three-dielectric medium with planar interfaces,” *Am. J. Phys*, vol. 46, no. 8, pp. 1172–1179, 1978.
- [163] M. Ianovici and J. J. Morf, “Calculation of the potential distribution around a charge or a current in the presence of three dielectric media using the image method,” *IEEE Transactions on Electrical Insulation*, , no. 2, pp. 165–170, 1977.

Appendix A

A Primer on Bohmian Mechanics

In the beginning of the twentieth century, some surprising phenomena appeared, for instance, the black-body radiation [150] and the photoelectric effect [151], which were beyond the scope of the classical explanation. In order to interpret these phenomena, physicists had to abandon classical mechanics to develop novel and abstract formalisms. In 1924, Louis de Broglie wrote in his doctoral thesis that matter, apart from its intrinsic particle-like behavior, could exhibit also a wave-like one [152]. Three years later he developed an interpretation of quantum theory based on non-classical trajectories guided by wave field, which was the origin of the pilot-wave quantum formulation [153]. This interpretation of quantum theory is referred in the literature as De Broglie-Bohm theory, also known as Bohmian mechanics. In 1952, David Bohm rediscovered de Broglie's pilot-wave theory and he was the first to really appreciate the deep fundamental issues of the Bohmian theory, for example, the so-called measurement problem [154, 155]. Before closing the topic of the historical development of Bohmian mechanics, let me mention another renowned physicist—John Bell. In 1964, inspired by Bohm's work on *nonlocal* hidden variables, he derived the famous *Bell inequalities* [156], which has been called “the most profound discovery of science” [157]. During last time, a renewed interest in the foundations of quantum mechanics appeared, and the Bohmian interpretations of the quantum phenomena are revisited. Up to now, it has been shown that the Bohmian mechanics is a correct interpretation for all non-relativistic quantum phenomena in the sense that all non-relativistic quantum phenomena can be equivalently predicted using Bohmian or other empirically equivalent theories (the orthodox or Copenhagen theory). From a practical point of view, Bohmian mechanics is a useful tool to make predictions or to explain quantum phenomena. Hereafter, I will give a brief description of the Bohmian mechanics. A detailed introduction can be found in the book [112].

A.1 The Bohmian Mechanics for Many-Particle Systems

In this appendix, we present Bohmian mechanics by describing the dynamics of a non-relativistic quantum system of N particles with their positions defined as $\vec{x} = \{x_1, \dots, x_N\}$. In the Bohmian theory, a quantum state is described by a wave function $\Psi(\vec{x}, t)$ and N trajectories $\{x_1[t], \dots, x_N[t]\}$ in physical space. These N trajectories can be also considered as a unique trajectory $\vec{x}[t]$ in the configuration space. Owing to the mentioned additional trajectories, this interpretation is different from that of the orthodox theory mentioned in Subsection 2.1.1¹. For simplicity, I will only consider one-dimensional (1D) physical space with particle 1 at position x_1 , particle 2 at position x_2 , \dots , particle N at position x_N . An extension of the results to three-dimensional (3D) physical space has no fundamental difference. The first element of describing the Bohmian quantum state is the wave function $\Psi(\vec{x}, t)$, which is ruled by the N -particle Schrödinger equation:

$$i\hbar \frac{\partial \Psi(\vec{x}, t)}{\partial t} = \left(\sum_{k=1}^N -\frac{\hbar^2}{2m} \frac{\partial^2}{\partial x_k^2} - U(\vec{x}, t) \right) \Psi(\vec{x}, t) \quad (\text{A.1})$$

being $U(\vec{x}, t)$ the electron-electron interactions. By rewriting the equation (A.1) with its complex conjugate $\Psi^*(\vec{x}, t)$, one obtain:

$$-i\hbar \frac{\partial \Psi^*(\vec{x}, t)}{\partial t} = \left(\sum_{k=1}^N -\frac{\hbar^2}{2m} \frac{\partial^2}{\partial x_k^2} - U(\vec{x}, t) \right) \Psi^*(\vec{x}, t) \quad (\text{A.2})$$

Rearranging the equations (A.1) and (A.2) in the way $\left(\Psi^* \cdot \frac{d\Psi}{dt} - \Psi \cdot \frac{d\Psi^*}{dt} \right)$, one gets:

$$\frac{\partial |\Psi(\vec{x}, t)|^2}{\partial t} = \sum_{k=1}^N \frac{\partial}{\partial x_k} \left(\frac{i\hbar}{2m} \left(\Psi^*(\vec{x}, t) \frac{\partial}{\partial x_k} \Psi(\vec{x}, t) - \Psi(\vec{x}, t) \frac{\partial}{\partial x_k} \Psi^*(\vec{x}, t) \right) \right) \quad (\text{A.3})$$

It is easy to realize that (A.3) is a *local* continuity equation derived from the many-particle Schrödinger equation, where the probability density is interpreted as $\rho(\vec{x}, t) = |\Psi(\vec{x}, t)|^2$,

¹The orthodox theory is also called the Copenhagen interpretation of quantum mechanics, or standard quantum mechanics. It was formulated by Niels Bohr and Werner Heisenberg during their collaboration in Copenhagen around 1927. It is the only theory taught at most universities. In the Copenhagen interpretation, a quantum state is represented only by the wave function $\Psi(\vec{x}, t)$. The wave function contains a full information about that system before an observation, and there has no additional “hidden” parameters. The system exhibits its wave-like or particle-like properties depending on the experimental arrangement.

the k -th component of the current density, $J_k(\vec{x}, t)$, is defined as

$$J_k(\vec{x}, t) = \frac{i\hbar}{2m} \left(\Psi(\vec{x}, t) \frac{\partial}{\partial x_k} \Psi^*(\vec{x}, t) - \Psi^*(\vec{x}, t) \frac{\partial}{\partial x_k} \Psi(\vec{x}, t) \right) \quad (\text{A.4})$$

and the electron-electron interaction $U(\vec{x}, t)$ is assumed to be a hermitian, i.e., $U^*(\vec{x}, t) = U(\vec{x}, t)$. In summary, the Schrödinger equation includes the local conservation law.

The second element of the Bohmian state is the trajectories $\{x_1[t], \dots, x_N[t]\}$. Inspired by the local continuity equation (A.3), if the k particle current density is interpreted as $J_k(\vec{x}, t) = \rho(\vec{x}, t)v_k(\vec{x}, t)$, then, a Bohmian velocity of the k particle is obtained:

$$v_k(\vec{x}, t) = \frac{J_k(\vec{x}, t)}{|\Psi(\vec{x}, t)|^2} \quad (\text{A.5})$$

where the local continuity equation (A.3) can be rewritten as:

$$\frac{d\rho(\vec{x}, t)}{dt} + \sum_{k=1}^N \nabla_k \cdot J_k(\vec{x}, t) = \frac{d\rho(\vec{x}, t)}{dt} + \sum_{k=1}^N \nabla_k \left(\rho(\vec{x}, t)v_k(\vec{x}, t) \right) = 0 \quad (\text{A.6})$$

Having known the k particle velocity in (A.5), then, the trajectory $x_k[t]$ is computed as:

$$x_k[t] = x_k[t_0] + \int_{t_0}^t v_k(\vec{x}[t'], t') dt' \quad (\text{A.7})$$

being $x_k[t_0]$ the k particle initial position at initial time t_0 . In the Bohmian theory, the trajectories move continuously under the guidance of the wave function $\Psi(\vec{x}, t)$, and the probability density $\rho(\vec{x}, t) = |\Psi(\vec{x}, t)|^2$ is interpreted as the spatial distribution of an ensemble (over many experiments) of trajectories. Such an ensemble of experiments is assumed to be achieved by repeating the experiment j many times with $j = 1, \dots, M$ being $M \rightarrow \infty$. In an experiment j , in principle, the initial positions for the many-particle trajectories cannot be known with certainty. The initial positions of $\{x_1[t], \dots, x_N[t]\}$ at time t_0 associated with the wave function $\Psi(\vec{x}, t)$ have to be selected according to the distribution (*Quantum equilibrium hypothesis*):

$$|\Psi(\vec{x}, t_0)|^2 = \lim_{M \rightarrow \infty} \frac{1}{M} \sum_{j=1}^M \prod_{k=1}^N \delta(x_k - x_k^j[t_0]) \quad (\text{A.8})$$

From a computational point of view, on the condition that an infinite ensemble of well-selected trajectories whose initial positions are defined according to the distribution $|\Psi(\vec{x}, t_0)|^2$ in equation (A.8), and that the k particle trajectory $x_k[t]$ is given by the equation (A.7), then, at any time t , according to the continuity equation (A.6), the ensemble of trajectories reproduces $|\Psi(\vec{x}, t)|^2$, that is:

$$|\Psi(\vec{x}, t)|^2 = \lim_{M \rightarrow \infty} \frac{1}{M} \sum_{j=1}^M \prod_{k=1}^N \delta(x_k - x_k^j[t]) \quad (\text{A.9})$$

The expression (A.9) explicitly confirms that the Bohmian trajectories exactly reproduce that of the position measurement in the orthodox theory, and Bohmian trajectories also can be used to describe quantum systems.

A.1.1 Rediscovering of the Bohmian Mechanics

It will be useful to derive Bohmian mechanics from a different development. Now, the Bohmian trajectory will be introduced following Bohm's original paper [154]. The many-particle wave function is rewritten in a polar form $\Psi(\vec{x}, t) = R(\vec{x}, t)e^{iS(\vec{x}, t)/\hbar}$ being $R(\vec{x}, t)$ and $S(\vec{x}, t)$ real functions, and is substituted into the Schrödinger equation (A.1). By construction, the imaginary part of the resulting equation gives:

$$\frac{\partial R^2(\vec{x}, t)}{\partial t} + \sum_{k=1}^N \frac{\partial}{\partial x_k} \left(\frac{1}{m} \frac{\partial S(\vec{x}, t)}{\partial x_k} R^2(\vec{x}, t) \right) = 0 \quad (\text{A.10})$$

which is the continuity equation identical to the one in (A.3) or in (A.6). The real part of the Schrödinger equation gives the so-called quantum Hamilton-Jacobi equation:

$$\frac{\partial S(\vec{x}, t)}{\partial t} + \sum_{k=1}^N \frac{1}{2m} \left(\frac{\partial S(\vec{x}, t)}{\partial x_k} \right)^2 + U(\vec{x}, t) - \sum_{k=1}^N \frac{\hbar^2}{2m} \frac{1}{R(\vec{x}, t)} \frac{\partial^2 R(\vec{x}, t)}{\partial x_k^2} = 0 \quad (\text{A.11})$$

The last term on the left side of the equation (A.11) gives the so-called quantum potential, as:

$$Q(\vec{x}, t) = \sum_{k=1}^N Q_k(\vec{x}, t) = \sum_{k=1}^N -\frac{\hbar^2}{2m} \frac{\partial^2 R(\vec{x}, t) / \partial x_k^2}{R(\vec{x}, t)} \quad (\text{A.12})$$

Apart from this term $Q(\vec{x}, t)$, the equation (A.11) with the rest terms is the classical Hamilton-Jacobi equation. Therefore, the velocity of a k -particle is defined as:

$$v_k(\vec{x}, t) = \frac{1}{m} \frac{\partial S(\vec{x}, t)}{\partial x_k} \quad (\text{A.13})$$

In fact, it can be easily proved that the Bohmian velocity definition in (A.13) is identical to the expression (A.5) [112]. Interestingly, a time derivative of the k particle Bohmian

velocity in (A.13) gives a quantum Newton-like equation:

$$\begin{aligned} m \frac{d}{dt} v_k(\vec{x}[t], t) &= \left[\frac{\partial^2 S(\vec{x}, t)}{\partial x_k^2} \right]_{\vec{x}=\vec{x}[t]} \dot{x}_k[t] + \left[\frac{\partial}{\partial x_k} \frac{\partial S(\vec{x}, t)}{\partial t} \right]_{\vec{x}=\vec{x}[t]} \\ &= \left[- \frac{\partial}{\partial x_k} \left(U(\vec{x}, t) - \sum_{k=1}^N \frac{\hbar^2}{2m} \frac{1}{R(\vec{x}, t)} \frac{\partial^2 R(\vec{x}, t)}{\partial x_k^2} \right) \right]_{\vec{x}=\vec{x}[t]} \end{aligned} \quad (\text{A.14})$$

In this quantum Newton-like equation, Bohmian trajectories are solutions of the quantum Newton second law (A.14), and both potential $U(\vec{x}, t)$ and quantum potential $Q(\vec{x}, t)$ introduce correlations between the degrees of freedom of the many-body quantum system.

Up to now, I have proved that the Bohmian trajectory can be used to describe any non-relativistic quantum system. Once the Bohmian trajectories are known, any quantity of the system is known. From equation (A.5), it seems that the many-particle wave function solution of the many-particle Schrödinger equation has to be known if one wants to compute the Bohmian trajectories. As a consequence, the many-body problem (explicitly discussed in Chapter 1) also appears in the Bohmian mechanics. Then, numerical approaches are also required in the Bohmian mechanics to provide approximations to the many-particle problem. Next, I will introduce a natural and original approach—based on the conditional wave function—to provide one attractive approximation for the many-body problem.

A.2 Conditional Wave Function

As discussed in Chapter 2, the direct solution of the many-particle Schrödinger equation is inaccessible because of the need of computing the equation in huge N-dimensional configuration space. Among all the accepted approaches for this many-body problem, the Bohmian mechanics provides a natural and original solution, by using the conditional wave function [158]. Typically, a N-particle quantum system in Bohmian theory is described by the wave function $\Psi(x_1, \dots, x_N, t)$ and trajectories $\{x_1[t], \dots, x_N[t]\}$ in physical space. Because of the waves and trajectories in Bohmian mechanics, some degrees of freedom of the many-particle wave function $\Psi(x_1, \dots, x_N, t)$ can be substituted with its corresponding Bohmian trajectories $\vec{x}_b[t] = \{x_1[t], \dots, x_{a-1}[t], x_{a+1}[t], \dots, x_N[t]\}$. This new wave function with reduced degrees of freedom, $\phi(x_a, t) = \Psi(x_a, \vec{x}_b[t], t)$, is called *conditional wave function*. From such wave function $\phi(x_a, t)$, an approach for solving the many-body problem is proposed [42]. In the following, firstly, I will explain why the trajectory $x_a[t]$ can be computed by using the conditional wave function. Secondly, a mathematical description of the equation of motion of the conditional wave function will be described.

A.2.1 Bohmian Velocity Computed from the Conditional Wave Function

First of all, let us compute the Bohmian velocity from the conditional wave function. The particle positions are divided as $\vec{x} = \{x_a, \vec{x}_b\}$ with $\vec{x}_b = \{x_1, \dots, x_{a-1}, x_{a+1}, \dots, x_N\}$, and with Bohmian trajectories $\vec{x}_b[t] = \{x_1[t], \dots, x_{a-1}[t], x_{a+1}[t], \dots, x_N[t]\}$. The main idea in the work [42] is that an a particle Bohmian trajectory $x_a[t]$ computed from the many-particle wave function $\Psi(\vec{x}, t)$, can be alternatively simulated from a simpler single-particle conditional wave function $\phi(x_a, t) = \Psi(x_a, \vec{x}_b[t], t)$. The conditional wave function $\phi(x_a, t)$ is a slice of the many-particle wave function. We write the single-particle wave function in a polar form $\phi(x_a, t) = r_a(x_a, t)e^{is_a(x_a, t)/\hbar}$ with $s_a(x_a, t)$ identical to the angle $S(x_a, \vec{x}_b[t], t)$ of $\Psi(x_a, \vec{x}_b[t], t)$ and with $r_a(x_a, t)$ to $R(x_a, \vec{x}_b[t], t)$. For a trajectory $x_a[t]$, the velocity $v_a[t]$ is computed from the spatial derivative of $S(x_a, \vec{x}_b, t)$ on x_a expressed in equation (A.13) when all the other positions are fixed at $\vec{x}_b = \vec{x}_b[t]$, that is,

$$v_a[t] = \frac{1}{m} \left(\frac{\partial S(x_a, \vec{x}_b, t)}{\partial x_a} \right)_{\vec{x}_b = \vec{x}_b[t]} \approx \lim_{\Delta x \rightarrow 0} \frac{1}{m} \frac{S(x_a + \Delta x, \vec{x}_b[t], t) - S(x_a, \vec{x}_b[t], t)}{\Delta x} \approx \frac{1}{m} \frac{\partial s_a(x_a, t)}{\partial x_a} \quad (\text{A.15})$$

which explains why the simpler single wave function $\phi_a(x_a, t)$ can be used to compute the Bohmian trajectory $x_a[t]$. In fact, the velocity $v_a[t]$ is only dependent on the spatial derivative of the position x_a either using $s_a(x_a, t)$ or $S(x_a, \vec{x}_b[t], t)$.

A.2.2 Equation of Motion of the Conditional Wave Function

Once the conditional wave function has been defined, it is necessary to seek what is the equation of motion for $\phi_a(x_a, t)$. In principle, an arbitrary single-valued function $\phi_a(x_a, t)$, which has well-defined first-order temporal derivative and second-order spatial derivative, can be solved from a Schrödinger like equation if the potential $W(x_a, t)$ is selected as:

$$W(x_a, t) = \frac{i\hbar \frac{\partial \phi_a(x_a, t)}{\partial t} + \frac{\hbar^2}{2m} \frac{\partial^2 \phi_a(x_a, t)}{\partial x_a^2}}{\phi_a(x_a, t)} \quad (\text{A.16})$$

Substituting $\phi_a(x_a, t)$ with its polar form into (A.16) and rearranging the equation, then, the real part of the potential $W(x_a, t)$ is:

$$\text{Real}[W(x_a, t)] = - \left(\frac{1}{2m} \left(\frac{\partial s_a(x_a, t)}{\partial x_a} \right)^2 - \frac{\hbar^2}{2m r_a(x_a, t)} \frac{\partial^2 r_a(x_a, t)}{\partial x_a^2} + \frac{\partial s_a(x_a, t)}{\partial t} \right) \quad (\text{A.17})$$

And the imaginary part:

$$\text{Imag}[W(x_a, t)] = \frac{\hbar}{2r_a^2(x_a, t)} \left(\frac{\partial r_a^2(x_a, t)}{\partial t} + \frac{\partial}{\partial x_a} \left(\frac{r_a^2(x_a, t)}{m} \frac{\partial s_a(x_a, t)}{\partial x_a} \right) \right) \quad (\text{A.18})$$

If the function $\phi(x_a, t)$ preserves the norm, then, the imaginary part $\text{Imag}[W(x_a, t)] = 0$. Replacing $r_a(x_a, t)$ with $R(x_a, \vec{x}_b[t], t)$, $s_a(x_a, t)$ with $S(x_a, \vec{x}_b[t], t)$ in (A.16) and carefully computing the first-order temporal derivative in equations (A.17) and (A.18) with:

$$\begin{aligned} \frac{\partial S(x_a, \vec{x}_b[t], t)}{\partial t} &= \left(\frac{\partial S(x_a, \vec{x}_b, t)}{\partial t} \right)_{\vec{x}_b = \vec{x}_b[t]} + \sum_{\substack{k=1 \\ k \neq a}}^N \frac{\partial S(x_a, \vec{x}_b[t], t)}{\partial x_k} v_k(\vec{x}[t], t) \\ &= \left(-\frac{1}{2m} \left(\frac{\partial S(x_a, \vec{x}_b, t)}{\partial t} \right)^2 - U(x_a, \vec{x}_b, t) - Q(x_a, \vec{x}, t) \right)_{\vec{x}_b = \vec{x}_b[t]} \\ &\quad + \sum_{\substack{k=1 \\ k \neq a}}^N \frac{\partial S(x_a, \vec{x}_b[t], t)}{\partial x_k} v_k(\vec{x}[t], t) \end{aligned} \quad (\text{A.19})$$

$$\begin{aligned} \frac{\partial R^2(x_a, \vec{x}_b[t], t)}{\partial t} &= \left(\frac{\partial R^2(x_a, \vec{x}_b, t)}{\partial t} \right)_{\vec{x}_b = \vec{x}_b[t]} + \sum_{\substack{k=1 \\ k \neq a}}^N \frac{\partial R^2(x_a, \vec{x}_b[t], t)}{\partial x_k} v_k(\vec{x}[t], t) \\ &= \left(-\sum_{k=1}^N \frac{\partial}{\partial x_k} \left(\frac{1}{m} \frac{\partial S(x_a, \vec{x}_b, t)}{\partial x_k} R^2(x_a, \vec{x}_b, t) \right) \right)_{\vec{x}_b = \vec{x}_b[t]} \\ &\quad + \sum_{\substack{k=1 \\ k \neq a}}^N \frac{\partial R^2(x_a, \vec{x}_b[t], t)}{\partial x_k} v_k(\vec{x}[t], t) \end{aligned} \quad (\text{A.20})$$

being $U(\vec{x}, t)$ the potential and $Q(\vec{x}, t)$ the quantum potential defined in equation (A.12). Finally, the equation (A.16) can be rewritten as:

$$i\hbar \frac{\partial \phi_a(x_a, t)}{\partial t} = \left(-\frac{\hbar^2}{2m} \frac{\partial^2}{\partial x_a^2} + U_a(x_a, \vec{x}_b[t], t) + G_a(x_a, \vec{x}_b[t], t) + iJ_a(x_a, \vec{x}_b[t], t) \right) \phi_a(x_a, t) \quad (\text{A.21})$$

where I define:

$$G_a(\vec{x}, t) = U_b(\vec{x}_b, t) + \sum_{\substack{k=1 \\ k \neq a}}^N \left(\frac{1}{2m} \left(\frac{\partial S(\vec{x}, t)}{\partial x_k} \right)^2 + Q_k(\vec{x}, t) - \frac{\partial S(\vec{x}, t)}{\partial x_k} v_k(\vec{x}[t], t) \right) \quad (\text{A.22})$$

$$J_a(\vec{x}, t) = \sum_{\substack{k=1 \\ k \neq a}}^N \frac{\hbar}{2R^2(\vec{x}, t)} \left(\frac{\partial R^2(\vec{x}, t)}{\partial x_k} v_k(\vec{x}[t], t) - \frac{\partial}{\partial x_k} \left(\frac{R^2(\vec{x}, t)}{m} \frac{\partial S(\vec{x}, t)}{\partial x_k} \right) \right) \quad (\text{A.23})$$

$$U(\vec{x}, t) = U_a(x_a, \vec{x}_b, t) + U_b(\vec{x}_b, t) \quad (\text{A.24})$$

Here $U(\vec{x}, t)$ is the potential appears in equation (A.1). The single-particle pseudo-Schrödinger equation (A.21) is the main result of the algorithm in the work [42]. Up to here, there are some discussions about the potential terms in (A.21):

- The term $U_a(x_a, \vec{x}_b[t], t)$ is a real-valued potential whose exact dependence on positions are known. It has to be computed from particular Bohmian positions of all particles except $x_a[t]$.
- The term $G_a(x_a, \vec{x}_b[t], t)$ is a real-valued potential whose dependence on positions are unknown and need some educated guess. In fact, it contains exchange interaction between particles except a -particle.
- The term $iJ_a(x_a, \vec{x}_b[t], t)$ is an imaginary-valued potential whose dependence on positions are unknown and need some educated guess. It claims that the single-particle wave function $\phi_a(x_a, t)$ is not conserved. Generally speaking, the many-particle wave function $\Psi(x_a, \vec{x}_b, t)$ is conserved in the whole configuration space, but not in only x_a space.

By using the equation (A.21) for computing an a particle position $x_a[t]$, the many-particle Bohmian trajectories $\{x_1[t], \dots, x_N[t]\}$ can be known once the N -coupled single-particle pseudo-Schrödinger equations are solved, and there is no need to solve directly the many-particle Schrödinger equation (A.1). Therefore, an approach based on the conditional wave function can be a reasonable approximation to solve the many-particle problem. The computational simplification comes at the price that some potential terms ($G_a(x_a, \vec{x}_b[t], t)$ and $iJ_a(x_a, \vec{x}_b[t], t)$) in the single-particle pseudo-Schrödinger equation (A.21) are unknown and required educated guesses. Some examples of the applications of the conditional wave functions can be found in the work [42].

A.3 Bohmian Mechanics in Phase Space

Generally, the phase space formulation of quantum mechanics places the position x and momentum p coordinates in equal footing. This formulation provides some benefits [159]. It provides a convenient formalism to model an open system that interacts with its environment via collisions. This explains why the scientific community has done a constant effort to construct the phase space formulations of quantum mechanics. With our perspective of more than a century, the different attempts seem a bit surprising. All orthodox attempts have inherent difficulties due to the fact that the orthodox theory itself forbids simultaneous definition of position and momentum for one particle. For instance, the Wigner or Husimi functions are called quasi-probability distributions, which we will

explicitly discuss later. On the contrary, as mentioned many times in this thesis, since the concept of particle trajectory is intrinsic in the Bohmian theory, a phase space with well-defined position x and momentum $p = mv(x[t], t)$ becomes a *natural* construction in this theory, where $v(x[t], t)$ is the Bohmian velocity and m is the electron mass.

The phase space distribution is a main tool in the phase space formulation of quantum mechanics. In the construction of the phase space distribution, the expression of the correlation between position x and momentum p by a joint probability distribution in phase space, $F(x, p)$, will be considered. For simplicity, in this part, single-particle system will be discussed. All conclusions elaborated about one-particle phase space probability functions can be straightforwardly generalized for many-particle systems, only with a large increment of notation complexity. A well-defined probability distribution in the phase space, say $F(x, p)$, for a quantum (or classical) system is constructed if it fulfills the probabilities axioms:

$$F(x, p) \geq 0 \quad (\text{A.25})$$

$$\int \int F(x, p) dx dp = 1 \quad (\text{A.26})$$

The phase space distribution should be nonnegative to permit a probability (or mean value) interpretation. In addition, the marginal distribution of the phase space distribution should give the usual position or charge probability distributions:

$$Q(x) = \int F(x, p) dp \quad (\text{A.27})$$

Expression (A.27) is an important quantity in quantum transport because it is related to the charge density, which is a very relevant magnitude in any self-consistent solution of the electron transport. In characterizing the electrical conduction of an electron system, the current density as another important quantity is built from this distribution, as:

$$J(x) = \int pF(x, p) dp \quad (\text{A.28})$$

In the following, I will construct the Bohmian, Wigner and Husimi distributions by satisfying the mentioned probabilities axioms and test how these distributions can be used in the practical computation of quantum transport. More details about the comparison of Wigner, Husimi and Bohmian distributions can be found in the paper [109].

A.3.1 The Bohmian Phase Space Distribution

If one is interested in a probability distribution in phase space, it seems appropriate to use a quantum theory that has a well-defined phase space, i.e. a theory that explicitly

accounts for well-defined positions and local momenta. Bohmian mechanics is a theory which provides a well-defined position and momentum for a particle [154, 155]. Thus, contrarily to the orthodox theory, the Bohmian theory allows the existence of a *physical* and *natural* phase space². Once the well-defined Bohmian trajectories are known, the quantum Bohmian phase space distribution can be defined as:

$$F_B(x, p, t) = \lim_{M \rightarrow \infty} \frac{1}{M} \sum_{j=1}^M \delta(x - x^j[t]) \delta(p - p^j[t]) \quad (\text{A.29})$$

where the subindex B represents the Bohmian mechanics, M is the number of different trajectories of an ensemble of experiments with different initial position³, $x^j[t]$ is a position of the trajectory at time t , while $p^j[t] = mv(x^j[t], t)$ is the momentum of the particle. Let us emphasize that, by construction, the phase space distribution constructed with Bohmian mechanics is always non-negative and it satisfies all the probability axioms in order to be a correct probability distribution. As we know, the number of Bohmian trajectories with momentum p at the position x must be positive (or zero if there are no particles there).

Substituting the Bohmian distribution (A.29), into equations (A.27), the charge density can be calculated:

$$Q_B(x) = \lim_{M \rightarrow \infty} \int \frac{1}{M} \sum_{j=1}^M \delta(x - x^j[t]) \delta(p - p^j[t]) dp = \lim_{M \rightarrow \infty} \frac{1}{M} \sum_{j=1}^M \delta(x - x^j[t]) = |\Psi(x)|^2 \quad (\text{A.30})$$

In the charge density expression, I have used the property of the Bohmian trajectory in equation (A.9). Equivalently, the current density is:

$$\begin{aligned} J_B(x) &= \lim_{M \rightarrow \infty} \int \frac{1}{M} \sum_{j=1}^M \delta(x - x^j[t]) \delta(p - p^j[t]) \cdot p \, dp \\ &= \lim_{M \rightarrow \infty} \frac{1}{M} \sum_{j=1}^M \delta(x - x^j[t]) p^j[t] = |\Psi(x)|^2 \frac{\partial S(x)}{\partial x} \end{aligned} \quad (\text{A.31})$$

being $S(x)$ the angle of the polar representation of the wave function $\Psi(x, t) = R(x)e^{(iS(x)/\hbar)}$ defined in the text in equation (A.1). In the current density (A.31), the definition of the Bohmian velocity (A.13), which is an univalent function, is used.

²We notice that the variables x and p in the Bohmian phase space $\{x, p\}$ are directly defined in the theory itself. They are part of the ontology of Bohmian mechanics. For this reason, the Bohmian phase space is a *natural* phase space.

³Let us emphasize that the different $x^j[t]$ and $p^j[t]$ associating to single-particle are different realizations of an ensemble of experiments $j = 1, \dots, M$ with the same conditions.

A.3.2 The Wigner and Husimi Distributions

In this subsection, I will define the Wigner and Husimi Phase Space probability distributions, and then, compare the Bohmian with the Wigner and Husimi distributions with some numerical results in the following subsection.

Wigner Distribution

For a given state $|\Psi\rangle$, one can construct the density matrix operator $\hat{\rho} = |\Psi\rangle\langle\Psi|$ and express it in the position representation $\langle x|\hat{\rho}|x'\rangle = \langle x|\Psi\rangle\langle\Psi|x'\rangle$ or in the momentum representation $\langle p|\hat{\rho}|p'\rangle = \langle p|\Psi\rangle\langle\Psi|p'\rangle$. The Wigner distribution can be interpreted as an intermediate representation between this two and it is given by a Wigner-Weyl transform of the density matrix as [77] :

$$F_W(x, p) = \frac{1}{2\pi\hbar} \int \Psi(x + \frac{y}{2})\Psi^*(x - \frac{y}{2})e^{i\frac{py}{\hbar}} dy \quad (\text{A.32})$$

where $\Psi(x) = \langle x|\Psi\rangle$. It is relevant to mention that the Wigner distribution is a quasi-probability distribution. It does not satisfy, in general, the condition given in equation (A.25) for a well-defined phase space probability distribution, i.e., negative values $F_W(x, p) < 0$ could appear in some regions of the phase space. The charge density can be computed by substituting the Wigner distribution into equation (A.27):

$$Q_W(x) = \int \frac{1}{2\pi\hbar} \int \Psi(x + \frac{y}{2})\Psi^*(x - \frac{y}{2})e^{i\frac{py}{\hbar}} dy dp = \int \Psi(x + \frac{y}{2})\Psi^*(x - \frac{y}{2})\delta(y)dy = |\Psi(x)|^2 \quad (\text{A.33})$$

which is identical to the charge density (A.30) in the Bohmian case. The current density is also computed by displacing the distribution in equation (A.28) with the Wigner one. Here, I just give the result of the current density and a more detailed discussion about how to derive the result can be found in the paper [109]. The current density computing from the Wigner distribution is:

$$J_W(x) = |\Psi(x)|^2 \frac{\partial S(x)}{\partial x} \quad (\text{A.34})$$

We can clearly see, that this result is also the one obtained for the Bohmian distribution. At this point, we see that $F_W(x, p)$ is a good candidate to study quantum transport. However, it is “dangerous” to take seriously the Wigner (quasi) phase space when further developing the Wigner function for the quantum transport, for example, when including transitions between the phase space points $\{x, p\}$ and $\{x, p'\}$ due to the (Fermi Golden rule) scattering.

Husimi Distribution

The Husimi distribution (F_H) is another possible phase space distribution built from the Copenhagen school [160] :

$$F_H(x, p) = \frac{1}{\pi\hbar} \int F_W(x', p') e^{-\frac{(x-x')^2}{2s^2}} e^{-\frac{(p-p')^2 2s^2}{\hbar^2}} dx' dp' \quad (\text{A.35})$$

where s is an arbitrary parameter, and each choice of s gives a different basis function set $\{x, p\}$. The charge density $Q_H(x)$ is [109]:

$$Q_H(x) = \frac{1}{\sqrt{2\pi s^2}} \int |\Psi(x')|^2 e^{-\frac{(x-x')^2}{2s^2}} dx' \quad (\text{A.36})$$

and the current density is [109]:

$$J_H(x) = \frac{1}{\sqrt{(2\pi s^2)}} \int |\Psi(x')|^2 \frac{\partial S(x')}{\partial x'} e^{-\frac{(x-x')^2}{2s^2}} dx' \quad (\text{A.37})$$

We can clearly see, that this results are the ones obtained for the Wigner or Bohmian distributions, but smoothed by a Gaussian function. The difficulties in properly providing the current and charge densities are a dramatic drawback for the correct simulation of quantum electronic devices with the Husimi distribution. Once the Bohmian, Wigner and Husimi distributions have been constructed, in the following, I will provide some simple simulations to test the mentioned properties of these distributions.

A.3.3 Comparing the Bohmian, Wigner and Husimi Distributions

According to the conceptual discussions in the previous sections, here, I provide numerical examples for the three mentioned quantum phase space distributions and the related charge density and current density. For simplicity, we consider a simple one-dimensional Gaussian wave packet impinging in a symmetric double barrier. At the initial time t_0 , the wave function of a Gaussian wave packet at the left of the barrier is :

$$\Psi(x, t_0) = \left(\frac{1}{2\pi a_0^2}\right)^{\frac{1}{4}} e^{ik_0(x-x_0)} \exp\left(-\frac{(x-x_0)^2}{4a_0^2}\right) \quad (\text{A.38})$$

where $a_0 = 7.5$ nm is the initial spatial variance of the wave packet, $x_0 = 100$ nm is the initial central position and $k_0 = 0.69$ nm⁻¹ is the central wave vector. In addition, for the Husimi evolution, I used also the same dispersion: $s = 7.5$ nm.

The time evolution of the initial wave packet is computed by numerically solving the Schrödinger equation (A.1) for a single-particle system. Then, I compute the three

quantum phase space distributions at three different times corresponding to the initial time $t_0 = 0$ ps, the time $t_1 = 0.09$ ps when the wave packet is interacting with the barrier and the time $t_2 = 0.3$ ps when the interaction is nearly finished and the initial wave packet is clearly split into a transmitted and a reflected components. The information corresponding to these three times are plotted in figures A.3.1, A.3.2 and A.3.3, respectively.

Let us start by comparing the evolutions of the Bohmian, Wigner and Husimi distributions in figures A.3.1-A.3.3. It is clearly seen that the Bohmian and Husimi distributions have non-negative values everywhere at any time, satisfying clearly the first probability axiom (A.25). At the initial time, the Wigner distribution is also non-negative, however, in later times at t_1 and t_2 , negative values appears in some regions of the phase space.

Next, let us compare the charge and current densities calculated using equations (A.27) and (A.28) for the three quantum distributions. It is relevant to emphasize that the values obtained from the Bohmian and Wigner distributions are always completely identical. However, the values of equations (A.36) and (A.37) for the Husimi distribution does not provide the correct charge and current densities obtained from the wave function. It clearly see that the module squared of the wave packet (blue lines) in figures A.3.1b, A.3.2b and A.3.3b are equivalent to the charge density of the Bohmian and Wigner distributions, but not to the Husimi one.

After confirming, from the numerical simulations, the unphysical features that we obtain from the distributions (i.e. the negative values of the Wigner distribution, the mistaken results for the charge and current densities for the Husimi distribution and the success in both aspects of the Bohmian distribution), I further clarify the consequences of the negative values appeared in the Wigner distribution. After the interaction with the double barrier, say at the time t_2 , the initial wave packets $\Psi(x, t)$ splits into a reflected $\Psi_R(x, t)$ part and a transmitted $\Psi_T(x, t)$ part. However, in addition, there are large non-zero values (negative and positive, because when integrating in this region of the phase space the result must be zero) of $F_W(x, p)$ in the middle of the barrier, $x = 150$ nm, at places where no probability presence of the electron is supposed to be according to figure A.3.3b. If one tries to gives a physical meaning to $F_W(x, p)$ at these points in figure A.3.3c (as a *true* physical probability distribution of the electron at the phase space), one must be very careful. For example, let us imagine that we introduce an *ad-hoc* scattering term (due to impurities, for example) in the quantum equation of motion of the Wigner function. If such *ad-hoc* scattering mechanics is introduced as a transition from an old phase space point $\{x_C, p\}$ (for example, $x_C = 150$ nm) towards the new point $\{x_C, p'\}$ through the Fermi Golden rule probability $W_{p', p}$, we are moving electrons

Table A.1: In this table, it is represented which distribution fulfills the requirements in order to be a complete probability distribution. It clearly see that the Bohmian distribution is the only one successful.

	F_B	F_W	F_H
Positive distribution	Yes	No	Yes
Get the exact $Q(x)$	Yes	Yes	No
Get the exact $J(x)$	Yes	Yes	No

from places ($x_C = 150$ nm) where there is no electron. The mistake is because we introduce the scattering mechanism by hand as an extra *ad-hoc* term in the quantum equation of movement. Obviously, this spurious effect is not present if the scattering (with the impurity) is introduced directly in the Hamiltonian inside the quantum equation of motion. This spurious effect does not occur within the Bohmian distribution, because as seen in figure A.3.3a, there is only non-zero probabilities at locations where the electron may be reflected or transmitted, but not in other regions. Furthermore, in Chapter 4, I have a detail discussion how the Wigner distribution function could provide unphysical results (negative charge density) in a quantum transport with scatterings.

In summary, the characteristics of the three distributions are seen in table A.1. In any case, contrarily to the Copenhagen school, Bohmian mechanics allows a well-defined probability distribution in phase space (according to the rules (A.25)-(A.28)) to exactly reproduce the charge and current densities used in the development of quantum electron transport simulators. These good properties are just a consequence of the ontology of the Bohmian theory, which allows well-defined momentum and position, simultaneously, for an electron. In the authors' opinion, the Bohmian distribution has an enormous potential to be developed and exploited, in general, for study any (non-relativistic) quantum system and, in particular, for quantum electron transport [42, 67, 161].

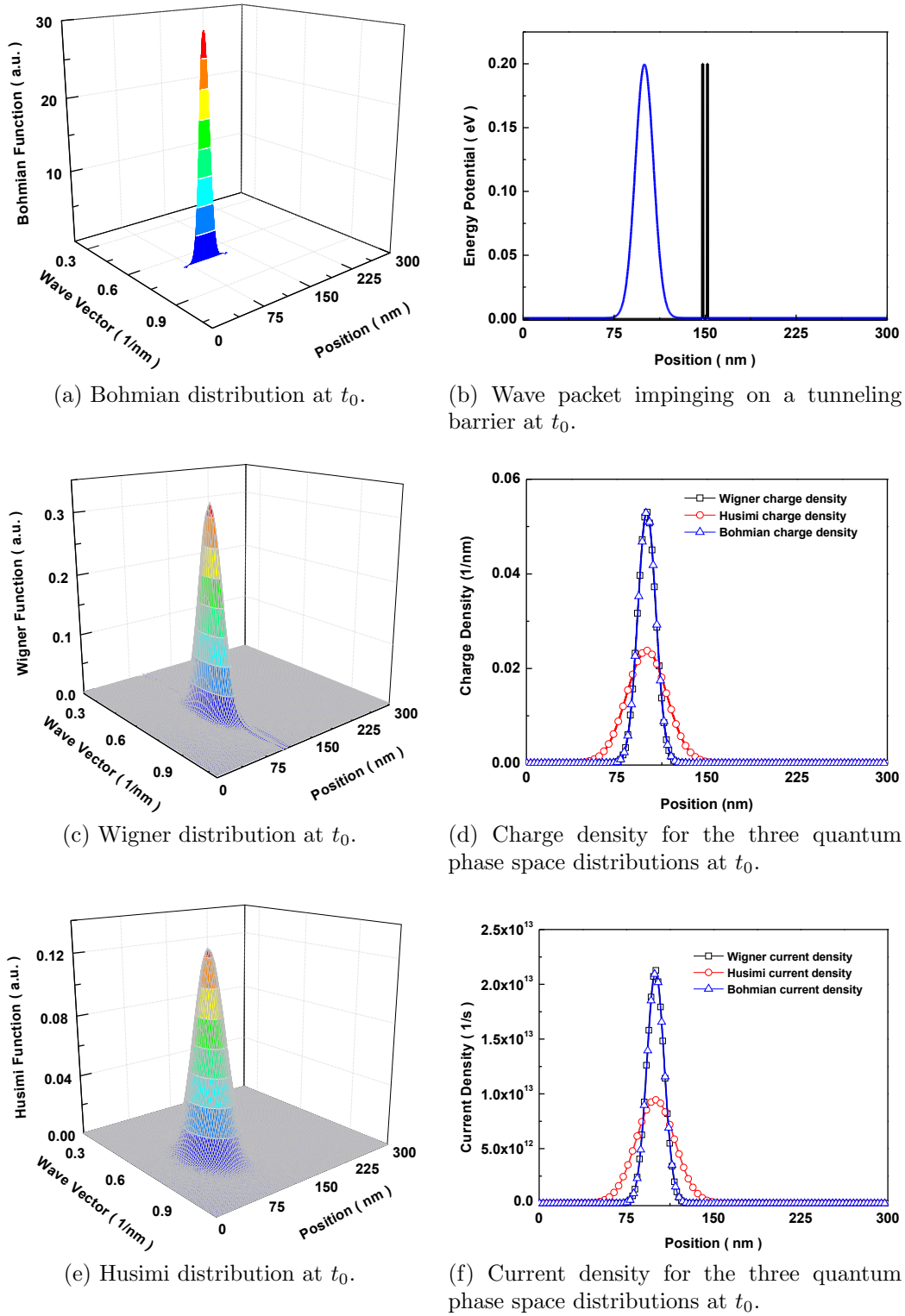


Figure A.3.1: Simulation of the (a) Bohmian distribution, (c) Wigner distribution and (e) Husimi distribution at the initial time t_0 . (b) simulation of the wave packet impinging on a double barrier, the simulation parameters are: $E = 0.09$ eV, $m^* = 0.2m_0$, where m_0 is the free-electron mass, the barrier height is 0.2 eV, the barrier width is 0.8 nm and the well depth is 3.2 nm (d) and (f) are the charge and current densities for the three phase space distributions, respectively.

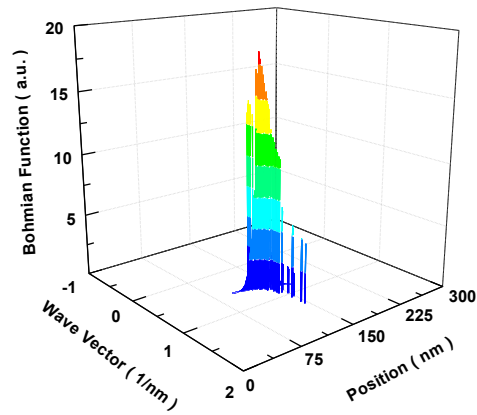
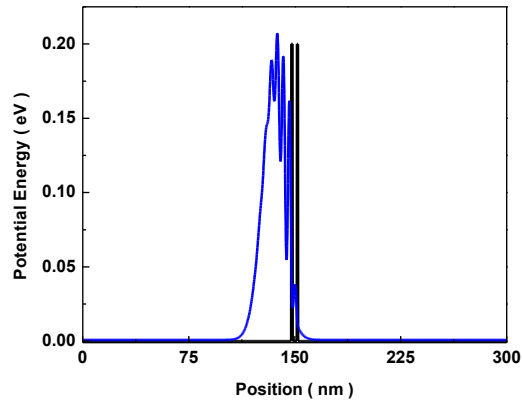
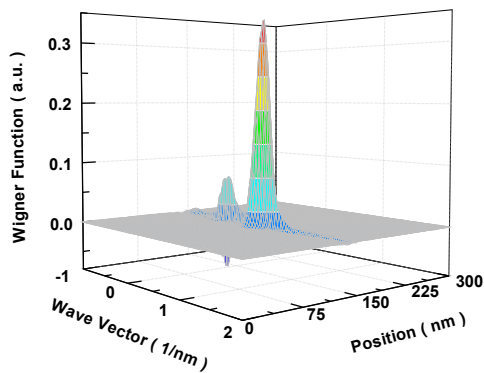
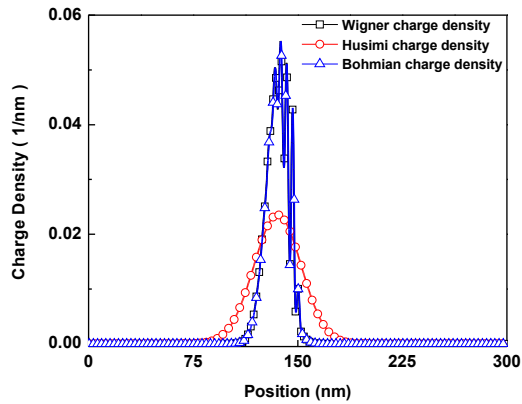
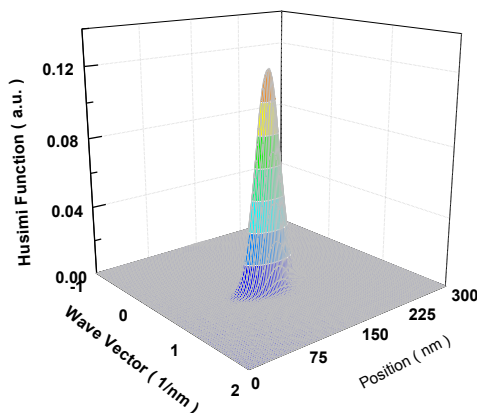
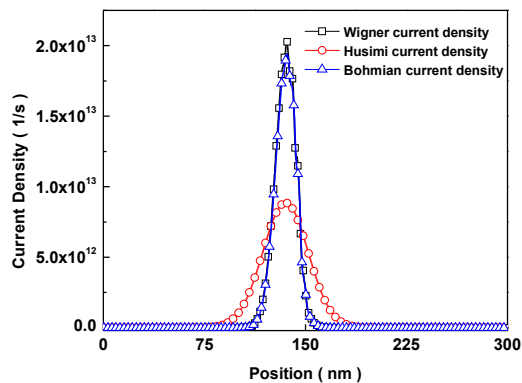
(a) Bohmian distribution at t_1 .(b) Wave packet impinging on a tunneling barrier at t_1 .(c) Wigner distribution at t_1 .(d) Charge density for the three quantum phase space distributions at t_1 .(e) Husimi distribution at t_1 .(f) Current density for the three quantum phase space distributions at t_1 .

Figure A.3.2: Simulation of the (a) Bohmian distribution, (c) Wigner distribution and (e) Husimi distribution at the time t_1 . (b) simulation of the wave packet impinging on a tunneling barrier with the same parameters as in Fig. A.3.1. (d) and (f) are the charge density and current density for the three phase space distributions, respectively.

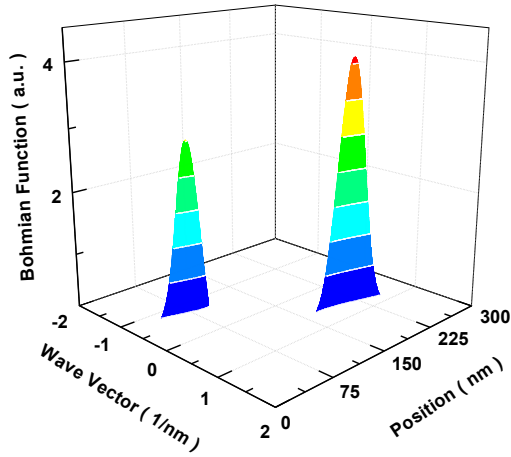
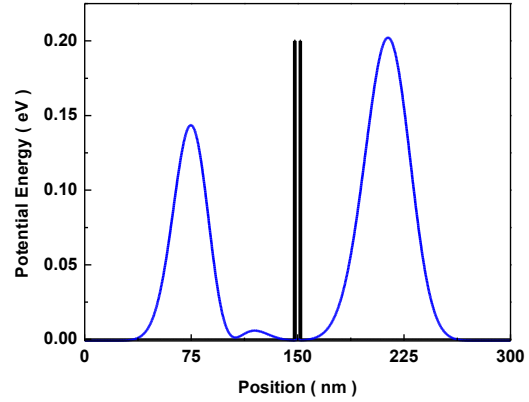
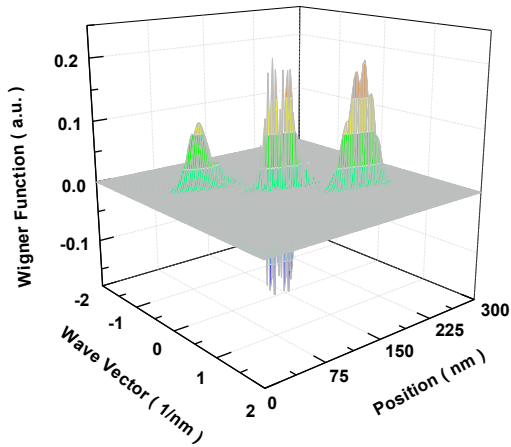
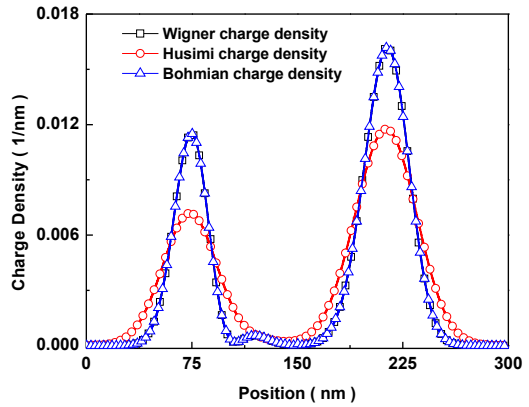
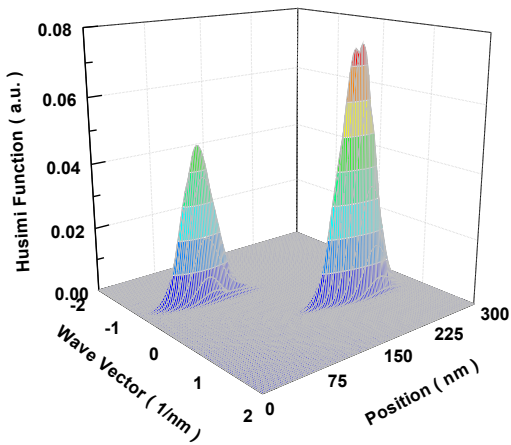
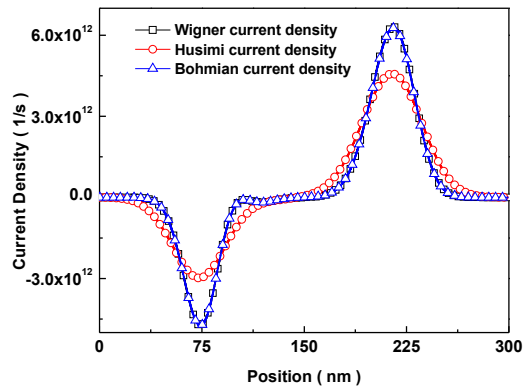
(a) Bohmian distribution at t_2 .(b) Wave packet impinging on a tunneling barrier at t_2 .(c) Wigner distribution at t_2 .(d) Charge density for the three quantum phase space distributions at t_2 .(e) Husimi distribution at t_2 .(f) Current density for the three quantum phase space distributions at t_2 .

Figure A.3.3: Simulation of the (a) Bohmian distribution, (c) Wigner distribution and (e) Husimi distribution at the time t_2 . (b) simulation of the wave packet impinging on a tunneling barrier with the same parameters as in Fig. A.3.1. (d) and (f) are the charge density and current density for the three phase space distributions, respectively.

Appendix B

Using the Image Method to Solve the Problem of a Point Charge in Presence of Three Dielectric Media with Planar Interfaces

The image method described in any physical textbook is used for computing the potential and the electrical distribution around electrostatic charges in the presence of conductors or dielectrics. In the case of a point charge q near a conducting plane, by using the boundary conditions, we can directly write the field due to q and to an imaginary point charge $-q$ at a suitable position. In this section, we will extend the method of the images to the case of an electrostatic point charge in the presence of three arbitrary different dielectric media, i.e. two semi infinite media separated by a sheet.

The figure 5.1.1 in Chapter (5) shows a geometry of the problem: a point charge is imbedded in a three-dielectric medium with infinite planar interfaces. Without loss of generality, we locate the point charge q at an arbitrary point $A_1(x_0, y_0, z_0)$ in the second layer. For simplicity, we consider the situation of planar interfaces perpendicular to the y axis and characterized by the sequence of dielectric constants:

$$\varepsilon_1, \quad y \leq Y_1 \quad (\text{B.1})$$

$$\varepsilon_2, \quad Y_1 \leq y \leq Y_2 \quad (\text{B.2})$$

$$\varepsilon_3, \quad y \geq Y_2 \quad (\text{B.3})$$

Using the method of images [162, 163], a straightforward calculation of potential Φ at an arbitrary point $P(x, y, z)$ described by rectangular coordinates is:

$$\Phi_1 = \frac{T_{12}q}{4\pi\epsilon_1} \left[\frac{1}{r_0} + \sum_{n=1}^{\infty} (L_{12}L_{32})^{n-1} \left(\frac{L_{12}L_{32}}{r_{na}^+} + \frac{L_{32}}{r_{nb}^+} \right) \right], \quad y \leq Y_1 \quad (\text{B.4})$$

$$\Phi_2 = \frac{q}{4\pi\epsilon_2} \left[\frac{1}{r_0} + \sum_{n=1}^{\infty} (L_{12}L_{32})^n \left(-\frac{L_{32}}{r_{na}^-} - \frac{1}{r_{nb}^-} - \frac{1}{r_{nb}^+} - \frac{L_{12}}{r_{na}^+} \right) \right], \quad Y_1 \leq y \leq Y_2 \quad (\text{B.5})$$

$$\Phi_3 = \frac{T_{32}q}{4\pi\epsilon_3} \left[\frac{1}{r_0} + \sum_{n=1}^{\infty} (L_{12}L_{32})^{n-1} \left(\frac{L_{12}L_{32}}{r_{na}^-} + \frac{L_{12}}{r_{nb}^-} \right) \right], \quad y \geq Y_2 \quad (\text{B.6})$$

where $T_{i2} = \frac{2\epsilon_i}{\epsilon_i + \epsilon_2}$ and $L_{i2} = \frac{\epsilon_2 - \epsilon_i}{\epsilon_2 + \epsilon_i}$ with $i = 1, 3$. The distances between point P and the infinity array of charges are given by:

$$r_0 = [(x - x_0)^2 + (y - y_0)^2 + (z - z_0)^2]^{\frac{1}{2}} \quad (\text{B.7})$$

$$r_{na}^- = [(x - x_0)^2 + (y - y_0 + 2n(Y_2 - Y_1))^2 + (z - z_0)^2]^{\frac{1}{2}} \quad (\text{B.8})$$

$$r_{nb}^- = [(x - x_0)^2 + (y + y_0 - 2Y_1 + 2(n-1)(Y_2 - Y_1))^2 + (z - z_0)^2]^{\frac{1}{2}} \quad (\text{B.9})$$

$$r_{nb}^+ = [(x - x_0)^2 + (y + y_0 - 2Y_2 - 2(n-1)(Y_2 - Y_1))^2 + (z - z_0)^2]^{\frac{1}{2}} \quad (\text{B.10})$$

$$r_{na}^+ = [(x - x_0)^2 + (y - y_0 - 2n(Y_2 - Y_1))^2 + (z - z_0)^2]^{\frac{1}{2}} \quad (\text{B.11})$$

It has been proved that the infinite series in the potential expressions can be truncated and that the number of terms $10 \sim 20$ is sufficient enough to achieve a good precision [163]. In BITLLES simulator, within reasonable limits for a rapid calculation, we define $n = 100$.

Appendix C

Publications and Conferences

Publications

- A:** Z. Zhan, E. Colomés and X. Oriols, “*Limitations of the intrinsic cut-off frequency to correctly quantify the speed of nanoscale transistor*”, IEEE Trans. Electron Devices 64 (2017).
- B:** Z. Zhan, E. Colomés and X. Oriols, “*Unphysical features in the application of the Boltzmann collision operator in the time dependent modelling of quantum transport*”, J. Comput. Electron. 15: 1206-1218 (2016).
- C:** Z. Zhan, E. Colomés, A. Benali, D. Marian and X. Oriols, “*Time-dependent simulation of particle and displacement currents in THz graphene transistors*”, J. Stat. Mech. Theor. Exp. 2016: 054019 (2016).
- D:** E. Colomés, Z. Zhan and X. Oriols, “*Comparing Wigner, Husimi and Bohmian distributions: which one is a true probability distribution in phase space?*”, J. Comput. Electron. 14: 894-906 (2015).
- E:** D. Marian, E. Colomés, Z. Zhan, X. Oriols, “*Quantum noise from a Bohmian perspective: fundamental understanding and practical computation in electron devices*”, J. Comput. Electron. 14: 114-128 (2015).
- F:** F. L. Traversa, Z. Zhan and X. Oriols, “*Absorption and injection models for open time-dependent quantum systems*”, Phys. Rev. E 90: 023304 (2014).
- G:** E. Colomés, Z. Zhan, D. Marian and X. Oriols, “*Quantum dissipation with conditional wave functions: Application to the realistic simulation of nanoscale electron devices*” (Submitted).

Conferences

- C1:** Z. Zhan, E. Colomés and X. Oriols, “*The role of the displacement current in quantifying the speed of ballistic nano devices: beyond the quasi-static approximation*”. International Workshop on Computational Nanotechnology (**IWCN 2017**), Windermere (UK), June 2017 (Oral).
- C2:** Z. Zhan, E. Colomés and X. Oriols, “*Potential problems in the application of Wigner-Boltzmann equation in the time-dependent modelling of dissipative quantum transport*”. 2nd International Wigner Workshop 2017 (**IW²**), Windermere (UK), June 2017 (Oral).
- C3:** Z. Zhan, E. Colomés and X. Oriols, “*The role of displacement current in quantifying the speed of nano devices based on 2D materials*”. 7th edition of the largest European Conference & Exhibition in Graphene and 2D Materials (**Graphene 2017**), Barcelona (Spain), March 2017 (Poster).
- C4:** X. Oriols, E. Colomés, Z. Zhan and D. Marian, “*Quantum simulation of 2D materials with dissipation*”. 7th edition of the largest European Conference & Exhibition in Graphene and 2D Materials (**Graphene 2017**), Barcelona (Spain), March 2017 (Poster).
- C5:** A. Benali, Z. Zhan, A. Alarcon, G. Albareda, F.L. Traversa, M. Yaro and X. Oriols, “*The BITLLES simulator for semiclassical and quantum nanoelectronic devices*”. International Conference on Computing Wireless and Communication Systems (**ICCWCS 2016**), Settat (Morocco), November 2016 (Oral).
- C6:** Z. Zhan, E. Colomés, A. Benali, and X. Oriols, “*Improving the intrinsic cut-off frequency of graphene transistors without channel length scaling: going beyond the quasi-static approximation*”. , 6th edition of the largest European Conference & Exhibition in Graphene and 2D Materials (**Graphene 2016**), Genova (Italy), April 2016 (Poster).
- C7:** E. Colomés, D. Marian, Z. Zhan and X. Oriols, “*Optical versus quantum trajectories in the 2D Dirac equation: Targeting high-frequency performance and noise in graphene transistors*”. 6th edition of the largest European Conference & Exhibition in Graphene and 2D Materials (**Graphene 2016**), Genova (Italy), April 2016 (Poster).
- C8:** X. Oriols, Z. Zhan, E. Colomés and D. Marian, “*Dissipative quantum transport using one-particle time-dependent (conditional) wave functions*”. 18th International

Workshop on Computational Electronics (**IWCE 2015**), West Lafayette, Indiana (USA), September 2015 (Oral).

C9: Z. Zhan, E. Colomés, A. Benali, and X. Oriols, “*The electron transit time is not the ultimate responsible for the high-frequency noise: The frontier between electronics and electromagnetism*”. 7th international conference on Unsolved Problems on Noise (**UPoN 2015**), Barcelona (Spain), July 2015 (Poster).

C10: Z. Zhan, F. L. Traversa and X. Oriols, “*The shortest simulation-box for time-dependent computation of (Bohmian) wave packets*”, 17th International Workshop on Computational Electronics (**IWCE 2014**), Paris (France), 2-6 June 2014 (Poster).